Structural and functional studies of *Saccharomyces cerevisiae* Ccr4-Not complex with Electron microscopy

Strukturelle und funktionelle Untersuchungen von *Saccharomyces cerevisiae* Ccr4-Not Komplexen mittels Elektronenmikroskopie

Doctoral thesis for a doctoral degree
at the Graduate School of Life Sciences,
Julius-Maximilians-Universität Würzburg,
Section: Biomedicine

submitted by

Boyuan Song

from

Kunming

Würzburg 2020

Submitted on: …….

Office stamp

Members of the Thesis Committee

Chairperson: Prof. Dr. Christoph Sotriffer

Primary Supervisor: Prof. Dr. Bettina Böttcher

Supervisor (Second): Prof. Dr. Andreas Schlosser

Supervisor (Third): Prof. Dr. Utz Fischer

Date of Public Defence: ……..……

Date of Receipt of Certificates: ……

An instinctive interest in confusion and incoherence seems also to be part of what excites curiosity and promotes adaptability. Part of the fascination of any puzzle, scientific or non-scientific, is the excitement of feeling that what looks incoherent might yet be made sense of, the excitement of straining to see shapes emerging from a literal or metaphorical mist.

— Michael McIntyre

Affidavit

I hereby confirm that my thesis entitled "Structural and functional studies of Saccharomyces cerevisiae Ccr4-Not complex with Electron microscopy" is the result of my own work. I did not receive any help or support from commercial consultants. All sources and / or materials applied are listed and specified in the thesis.

Furthermore, I confirm that this thesis has not yet been submitted as part of another examination process neither in identical nor in similar form.

Würzburg, 30.08.2020
Place, Date Signature

Eidesstattliche Erklärung

Hiermit erkläre ich an Eides statt, die Dissertation "Strukturelle und funktionelle Untersuchungen von Saccharomyces cerevisiae Ccr4-Not Komplexen mittels Elektronenmikroskopie" eigenständig, d.h. insbesondere selbständig und ohne Hilfe eines kommerziellen Promotionsberaters, angefertigt und keine anderen als die von mir angegebenen Quellen und Hilfsmittel verwendet zu haben.

Ich erkläre außerdem, dass die Dissertation weder in gleicher noch in ähnlicher Form bereits in einem anderen Prüfungsverfahren vorgelegen hat.

Würzburg, 30.08.2020
Ort, Datum Unterschrift

ACKNOWLEDGEMENT

I wish to express my profound gratitude to my thesis supervisor, Prof. Dr Bettina Böttcher, for allowing me to carry out my studies in her lab, and for her support and guidance throughout these years that are instrumental in the success and completion of my thesis. It has been an absolutely fascinating journey for me through the territories of structural biology and electron cryo-microscopy.

I would also like to thank my two other thesis committee members, Prof. Dr Andreas Schlosser and Prof. Dr Utz Fischer, for their steady strong support and encouragement throughout my project. The many good advices and insights during our thesis committee meetings were undoubtedly invaluable and inspirational.

I also wish to extend my sincere gratitude towards all my dear colleagues, past and present, from the AG Böttcher. For the pleasant times we spent both inside the lab and outside at our festive gatherings. And this also goes to the rest of the Strubis and Mass Spec staff at the RVZ , as well as at the Biozentrum whom in one way or another have helped me in a great deal along the way.

Last but not the least, I would like to also thank all my family and friends who have given me unfathomable amount of moral support, understanding and encouragement in the meantime. This goes especially towards my beloved parents and fiancée Bianca who accompanied me throughout this challenging journey.

ABSTRACT

The degradation of poly-adenosine tails of messenger RNAs (mRNAs) in the eukaryotic cells is a determining step in controlling the level of gene expression. The highly conserved Ccr4-Not complex was identified as the major deadenylation complex in all eukaryotic organisms. Plenty of biochemical studies have shown that this complex is also involved in many aspects of the mRNA metabolism, but we are still lacking the detailed structural information about its overall architecture and conformational states that could help to elucidate its multifunction and the way it is coordinated in the cells. Such information can also provide a basis to finding a possible way of intervention since the complex is also involved in some diseases such as cancer and cardiovascular disorders in humans. Meanwhile, the single particle Cryo-EM method has been through a "resolution revolution" recently due to the use of the newly developed direct electron detectors and has since resolved the high-resolution structures of many macromolecular protein complexes in their near-native state. Therefore, it was employed as a suitable method for studying the Ccr4-Not complex here.

In this work, the Falcon 3EC direct detector mounted on the 300kV Titan Krios G3i Cryo-EM was evaluated for its practical performance at obtaining high-quality Cryo-EM data from protein samples of different molecular sizes. This served as a proof of principle for this detector's capabilities and as a data collection guidance for studying the macromolecular complexes, such as the Ccr4-Not, when using an advanced high-performance microscope system. Next, the endogenous yeast Ccr4-Not complex was also purified via the immuno-affinity purification method and evaluated using negative staining EM to assess the conditions of the complex before proceeding to sample preparation for Cryo-EM. This has shown that the complex had an unexpected inherently dynamic property *in vitro* and extra optimisation procedures were needed to stabilise the complex during the purification and sample preparation. In addition, by using the label-free quantitative Mass spectrometry to examine the co-immunoprecipitated complex via different tagged subunits, it was deduced that two of the subunits (Not3/Not5) that shared some sequence similarity might compete for association with the scaffold subunit of the complex. An uncharacterised protein was also identified co-immunoprecipitating with the Caf130 subunit of the yeast complex. Cryo-EM data from the purified complex provided a low-resolution map that represents a surprisingly smaller partial complex as compared to 3D structures from previous studies, although gel electrophoresis and Mass spectrometry data have identified all of the nine subunits of the Ccr4-Not core complex in the sample. It was concluded that due to the presence of many predicted unstructured regions

in the subunits and their dynamic composition in solution, the native complex could have been spontaneously denatured at the air/water interface during the sample preparation thus limiting the resolution of the Cryo-EM reconstruction.

The purified complex was also examined for its deadenylase and ubiquitin ligase activity by *in vitro* assays. It was shown that the native complex has a different rate of activity and possibly also a different mode of action compared to the recombinant complexes from other species under similar reaction conditions. The Not4 E3 ligase was also shown to be active in the complex and was likely auto-ubiquitinated in the absence of a substrate. Both types of assays have also shown that the conformational flexibility does not seem to affect the enzymatic reactions when using a chemically crosslinked form of the complex for the assay, which implies that there can be other underlying mechanisms coordinating its structural and functional relationship.

The findings from this work have therefore moved our understanding of the Ccr4-Not complex forward by looking at the different structural and functional behaviours of the endogenous complex, especially highlighting the obstacles in sample preparation for the native complex in high-resolution Cryo-EM. This would serve as foundation for future studies on the mechanism of this complex's catalytic functions and also for optimising the Cryo-EM sample to generate better data that could eventually resolve the structure to a high-resolution.

ZUSAMMENFASSUNG

Der Abbau des Poly(A)-Schwanzes von Messenger-RNAs (mRNA) in den eukaryotischen Zellen ist ein entscheidender Schritt bei der Kontrolle des Niveaus der Genexpression. Der hochkonservierte Ccr4-Not-Komplex wurde in allen eukaryotischen Organismen als der Hauptdeadenylierungskomplex identifiziert. Zahlreiche biochemische Studien haben gezeigt, dass dieser Komplex auch an vielen Aspekten des mRNA-Metabolismus beteiligt ist. Uns fehlen jedoch noch die detaillierten Strukturinformationen über seine Gesamtarchitektur und seine Konformationszustände, die zur Aufklärung seiner Multifunktion und seiner Koordinierung in den Zellen beitragen könnten. Solche Informationen können auch Grundlage für die Suche nach einem möglichen Interventionsweg bieten, da der Komplex auch an einigen Krankheiten wie Krebs und Herz-Kreislauf-Erkrankungen des Menschen beteiligt ist. In der Zwischenzeit hat die Einzelpartikel-Kryo-EM-Methode aufgrund der Verwendung der neu entwickelten direkten Elektronendetektoren kürzlich eine „Auflösungsrevolution“ durchlaufen und seitdem die hochauflösenden Strukturen vieler makromolekularer Proteinkomplexe in ihrem nahezu nativen Zustand aufgelöst. Daher wurde es hier als geeignete Methode zur Untersuchung des Ccr4-Not-Komplexes eingesetzt.

In dieser Arbeit wurde der Falcon 3EC-Direktdetektor, der an das 300-kV-Titan Krios G3i Kryo-EM montiert ist, auf seine praktische Leistung bei der Gewinnung hochwertiger Kryo-EM-Daten aus Proteinproben unterschiedlicher Molekülgröße untersucht. Dies diente als Grundsatznachweis für die Fähigkeiten des Detektors und als Leitfaden für die Datenerfassung zur Untersuchung der makromolekularen Komplexe wie Ccr4-Not bei Verwendung eines fortschrittlichen Hochleistungsmikroskopsystems. Als nächstes wurde der endogene Hefe-Ccr4-Not-Komplex auch über das Immunaffinitäts-Reinigungsverfahren gereinigt und unter Verwendung einer negativ gefärbten EM bewertet, um die Bedingungen des Komplexes zu bewerten, bevor mit der Probenvorbereitung für Kryo-EM fortgefahren wurde. Dies hat gezeigt, dass der Komplex in vitro eine unerwartete inhärent dynamische Eigenschaft aufwies und zusätzliche Optimierungsverfahren erforderlich waren, um den Komplex während der Reinigung und Probenvorbereitung zu stabilisieren. Darüber hinaus wurde unter Verwendung der markierungsfreien quantitativen Massenspektrometrie zur Untersuchung des co-immunpräzipitierten Komplexes über verschiedene markierte Untereinheiten abgeleitet, dass zwei der Untereinheiten (Not3 / Not5), die eine gewisse Sequenzähnlichkeit teilen, um die Verbindung mit der Gerüstuntereinheit des Komplexes konkurrieren könnten. Es wurde auch

ein nicht charakterisiertes Protein identifiziert, das zusammen mit der Caf130-Untereinheit des Hefekomplexes immunpräzipitiert. Kryo-EM-Daten aus dem gereinigten Komplex lieferten eine Karte mit niedriger Auflösung, die im Vergleich zu 3D-Strukturen aus früheren Studien einen überraschend kleineren Teilkomplex darstellt, obwohl Gelelektrophorese- und Massenspektrometriedaten gezeigt haben, dass alle neun Untereinheiten des Ccr4-Not Kernkomplexware in der Probe vorhanden waren. Daraus kann man schließen, dass aufgrund des Vorhandenseins vieler vorhergesagter unstrukturierter Regionen in den Untereinheiten und ihrer dynamischen Zusammensetzung in Lösung der native Komplex während der Probenvorbereitung an der Luft / Wasser-Grenzfläche spontan denaturiert werden konnte, wodurch die Auflösung des Kryo-EM Wiederaufbaus begrenzt wurde.

Der gereinigte Komplex wurde auch durch In-vitro-Tests auf seine Deadenylase- und Ubiquitin-Ligase-Aktivität untersucht. Es wurde aufgezeigt, dass der native Komplex eine andere Aktivitätsrate und möglicherweise auch eine andere Wirkungsweise aufweist als die rekombinanten Komplexe anderer Spezies unter ähnlichen Reaktionsbedingungen. Es wurde auch dargestellt, dass die Not4 E3-Ligase in dem Komplex aktiv ist und wahrscheinlich in Abwesenheit eines Substrats automatisch ubiquitiniert wird. Beide Arten von Assays haben auch gezeigt, dass die Konformationsflexibilität die enzymatischen Reaktionen bei Verwendung einer chemisch vernetzten Form des Komplexes für den Assay nicht zu beeinflussen scheint, was impliziert, dass es andere zugrunde liegende Mechanismen geben kann, die seine strukturelle und funktionelle Beziehung koordinieren.

Die Ergebnisse dieser Arbeit haben daher unser Verständnis des Ccr4-Not-Komplexes weiterentwickelt, indem wir die unterschiedlichen strukturellen und funktionellen Verhaltensweisen des endogenen Komplexes untersucht und insbesondere die Hindernisse bei der Probenvorbereitung für den nativen Komplex im hochauflösendem Kryo-EM hervorgehoben haben. Dies würde als Grundlage für zukünftige Forschungen dienen, die Mechanismen seiner katalytischen Funktionen weiter zu untersuchen und auch die Kryo-EM-Probe zu optimieren, um bessere Daten zu generieren, die die Struktur schließlich in eine hohe Auflösung auflösen könnten.

TABLE OF CONTENTS

1 Introduction

All eukaryotic organisms have a complex cellular environment that requires precise and efficient management. In order to carry out any of the numerous cellular activities and maintain homeostasis, genes embedded in the Deoxyribonucleic acid (DNA) molecules need to be expressed in either of its two functional products, ribonucleic acids (RNAs) or proteins respectively (Lodish and Darnell, 2000). Essentially, the transcription and translation processes are subjected to scrupulous controls to minimise waste of the precious cellular resources and maintain normal cellular health. On top of that, eukaryotic cells have also evolved additional regulatory measures at epigenetic, post-transcriptional and post-translational levels to further improve expression fidelity and adaptability during cell growth and development (Jaenisch and Bird, 2003, Wang et al., 2014). One highly conserved protein complex, the Ccr4-Not, has been known as a major deadenylase in cells and is also involved extensively in the regulation of gene expression, especially in the cellular mRNA turnover. However, the lack of a high-resolution structure for the overall complex means that a holistic picture of how the complex coordinates those inter-dependent regulatory pathways remain unclear. This chapter attempts to briefly outline the generic mRNA degradation pathway and the currently knowledge on the structural and functional organisation of this 9-subunit macromolecular complex being studied here. Then, a short introduction on the use of Single-particle CryoEM for structure determination of protein complexes such as the Ccr4-Not ensues.

1.1 Messenger RNA degradation in the cytoplasm

A regulated level of protein production is essential for proper cellular maintenance as well as for cell development and responses. This can be achieved directly by either preserving or eliminating the messenger RNA (mRNA) molecules available for translation in the cytoplasm. Since the synthesis of mRNAs depends mostly on the gene activation and transcription, the cells appear to have evolved two general nuclease degradation pathways to sweep up any transcripts that they deem counterproductive as illustrated in Figure 1 (Also reviewed by (Wahle and Winkler, 2013)).

The mRNA molecules themselves are inherently unstable in such a complicated cytoplasmic environment (Ross, 1995), therefore require protection from the nucleases by

forming the messenger ribonucleoproteins (mRNPs) with various auxiliary proteins as well as the 5' Cap structure and the 3' poly(A) tail. Both mRNA degradation pathways require an initial shortening of the poly(A) tail (deadenylation) involving the Pan2-Pan3 complex, followed by another deadenylase complex, Ccr4-Not, which removes the remainder tail up to near the 3'UTR using its two nuclease subunits (Maryati et al., 2015). This biphasic deadenylation process prepares the mRNA for entering into either the 5' to 3' or the 3' to 5' decay pathway. Interestingly, the Pan2 nuclease activity is facilitated by the poly(A) binding proteins on the tail region (Boeck et al., 1996), yet PABP binding inhibits deadenylation via Ccr4 (Tucker et al., 2002a). This implies that the Pan2-Pan3 digestion is an initiating step for the decay pathways, since the partially deadenylated mRNA is still capable of restoring translation from its cellular reservoir under some specific cellular conditions. Meanwhile, the Ccr4-Not deadenylation dedicates the mRNA for a complete decay (Yamashita et al., 2005, Zhang et al., 2010).

The deadenylated mRNA will then continue with the removal of the 5' ($^{m7}G_{ppp}N$-) cap structure in a process termed "deadenylation-dependent degradation". The decapping complex consists of the Dcp1 and 2 proteins, with Dcp2 bearing the hydrolytic active site and is facilitated by Dcp1 (She et al., 2008). The decapping reaction is also mediated by several effector proteins such as Pat1, Dhh1, Lsm1-7 complex and Edc3 which disrupt the translation elongation complex (Parker, 2012). Lsm1-7 binds to the deadenylated 3' end of the mRNA while Dhh1 binds to the 5' end of the mRNA, then Pat1 bridges the two to displace the remaining translation initiation complex and the eIF4E/G components that are maintaining the mRNA circularisation. Thereafter, they recruit the decapping complex for the cap structure hydrolysis into $^{m7}G_{pp}$ and $_{p}N$ components (Sharif and Conti, 2013, Tharun and Parker, 2001, Fromm et al., 2012). The new 5' end of the mRNA with an exposed monophosphate is further degraded by the Xrn1 exonuclease in 5' to 3' direction, following its recruitment by a heterodimeric interphase formed between Pat1 and Dcp1 (Braun et al., 2012, Houseley and Tollervey, 2009). At the other end, the deadenylated mRNA is susceptible to the 3' to 5' decay pathway (Anderson and Parker, 1998). This is carried out by the Exosome exonuclease complex (Januszyk and Lima, 2014). The catalytically inactive Exo9 complex is made of 3 top-ring subunits and 6 bottom-ring subunits in a double ring duplex structure (Wasmuth et al., 2014). It requires the binding of an activator protein Rrp44 to form the final active Exo10 complex (Bonneau et al., 2009). In addition, another effector complex, Ski2-3-7-8, facilitates the feeding of the mRNA strand into the Exosome catalytic site by interacting with the degrading RNA substrate (Halbach et al., 2013). The Exosome degrades the substrate until the

7-methylguanosine diphosphate at the 5’ end and a scavenger decapping enzyme, DcpS takes over the pyrophosphate cap for a complete degradation (Liu et al., 2002).

(Continues next page)

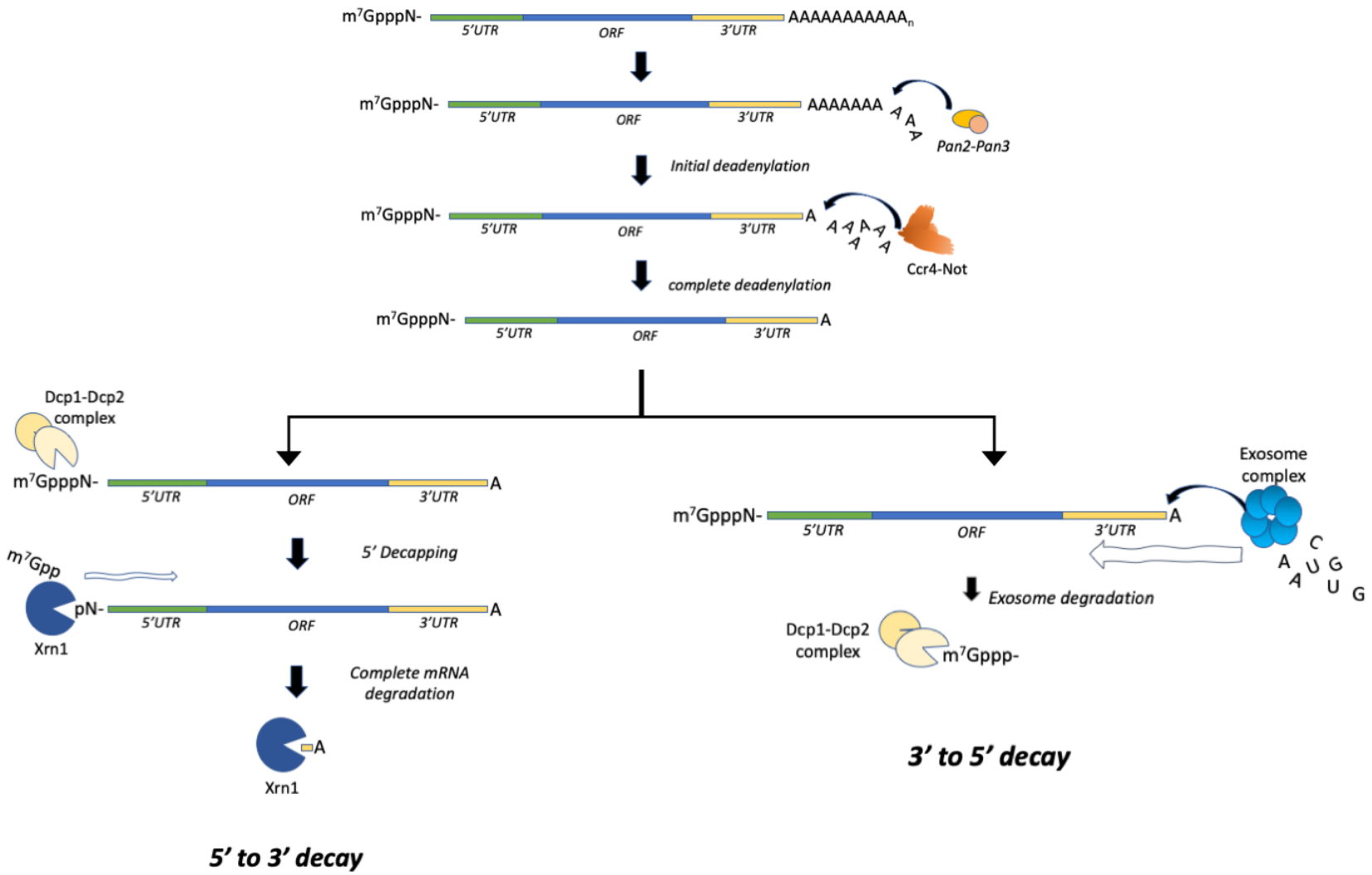

Figure 1 Illustration of mRNA decay pathways. Cytoplasmic mRNAs are first deadenylated by the Pan2-Pan3 complex which initiates the decay mechanism. The Ccr4-Not complex is then recruited to the initiated target mRNA and removes the rest of the poly(A) tail to destine the mRNA for decay, either from the 5' end or the 3' end. 5' direction degradation continues from the cleavage of the 5' cap structure by the decapping complex (Dcp1-Dcp2). The exposed phosphate end is attacked by the exonuclease Xrn1 towards the 3' end. 3' direction decay happens after the complete deadenylation and the activated cytoplasmic Exosome complex degrades the mRNA towards the 5' end. Eventually, the decapping complex finishes the cap structure.

The deadenylation-dependent degradation pathway processes the majority of mRNA decay. However, the chosen directionality of the nucleolytic decay varies between yeast and mammals (Wang and Kiledjian, 2001). In addition, there are also the aberrant translation specific quality control degradation pathways, such as the non-sense mediated decay (NMD), Non-stop mediated decay (NSD) and No-go decay (NGD) (Doma and Parker, 2007). These measures are distinct from the generic degradation pathways, as specific protein factors in each situation will target the faulty transcripts differently that had the translational machinery disrupted.

The Ccr4-Not complex in this case, was found to have multiple roles in determining the mRNA fate. Hence, it was coined the term “control freak” in this respect due to its presence all over the mRNA metabolic landscape. (reviewed by (Miller and Reese, 2012, Collart, 2016)). Therefore, it is of particular interest to understand more on how this complex works by elucidating the structural organisation and functions of this macromolecular complex. More details on this complex are elaborated in the subsequent part.

1.2 The Ccr4-Not complex

The regulation of gene expression can take effect at multiple levels from genes to proteins. Eukaryotic cells have to remain responsive to environmental and physiological changes as well as to cellular signalling all the time, which is reflected mostly in up or down regulation of specific genes. Deadenylation is an essential step that determines the mRNA stability and its abundance in cells, and this process is conferred by the highly conserved Ccr4-Not complex in all eukaryotic organisms (Collart, 2016). This complex also functions in the nucleus to influence transcription initiation and elongation, chromatin structures and nuclear export of mature mRNAs. In the cytoplasm, this complex takes part in co-translational protein quality control and translation inhibition (Figure 2). However, the contention of this complex being the major deadenylase of mRNAs while also being a multifunctional regulator of gene expression throughout the cell did not emerge all at once (reviewed by (Collart, 2003)).

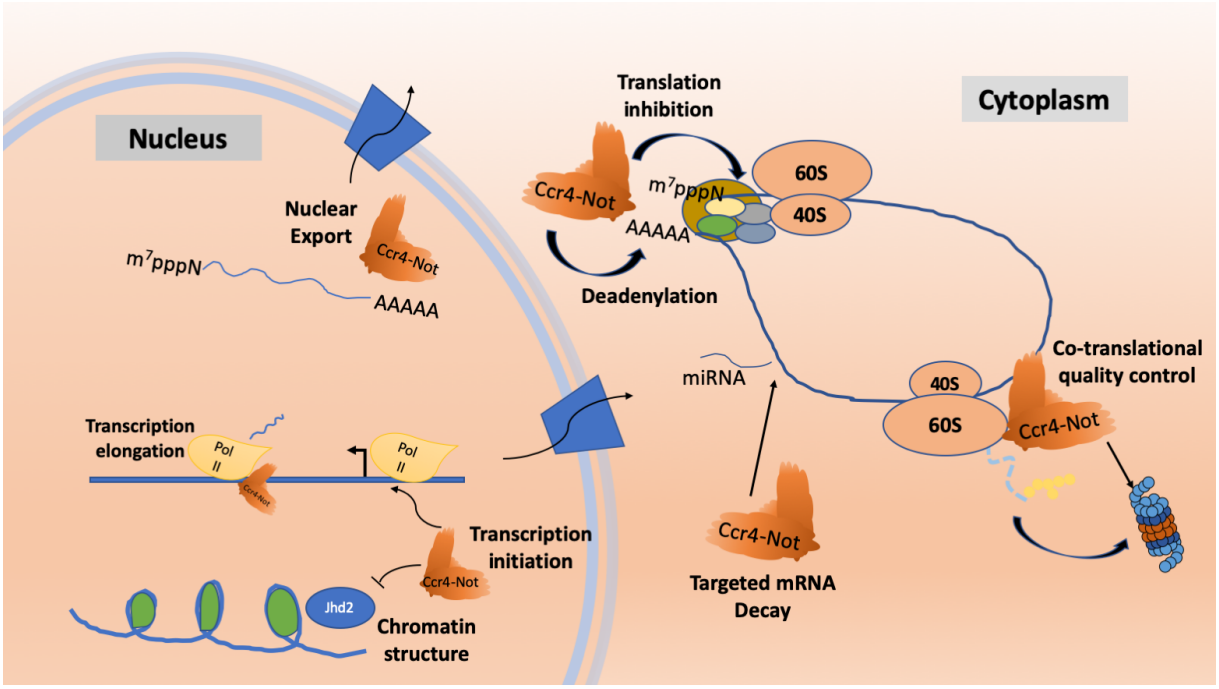

Figure 2 Cellular functions involving the Ccr4-Not complex. In the nucleus, the Ccr4-Not complex influences gene expression at the epigenetic level by repressing the chromatin remodeler Jhd2. Transcriptional process is also influenced by the Ccr4-Not at both the transcription initiation and elongation steps. The complex interacts with mRNA exporting protein assembly to dedicate unidirectional export of mature mRNAs. In the cytoplasm, Ccr4-Not is involved in mRNA degradation through deadenylation of mRNA poly(A) tail and targeted decay pathways. Ccr4-Not also couples to mature ribosome and translation initiation complex that has repercussion on translation and protein quality control concurrently. Reproduced with permission and modified according to CC license from (Collart, 2016).

1.2.1 An overview of the Ccr4-Not complex

The Ccr4-Not complex is considered a stable 9-subunits protein complex in the yeast (*Saccharomyces cerevisiae*) and consists of Not1 to Not5 proteins, Ccr4, Caf1, Caf40 and the unique Caf130 (Chen et al., 2001, Liu et al., 1998). In higher eukaryotic organisms, homologues to the yeast subunits, in addition to some splice variants and species-specific subunits, can form the consensus Ccr4-Not complex (Albert et al., 2002) that performs novel functions besides deadenylation and regulation of translation and transcription (Collart, 2016). In this thesis, the Baker's yeast nomenclature will be used for describing the subunits unless otherwise specified (Table 1).

Not1 and Not2 were initially identified as *CDC39* and *CDC36* respectively, of the cell division cycle (CDC) genes (Reed, 1980) for their linked mutant phenotype in cell cycle arrest in the G1 phase under a restrictive growth temperature. Further study had shown Not1 in yeast as the ROS1 (rescue of sterility) mutant that recovers cells having a mutant *STE4* gene. The Ste4 protein is a Gß-protein subunit needed for the pheromone response pathway during mating (Nomoto et al., 1990). A similar phenotype was discovered in Not2 mutants which led to the idea that Not1 and Not2 were responsible for the pheromone-inducible G-protein transduction pathway (Neiman et al., 1990). The other two NOT (Negative-on-TATAless) proteins, Not3 and Not5, were named based on their negative regulation of transcription on the *HIS3* gene having a TATA-less mutant core promoter (Collart and Struhl, 1994, Oberholzer and Collart, 1998). Not4 protein, though defined as a RING (Really Interesting New Gene) E3 Ubiquitin ligase (Collart, 2003), was isolated in genetic screen studies as MOT2 (modulator of transcription) or SIG1 (suppressor of inhibitory G protein) for its regulatory relationship with the mating-specific genes in the pheromone signalling pathway (Cade and Errede, 1994, Leberer et al., 1994). These findings also linked the NOT proteins to potentially influencing the TATA box binding protein (TBP) involved in transcription initiation. The co-immunoprecipitation Mass spectrometry result of the core Ccr4-Not complex subunits (Liu et al., 1998) thus also redefined the CDC proteins as Not1 and Not2 instead.

In a screen for the repressor of mutant *ADH2* gene, which is non-repressible by glucose, the Ccr4 protein was identified as a Carbon Catabolite Repressor (CCR) that reduced *ADH2* mRNA abundance as well as down-regulating the non-fermentative expression of a few other glucose sensitive genes (Denis, 1984, Denis and Malvar, 1990). Meanwhile, the Caf1 (POP2) protein was named for its participation in the PGK-promoter directed over-production of the glucose-repression pathway and temperature insensitive cell growth (Sakai et al., 1992).

Subsequently, its homologue was found in mouse as a Ccr4-associated factor (CAF) (Draper et al., 1994). The other yeast subunits, Caf40 and Caf130 were later identified in the co-immunoprecipitation Mass spectrometry data of a native Ccr4-Not complex (Chen et al., 2001) but they are less characterised.

Table 1 Nomenclature of the Ccr4-Not complex in different organisms shows evolutionarily conserved subunits and functions. [1] Not5 is the functional ortholog in the other species. [2]CNOT4 is not a stable component of the complex in mammals. [3]Caf130 is specific to S. cerevisiae and no clear homologue has been found in other organisms. Theoretical molecular mass shown in Kilo Daltons (Uniprot). Adapted from Collart, 2012 and Stowell et al., 2016.

S. cerevisiae	*S. pombe*	*D. melanogaster*	*H. sapiens*	**Cellular functions**
Not1(CDC39) 240kDa	**Not1** 237kDa	**Not1** 281kDa	**CNOT1** 267kDa	Scaffold protein
Not2(CDC36) 22kDa	**Not2** 34kDa	**Regena (Rga)** 59kDa	**CNOT2** 60kDa	Transcription repression
Not3, Not5[1] 94kDa, 66kDa	**Not3** 73kDa	**Not3** 92kDa	**CNOT3** 82kDa	
Not4 (MOT2) 66kDa	**Mot2** 54kDa	**Not4** 118kDa	**CNOT4[2]** 64kDa	E3 ligase
Ccr4 95kDa	**Ccr4** 76kDa	**Twin** 63kDa	**CNOT6/6L** 63kDa	Nucleases
Caf1 50kDa	**Pop2** 38kDa	**Pop2** 40kDa	**CNOT7/8** 33kDa	
Caf40 42kDa	**Rcd1** 32 kDa	**Rcd-1** 34 kDa	**CNOT9** 34 kDa	Protein/RNA interaction
Caf130[3] 130 kDa				Unknown functions
	Mmi1 54 kDa	**Not11** 28 kDa	**CNOT11** 55 kDa	RNA binding
		Not10 70 kDa	**CNOT10** 82 kDa	Complex integrity

1.2.2 Functions of the Ccr4-Not Complex

1.2.2.1 Generic mRNA degradation

Deadenylation of the cytoplasmic mRNA is mainly performed by the Pan2-Pan3 complex and Ccr4-Not complex as depicted above. There are two 3' to 5' exonucleases in the later complex. Ccr4 has been shown to directly interact with Caf1 via a Leucine rich repeat (LRR) domain (Clark et al., 2004) and Caf1 is in direct contact with the scaffold Not1 (Basquin et al., 2012). Both subunits are catalytically active, but Ccr4 is shown to be the dominant deadenylase in both the yeast and the human (Webster et al., 2018, Tucker et al., 2002b), and Caf1 is more important in the microRNA gene silencing pathway and for interactions with other factors (Piao et al., 2010). In yeast, Caf1 and the N-terminal part of Not1 can interact with the PABP bound decapping activator, Dhh1, and regulate deadenylation (Maillet and Collart, 2002, Tucker et al., 2001). For Metazoans, the Ccr4-Not complex was found to be bridged to the PABP via Tob1, a BTG/TOB family protein that is not conserved in yeasts and its expression is specific to cell proliferation control (Funakoshi et al., 2007). Although the precise mechanism of recruitment for the Ccr4-Not complex to the mRNA for generic degradation is still ambiguous, these evidences alluded the necessity for recruiting the whole Ccr4-Not complex, including the other factors, to contribute additional specificity in deadenylation and other gene silencing functions.

1.2.2.2 mRNA decay for translational quality control

When the normal translation process is disrupted by a defective mRNA template or starts producing aberrant polypeptides, the mRNA can be degraded co-translationally (Hu et al., 2009). Amongst the three main quality control pathways of mRNA decay (Doma and Parker, 2007), the Ccr4-Not complex is involved in at least two of them (Collart, 2016, Parker, 2012). The Non-sense Mediated Decay (NMD) involves six factors, Upf1,2,3 and Smg 5,6,7, and is stimulated when the 'Stop' codon is present in an ORF or premature termination is recognised by the elongating ribosome (Kervestin and Jacobson, 2012). Phosphorylation of Upf1 recruits the Smg5-7 heterocomplex to the erroneous mRNA and Ccr4-Not is also recruited via the interaction between Caf1 and Smg7 to facilitate deadenylation (Loh et al., 2013). In No-stop decay (NSD), mRNAs that lack the termination codon are rapidly degraded in a 3' to 5' way in the presence of the Ski complex and Exosome (van Hoof et al., 2002) , as well as in a 5' to 3' way with accelerated decapping when Ski7 and Exosome are absent (Inada and Aiba, 2005). Ccr4-Not can even concomitantly ubiquitylate the nascent polypeptide for

recycling via the Not4 E3 ligase mediated proteasomal degradation (Dimitrova et al., 2009, Inada and Makino, 2014).

1.2.2.3 Targeted mRNA decay

The Ccr4-Not complex can be recruited to target mRNAs for accelerated degradation via RNA binding proteins (RBPs) that recognise distinct sequence elements on the 3' untranslated region (3' UTR) just upstream of the poly(A) tail (Fabian et al., 2013a, Collart, 2016). In higher eukaryotes, the Ccr4-Not complex also mediates micro-RNA induced gene silencing through similar interaction with a subunit of the silencing complex to repress translation (Braun et al., 2011). These adaptor proteins, such as the Tristetraproline (TTP) family of proteins, Nanos, the BTG/TOB family of proteins and GW182, either interact directly with a region on the Not1 scaffold protein or indirectly with one of the subunits of the Ccr4-Not complex (Fabian et al., 2013a, Bhandari et al., 2014a, Doidge et al., 2012, Filipowicz and Sonenberg, 2015).

1.2.2.3.1 A/U-rich response elements (ARE)

Translational repression of mRNAs encoding the cytokines and lymphokines are regulated rigorously during cellular responses, e.g. *TNF-α*, *IFNs, c-fos and GM-CSF* etc. (Chen and Shyu, 1995). These mRNAs generally contain a cis-regulatory ARE on their 3' UTR and could be targeted by proteins that recognise this sequence element for rapid degradation with the Ccr4-Not complex by deadenylation-dependent decapping (Sanduja et al., 2012). The canonical recognition sequence has an AUUUA triplicate motif onto which the adaptor protein binds. TTP is a Zinc-finger repeats containing ARE binding protein that has been found to cause rapid mRNA decay (Brooks and Blackshear, 2013). Its C-terminal domain interacts with an unoccupied N-terminal region of the human CNOT1 that shows a MIF4G domain structure (Sandler et al., 2011, Fabian et al., 2013b). The role of the cis-acting ARE with Ccr4-Not becomes more perplexing as studies have shown that different ARE binding proteins can either stabilise or destabilise mRNAs (Bolognani and Perrone-Bizzozero, 2008, Otsuka et al., 2019)

1.2.2.3.2 Pumilio Response Element (PRE)

The Pumilio family (PUF) of proteins are conserved from yeast to human (Wreden et al., 1997, Olivas and Parker, 2000, Wickens et al., 2002, Menon et al., 2004). There are six types of PUF proteins in yeasts and they have structurally similar RNA binding domains that

can recognise the PRE motif situated at the 3' UTR of their respective target mRNAs (Webster et al., 2019), e.g. Mpt5 binds to the 3' UTR of *HO* mRNA that regulates the mating type in yeast (Goldstrohm et al., 2006). Puf3 from *Drosophila* can recognise the PRE containing mRNA of *Hunchback* and *Cyclin B* genes and induces their cellular degradation during embryonic development (Wreden et al., 1997, Wickens et al., 2002, Kadyrova et al., 2007a). Human homologues of Puf recognise a consensus motif (UGUANAUA) where the guanosine residue is believed to be conserved and the 5th residue (N) varies in different mRNAs to expand interactions among the other PUF proteins (Lapointe et al., 2015, Webster et al., 2019).

The PUF proteins respond to a specific mRNA directly via this cis-acting element or in other species, by associating with a metazoan-specific adaptor protein such as the Nanos proteins first (Wickens et al., 2002, Spassov and Jurecic, 2003). PUF binding can promote Ccr4-Not dependent deadenylation and degradation of mRNA by interacting with the Not1, Caf1 or Caf40 subunits (Webster et al., 2019, Kadyrova et al., 2007b, Goldstrohm et al., 2007). Furthermore, target mRNA that is bound by Nanos will be translationally repressed and the subsequent recruitment of the Ccr4-Not complex leads to rapid degradation of the mRNAs (Suzuki et al., 2010). Nanos proteins in vertebrates have conserved short linear motif (SLiM) at the N-terminus that also binds the C-terminal domain of Not1 for the recruitment of Ccr4-Not complex, and it is essential for Nanos' function in fly embryonic development (Bhandari et al., 2014b, Suzuki et al., 2012). An additional interaction domain in mouse Nanos2 for binding to CNot8 (Caf1 in yeast) can distinguish itself in functionality from the Nanos3 (Suzuki et al., 2012) and this may suggest a strategy in higher eukaryotes to diversify effectors of multiple translational repression pathways.

1.2.2.3.3 miRNA directed decay

miRNAs are short non-coding RNAs that have complementary sequences for binding with the repressed target and mediate assembly of the miRNA-induced silencing complex (miRISC) by recruiting the Argonaut family of proteins (Ago) as well as its adaptor proteins (Huntzinger and Izaurralde, 2011, Fabian and Sonenberg, 2012). Ago proteins bound on the target mRNA lead to the recruitment of the GW182 family of proteins, which is an essential effector in miRNA directed gene silencing (Braun et al., 2013, Fabian and Sonenberg, 2012, Huntzinger and Izaurralde, 2011). GW182 consists of a N-terminal Ago binding domain followed by a ubiquitin binding domain, a Q-rich region and a C-terminal domain (Braun et al., 2013). The N- and C-terminal regions contain multiple Glycine/Tryptophan (GW) repeats

that serve as protein-protein docking interfaces (Fabian and Sonenberg, 2012). The N-terminal GW domain of GW182 binds Ago1 while the C-terminal GW domain, also known as the silencing domain (SD), contains a PAM2 motif that is essential for the interaction of GW182 with the PABP protein that binds on the 3' poly(A) tail (Fabian et al., 2009, Zekri et al., 2009, Huntzinger et al., 2010). Ccr4-Not has been shown to be recruited by GW182 to target mRNAs to promote their degradation (Braun et al., 2011, Fabian et al., 2011, Chekulaeva et al., 2011). Human GW182 contains two Ccr4-Not interacting motifs (CIM) around its C-terminal region in addition to its GW repeats, that facilitate interaction with the Ccr4-Not complex (Chekulaeva et al., 2011). Human CNOT9 (Caf40 in yeast) protein has been found to possess two essential domains that preferentially bind the tryptophan residues on the GW182 protein (Mathys et al., 2014b, Chen et al., 2014b) therefore reciprocate its recruitment.

1.2.2.4 Deadenylation-independent repression of translation

DDX6, or Dhh1 in yeast, is a DEAD box family of ATPase-dependent RNA helicase that can inhibit translation in higher eukaryotes (Parker and Sheth, 2007). It is capable of recruiting the Ccr4-Not complex via the Not1 N-terminal MIF4G domain and such interaction leads to its conformational change and subsequent ATPase activation (Mathys et al., 2014a). This might suggest that decapping of some mRNAs are dependent on the presence of Ccr4-Not and can compete with the ARE binding proteins for the interaction domain on Not1 if other adaptor binding interfaces do not co-exist. However, whether deadenylation by the recruited Ccr4-Not deadenylase can occur concurrently to repress translation is less understood.

1.2.2.5 Co-translational protein quality control

The yeast Ccr4-Not complex includes an E3 ubiquitin ligase, Not4. Although the protein has conserved functions, it is not a constituent subunit of the complex in higher eukaryotes (Collart, 2016). Not4 contains an N-terminal RING ligase domain that interacts with the cognate E2 ligases, Ubc4/Ubc5 in yeast and ubiquitinates target proteins for entering the proteasomal degradation system (Collart, 2013, Mulder et al., 2007b). For example, Egd1 and Egd2, which belong to the nascent polypeptide complex (NAC), are ubiquitinated by Not4 (Panasenko et al., 2006, Mulder et al., 2007a). Egd ubiquitination could facilitate NAC association with the ribosome, as well as the proteasome (Panasenko et al., 2009). Not4 is also found to contribute to functional integrity via interaction with Ecm29 on the regulatory particle (RP) during the proteasome assembly (Panasenko and Collart, 2011).

Not4 is not essential for deadenylase activity or for assembly of the Ccr4-Not complex (Bai et al., 1999). Instead, it has been linked to co-translational protein quality control because stalling ribosomes during translation elongation results in co-translational degradation of the arrested nascent polypeptide by the proteasome (Dimitrova et al., 2009). Polysome fractionation showed that Not4 associates with the polysome and this is elevated by the co-translational quality control inducing factors. In addition, increased presence of polyubiquitinated proteins and protein aggregation are observed for Not4 mutants (Halter et al., 2014, Dimitrova et al., 2009, Collart and Panasenko, 2012, Panasenko and Collart, 2011). Such evidence alludes to the role of Not4 in concomitant protein degradation from the arrested translation. The poly(A) tail-independent protein degradation of the translational arrested products indicates that Not4 is not necessarily recruited by binding to the poly(A) tail (Matsuda et al., 2014). However, more information is needed to understand how the Not4 and the rest of the Ccr4-Not complex in higher eukaryotes are coordinated in such event.

1.2.3 Structural organisation of the complex

The Ccr4-Not complex in *S. cerevisiae* is formed around the Not1 scaffold protein with 8 other subunits and this docking platform is highly conserved (Bawankar et al., 2013, Chen et al., 2001, Bai et al., 1999). The other subunits are grouped in a modular convention according to their functions, namely, N-terminal module, the deadenylase module, the Caf40 module, the ubiquitination module and the NOT module. Deletion of Not1 is lethal and mutations critically jeopardise cell viability (Maillet et al., 2000). This implies that formation of the consensus complex is essential for the organism. Not1 is made up of the N-terminal HEAT repeats domain that has no definitive binding sites other than in metazoans and its C-terminal domain is also formed by stacked HEAT helical repeats that bind with the Not proteins (Bawankar et al., 2013). The central region of Not1 consists of two subunit binding sites, MIF4G and DUF3819, where Caf40 and the Caf1/Ccr4 heterodimer could bind respectively (Basquin et al., 2012) (Figure 3). CNOT1 in humans also provides similar docking interfaces for the ortholog subunits (Raisch et al., 2018), and additionally binds CNOT10/11 on its N-terminal region (Bawankar et al., 2013).

Currently, two electron microscopy studies have provided the general landscape of the subunits in those yeast Ccr4-Not complexes (Ukleja et al., 2016a, Nasertorabi et al., 2011). EM map in one of the studies thus showed an overall L-shaped molecule with a longer (~19nm) N-terminal arm and a shorter (~18nm) C-terminal arm (Nasertorabi et al., 2011). Meanwhile the

other structure showed a much smaller and more compact architecture, on top of their differing theoretical molecular mass among species. Due to the high structural heterogeneity and flexibility in the purified complex, only a low-resolution EM map (~20Å) (Ukleja et al., 2016a) could be obtained at their best, suggesting that the entire assembly must be very dynamic.

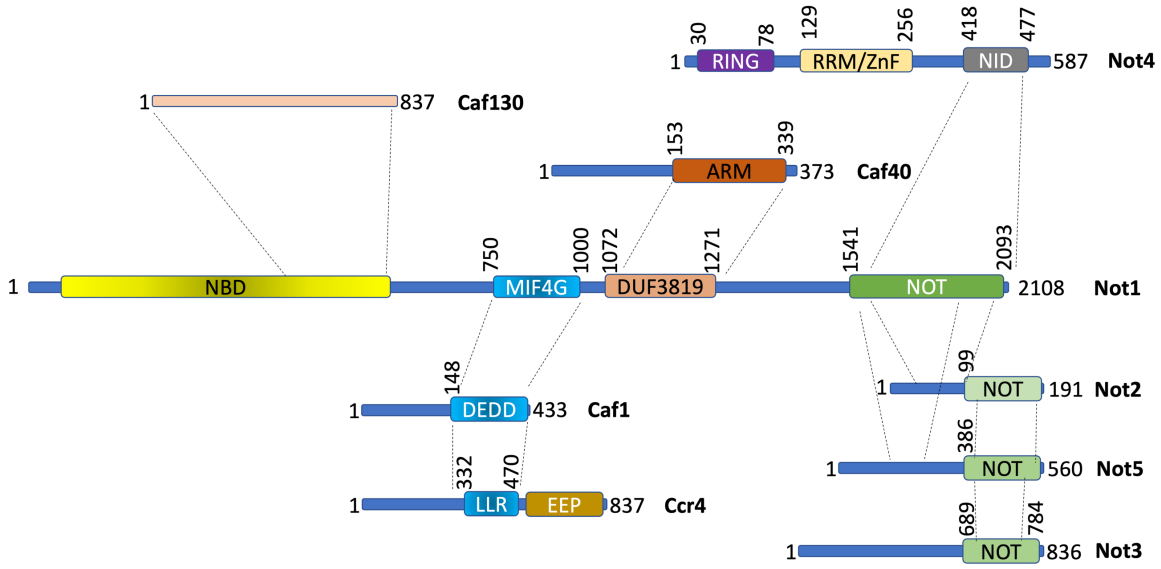

Figure 3 Illustration of Ccr4-Not subunits domain organisation. Domain structures present on each subunit of the S. cerevisiae Ccr4-Not complex and their respective interaction domains are linked by dotted lines. Not1 NBD (Not binding domain) on the N-terminal arm serves as a docking site for Caf130 in S. cerevisiae and in humans it binds to CNOT10/11. Not1 MIF4G domain has structural homology with eIF4G and interact with Caf1. Ccr4 uses its LLR domain to interact with Caf1. Caf40 binds Not1 at DUF3819 region using the convex side of its ARM motif. Yeast Not4 is stably bound to Not1 with its unstructured C-terminal tail (Not-interacting domain, NID) but in metazoan interacts with Caf40 in order to be linked to the Ccr4-Not complex. Not2/Not5 are capable of forming dimers while interacting with Not1 using their mostly unstructured N-terminal end. Not3 has a similar predicted domain architecture as Not5 but they appear to be mutually exclusive in binding. Although Not3 is co-immunoprecipitated with yeast Ccr4-Not, it is not present in metazoans. Reproduced with permission and modified according to CC license from (Collart, 2016, Xu et al., 2014).

1.2.3.1 The N-terminal module

The N-terminal module is defined by a section of the Not1 N-terminal arm, which in *S. cerevisiae* is between the amino acid residue 1 and 750, and most likely docks the yeast specific Caf130 protein (Basquin et al., 2012, Nasertorabi et al., 2011) (Figure 4). The metazoan Ccr4-Not complex has two unique subunits, CNOT10/11, which also bind to the N-terminal arm of Not1 at a region within the Not-binding domain (NBD), but are not homologous of the Caf130 (Bawankar et al., 2013). The exact function of this N-terminal module in yeast and *Drosophila* is still unclear and perhaps it provides binding sites for novel adaptor proteins that recruit the Ccr4-Not complex transiently. In *Trypanosomes*, its CNOT10 protein is found to be instrumental to the Ccr4-Not complex integrity and it also involves in the deadenylation activity (Färber et al., 2012). In human cells, Tristetraproline (TTP) has been shown to bind within the N-terminal region, but the CIM (C-terminal Interacting Motif) of TTP responsible for this interaction in human is not conserved in the yeast homologue of TTP (Collart, 2016). This suggests that the N-terminal module could have gained its functions during evolution.

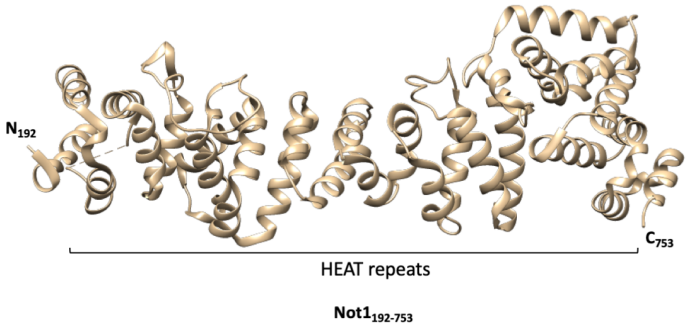

Figure 4 Illustration of the partial Not1 N-terminal structure. It is formed mainly by perpendicularly stacked helical repeats with the acronym, HEAT (Huntingtin, elongation factor 3 (EF3, protein phosphatase 2A(PP2A) and kinase TOR1). This rigid structure provides ample interaction surfaces for subunit binding. The HEAT repeats are structurally related to the Armadillo motif. PDB-4B8B (Basquin et al., 2012) using UCSF Chimera (Pettersen et al., 2004).

1.2.3.2 The Deadenylase module

This module is located near the central region of the Not1 scaffold where Caf1 interacts with the MIF4G domain, as shown by the crystal structure of a truncated trimeric interaction domain of Not1-Caf1-Ccr4 (Basquin et al., 2012) (Figure 5). This module is conserved in all eukaryotes (Albert et al., 2000, Temme et al., 2004, Chen et al., 2001). The two exonucleases tethered here are both active *in vivo*, however, Ccr4 shows preferential deadenylation activity as compared to Caf1 (Stowell et al., 2016, Tucker et al., 2002a). Although Caf1 seems

necessary for the overall deadenylation activity in *Drosophila*, Ccr4 is more crucial for the targeted mRNA decay (Temme et al., 2004). In human, presence of the two splice-variant orthologs for each of the nucleases plausibly implies that of an increased target specificity and diversity as they are found to be mutually exclusive during deadenylation (Lau et al., 2009).

In *S. cerevisiae* the Ccr4 protein is 837 amino acids long and has a leucine-rich repeat (LRR) domain needed for its association with Caf1 (at amino acids 365- 433) (Draper et al., 1994). The catalytic domain at its C-terminal end shares homology with a Mg^{2+}-dependent EEP (Endonuclease/Exonuclease/Phosphatase) DNase/phosphatase family of proteins (Dlakić, 2000). The crystal structure of the human homologue of Ccr4 (CNOT6L) has been solved in complex with AMP and single stranded DNA (Wang et al., 2010) and it shows a lack of a structured N-terminal region and no contact with the Not1 scaffold, similar to the yeast subunits below (Figure 5, green).

Caf1 has a less conserved N-terminal region and a conserved RNaseD domain at the C-terminal end belonging to the DEDD family of exonucleases (Thore et al., 2003, Daugeron et al., 2001). It hydrolyses the substrate mRNA's phosphodiester link by a two-metal ion directed mechanism (Jonstrup et al., 2007). The crystal structure of yeast Caf1 showed a slightly concaved molecule with central catalytic beta-sheets that are flanked by alpha helices (Figure 5, red centre). The catalytic activity also depends on the Zn^{2+} and Mn^{2+} ion concentration *in vivo* (Andersen et al., 2009).

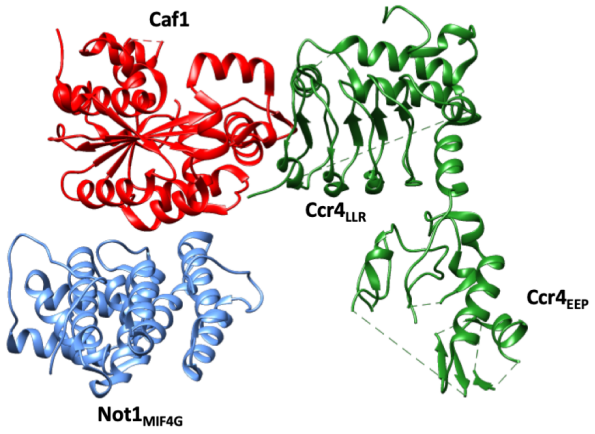

Figure 5 Illustration of the yeast Nuclease module structure. Crystal structure of the Not1-Caf1-Ccr4 shows Caf1 interaction with the Not1 MIF4G domain. Ccr4 associates with Caf1 using its Leucine-rich repeats (LLR) and the nuclease domain (EEP) is at a distance from the scaffold. PDB-4B8C (Basquin et al., 2012) using UCSF Chimera.

1.2.3.3 The Caf40 module

Caf40 protein was first discovered as Rcd1 (Required for Cell Differentiation) in *S. pombe* which is essential for the nitrogen-starvation-induced sexual differentiation (Okazaki et al., 1998). Its mouse homologue was described as a transcriptional co-factor in the retinoic acid-induced differentiation of teratocarcinoma cells and is also involved in lung development (Hiroi et al., 2002). In budding yeast, this is still a protein with unknown functions but structures of the human and *S. cerevisiae* Caf40/Not1 interaction domain have been solved by X-ray crystallography (Mathys et al., 2014a, Bawankar et al., 2013). In the CNOT9-CNOT1 dimer, the binding interface is formed by the first two helical repeats of CNOT9 (Caf40) to a long helical region on the CNOT1 (Figure 6) (Mathys et al., 2014a). Both structures showed similarly that it is the back of the Caf40 arch that interacts with the Not1 scaffold domain. The six short helices (H1 to H6) on the concaved, solvent exposed surface of the ARM repeats domain provide an interaction site with positively charged residues facing outward which putatively binds negatively charged nucleic acid molecules or other proteins (Figure 6). This type of interface could be convened by both the Armadillo repeats (ARM) domain and the PUM domain because they are structurally similar (Rubinson and Eichman, 2012).

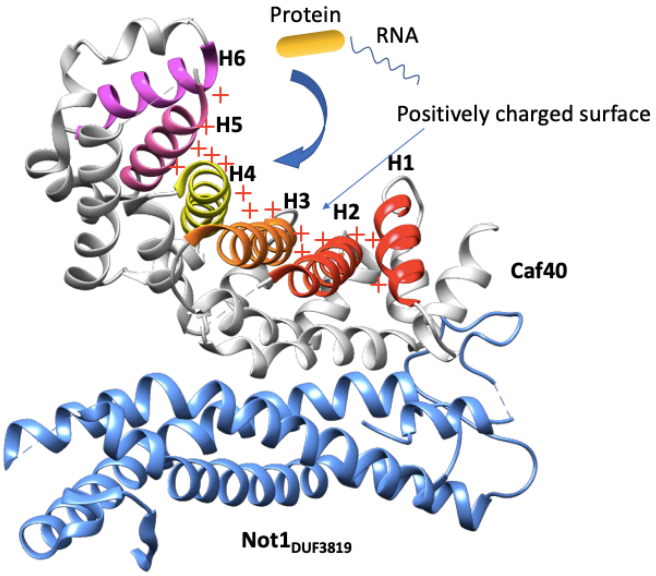

Figure 6 Illustration of Caf40 module structure. Caf40 binds to the DUF3819 region (Domain of unknown function) with alpha helix on the back of the ARM motif. DUF3819 is formed by long helices twined with each other unlike the HEAT repeats at the extremities of Not1. Caf40 shows an Armadillo repeat motif (ARM) conformation with stacked short helices in a concaved shape. This arched surface could interact with other protein co-factors or single stranded nucleic acid relevant in Ccr4-Not functions (Garces et al., 2007). PDB-4CV5 (Mathys et al., 2014) using UCSF Chimera.

1.2.3.4 The Ubiquitination module

The Not4 protein consists of a conserved N-terminal RING domain, followed by a short RNA recognition motif (RRM) and then a C-terminal tail region, that vary across species in the sequence and has no predicted secondary structures (Bhaskar et al., 2015). Similar to the yeast, the RING domain in higher eukaryotes harbours a Zinc ion coordinating motif (C4C4) formed by eight cysteine residues (Hanzawa et al., 2001), which is also the core of an E3 ubiquitin ligase with the cognate E2 proteins, e.g. Ubc4/5 in yeast and UBE2D2 in humans (Bhaskar et al., 2015, Albert et al., 2000). The E2-E3 binding interface is thus conserved between the yeast and the human homologues. The C-terminal unstructured tail region of Not4 wraps around a similar stretch of the HEAT repeats of the Not1 C-terminus but on the opposite side to the NOT module subunits (Bhaskar et al., 2015) (Figure 7 and Figure 8, Amino end of the partial Not1 structure). The interaction in yeast depends on only a few key amino acids (L463, F464, W466) where mutations can block Not4-Not1 binding easily (Bhaskar et al., 2015). Since the tail domain sequence is not conserved in metazoans, it explains the observations that Not4 is not a stable component of the Ccr4-Not complex other than in the yeast (Temme et al., 2010, Lau et al., 2009). However, this is counterintuitive to the emerging role of a coupled Ccr4-Not complex in co-translational quality control. (Collart, 2013, Laribee et al., 2007). Recently, a short 23 amino acid motif (CBM) conserved in metazoans only was found along the C-terminal tail of human CNOT4(Not4) that binds human CNOT9(Caf40) and could mediate rapid mRNA decay in a deadenylation-dependent manner (Keskeny et al., 2019). This has brought Not4 back into the vicinity of the Ccr4-Not complex in higher eukaryotes and such interaction could have novel functional relevance that is specific to CNOT9 or CNOT4 mediated gene silencing pathways.

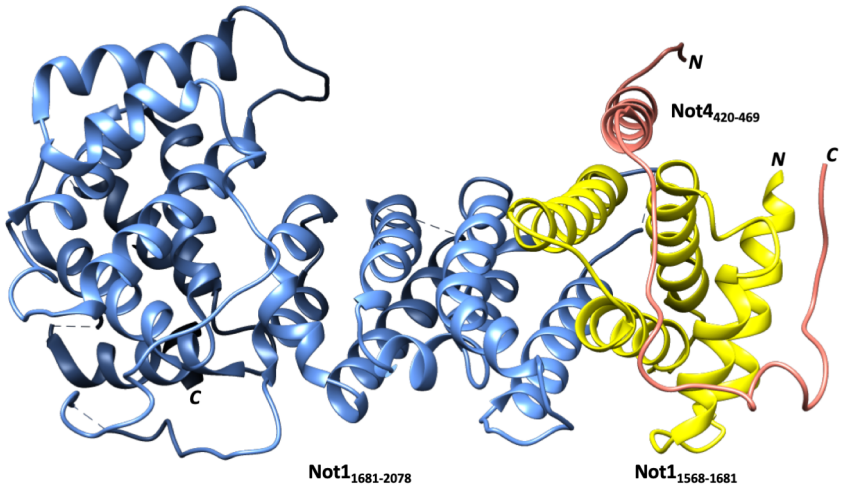

Figure 7 Illustration of the ubiquitination module interaction interface structure. This crystal structure shows the minimal interacting residues between Not1 (yellow portion) and Not4 (salmon portion) at both their C-terminal ends. Interaction surface is formed largely by the unstructured tail of Not4 wrapping over 4 stacked helices and one short N-terminal helix. Much of the N-terminal region of Not4 is unsolved, including the more unstructured region and a predicted Zinc finger/RNA recognition motif (RRM) block. Adapted from PBD-5AJD (Bhaskar et al., 2015) using UCSF Chimera.

1.2.3.5 The NOT module

This is the signature module of the functional Ccr4-Not complex and consists of the Not1 C-terminal NOT interaction region, Not2, Not5 subunits (Bhaskar et al., 2013a) and may also include Not3, which is in sequence related to Not5 but functionally less important in the eukaryotes (Collart, 2016, Oberholzer and Collart, 1998) . Mutations on Not2 or Not5 were shown to be deleterious, especially in the embryonic development (Kamath and Ahringer, 2003, Maillet et al., 2000). For example, the human homologue CNOT3 (Not5 in yeast) was identified as a tumour suppressor in T-cell acute lymphoblastic and its mutation attributed to a degenerative development (Venturini et al., 2012). Expression of CNOT2 is also linked to the tumour cell metastatic potential (Venturini et al., 2012). Crystal structures of the partial NOT module trimeric complex from budding yeast (Bhaskar et al., 2013a) and from the human homologue (Boland et al., 2013a) had been solved. This trimeric complex is formed by the N-terminal tail of the NOT proteins looping onto the Not1 C-terminal part with two perpendicularly stacked HEAT repeats (Figure 8). The NOT box is a conserved dimerisation domain among the Not-box protein subunits, and that similar mode of interaction extends into the metazoans (Zwartjes et al., 2004). The N-termini of both Not3 and Not5 also share great resemblance with a predicted coiled-coil domain that could mediate DNA recognition (Collart, 2003, Albert et al., 2000). Despite having the congruent putative binding domain to the Not5 based on their sequence similarity and also co-immunoprecipitating with the Ccr4-Not

complex (Chen et al., 2001), neither biochemical nor structural evidence had shown that Not3 would co-occupy Not1 with the rest of the NOT module. Instead, it might even be competing with Not5 for binding on Not1 *in vivo (See Results 4.3)*.

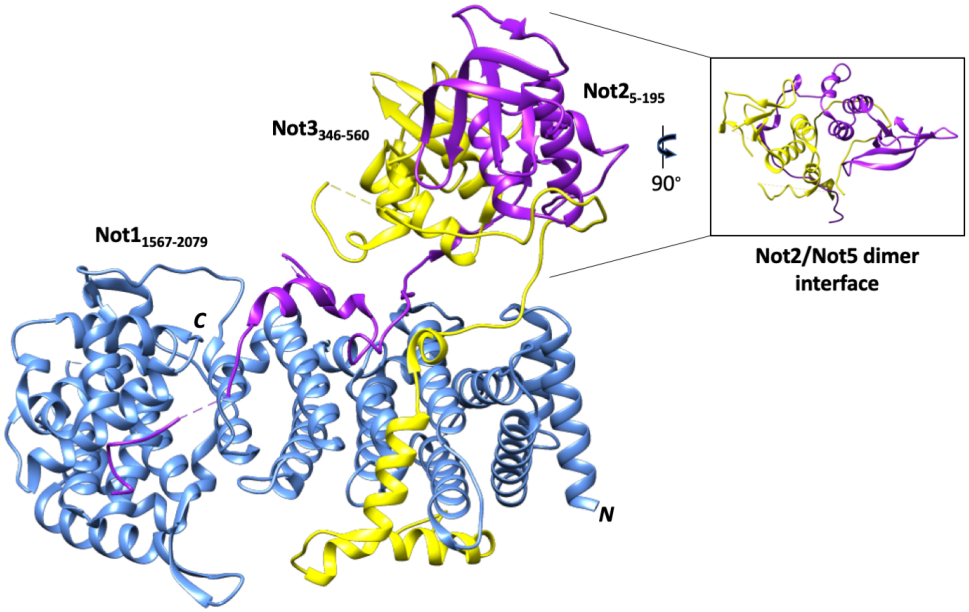

Figure 8 Illustration of the NOT module structure. This crystal structure of the NOT module shows the Not2/Not5 (yellow/magenta) dimer interaction with their conserved Not box domain. N-terminal region of both subunits has partially structured short helices and loops that wind around the HEAT repeats structure on Not1 at a location slightly towards the C-terminal end, next to the binding site of Not4. Adapted from PBD-4BY6 (Bhaskar et al., 2013) using UCSF Chimera.

In summary, current understanding of the Ccr4-Not complex architecture which is largely deduced from the only two EM structures in previous studies is compiled into Figure 9 below. The endogenous *S. cerevisiae* complex has been resolved to 33Å using negative stain EM (EMDB-1910) (Nasertorabi et al., 2011) and the putative organisation of the subunits had been annotated on the EM map according to their corresponding theoretical molecular mass that take up the EM density. The *S. pombe* structure, despite using both negative stain and CryoEM methods (EMDB-3232), could only resolve to 20Å resolution (Ukleja et al., 2016a). The subunits were vaguely mapped using immunolabeling, but the complex architecture was still limited by the final resolution in details. Due to the large overall size and the dynamic conformational states of this complex, it was nearly impossible to resolve the entire assembly by X-ray crystallography or NMR methods. From only the structures of fragments of the complex thus far (Ukleja et al., 2016c), we cannot present a holistic picture to unveil how those multiple functions are coordinated by the subunits and how the complex interacts with its numerous substrates. Therefore, a high-resolution single particle Cryo-EM map would be suitable to complement and improve upon the previous

findings at presenting a comprehensive structural characterisation of the complex. A basic introduction on the use of Cryo-EM for biological studies is laid out in the following sections.

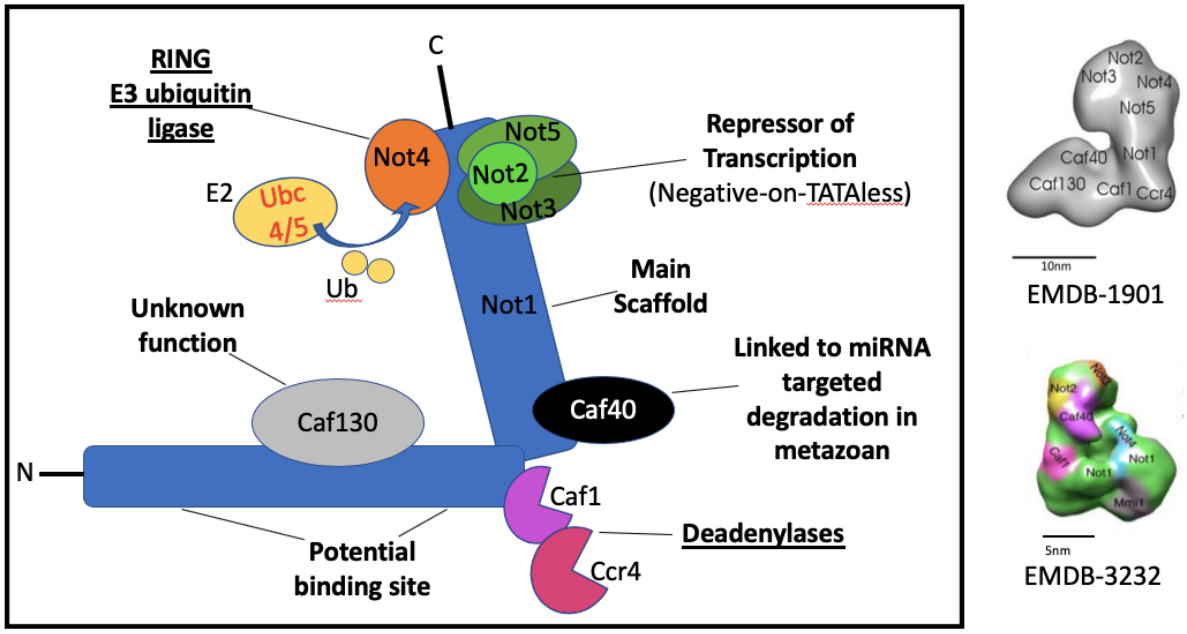

Figure 9 Overview of the Ccr4-Not complex architecture. Based on previous low-resolution EM structures from the endogenous S. cerevisiae (Nasertorabi et al., 2011) and S. pombe (Ukleja et al., 2016a) complex on the right, the putative organisation of the various subunits on the consensus L-shaped scaffold is illustrated and annotated with their reported cellular functions (Ukleja et al., 2016c). The figure is not drawn to scale. EM map reproduced with permission according to CC license from the respective papers indicated by their EM Data Base accession numbers.

1.3 Electron microscopy for structural studies of macromolecular assembly

Protein molecules are the basis of almost all physiological and biochemical functions in the cells. Often their functional form is not a single protein, but a macromolecular complex formed by a handful of protein subunits. Such sophisticated structural organisations have given rise to a plethora of divergent regulatory and functional specificities. Regardless of whether it is a membrane bound channel or a soluble protein complex, understanding their molecular architectures is critical to knowing how they work. This would also apply to the macromolecular Ccr4-Not complex here, which is a major regulator in numerous cellular pathways. By using the EM methods, this large heterogeneous complex could be characterised entirely without the need for protein crystallisation, which is foreseeably challenging as in this case to the X-ray crystallography method.

For many years, X-ray crystallography and nuclear magnetic resonance (NMR) techniques have been the premium methods for solving the molecular structure of proteins at atomic resolution, based on the number of Protein Data Bank (PDB) entries. However, the caveats to this are the difficulties imposed by the size of the molecules being examined, the ability to form sizable, well diffracting protein crystals, and also the level of purity and amount required for the sample to either crystallise or to remain yet soluble. Structurally flexible and heterogenous macromolecular assemblies, such as the APC/C, Spliceosome and Proteasomal complex and most of the membrane proteins, can be very challenging to crystallize even with extensive molecular engineering. They are certainly too large for nuclear magnetic resonance methods either. Electron microscopy, on the other hand, needs comparably less purified material, does not confine proteins within crystal lattices and can accommodate much larger macromolecular sizes. Structure determination by electron microscopy has evolved and improved in many aspects over the past decades, especially with the advances in software methods and hardware development in recent years (Kühlbrandt, 2014). Many high-resolution structures of macromolecular complexes from a range of biological samples have been reported (Bartesaghi, 2015, Bartesaghi et al., 2018, Fromm et al., 2015, Schilbach et al., 2017, Rasmussen et al., 2019, Fica and Nagai, 2017, Grimm et al., 2019).

Although X-ray data can resolve structures beyond 3Å routinely, the requirement for crystallisation excluded precious conformational freedom and the compositional variability information within a native complex (Acharya and Lloyd, 2005). The single particle cryo-EM method has the advantage of maintaining a near-native, fully hydrated condition. It also has a more flexible size limitation on the biological samples, where it is possible to resolve small

molecules below 50kDa (Herzik et al., 2019, Zhang et al., 2019), as well as large virus particles of several MDa in size (Song et al., 2019) to better than 4Å resolution.

1.3.1 Overview of the transmission electron microscope (TEM)

The transmission electron microscope functions essentially like a typical optical microscope. Except that it utilises electrons instead of photons and focuses by the magnetic lens rather than the physical glass lens. The TEM is divided into five major sections as shown in the schematic diagram in Figure 10. Three types of electron guns are commonly used to generate the electron beam in TEM, namely, the thermionic, Schottky (Field assisted thermionic) and Field-emission gun (FEG). A thermionic emitter is typically made of thin tungsten filament or a LaB_6 crystal mounted on a tungsten filament tip. The thermal energy generated from passing a current through the filament is used to overcome the work function for the electron emission. In FEG, the work function is solely overcome by a strong extraction electric field near the emitter tip at a much lower heating temperature. More advanced electron microscopes usually use the Schottky or FEG with a higher electron acceleration voltage (200 keV – 300 keV) to provide the extra coherent and strong electron beams needed for the high resolution Cryo-EM applications. The illumination system is made up of the electron gun, condenser lenses and the condenser aperture which regulate the electron dose, illumination area and incident beam angle. Following which is the objective lens system and the specimen stage where the biological sample prepared on the EM grid sits on a sample holder that is mounted on the goniometer. The sample can either be at room temperature on a single-tilt holder (e.g. for the negative stain method) or at cryogenic temperature (Cryo-EM) using an attached liquid nitrogen Dewar on the cryo-holder. The goniometer controls the mechanical movement of the sample grid in x-y-z-direction plus an axial rotational movement of +/- 70°, typically in TEMs dedicated for biological samples. In this simplified view, after passing through the upper objective lens, electron beams from the sample plane are then received by the lower objective lens in the same system where the scattered beams are coherently recombined (focused) along the optical axis and behind the lower objective lens to form an image of the sample. This lens system is the most essential component of the whole TEM because the quality of the image contributes greatly towards the overall resolution of the microscope. Further on, the image formed by the objective lens at the image plane is passed on by the penultimate intermediate and projection lens system which consists of several electron lenses that relay on to the detection medium such as a photographic film, a charge-coupled device (CCD), a CMOS

camera or the direct electron detector (DED). Incident electrons interact with the detection medium and the image is stored, either as chemically developed micrographs on emulsion films which are then transformed digitally using a scanner densitometer, or directly as digital micrographs when electronic detectors are used.

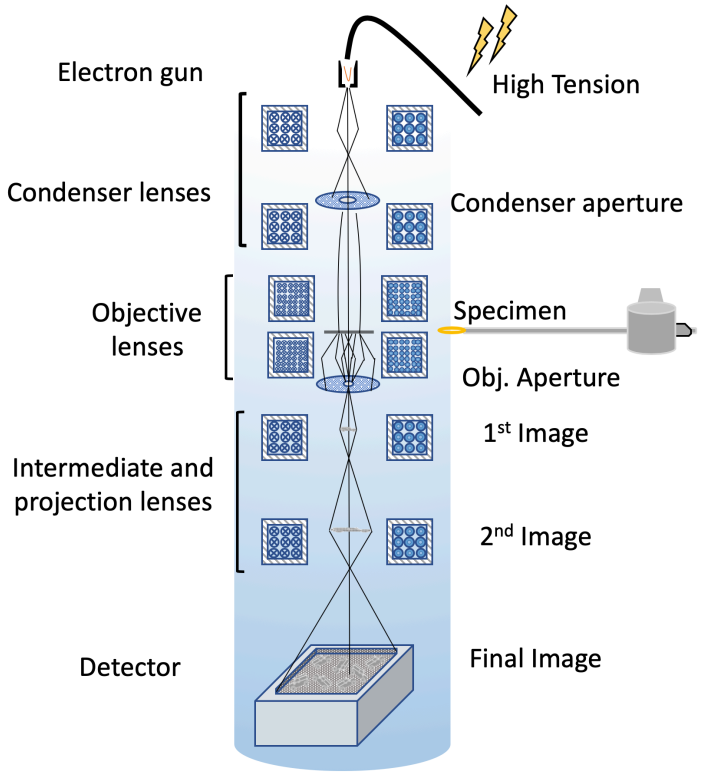

Figure 10 Schematic ray path of a Transmission electron microscope (TEM) used for Cryo-EM of biological specimen.

1.3.2 Specimen preparation

Due to the high vacuum environment required for EM imaging, any liquid water will evaporate once inside the microscope and dehydrate the biological sample. This inevitably affects the native state and fine internal structures of any macromolecular assemblies. The conventional method for examining particulate specimens preserves the purified proteins by embedding them into a layer of heavy metal salt crystals e.g. Uranyl acetate (UA) (van Bruggen et al., 1962) and let air-dry on the EM grid (Brenner and Horne, 1959). The heavy metal salt generates a much more electron dense background than the particle occupied, solvent-excluded areas void of the stain. The shape of the molecules will be revealed as brighter regions indicative of less electron scattering compared to the surrounding. Thus, it is called 'negative staining'. This method is routinely used for rapid evaluation of the sample conditions and

purification outcomes in terms of the particle size, homogeneity and morphology, therefore provides feedbacks for improving buffer and purification conditions if necessary (Passmore and Russo, 2016). Although the structural distortion from drying is tolerable when only distinguishing the overall shape and distribution of the protein particles, dehydration still needs to be circumvented to preserve more structural details within the protein molecules. Additionally, the heavy metal stain does not infiltrate the protein molecule completely, structural information from within the particle is not harnessed in the final image (Reviewed by (Orlova and Saibil, 2011)).

Eventually, Dubochet and colleague (Dubochet and McDowall, 1981) had successfully devised a method for vitrifying the protein suspension in thin film of water for EM, based on the idea that ultrafast cooling of water or a solution thin film to cryogenic temperature avoided crystalline ice formation and retains sufficient thermal stability during EM imaging (Brüggeller and Mayer, 1980). Ideally, an aqueous solution is spread evenly across a hydrophilic surface and blotted with filter paper to form the thin film subtended within each grid hole on the EM grid. The grid is then plunged into a cryogen such as the liquid ethane or propane to create the vitrified state of water, which is apparently electron transparent. The result is a population of near-native, hydrated biological molecules encapsulated in thin layer of vitreous ice. However, as Cryo-EM studies for structurally heterogenous samples become more challenging and adventurous, successful structural determination increasingly depends on factors, such as the protein assembly's stability and particle-surface interactions, that could lead to denaturation during sample preparation and thus limiting the data quality (Noble et al., 2018, Glaeser and Han, 2017) (Figure 11). Remedies for such cases include optimising buffer conditions to lower the dissociation constant K_d of the subunits (Passmore and Russo, 2016), rendering different particle behaviours in the thin film (D'Imprima et al., 2019) and using chemical cross-linkers, such as Glutaraldehyde, in the Grafix method (Kastner et al., 2008b) for stabilization. These strategies may help to maintain the particle integrity during the purification and vitrification steps. However, caution is required due to the propensity of these procedures to generate preferential particle orientation and crosslinking artefacts, especially with malleable assemblies in terms of their conformational and compositional heterogeneity (Orlova and Saibil, 2011).

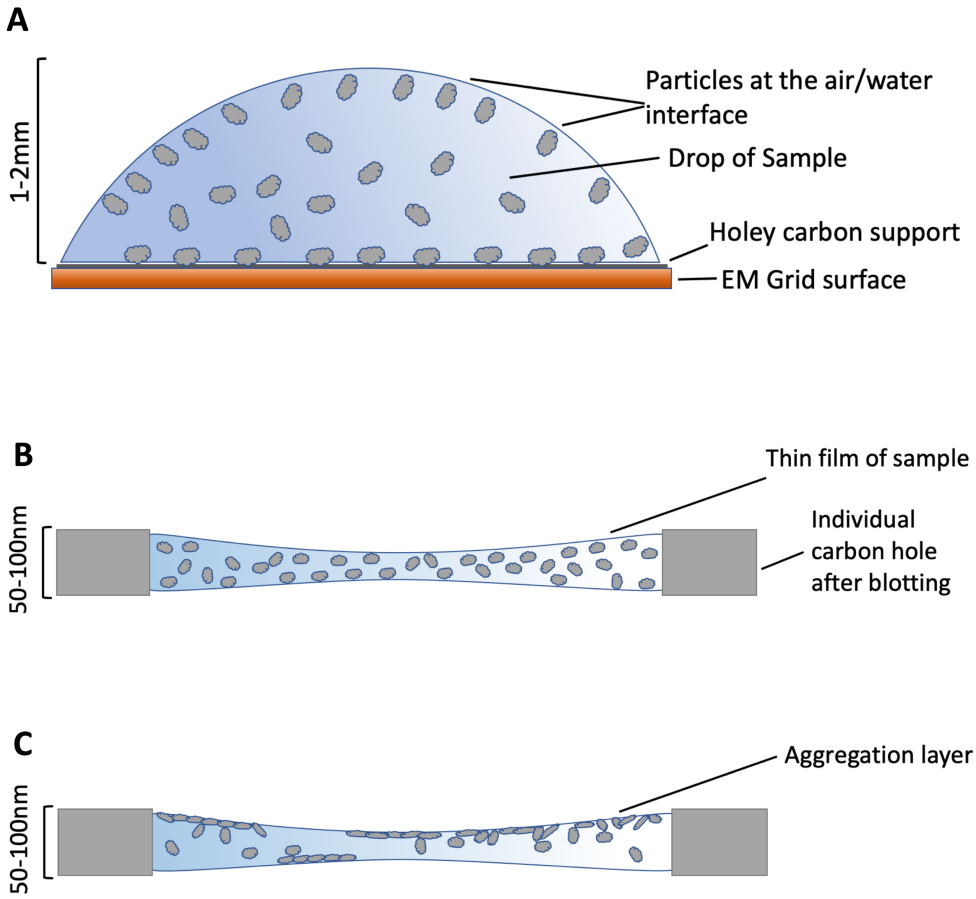

Figure 11 Illustration of particle behaviour during sample preparation. Not drawn to scale. A) A droplet of sample when applied on the grid. A subset of the protein particles tends to adsorb to the newly formed air/water interfaces on the meniscus and at the contact surface with the carbon support, while the rest remain in suspension. B) Ideal thin film formed after blotting away the excess liquid. Protein particles are expected to be suspended mostly in random orientations and individually. C) Thin film formed in practice may contain damaged particles and layers of denatured proteins as a result of them interacting with the air/water interface and unfold. Blotting reduced the surface-to-volume ratio appreciably and more particles would encounter the air/water interface which caused damage and aggregation.

1.3.3 Principles of image formation

Electrons passing through the thin specimen interact with the biological matter to an extent, depending on their atomic numbers and the accelerating electron energy (Orlova and Saibil, 2011). A tiny portion of the parallel incident electron rays gets scattered under the influence of the electrostatic force as they pass close by the constituent atoms of the protein molecules. The scattering can either be elastic (no energy loss or transfer to the surrounding) or inelastic (energy from the primary electrons is lost or absorbed by the surrounding due to collisions) (Kohl and Reimer, 2008, Orlova and Saibil, 2011). Therefore, inelastic scattering is also the main source of radiation damage that restricts resolution in the EM (Reimer, 1989). The scattered electrons (Scattered beam) travel further down the microscope column unparallel to the optical axis amongst the non-scattered beam (Reference beam). Similar to the optical train in the light microscope, the image is formed by the electromagnetic objective lens in the EM. The transmitted beams of scattered electrons are deflected by the electromagnetic field within the objective lens to focus onto the back focal plane of the objective lens. Due to imperfections in the electromagnetic lenses, such as the inherent spherical aberrations and astigmatism (Kohl and Reimer, 2008), only electrons scattered to a relatively small angle are focused constructively for image formation, while those scattered at too high angles in the exit beam are typically excluded by an objective aperture (Amplitude contrast) (Figure 10). Consequently, the scattered electrons travel a longer path between the specimen plane and the 1st image plane, as compared to un-scattered electrons in the reference beam. This will generate phase differences between the two parts of the exit electrons and produce wave interference (Phase contrast), which also depends on the amount of defocus and lens aberrations (Erickson et al., 1971). The electron beam interacts minimally with thin biological samples thus the amplitude contrast due to the loss of transmitted electrons contributes only ≈7% (Toyoshima and Unwin, 1988) to the overall image contrast of unstained specimens, compared to ≈35% in negative stained samples (Erickson and Klug, 1971) where the electron beams are heavily scattered by the stain that creates a high contrast background relative to the particle locations. The initial image is then formed at the image plane and is transmitted down the microscope column through a series of electromagnetic lenses that magnify and project this image from the 1st and 2nd image plane onto the electron film or detector surface (Figure 10).

1.3.4 Contrast transfer function (CTF)

The CTF of a microscope represents contrast fluctuations with respect to all spatial frequencies in the micrograph arising from the lens imperfections and the defocus used. Although both amplitude and phase contrast contribute in the final image, for weak phase objects i.e. protein specimens, the small fraction of amplitude component can also be treated as an additional phase shift in the phase contrast component (Erickson and Klug, 1971). The contrast of a thin phase object does not transfer completely at every spatial frequency, thus showing an oscillating pattern between the negative and positive contrast amplitude in the form of a sine function (Orlova and Saibil, 2011). The phase contrast transfer function is thus proportional to a sine-function of the phase shift in the scattered beam arising from the spherical aberration and defocus along the spatial frequencies. In practice, this function is also modulated by an envelope function which describes the effects of beam-induced sample decay and hardware instabilities, such as the variations in beam coherence and aberrations in the lenses, that reflect as a signal falloff towards higher spatial frequencies (Chiu and Glaeser, 1977). The envelope function attenuates the amplitude of the CTF up to a point where the signal transfer falls below the noise level, thereby marking the information limit of the microscope. Their relationships are as described below.

$$CTF_{phase}(k) = E(k)[-sin(\Delta\pi\lambda k^2 + \tfrac{\pi}{2}C_s\lambda^3 k^4 - \varphi)] \quad (1)$$

C_s: Spherical aberration
λ: Electron wavelength
k: Spatial frequency
Δ: defocus
E(k): Envelope function
φ: Integrated phase shift reduced from amplitude contrast

Useful information is only transferred within the low frequency range up to the first contrast reversal without the CTF correction. The positive/negative contrast fluctuation in the higher frequency range would otherwise result in artefacts and therefore deteriorate the image quality and distort the information content. The recorded image's Fourier transform (FT) can be treated as the product between the CTF and the FT of the true object plus the signal noise. Dividing the image by its CTF in the Fourier space would correct for the CTF but this is mathematically infeasible due to the CTF zeros. On top of that, the weakly transferred frequency ranges i.e. CTF<<1 being amplified through the division would be mainly consisting of noise. In order to retrieve all information at spatial frequencies where the CTF approaches the *x*-axis (zero amplitude), CTF correction can also be done by taking the sum of the products between all image FTs and their respective CTFs, then divided by the sum of all the squared CTFs plus a Wiener factor (This prevents the division by zero). This operation effectively flips all negative phases into the positive domain and restores the original amplitudes (Penczek, 2010).

1.3.5 Electron detectors

Historically, the EM image is recorded on photographic film that has a specially developed emulsion layer for detecting high-energy electrons at a low dose. The silver halide crystal in the emulsion layer forms the individual "effective pixel" after being sensitised by an incident electron. The film offers high image contrast, spatial resolution and a larger field of view compared to the electronic detectors (Orlova and Saibil, 2011). But it also suffers from low sensitivity (speed) and non-linear response of dynamic range, particularly in electron diffraction experiments. It is also less efficient in handling, in terms of the recording and digitisation conversion throughput. Electronic cameras later gained popularity over film to record directly into digital formats which can be processed and archived more conveniently and also avoided the time-consuming film cassette turnover when large dataset was collected. The Charge-coupled device (CCD), or in some cases also a Complementary metal oxide semi-conductor (CMOS) camera, generates digital data from the optical-analogue signal via a scintillator-optic fibre layer (electrons→photons→electrons→charge→signal). However, their disadvantage was for the poor spatial resolution due to the multiple scattering in the transduction path and the low signal-to-noise ratio (SNR) because of charge diffusion among nearby pixels (Faruqi and Henderson, 2007).

The Direct electron detectors (DED), however, have made great improvements in the SNR for low-dose imaging in cryo-EM compared to the predecessors (McMullan et al., 2009b). They can detect incident electrons directly (electron→charge→signal) without the generation and transduction of photons in contrast to the scintillator-based cameras. For example, the monolithic active pixel sensor (MAPS) made with a CMOS process, is embedded with local read-out circuits. Thus, it has a faster than CCD readout speed on top of an improved overall SNR and spatial resolution due to the direct exposure and detection of incident electrons (Orlova and Saibil, 2011, Faruqi and Henderson, 2007). The high readout speed permits movie recording during an exposure and beam-induced motion correction by the frames with dose-fractionation (Scheres, 2014, Zheng et al., 2017). MAPS with CMOS design can also be made radiation-hard thus prolonged the usage and stability under direct radiation exposure (Bogaerts et al., 2003, Battaglia et al., 2009a).

Two modes of data acquisition are available for the DEDs, viz. the integrating and the counting mode (Figure 12). In integrating mode, the charge accumulation from an incident electron at each pixel is aggregated across the detector and registered by the Analog-to-Digital convertor (ADC) within the detector circuit at a fixed frame rate and outputs a digital image after background subtraction (Flat-field and Dark-field corrections) (McMullan et al., 2014, Faruqi et al., 2015). Since the energy deposition of incident electrons follows a "Landau distribution" (Vinothkumar and Henderson, 2016), the resulting analogue voltage could vary broadly for each incident electron and determining the precise location of the incidence is made more difficult. In counting mode, the analogue signals from single electron events are treated similarly to a delta function and registered in binary format with the same weighting under a threshold (Kuijper et al., 2015, Faruqi et al., 2015). Therefore, counting improved the SNR drastically as true signals can be better isolated from the background noise (Campbell et al., 2012), hence more structural information can be retrieved when the images of the protein particles are averaged during the image processing in single-particle analysis (SPA). But this way of signal processing also limited the usable dose rate in order to detect individual electrons and avoiding coincidence-loss (double/missed counting). Electron counting is thus done in practice with a sufficiently low dose rate at the given read-out frame rate of the detector used so that individual electron events can be distinguished with better precision (Song et al., 2019). Consequently, a fast frame rate would allow shorter total exposure time with higher dose rates and vice versa.

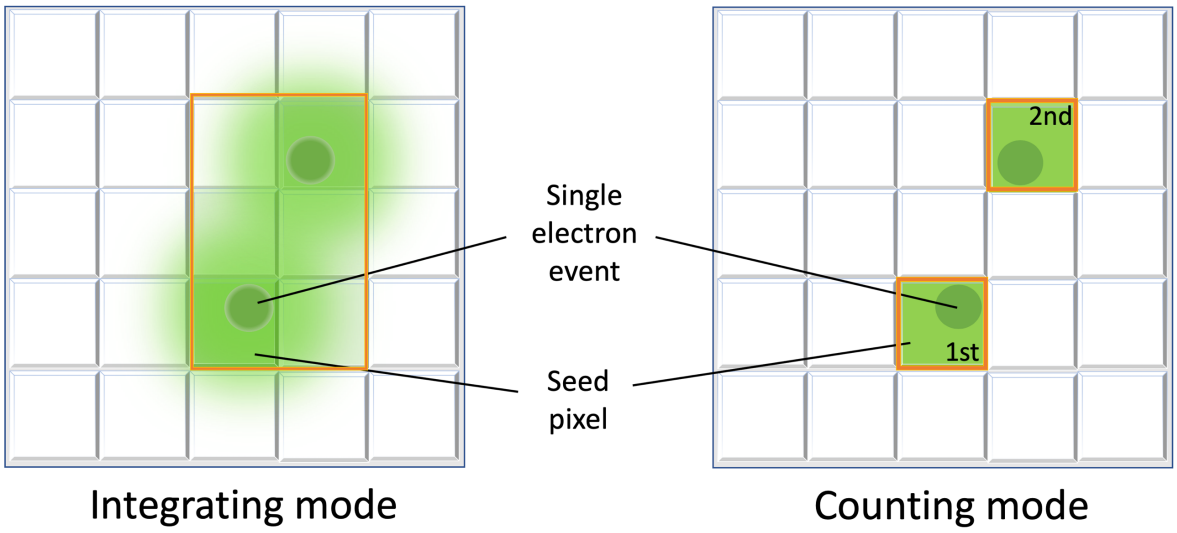

Figure 12 Illustration of integrating mode and counting mode. Left: Signal scattering due to the variation in energy deposited results in ambiguity in determining the electron impact location between two subsequent single electron events. Right: In counting mode, additional signal processing algorithm allows the true signal to be registered with better precision at locating the individual electron events. This relied largely on the improved sensitivity and faster read-out speed of the new direct detectors.

1.3.6 Single particle analysis (SPA)

Single particle analysis for Cryo-EM follows a technique (Frank, 1975) that aims to determine the structure of protein macromolecular complexes (particles) by recombining a set of randomly oriented single particle images produced by the TEM (Figure 13A).

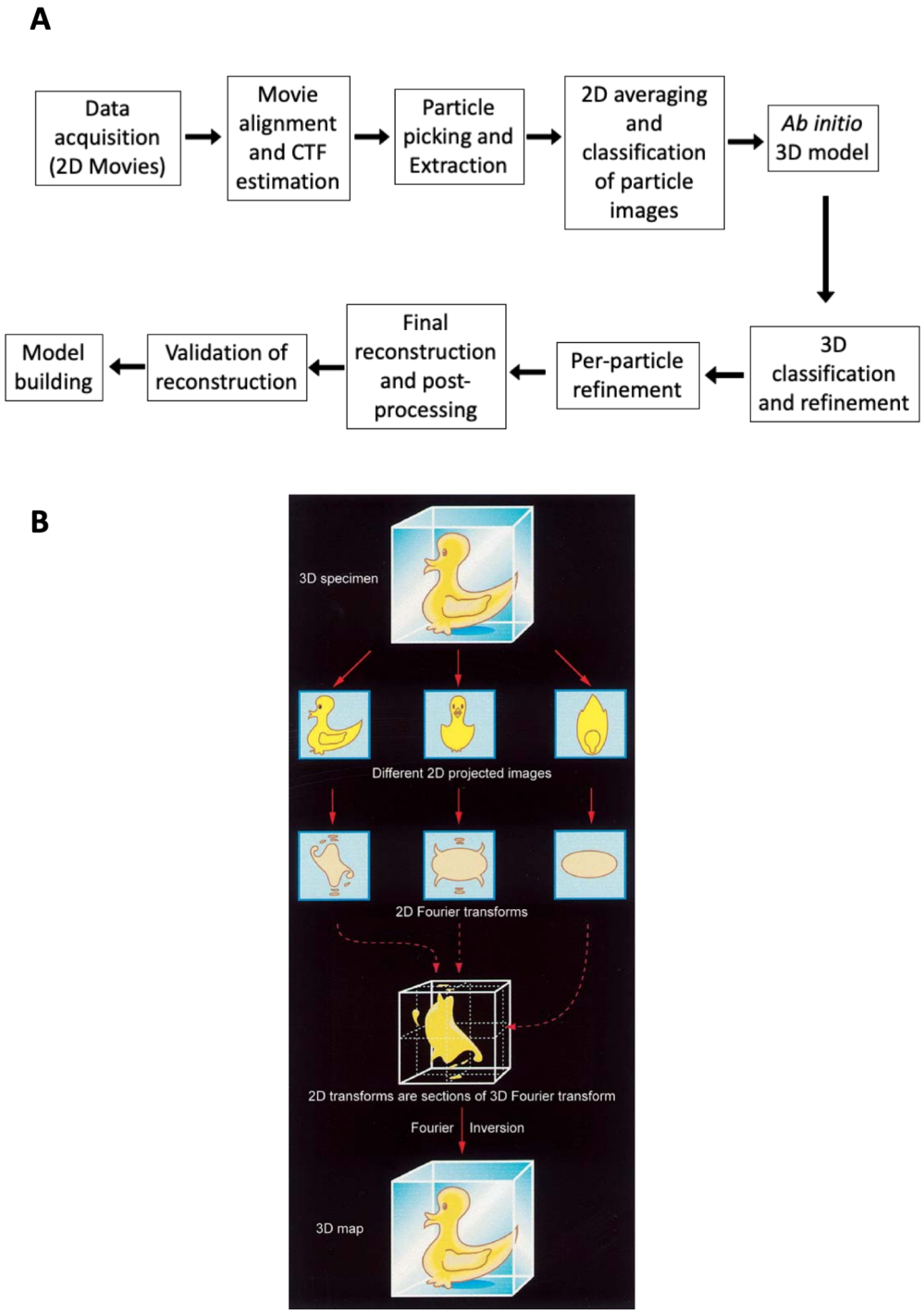

Figure 13 Single particle analysis for Cryo-EM. A) Flowchart of the SPA process showing the typical steps of the image processing and reconstruction. B) An illustration of the basis for 3D reconstruction based on the 'projection-slice theorem' and that the interconversions of the original object from the reconstructed map into projection images between real and Fourier space. (Baker and Henderson, 2006). Reproduced with permission from the International Union of Crystallography.

During each exposure, images are collected as movie frames and realigned to correct for beam-induced-motion, before stacking them into a single micrograph (Zheng et al., 2017). Subsequently, a dataset consisting of the selected particle images from each micrograph go through the iterative process of image alignment, 2D classification and averaging to statistically assign their relative orientation parameters based on their cross-correlation coefficients with an arbitrary reference. This also reinforces the weak signal within many similar projection images owing to their individually low SNR (Sigworth, 2016). The averaged 2D classes with improved SNR can then be used to generate an *ab initio* 3D model of the particle by using e.g. the common-line method (Elmlund and Elmlund, 2012) that serves as the basis for further iterative refinement of the orientation parameters via projection matching (Penczek et al., 1994). More recently, the stochastic gradient descent (SGD) method for estimating the optimal orientation parameters (Punjani et al., 2017, Zivanov et al., 2018) was also implemented for generating the initial 3D volume from the 2D particle images with random initialisation to escape false minima in the solutions. The algorithms for the 2D and 3D refinement calculations rely on the cross-correlation coefficient between the images and the references, and the accuracy is influenced directly by the image SNR for the dataset. For reconstructing the 3D structure, the 2D particle images are deemed to represent the 3D coulomb potential of the protein density in real space towards a particular direction of projection. Their FT can be treated as planes sharing a common origin that constitute the FT of the original object, as described by the "projection-slice theorem" (De Rosier and Klug, 1968) (Also reviewed in (Nogales and Scheres, 2015)) (Figure 13B). Given an adequately distributed population of the projected views, a 3D map of the particle of interest can be reconstructed *in silico*. Therefore, the accurate and comprehensive determination of the relative orientations of the particle images is instrumental to the high-resolution reconstruction procedure in SPA.

1.4 Aims of this study

The Ccr4-Not complex is a highly conserved, multifunctional macromolecular complex in the eukaryotic organisms. Many of the cellular pathways that involve this complex have been linked to pathophysiological developments such as cancer, cardiovascular diseases and immunoregulation (Miller and Reese, 2012, Shirai et al., 2014, Rodríguez-Gil et al., 2017). However, the high-resolution molecular structure for the entire native complex is currently still unavailable. This project uses the *S. cerevisiae* as a convenient and representative model organism for the attempt to purify the yeast endogenous Ccr4-Not complex and to determine its structure using Single particle Cryo-EM. The purified complex's composition and *in vitro* activities will also be examined and validated using enzymatic assays and Mass spectrometry. Gaining more information on the complex's structural architecture can help to elucidate the mechanisms behind its cellular functions and interactions which in turn advances our understanding of how different aspects of mRNA metabolism are coordinated during gene expression.

2 Materials

2.1 Chemicals

General chemicals used in the study are as listed below:

Name	Identifier	Supplier
2-Propanol	9866.5	Roth
2-Mercaptoethanol	M3148	Sigma Aldrich
Deoxynucleoside triphosphate set (dNTP)	K039.1	Carl Roth
25% Glutaraldehyde solution, EM grade	#16216	EMS
3x FLAG Peptide	A6001-4mg	ApexBio
3x FLAG® Peptide	F4799	Sigma
Acetic acid, glacial. 99%	3738.1	Carl Roth
Acetone	9372.4	Carl Roth
Acrylamide/Bis-acrylamide, 30% solution	A3699-100ML	Sigma
Adenine	A14906	Alfa Aesar
Agar-agar	#1347.1	Carl Roth
Agarose	#3810.2	Carl Roth
Ammonium persulfate	13375.01	Serva
Ammonium sulfate	3746.3	Carl Roth
Ampicillin	A9393-25G	Sigma
ANTI-FLAG M2 Affinity Gel	A2220	Sigma
ANTI-FLAG® antibody produced in rabbit	F7425	Sigma
BlueEasy Prestained Protein Marker	MWP06	NIPPON Genetics
Bromophenol blue	B8026-5G	Sigma Aldrich
cOmplete, Protease inhibitor cocktail (EDTA free)	11836170001	Roche
Coomassie Brilliant Blue R-250	3862.1	Carl Roth
D-Sorbitol	S1876-5KG	Sigma
Dithiothreitol (DTT)	6908.2	Carl Roth
Ethane	Ethan 3.5	Linde
Ethanol, Denat. 96%	9065.4	Carl Roth
Ethylenediaminetetraacetic acid (EDTA)	CN06.1	Carl Roth
GeneRuler 1 kb plus DNA Ladder	SM1331	Thermo Scientific
Geneticin (G418)	11811023	Gibco
Glucose	G8270-5KG	Sigma
Glycerol	3783.5	Carl Roth
Glycine	3908.2	Carl Roth
Goat anti-rabbit antibody, HRP conjugated	# 31460	Thermo Scientific
HEPES	#441487	VWR
Hydrochloric acid (HCl)	P074.1	Carl Roth
Imidazole	#X998.4	Carl Roth
Isopropyl-b-D-thiogalactopyranoside (IPTG)	CN08.4	Carl Roth

Liquid nitrogen	-	In house supply
Methanol	4627.2	Carl Roth
NuPAGE MOPS SDS running buffer (20x)	NP001	Life Technologies
Page Ruler Pre-Stained Protein Ladder	26630	Thermo Scientific
PEG 4000	0156.3	Carl Roth
PEG 8000	89510	Sigma-Aldrich
Phenylmethylsulfonyl fluoride (PMSF)	15460422	Roche
Pierce™ ECL Western Blotting Substrate	32209	Thermo Scientific
Potassium chloride (KCl)	6781.2	Carl Roth
Silver nitrate	209139-25G	Sigma
Sodium Azide	S2002-5G	Sigma-Aldrich
Sodium chloride (NaCl)	HN00.2	Carl Roth
Sodium dodecyl sulfate (SDS)	L4390-500G	Sigma
Spectrum membrane tubing, 6-8,000 MWCO	#132660	Spectrum Lab Inc.
Sucrose	#9286.1	Carl Roth
SYBR Green DNA stain	S7563	Thermo Scientific
Tetraacetylethylenediamine (TEMED)	2367.3	Carl Roth
Tris[2-carboxyethyl] phosphine (TCEP)	646547-10X1ML	Supelco
Tris[hydroxymethyl]-aminomethane (Tris)	#4855.2	Carl Roth
Triton X-100	X100-500ML	Sigma
Tryptone	95039-5KGF	Sigma
Uranyl acetate	77870	Serva
Yeast extract	86401.5000	VWR

2.2 DNA Oligonucleotides

Sequence (5' – 3')	Direction	Remark
CGGAAGGAAAATTATCGCCGGTAATCTGGAAGTGC TGTTTCAGGGCCCGAGGGAACAAAAGCTGGAG	FWD	N4F
ATAAAATTATGGTTAATGCAAACAAGAAAAATATT TAGAGTCGGACTATAGGGCGAATTGGG	REV	N4F
AAGCAATCTCTTGCTGCAGAGGAATAC	FWD	COLSEQ-N4
GTATTAATTGTAGCCGCGTTC	REV	KANMX
GACGTTGCGGTAACGACTTCGTATATAATGAAGAAG ATTTCGAAAAACTGCTGGAAGTGCTGTTTCAGGGCC CGAGGGAACAAAAGCTGGAG	FWD	N5F
CATTTACCTAGTAAATCACGATGAGAATTATATAAG TAAAAGGAAACTGTCTATAGGGCGAATTGGG	RVE	N5F
TTCAACAAGGTAGATCGCTG	FRD	COLSEQ-N5
GACTGTCAAGGAGGGTATTCTG	REV	KANHISNAT
GTTCTGTTCCAGGGGCCC GGATCC ATGTCTTCTT CTAAACGTAT	FWD	6HUBC4
TGCTAAAGAACTAAGTGATCTAGAAAG AGATCCAC CTACTTCATG		
ATCCTCTAGTACTTCTCGACAAGCTT TTATACAGCGTATTTCTTTG	REV	6HUBC4
CAAAGAAATACGCTGTATAAAAGCTTGTCGAGAAG TACTAGAGGAT	FWD	Vector
ATACGTTTAGAAGAAGACATGGATCCGGGCCCCTG GAACAGAAC	REV	Vector
GTTCTGTTCCAGGGGCCCGGATCC	FWD	COLSEQ-UBC4
TTATACAGCGTATTTCTTTG	REV	COLSEQ-UBC4

All DNA oligos were ordered from Biomer.net GmbH

2.3 RNA Oligonucleotides

Sequence ([6FAM] 5' – 3')	Remark
CACAUCCAACUUCUCUAAAUAAAAAAAAAAAAAAAAAAAAAAAA	A25
CACAUCCAACUUCUCUAAAU	A0

All RNA oligos were ordered from Sigma-Aldrich Co.

2.4 Plasmid

Name	Remark
p3FLAG-KanMx	3xFLAG-KanMX cassette (originally pBS-SK(-))
pST50_8His_Ubc4_3C_pLIB-Compatible_SY01 (pUBC4)	6xHist-yUbc4 cloning

2.5 Escherichia coli strains

Name		Remarks
DH5a	F$^-$ Φ80*lac*ZΔM15 Δ(*lac*ZYA-*arg*F) U169 *rec*A1 *end*A1 *hsd*R17(r_k^-, m_k^+) *pho*A *sup*E44 *thi*-1 *gyr*A96 *rel*A1 λ^-	p3xFLAG-KanMX plasmid cloning
BL21 (DE3)	F- *mcrA* Δ(*mrr-hsd*RMS-*mcr*BC) Φ80*lac*ZΔM15 Δ *lac*X74 *rec*A1 *ara*D139 Δ(*araleu*)7697 *gal*U *gal*K *rps*L (StrR) *end*A1 *nup*G	Ubc4 expression

2.6 Saccharomyces cerevisiae strain

Name		Remarks
S288c	*MATα SUC2 gal2 mal2 mel flo1 flo8-1 hap1 ho bio1 bio6*	Ccr4-Not expression

3 Methods

3.1 Molecular biology

3.1.1 DNA gel electrophoresis

The negatively charged DNA molecules were separated in an electric field according to their molecular sizes/ length in bases by agarose gel electrophoresis using 1% (w/v) agarose in TAE buffer (40 mM Tris pH8.3, 20 mM acetic acid, 1 mM EDTA) and supplemented with 1:12000 dilution (v/v) SYBR green DNA stain (Invitrogen,#S7563) in-gel. 5 parts of DNA sample was mixed with 1-part 6x DNA loading dye (ThermoFischer, #SM1333) and 30µl per sample was loaded into a well. Gel was run at 90V for 45min at room temperature using a power supply (PowerPac HC, BioRad). Visualisation and recording of the DNA bands were done with Bio-Rad GelDoc imager (BioRad) under UV transillumination.

3.1.2 PCR product extraction

DNA fragments used for cloning and homologous recombination were prepared using an DNA Extraction kit (Nippon Genetics, FG-91202) after a purification step by DNA gel electrophoresis. DNA bands were visualised with a UV lightbox and cut out using a clean scalpel. 400mg of gel was mixed with the supplied GP1 solution from the kit and vortexed for 15s. The tube was incubated at 55°C until all gel fragments had melted. The mixture was transferred to the supplied spin column and spun for 30s at 13,000 rpm. 600µl of GP2 from the kit was added to the column and spun as in previous step. The column was then spun for 2min at 13,000 rpm to remove excess liquid. 20µl of water was added onto the centre membrane of the column and incubated at RT for 2min before spinning for 2min at 13,000 rpm into a fresh tube. DNA concentration was estimated by Nanodrop spectrophotometer (ND-1000, ThermoFischer Scientific) blanked with water. DNAs were always stored in water at -20°C.

3.1.3 Polymerase chain reaction (PCR)

PCR reactions were used to **a**) Clone the Ubc4 gene from host genomic DNA for recombinant protein expression, **b**) Generate DNA fragments used for transformation via homologous recombination, **c**) & d) Perform colony PCR to validate the transformation. PCR reactions were set-up specific to each application as elaborated below.

a) Gibson assembly and cloning of 6xHis-Ubc4 gene

Cloning of the N-terminal 6xHist-tagged Ubc4 gene was done using Gibson assembly (Adopted from Cold Spring Harbour Protocol, 2017. doi:10.1101/pdb.rec090019) of the PCR amplified expression vector and the coding sequence from S288c yeast genome (Figure 14). 4µl of the yeast Ubc4 gene insert PCR product and 1µl of the linear vector PCR product were added to 15µl home-made Gibson assembly master mix (Table 5) in a 0.5mL Eppendorf tube and kept on ice until use. The tube was then incubated in a 50°C water bath for 1hr with gentle shaking every 10min. The reaction product was heated to 95°C for 1min to deactivate the enzymes. 1µl of DpnI (NEB) enzyme was added to the tube and incubated for 1 hour at 37°. Treated plasmids were used directly for transformation of bacteria.

Figure 14 Gibson assembly for 6xHis-Ubc4 cloning. A) The linear vector including the up and down stream annealing site were PCR amplified using primer pair Vector. B) PCR amplification of the coding sequence of Ubc4 from genomic DNA, forward primer includes a N-terminal 8xHist tagging sequence followed by the gene sequence without the endogenous Start codon and anneals to the complementary non-coding sequence of the genomic DNA. Product of T5 exonuclease digestion with 3' overhangs in A and B are only illustrated for clarification, all enzymatic reactions occur in a single tube simultaneously during incubation. C) The linear vector and amplified Ubc4 gene DNA were mixed and incubated in the reaction mix containing the enzymes. T5 exonuclease digests in 5' to 3' direction and generates 3' overhangs. Phusion polymerase completes the unpaired bases on the annealed DNA strands. Taq ligase repairs the double strands from any DNA nicks.

Table 2 PCR reaction for Ubc4 cloning (vector)

Materials	Stock Concentration	Final concentration	Vol. used for 20µL reaction (µL)
dNTP mix	10mM	200µM	0.4
Vector Fwd	10µM	0.5µM	1
Vector Rev	10µM	0.5µM	1
Phusion HSII buffer	10X	1X	2
Plasmid DNA	-	<20ng/µL	1
Water	-	-	14.4
Polymerase	1U/µL	0.2U/µL	0.2

Steps		Temperature	Time
Initial denaturation		98°C	1min
	Denaturation	98°C	10s
20x	*Annealing*	50°C	20s
	Extension	72°C	45s
Final extension		72°C	5min
Hold		4°C	-

Table 3 PCR reaction for Ubc4 cloning (Insert)

Materials	Stock Concentration	Final concentration	Vol. used for 20µL reaction (µL)
dNTP mix	10mM	200µM	0.4
Forward Primer	10µM	0.5µM	1
Reverse Primer	10µM	0.5µM	1
Phusion HSII buffer	10X	1X	2
Genomic DNA	-	<20ng/µL	1
Water	-	-	14.4
Polymerase	1U/µL	0.2U/µL	0.2

Steps		Temperature	Time
Initial denaturation		98°C	1min
	Denaturation	98°C	10s
20x	*Annealing*	60°C	20s
	Extension	72°C	30s
Final extension		72°C	5min
Hold		4°C	-

Table 4 5x Reaction buffer for Gibson assembly.

Material	**Volume (µl)**
1M Tris pH7.5	3000
1M $MgCl_2$	300
100mM dNTP	60
1M DTT	300
PEG 4000	1.5g
100mM NAD	300
Water	Up to 6ml
Mix all components and store 40µl aliquots at -20°C.	

Table 5 Gibson assembly reaction master mix.

Material	**Volume**	**Remarks**
5x Reaction buffer	40µl	Table 4 above
T5 Exonuclease	1.6µl	NEB
Phusion polymerase	2.5µl	Invitrogen
Taq DNA ligase	20µl	NEB
Water	85.9µl	
* Mix well and aliquot 20µl per assembly reaction, store at -20°C.		

b) Generating PCR fragments for yeast homologous recombination

C-terminal tagging of Ccr4-Not subunits via PCR fragments were modified from the methods in Knop et. al. (1999). In 3xFLAG tagging of Not4 and Not5, the forward primer had 50 bases of 5' overhang homologous to the gene of interest's coding sequence just before the endogenous Stop codon, followed by an annealing sequence on the p3xFLAG-KanMX plasmid adjoined by the coding sequence of the 3xFLAG tag and a stop codon. The reverse primer was made up of 50 bases of overhang homologous to the 5' end of the non-coding genomic DNA strand upstream of the Stop codon, followed by an annealing sequence on the resistance marker cassette's 3' end on the plasmid(Figure 15). DNA fragments were generated by setting-up standard PCR reactions according to Table 6 and

Table 7. PCR products were then purified by agarose gel electrophoresis and extracted using a kit (FG-91202, Nippon Genetics) as described above. Purified DNAs were stored in water and kept at -20°.

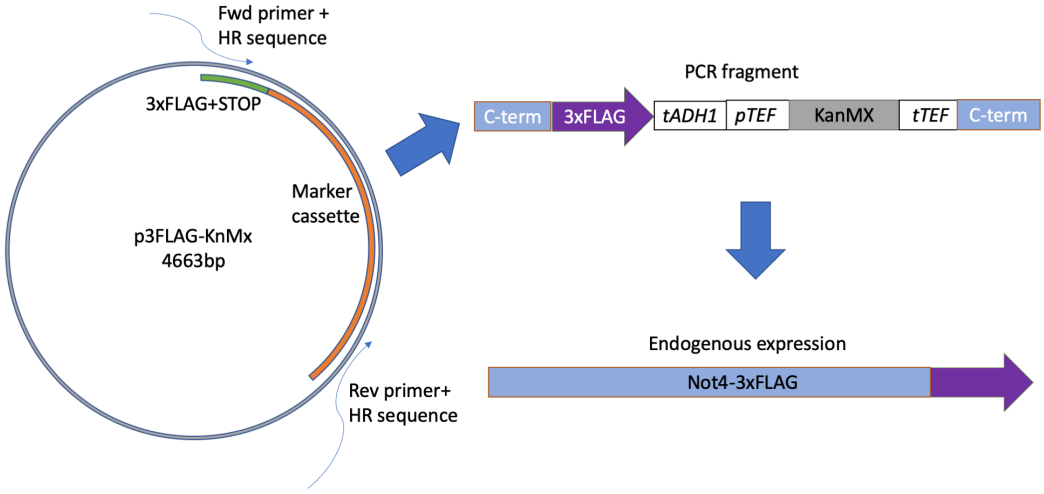

Figure 15 Protein tagging by homologous recombination. Forward primer anneals at the start of the 3xFLAG tag sequence and amplifies towards 3' end of the marker cassette, the reverse primer anneals at the end of the marker cassette and amplifies towards the 5' end of the 3xFLAG sequence. Resulting DNA fragment consists of the sequence for a C-terminally tagged end of the protein of interest with a STOP codon, then followed by the selection marker gene with its own expression signal sequences. Lastly, it ends with the homologous DNA sequence originally adjacent to the end of the coding sequence of the gene of interest (omitting the STOP codon). The flanking homologous sequence were integrated into the genome by homologous recombination and the endogenously expressed protein will contain an affinity tag at the C-terminus of the polypeptide. Genomic DNA sequences used in primer design included in Appendix 8.2

Table 6 PCR reaction for Not4 HR fragment

Materials	**Stock Concentration**	**Final concentration**	**Vol. used for 20µL reaction (µL)**
dNTP mix	10mM	200µM	0.4
Forward Primer	10µM	0.5µM	1
Reverse Primer	10µM	0.5µM	1
Q5 reaction buffer	10X	1X	2
Template DNA	-	< 2ng/µL	1
Water	-	-	14.4
Polymerase	1U/µL	0.02U/µL	0.2

Steps		**Temperature**	**Time**
Initial denaturation		98°C	1min
	Denaturation	98°C	30s
30x	*Annealing*	60°C	30s
	Extension	72°C	2min
Final extension		72°C	2min
Hold		4°C	-

Table 7 PCR reaction for Not5 HR fragment.

Materials	**Stock Concentration**	**Final concentration**	**Vol. used for 20µL reaction (µL)**
dNTP mix	10mM	200µM	0.4
Forward Primer	10µM	0.5µM	1
Reverse Primer	10µM	0.5µM	1
Phusion HSII buffer	10X	1X	2
Template DNA	-	<2ng/µL	1
Water	-	-	14.4
Polymerase	1U/µL	0.2U/µL	0.2

Steps		**Temperature**	**Time**
Initial denaturation		98°C	1min
	Denaturation	98°C	10s
20x	*Annealing*	60°C	30s
	Extension	72°C	2min
Final extension		72°C	5min
Hold		4°C	-

c) Bacterial colony PCR

Bacterial colonies that arise from the selective plate were picked using a sterile pipette tip. The tips were lightly streaked within a marked partition on a fresh selective agar plate containing 50µg/mL Ampicillin before being added directly to a PCR reaction mix for colony PCR (Table 8). The new plate was then incubated at 37°C overnight or until new colonies were visible.

Table 8 Colony PCR reaction for Ubc4 cloning

Materials	**Stock Concentration**	**Final concentration**	**Vol. used for 20µL reaction (µL)**
dNTP mix	10mM	200µM	0.4
Forward Primer	10µM	0.5µM	1
Reverse Primer	10µM	0.5µM	1
Phusion HSII buffer	10X	1X	2
Template DNA	-	<20ng/µL	1
Water	-	-	14.4
Polymerase	1U/µL	0.2U/µL	0.2

Steps		**Temperature**	**Time**
Initial denaturation		98°C	1min
	Denaturation	98°C	10s
20x	*Annealing*	60°C	30s
	Extension	72°C	40s
Final extension		72°C	5min
Hold		4°C	-

d) Yeast colony PCR

Colony PCR was carried out with minor modifications from Looke et. al., 2011. One half of a single colony of yeast was picked from the selective plate and resuspended in 200µl extraction buffer (200mM LiOAc, 1% w/v SDS solution). After heating for 5min at 90°C, 300µl of pure ethanol was added to the mixture and vortexed vigorously for 2min. The mixture was then spun down at 16,000 rpm for 5min. The pellet was washed with 70% v/v ethanol twice. Tubes containing the DNA sample were left on the bench to dry for 20min before resuspending in 100µl of water and spin down for 15s at 16,000 rpm. 1µl of the supernatant from each sample was used as template for the colony PCR reactions. PCR reactions were set up as below (Table 9).

Table 9 Colony PCR reactions for No4-3xFLAG and Not5-3xFLAG transformants.

Materials	**Stock Concentration**	**Final concentration**	**Vol. used for 20µL reaction (µL)**
dNTP mix	10mM	200µM	0.4
Forward Primer	10µM	0.5µM	1
Reverse Primer	10µM	0.5µM	1
Phusion HSII polymerase buffer	10X	1X	2
Template DNA	-	<2ng/µL	1
Ultrapure water	-	-	14.4
Polymerase	1U/µL	0.2U/µL	0.2

Steps		**Temperature**	**Time**
Initial denaturation		98°C	1min
	Denaturation	98°C	10s
20x	*Annealing*	50°C	30s
	Extension	72°C	30s
Final extension		72°C	5min
Hold		4°C	-

3.1.4 Determining protein concentration

Protein concentration was estimated using a ND-1000 UV spectrophotometer (ThermoFischer) in Protein A280 mode by applying 2µl of sample onto the pedestal. Absorbance at 280nm was measured under the general reference setting (1 Abs = 1mg/ml) and translated into a protein concentration based on the Beer-Lambert law. Each sample was measured thrice, and the mean was taken as the final reading. Calibration using BSA/water solution as protein concentration standards were carried out occasionally to monitor any deviations. 5mg/ml BSA stock solution and aliquots of dilutions at 1mg/ml, 0.5mg/ml, 0.2mg/ml, 0.1mg/ml, 0.05mg/ml and 0.025mg/ml protein concentrations were used. Each concentration was measured in triplicates and the mean was taken as the final reading.

3.1.5 SDS-PAGE

Separation of protein samples were carried out using denaturing sodium dodecyl sulphate polyacrylamide gel electrophoresis (SDS-PAGE) based on their molecular sizes. Proteins were denatured in the presence of high temperature, strong reducing agent and ionic detergent. The unfolded polypeptides, coated with negatively charged SDS molecules in the loading and running buffer, migrate through the gel matrix towards the cathode. Mobility of each polypeptide was inversely proportional to their molecular mass. Typically, 12% (v/v) polyacrylamide gels (Table 10) were casted using a mini gel system (miniVE HOEFER®, Amersham). Separating gel solution was poured first and allowed to polymerise on the bench for 45min. The stacking gel solution was then layered on top and the gel comb inserted. The gel was left on the bench to polymerise for 35min. 4 parts volume of sample was mixed with 1 part of 5x SDS loading buffer (0.25% w/v Bromophenol Blue, 0.5M DTT, 50% v/v glycerol, 10% w/v SDS, 0.25M Tris-Cl pH 6.8) and placed on a heat block set to 95°C for 5min then cooled on ice for 5min. A maximum of 35µl of heated sample was loaded per well. 3µl of prestained protein standard (BlueEasy, NipponGenetics) was loaded in one lane on the gel. Electrophoresis was performed in 1x SDS-running buffer (192mM Glycine pH 8.3, 25mM Tris-Cl, 0.1% w/v SDS) at 180V until the dye front exit the gel bottom.

Table 10 SDS-PAGE gel composition per mini gel (12%)

Components	Separating gel	Stacking gel
Water	2.6mL	3mL
Acrylamide/Bis-acrylamide, 30% solution	3.2mL	0.67mL
1.5M Tris pH 8.8	2mL	1.25mL
10% w/v SDS	80µL	50µL
10% w/v APS	80µL	50µL
TEMED	8µL	5µL

3.1.6 Western Blotting

Tagged protein subunits were detected after SDS-PAGE using western blotting (Towbin et al., 1979). Polyacrylamide gel after electrophoresis was washed twice in water for 5min. Thick blotting paper and nitrocellulose transfer membrane were cut to a similar size as the gel. Gel, blotting paper and membrane were incubated in transfer buffer (190mM Glycine pH 8.3, 25mM Tris-Cl, 0.1% w/v SDS, 20% v/v methanol) for 10min before assembling into the transfer cassette according to the illustration below (Figure 16). The transfer was performed at 4°C and 10mA in fresh transfer buffer overnight. After the transfer, the membrane was incubated for 5min with 0.02% w/v Ponceau Red solution and washed in 1xTBST (50mM Tris-Cl pH 7.6, 150mM NaCl, 0.1% v/v Tween 20) to verify the transfer of proteins from the gel to the membrane. The membrane was then incubated for 1hr at room temperature or overnight at 4°C with blocking buffer (5% w/v skimmed milk in TBST) and shaking at 120rpm. The blocked membrane was washed with TBS (50mM Tris-Cl pH 7.6, 150mM NaCl) for 5min before incubating with rabbit anti-FLAG primary antibody (Sigma, F7425) diluted 1: 1000 in blocking buffer for 1hr at room temperature or overnight at 4°C. After three washes in 1xTBST, the membrane was incubated with goat against rabbit Horse reddish peroxidase (HRP) conjugated secondary antibody (Invitrogen, #65-6120) diluted 1:15,000 in blocking buffer for 1 hour at room temperature on a rocking platform set to 30rpm. The membrane was then washed three times in 1xTBST and incubated in Pierce™ ECL Western Blotting Substrate (ThermoFischer) for 4min. Chemiluminescent signals were detected and recorded using the FX6 imager system (Vilber Inc.) in AUTO mode.

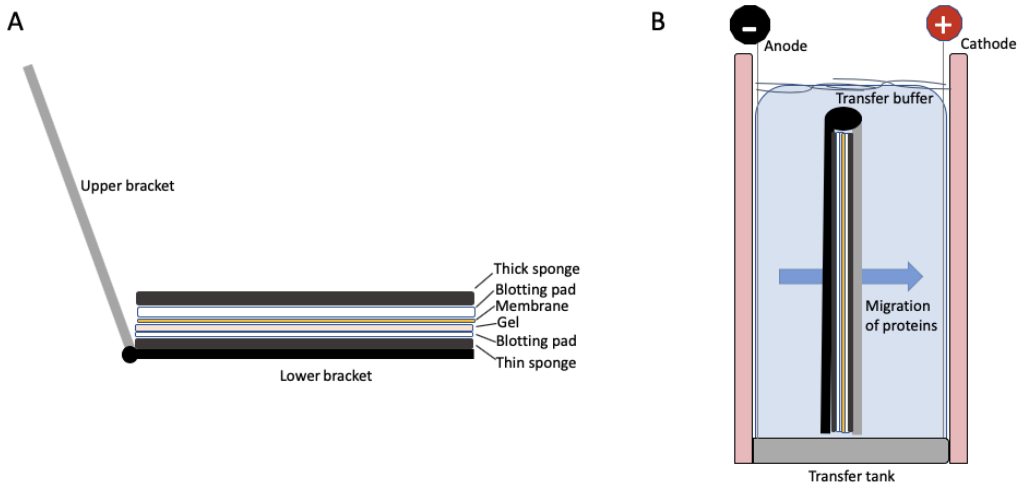

Figure 16 Illustration of a Western blot set-up. A) Set-up of the transfer stack. B) Position of the stack in the transfer tank and movement of protein during the transfer.

3.1.7 Coomassie staining

Protein bands from SDS-PAGE were visualised by the Coomassie staining method (Cold Spring Harb Protoc, 2007). Gels were washed in water for 3x 10min after separation and then incubated overnight in stain solution (1% w/v Coomassie Brilliant Blue, 10% v/v glacial acetic acid, 50% v/v methanol, 40% v/v water) on a rocker platform. De-staining was done by heating up the gels in de-stain solution (10% v/v glacial acetic acid, 50% v/v methanol, 40% v/v water) in an 800W microwave for 1-2min and incubated overnight on a shaker at room temperature. De-stained gels were imaged with an EPSON film scanner using positive scanning mode.

3.1.8 Silver staining

SDS-PAGE gels that contained less than ~2µg of estimated total protein per lane were visualised using the silver staining method (Blum et al., 1987) as protein bands were very faint at this level using the Coomassie method. The Pierce™ Silver Stain Kit (ThermoFischer, #24612) was used for most gels initially. After electrophoresis, gels were washed in water for 2x 10min. Gels in solution were under constant gentle shaking at all steps. Then the gels were fixed in Fixing solution (10% v/v glacial acetic acid, 30% v/v ethanol) for 2x 15min. Fixed gels were then placed in washing solution (10% v/v ethanol) for 2x 10min and then rinsed in water for 2x 5min. Gels were then incubated in Sensitiser working solution (1 part stock sensitiser to 500 parts water) for exactly 60s and immediately rinsed with water for 2x 60s. Subsequently, the gels were incubated in staining working solution (1part stain enhancer to 50

parts Silver stain solution) for 30min. Following two quick exchanges of water for 20s each, the gels were covered in developer working solution (1 part stain enhancer to 50 parts developer solution) for 3min before replacing the developer working solution with stopper solution (5% v/v glacial acetic acid). Gels were left in the stopper solution for 20min before replacing it in water. Alternatively, silver staining was also carried out using solutions made from molecular biology grade reagents. Fixer, washing and stopper solutions were made as the above. Gels from SDS-PAGE were first washed in water for 2x 15min. Then, gels were incubated 2x 10min in the fixer solution followed by washing three times in the washing solution for 10min each. Washed gels were quickly rinsed twice with water for 5min each and then incubated with the sensitising solution (0.02% w/v sodium thiosulfate, Sigma #72049) for exactly 60s. Following sensitising, gels were rinsed with water for 2x 30s and then incubated with stain solution (0.2% w/v $AgNO_3$, 0.04% v/v formaldehyde) for 20min. Stained gels were washed with water for 3x 10min and then covered in developer solution (2% w/v Na_2CO_3, 0.04% v/v formaldehyde) for 3min. Developed gels were rinsed once with water and quickly covered in stopper solution for 20min. Gels were washed in water for another 2x 10min and scanned using an EPSON film scanner in the Positive mode..

3.1.9 Size exclusion chromatography

a) Separation of the recombinant yeast Ubc4 protein was carried out using the Superdex 75 Increase 10/300 GL column (GE Healthcare) on an Äkta pure HPLC system (GE Healthcare). 300µl of protein solution (0.85mg/ml) containing the purified 6xHist-Ubc4 protein was eluted with the SEC buffer (20mM HEPES pH 8.0, 150mM NaCl, 1mM DTT) at 4°C, 0.5ml/min. The peak fractions from the isocratic elution were checked by SDS-PAGE. 50µl from each fraction under the 280nm absorbance peak was mixed with 12.5µl of 5x SDS loading buffer and heated at 95°C for 3min before loading 25µl per well onto a 10-20% TGX pre-cast gradient gel (Invitrogen). The gel was run at 110V for 1.5 hours in 1x SDS running buffer and visualised using the Coomassie stain solution.

b) Superose 6 10/300 GL column (GE Healthcare) mounted on an Äkta pure HPLC (GE healthcare) was used to filter the eluate from the 3xFLAG-tag protein purification. The column was calibrated before use with 100µl of a mixture containing 1mg/ml Blue Dextran (Amersham) and 3mg/ml beta-galactosidase (Sigma) in TBS buffer (50mM Tris-Cl pH 7.5, 150mM NaCl) at 4° and a flow rate of 0.5ml/min, to mark the void volume (7.2ml) and the

apparent retention volume of a 465 kDa tetrameric globular protein (Ve: ~15.8ml). Peak fractions were pooled and concentrated using a 30k MWCO Spin-X UF6 centrifugal concentrator (CORNING), 4000g, 60min and 4°C to ~100µl final volume. The protein concentration was estimated using a nanodrop (ND-1000, ThermoFischer) blanked with the SEC buffer and 50µl from each of the eluted peak fractions was used for SDS-PAGE analysis.

3.1.10 Competent *E. coli* cells and transformation

Bacterial glycerol stock was spread on Luria-Bertani(LB)-agar plate (0.01% w/v Tryptone, 0.01% w/v NaCl, 0.005% w/v Yeast Extract, 0.015% w/v BactoAgar) and incubated overnight at 37°C. One colony was then picked and inoculated 3mL LB medium (same as above but without BactoAgar) shaken overnight at 250rpm and 37°C. The overnight culture was added to 200mL LB media in a 500mL Erlenmeyer flask and incubated at 37°C, 250rpm until OD_{600} reached 0.2-0.7. The bacterial culture was spun down at 4000 rpm and 4°C for 15min (5810r with rotor A-4-81, Eppendorf AG). The pellet was resuspended in 200ml ice cold 20mM $MgCl_2$ and then pelleted again as above. Cells were washed twice in 50ml ice cold 85mM $CaCl_2$ with 20% sterile glycerol followed by centrifuging at 4000 rpm and 4°C for 20min and resuspending the pellet. After the last wash, 50µl of cell suspension was aliquot into 1.5ml Eppendorf tubes and snap frozen in liquid nitrogen. Frozen aliquots were stored at -80°C.

5µl of Gibson assembly reaction product was mixed with 50µl competent *E. coli* cell mix on ice, then incubated at 42°C for exactly 60s before placing it back on ice for 10min. The reaction mixture was transferred into 5ml LB media and incubated at 37°C for 6 hrs with shaking (225 rpm) before spreading onto a LB agar plate containing 100µg/mL Ampicillin. Plates were incubated at 37°C overnight and positive colonies were verified by colony PCR as described above.

3.1.11 Bacterial cell culture

A single colony of transformed bacteria was used to inoculate a 5ml LB starter culture overnight with shaking (250rpm) at 37°C. The starter was then used to inoculate the main culture of 2L LB medium containing 50µg/mL Ampicillin antibiotic in a smooth-walled 5L Erlenmeyer flask. The main culture was grown at 25°C for 18 hours with shaking (200rpm). OD_{600} was checked using a spectrophotometer to be around 0.4-0.6 before the induction. The 5L flask was then placed on ice for about 20min before stock IPTG was added to a final

concentration of 1mM. The culture was incubated at 200 rpm for an additional 3-4 hours at 37°C. Cells were harvested at 6000x g, 30min at 4°C (Avanti J-26 XP centrifuge with JLA-8.100 rotor). The cell pellet was resuspended in ice cold water twice and pelleted at the same setting before the final pellet was frozen in liquid nitrogen and stored at -80°C.

3.1.12 Bacterial protein purification for 6xHis-Ubc4

25g cell pellet from the above step was thawed in ~250mL ice-cold lysis buffer (50mM Tris-Cl pH 8, 500mM NaCl, 1mM DTT, 5% glycerol, 5mM PMSF). ~300mL of this mixture was passed three times through a cell disruptor (Microfluidics, M110P) at 10,000 psi with the mixing chamber and cooling coil covered with ice during processing. Raw lysate was centrifuged at 32,000x g, 4°C for 60min (Avanti J-26 XP with JA 16.250 rotor). The supernatant was centrifuged again as above. Cleared lysate was passed through a 2µm pore size Whatman® Puradisc 25 syringe filter using a large syringe. Filtered lysate was passed through a HisTrap™ FF column (GE Healthcare, #17-5255-01) pre-equilibrated with lysis buffer on an Äkta pure HPLC system at 1mL/min. The column was washed with 10 bed volume (BV) of wash buffer (Lysis buffer + 30mM Imidazole) at 1mL/min. Elution was done by passing 5 BV of elution buffer (Wash buffer + 500mM Imidazole). Eluted protein was collected into 50mL falcon tubes. 15ml of the eluate was added into a spin concentrator (Vivaspin® 20 3K, Sartorius) and spun at 4000 rpm, 4°C for 30min (8510r centrifuge with A-4-81 rotor, Eppendorf AG). The concentrated sample was topped up to 20mL with elution buffer containing no imidazole and spun again as above. This was repeated 5 times before the final concentrating step. The protein solution was then concentrated to ~0.85mg/mL at 4000 rpm, 4°C for 60min. The protein concentration was estimated using a Nanodrop spectrophotometer (ND-1000, ThermoFischer) in Protein A280 mode and blanked with elution buffer without imidazole. The protein solution was frozen in liquid nitrogen and stored at -80°C. Aliquots of the purified protein was checked using size exclusion chromatography and SDS-PAGE.

3.1.13 Yeast competent cells and transformation

3mL of YPD media (1% w/v Yeast extract, 2% w/v Tryptone, 2% w/v Glucose) was inoculated with the S288c cells and incubated overnight at 30°C, 230 rpm. 50mL of YPD media was inoculated with this overnight pre-culture and incubated for 4-6 hours at 30°C, 230 rpm until the final OD_{600} was ~0.4. The cells were spun down at room temperature with 1000x g

(8510r centrifuge with A-4-81 rotor, Eppendorf AG) and washed by resuspending in 20ml water, then spinning down as in the previous step. After removing the supernatant, the cell pellet was resuspended in 10ml SORB solution (100mM Lithium Acetate, 10mM Tris-Cl, pH 8.0, 1mM EDTA, pH 8.0, 1M D-Sorbitol) and then spun at 500x g, 5min at room temperature. The supernatant was removed, and cells were resuspended in 360µl SORB solution plus 40µl of UltraPure™ Salmon Sperm DNA solution (ThermoFischer, #15632011). Aliquots of 50µl from this preparation were stored at -80°C until use.

One aliquot of the competent cell mix and 20µl of homologous recombination PCR product was mixed by pipetting on ice. 300µl of sterile PEG solution (100mM Lithium acetate, 10mM Tris-Cl pH 8.0, 1mM EDTA pH 8.0, 40% w/v PEG 4000) was then added to the mixture and left at room temperature for 30min. 40µl of DMSO (Sigma) was added into the tube and incubated at 42°C for 15min in a water bath. The tube was then placed on ice for 5min and centrifuged at 2000 rpm, 2min, room temperature. After discarding the supernatant, cell pellet was resuspended in 100µl of water. The suspension was added to 3ml YPD medium in a 15ml tube and incubated for 6 hours at 30°C, 230 rpm. The tube was centrifuged at 1000 rpm, 5min and room temperature, then discarding the supernatant. The pellet was resuspended in ~100µl of YPD media and spread onto YPD agar plate (1% w/v Yeast extract, 2% w/v Tryptone, 2% w/v Glucose, 2% w/v Agar-agar) containing 300µg/ml G418 antibiotic (Gibco). The plate was incubated for 3 days at 30°C. Colonies were then picked to perform the colony PCR.

3.1.14 Yeast cell culture

One colony of yeast from the confirmed transformants on a selective plate was picked and added to 3ml YPD media to start the pre-culture. The pre-culture was incubated overnight at 30°C, 230 rpm and transferred into 250mL YPD media in a 500ml flat bottomed conical flask and incubated overnight at 30°C, 230rpm. 40ml of the overnight starter culture was used to inoculate 2L YPD in a 5L baffled Erlenmeyer flask. The culture was incubated for 18-20 hours, at 30°C and 140rpm. Multiples of 2L culture were used for harvesting larger amount of cell mass. Cells were harvested by centrifuging at 6000x g for 20min at 4°C (Avanti J-26 XP centrifuge with JLA-8.100 rotor). The cell pellet from a 10L batch of culture was resuspended in 50ml ice cold water and flash frozen by dripping the mixture into liquid nitrogen using a 25ml serological pipette. ~120g of pellets from this step were stored at -80°C. The pellet from consecutive batches of the same culture were stored together when necessary.

3.1.15 Yeast cell disruption and protein purification

120 - 150g of frozen pellet was weighed into a liquid nitrogen cooled 500ml stainless steel jar for the PM-100 planetary mill (Retsch). 20 stainless steel milling balls (Ø20mm) supplied by Retsch were also added into the jar. One round of milling was done at 500 rpm, 100% power, 3min total milling time with 1min interval and reversed directions between intervals. Milling was repeated 8 times with 3min of cooling the jar in liquid nitrogen in between. Complete cell disruption can be determined by comparing the cell powder before and after milling under a light microscope (VWR) in bright field mode at 400x magnification. Intact yeast cells appeared round and oval in shape with ~5µm in diameter.

For cell lysis, ~400g of the cell powder was weighed into a plastic bag and heat sealed. The bag was submerged in a sink filled with tap water at room temperature for 5min. The thawed powder was mixed with 5 parts volume of ice-cold lysis buffer (100mM HEPES-OH pH 7.5, 300mM NaCl, 2mM $MgCl_2$, 4mM PMSF, 20% Glycerol, 0.2% Triton X-100, 2mM TCEP) for 30min in a 1L beaker on ice using a magnetic stirrer. Raw lysate was centrifuged at 52,000x g, 4°C for 60min (Avanti J-26 XP centrifuge with JA-25.50 rotors) and the supernatant was transferred into fresh centrifuge tubes and centrifuged again similarly. ~300ml of cleared lysate was distributed into 50ml falcon tubes and incubated with 200µL of M2 anti-FLAG affinity beads slurry per tube (Sigma-Aldrich) for two hours in cold room with end-to-end rocking on a rotator. Beads were spun down and washed by resuspending three times in ice cold wash buffer (50mM HEPES-OH pH 7.5, 300mM NaCl, 1mM PMSF, 2mM TCEP, 1mM $MgCl_2$,0.05% Triton X-100) then centrifuged at 200x g, 4°C, 20min. Washed beads were pooled into one tube and incubated with 5 bed volume (BV) of ice cold elution buffer (50mM HEPES-OH pH 7.5, 150mM NaCl, 1mM $MgCl_2$, 2mM TCEP) containing 200µg/ml 3xFLAG peptide (4mg lyophilised peptide dissolved in 0.8ml water, the stock solution is 5mg/ml) (Sigma-Aldrich) for 2 hours with rocking in a cold room. The content after incubation was centrifuged at 500x g, 4°C, 30min and the supernatant was aspirated into a 30k MWCO spin concentrator (#VS0621, Sartorius) and centrifuged at 4000x g, 4°C, 45min. Protein concentration was estimated using a Nanodrop (ND-1000, ThermoFischer) blanked with the elution buffer for the incubation step, before and after concentrating. The concentrated sample carried on with either the size exclusion chromatography or the density gradient separation. A small aliquot of the eluate was analysed with SDS-PAGE and western blot to monitor the purification.

3.1.16 Modified yeast protein purification

Cell disruption and clarified lysate was prepared as described above. All the following processes were done in the cold room or on ice whenever possible, and the processed protein solutions were always maintained on ice to minimise protein degradation. 31.8g of solid ammonium sulfate was added slowly to 300ml cleared lysate in a 500ml beaker placed on ice or in a cold room and stirred until all solid dissolved, in order to reach 20% saturation according to Duong-Ly and Gabelli (2014). The solution was spun at 20,000x g for 30min, 4°C (Avanti J-26 XP centrifuge with JA-16.250 rotor) and discarded the pellet. Additional 50g of solid ammonium sulfate was added to ~350ml of the supernatant from the previous step to get 45% saturation and stirred on ice until all the solid had dissolved. The solution was spun again at 20,000x g for 30min, 4°C and the pellet was first washed with 100ml lysis buffer (50mM HEPES pH 8.0, 100mM NaCl, 5mM DTT, 10% v/v glycerol, 2mM PMSF) by inverting the tube gently and discarding the liquid. The washed pellet was resuspended in 100ml ice cold lysis buffer and dialysed overnight in the cold room using a 3,000 MWCO dialysis tubing (SPECTRUM) in 1L dialysis buffer (50mM HEPES pH 8.0, 150mM NaCl, 3mM DTT, 5% v/v glycerol, 2mM PMSF) with stirring. The protein solution after dialysis was distributed into fresh 50ml tubes and incubated with 500µL of M2 anti-FLAG affinity beads slurry per tube (Sigma-Aldrich) for 2 hours in the cold room with end-to-end rotation. The tubes were then centrifuged at 500x g, 4°C, 30min (5810r centrifuge with A-4-81 rotor, Eppendorf AG). After discarding the supernatant, 25ml of ice-cold wash buffer (50mM HEPES pH 8.0, 150ml NaCl, 1.5mM TCEP pH 7, 1mM PMSF) was used to resuspend and pool the beads into a single 50ml tube, using a 10ml serological pipet. Beads were centrifuged again at 500x g, 4°C, 30min and discarding the supernatant. 3 bed volumes (~2-6ml) of elution buffer (Wash buffer + 300µg/ml 3xFLAG peptide) was mixed with the sedimented beads by pipetting and incubated for 2 hours on a rocking platform (VWR) in the cold room. Beads were then aspirated into a 10ml plastic column (MoBiTec, #1014) and the filtrate was collected in a 15mL plastic tube on ice. The eluate was then transferred into a fresh 30k MWCO centrifugal concentrator (CORNING, Spin-X UF6) and concentrated to a final volume of ~250µl at 4000x g, 4°C, 60min (5810r centrifuge with A-4-81 rotor). The protein concentration was estimated using nanodrop blanked with the elution buffer and 3-5µg of protein sample was typically analysed using SDS-PAGE gels and 1-2µg for the western blot.

3.1.17 Label-free quantitative Mass spectrometry (LFQ-MS)

a) Pull-down of the tagged protein and its co-purifying proteins was carried out using the M2 anti-FLAG affinity beads (Sigma-Aldrich). 2g of cell powder prepared using the planetary ball mill was weighed into a 1.5ml Eppendorf tube and thawed on ice. 500µl of ice-cold lysis buffer (50mM HEPES pH 7.4, 150mM NaCl, 0.5% Triton X-100, 1mM DTT, 1mM PMSF, 10% v/v glycerol) was added to the lysate and mixed by pipetting. The lysate was centrifuged at 16,000 rpm, 4°C, 45min and the supernatant was centrifuged again in a fresh tube as before. 50µl of anti-FLAG affinity beads slurry was added to the cleared lysate and incubated for 2 hours in the cold room on the end-to-end rotator. The mixture was centrifuged at 500x g, 4°C, 15min and the supernatant was discarded. 500µl of ice-cold wash buffer (50mM HEPES pH 7.4, 800mM NaCl, 0.5% v/v Triton X-100, 10% v/v glycerol, 1mM DTT, 1mM PMSF) was added to resuspend the beads and the tube was centrifuged at 500x g, 4°C, 15min. The washing step was repeated twice and discarding the supernatant. Finally, the washed beads were transferred into a fresh 1.5ml Eppendorf tube containing 50µl of 2x loading buffer (4% w/v SDS, 10% v/v 2-mercaptoethanol, 20% v/v glycerol, 0.004% bromophenol blue, 125mM Tris-Cl pH 6.8). The tube was placed onto a heat block at 95°C for 2min and then immediately placed back on ice for 10min. A control sample was made by the same process in parallel, using the untagged S288c cells. Both the sample and control were then submitted to the Mass Spectrometry facility (University of Wuerzburg, Germany) for analysis.

b) Identification of the purified proteins from the modified purification method above was done as follows. 50g of cell powder was thawed on ice for 15min in a 250ml beaker and topped up to 100ml with ice cold 2x lysis buffer (100mM HEPES pH 8.0, 200mM NaCl, 10mM DTT, 20% v/v glycerol, 4mM PMSF). The lysate was maintained on ice for another 30min with constant stirring before centrifuging at 50,000x g, 4°C, 60min (Avanti J-26 XP centrifuge with JA-25.50 rotor). The supernatant was centrifuged again at the same setting. The final volume of the cleared lysate was estimated using a glass measuring cylinder and topped up to 100ml using ice cold 2x lysis buffer. 10.6g of solid ammonium sulfate was added to the lysate on ice until all solid dissolved. The solution was then centrifuged at 4000x g, 4°C, 30min (5810r centrifuge with A-4-81 rotor, Eppendorf AG) and the pellet was discarded. 14.3g of solid ammonium sulfate was added into the supernatant and stirred until all the solid dissolved. The solution was centrifuged at 4000x g, 4°C, 30min, then discarding the supernatant. The pellet was resuspended in 15ml ice cold lysis buffer (50mM HEPES pH 8.0, 100mM NaCl,

5mM DTT, 10% v/v glycerol, 2mM PMSF) and sealed into a 3,000 MWCO dialysis tubing (SPECTRUM). The solution was dialysed in 500ml dialysis buffer (50mM HEPES pH 8.0, 150mM NaCl, 3mM TCEP, 5% v/v glycerol, 2mM PMSF) overnight in the cold room. The dialysed solution was aspirated into a fresh 50ml tube and 100µl anti-FLAG affinity beads slurry (Sigma) was added. The mixture was incubated for 2 hours on a gyratory platform in the cold room. The beads were sedimented at 3000x g, 4°C, 15min and resuspended with 15ml of FLAG buffer (50mM HEPES pH 8.0, 150mM NaCl, 1mM TCEP pH 7, 1mM PMSF). This washing step was repeated twice, and all supernatant was discarded. The washed beads were then resuspended with 5ml FLAG buffer containing 300µg/ml 3xFLAG peptide (ApexBio Inc.) and incubated for 2 hours in the cold room on a gyratory platform. The mixture was passed through a 10ml Poly-Prep® column (BioRad) under gravity and the filtrate was concentrated using a 10k MWCO Spin-X UF6 centrifugal device (CORNING) to ~75µl. The control experiment was done in parallel using the untagged S288c cells prepared by exactly the same process. ~50µl of each sample was used for protein identification at the Mass spectrometry facility (University of Wuerzburg, Germany). Mass spectrometry data were stored and presented using the Spotfire server.

3.1.18 Density gradient centrifugation and fixation (Grafix)

The sucrose density gradients were set up using a gradient master machine (BioComp Instruments) in a 4ml ultracentrifuge tube (Beckman Coulter, #344062). The 10-45% (w/v) sucrose gradient were made by first dissolving 1g of sucrose in 10ml of an elution buffer from the purification step and 4.5g of sucrose in another 10ml of the same buffer. The lighter solution was laid over the heavy solution in the centrifuge tube using a syringe. The density gradient was formed by rotating the tubes on the gradient mixer stage (86°, 57s, 20rpm). Gradient tubes were kept at 4°C for one hour before loading of the samples. Protein sample loaded per tube was between 50- 300µl in volume. The tubes were balanced and mounted on a SW60Ti rotor (Beckman Coulter) and spun for 12- 18hrs at 35,000 rpm and 4°C using an Optima-L100XP ultracentrifuge (Beckman Coulter). The content of each tube was fractionated in 300µl fractions from the top and either further concentrated with a spin concentrator or precipitated using acetone for analysis by SDS-PAGE. Density gradient fixation was carried out according to Kastner et al. (2008) with minor alterations. 0.15-2% v/v of EM grade Glutaraldehyde solution (EMS) was added to the heavy sucrose solution before mixing. Standard density gradient centrifugation was carried out according to the above protocol. After fractionating,

each fraction was immediately quenched by adding 50µl 1M Tris-Cl (pH 7.6). An identical density gradient without the crosslinker was set up in parallel. Fractions containing the fixed protein particles were identified by checking the non-fixed density gradient using SDS-PAGE and western blot.

3.1.19 Deadenylase activity assay

Assays were adopted with modifications according to Raisch et. al. (2019) and Stowell et. al. (2016). Substrate used for testing the purified complex consisted of a 5' FAM fluorophore label and a short 3' UTR sequence followed by the 25-adenosine tail (see RNA oligos). The full-length A25 RNA substrate and the A0 substrate without the 25-adenosine tail were synthesised and used as markers. 1µl of 10µM stock RNA each was mixed with 25µl of 2x RNA loading dye (95% formamide, 0.025% w/v SDS, 0.025% w/v Bromophenol Blue, 0.5mM EDTA pH 8.0) and 23µl water. The reaction was set up as in Table 11 with 200nM of the A25 substrate and the purified complex each, and incubated at 30°C for up to 128min. Aliquots of 4µl were taken at each time point (t= 0, 2, 4, 8, 16, 32, 64min) and immediately mixed with equal volume of 2x RNA loading dye before heating to 95°C for 2min. Denaturing Urea-polyacrylamide TBE mini gel was prepared using a SureCast Gel Handcast System (ThermoFischer) and the gel solution was mixed as in Table 12. Gel solution was poured into the cast after adding TEMED and left on the bench to polymerise for 60min. Polymerised gel was placed into the gel tank filled in 1xTBE (89mM Tris-Cl pH 8.3, 89mM Boric acid, 2mM EDTA pH 8.0). 1µl of RNA marker and 8µl of sample per well were loaded onto the gel and ran at 300V until the dye front exited the gel end near the anode. Gels were documented with a FX6 gel imager using the FITC pre-set setting (Vilber Inc.).

Table 11 Deadenylase activity assay reaction set-up.

Stock reagent	Amount added (µl)	Final concentration
2x reaction buffer (20mM HEPES pH 7.6, 10mM KCl, 40mM NaCl)	25	1x
10µM RNA substrate (A25)	1	200nM
100mM $Mg(OAc)_2$	1	2mM
2µM Purified protein	5	200nM
Water	18	-
Total volume	50	

Table 12 20% denaturing Polyacrylamide TBE RNA gel composition.

Stock reagent	Amount added (ml)
30% 19:1 Acrylamide/bis-acrylamide solution	6.6
Urea	4.2
10x TBE (1M Tris-Cl pH 8.3, 1M Boric acid, 25mM EDTA pH 8.0)	1
10% w/v APS	0.05
TEMED	0.005
Water	2.34

3.1.20 Ubiquitination activity assay

The Not4 subunit of the Ccr4-Not complex is an E3 RING ubiquitin ligase that interacts with its E2 (Ubc4) *in vivo*. The ubiquitination activity was assayed using a ubiquitination system consisting of a recombinant human E1(Uba1), a recombinant yeast E2 (Ubc4) from bacterial overexpression and the affinity purified Ccr4-Not complex as the E3. The reaction was set up according to Table 13. An established assay for recombinantly expressed human Uba1(E1), Ubh7(E2) and Huwe1-c (E3) was compared as a positive control in parallel (Seenivasan and Liu, AG Lorenz). The negative control was set up similarly but without ATP. Reactions were incubated at 30°C, 120 rpm for 90min. 10µl aliquots were drawn at t= 0, 15, 30, 60,90min and mixed immediately with 2µl 5x SDS loading buffer. 9µl from each time point was visualised on Novex™ 10-20% Tris-Glycine Mini Gels (Invitrogen) by Coomassie staining. Gels were placed in the XCell SureLock Mini-Cell Electrophoresis tank (Invitrogen) and run at 110V for 1.5Hrs in 1xSDS running buffer. 3µl of each sample was run on a separate gel similarly and western blotted onto PVDF membrane (Amersham). The membrane was incubated with 1:1000 Ubiquitin (P4D1) Mouse mAb (CellSignal, #3936) overnight with shaking at 120rpm and then incubated with 1: 10,000 rat anti-mouse HRP conjugated secondary antibody (Invitrogen, #04-6020) for 1 hour at room temperature with shaking. Membrane was then incubated in Pierce™ ECL Western Blotting Substrate (ThermoFischer) and detected using the FX6 imager system (Vilber Inc.) in AUTO mode for chemiluminescence. Alternatively, membrane with Ccr4-Not samples were also detected using rabbit anti-FLAG antibody and goat anti-rabbit HRP conjugated antibody to locate the Not4-FLAG.

Table 13 Ccr4-Not complex ubiquitination activity assay set-up.

Components	Stock concentration (µM)	Final concentration (µM)
E1 (Uba1)	9	0.2
E2 (yUbc4)	47	5
E3 (Ccr4-Not)	3.8	2
Mono-ubiquitin	3758.4	100
$MgCl_2$	100,000	8000
ATP	1500	100
25mM HEPES pH 7.4	2x	1x

Table 14 Ubiquitination assay set up (positive control)

Components	Stock concentration (µM)	Final concentration (µM)
E1 (Uba1)	9	0.2
E2 (Ubh7)	100	5
E3 (Huwe1-c)	100	5
Mono-ubiquitin	3758.4	100
$MgCl_2$	100,000	8000
ATP	1500	300
25mM HEPES pH 7.4	2x	1x

3.2 Electron microscopy

3.2.1 Continuous carbon support EM grids

Copper grids (Agar Scientific, 400mesh, Ø3.05mm) were coated with a think continuous carbon layer and used for negative staining TEM. Firstly, the carbon film was produced by evaporating a graphite filament in the vacuum chamber of a DESK V sputter coater (Denton Vacuum) and depositing onto the freshly split side of 2 x 2cm mica surface (PLANO) placed on the stage. The chamber was evacuated to ~5.8×10^{-7} Torr before a current of around 15-20mA was passed through the graphite filament for 1-2s for evaporation to occur. Afterwards, the chamber was vented. Then, plain copper grids were cleaned by dipping into chloroform and 2-propanol first and submerged in water one by one onto a piece of blotting paper wrapped on a small metal mesh stage placed in a water-filled trough. The carbon film was then floated on water gently and the water level was lowered until the film laid onto of the array of grids. The grids were taken together with the blotting paper and air-dried overnight before use.

3.2.2 Negative staining EM

Self-made EM grids with continuous carbon support layer was glow-discharged for 60s at 1.8×10^{-2} Torr and medium power setting, using a plasma cleaner (Harrick Plasma). 4µl of protein sample was applied onto the glow-discharged EM grids for 1min. Excess liquid was removed using Whatman No.1 filter paper and the grid was washed three times with water followed by three times of 2% v/v Uranyl acetate solution (EMS). An additional drop of the heavy metal stain was incubated on the grid for 5min before blotting dry (Figure 17). Air-dried grids were mounted onto a single-tilt room temperature holder and checked using a 120kV T12 electron microscope (FEI). Micrographs were recorded mostly at nominal magnifications of 30,000 and 52,000x with a CCD detector (4K Eagle, FEI) to assess the protein particle distribution and morphology.

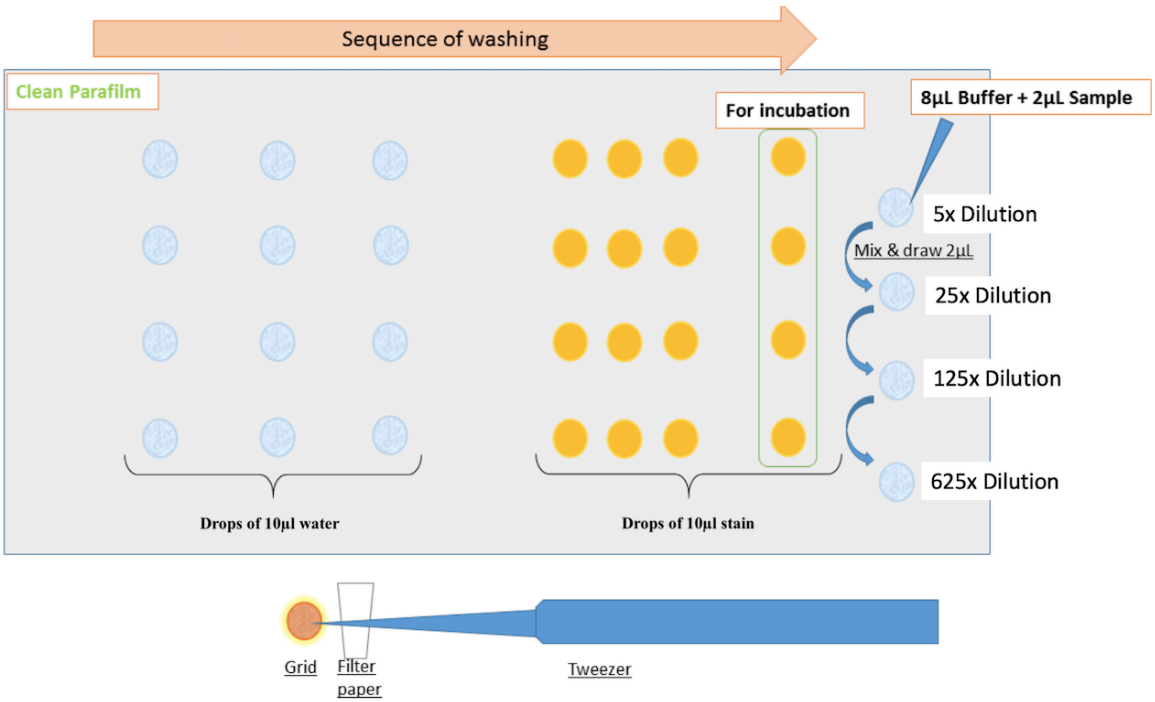

Figure 17 Negative staining procedure. Drops of water and stain solution are prepared on a clean parafilm sheet like above. After incubating the sample solution and blotting, a quick buffer exchange is done with touching the hydrophilic side of the grid on each droplet with blotting in between. The last drop of stain solution is let on the grid for a desirable incubation period before blotting the grid dry. Serial dilutions of the concentrated sample can be done on the spare area on the parafilm as shown.

3.2.3 Sample vitrification

Cryo-EM samples were prepared using a Vitrobot Mark IV (FEI). The blotting chamber was maintained as far as possible at 5-8°C, ≈ 89% relative humidity during processing with a Peltier cooling unit and one pieces of 4x4x11cm warm-water soaked sponge. 3µl of protein solution was applied to a Quantifoil® 1.2/1.3 400mesh EM grid (Quantifoil Micro Tools GmbH) freshly glow-discharged like the negative stain grids. Excess liquid was blotted away using Whatman™ 542 paper without extra waiting time at blot force -5 typically (Blot force was changed to between -10 and 5 if the ice layer on grid was too thin or too thick occasionally) and the grid was plunge-frozen into liquid ethane (Figure 18) immediately. Frozen grids were transferred into plastic grid boxes and stored in liquid nitrogen Dewar till use.

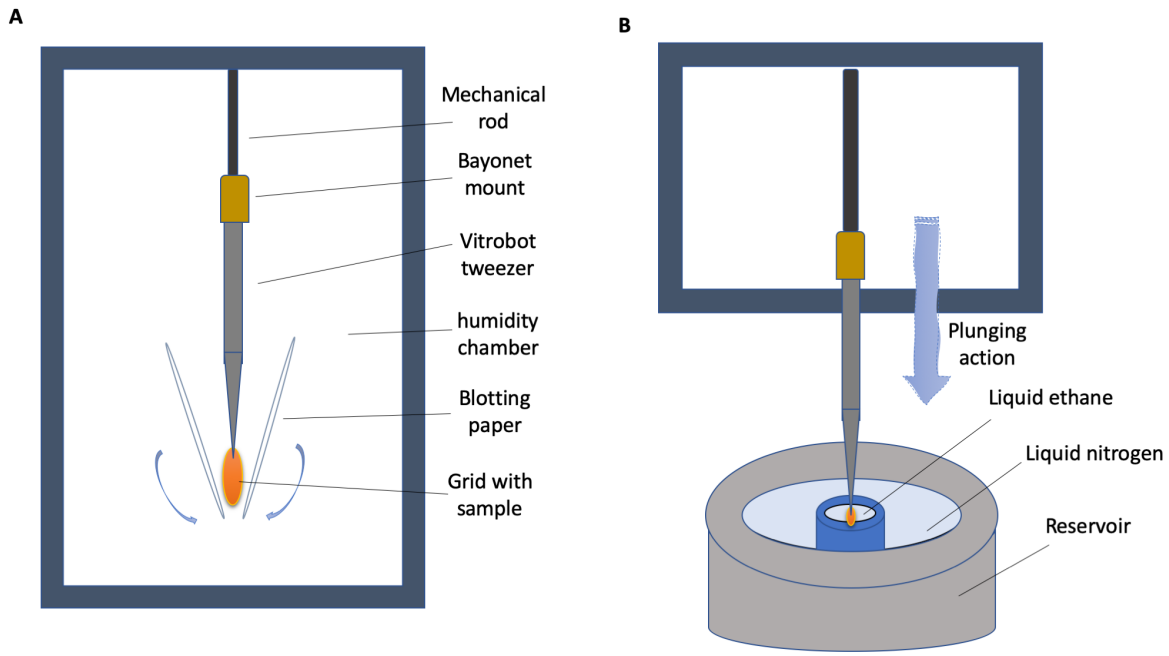

Figure 18 Illustration of sample vitrification using a Vitrobot device. A) Glow-discharged EM grid is held by a pair of fine forceps affixed onto the mechanical rod. The rod retracts into the humidity chamber and the sample is applied onto the hydrophilic side of the grid and then blotted using blotting papers to form the thin film in the grid holes. B) immediately after blotting the grid is plunged into the liquid ethane cooled by the liquid nitrogen in the reservoir and the sample is vitrified.

3.2.4 Electron cryo-microscopy

Vitrified protein samples were imaged using either the 120kV T12 electron microscope or the 300kV Titan Krios G3i electron microscope (FEI) at the settings below (Table 15). Sample checking on the 120kV electron microscope was essentially similar to negative stain samples except that a Gatan 626 cryo-holder cooled by an integrated liquid nitrogen Dewar was used. Samples checked with the 300kV microscope were first clipped into an Autogrid ring at liquid nitrogen temperature before transferring to the Autoloader via a grid cassette kept in a transfer Dewar. Movies were recorded at 75,000x magnification and pixel size of 1.0636Å by the Falcon 3EC direct detector (FEI). Similar procedures were used accordingly in the part for the study of the detector's performance within this project as stated in the paper (Song et. al., 2019)

Table 15 Low dose Cryo-EM data recording settings

Acceleration voltage	120kV	300kV
Cathode type	LaB_6	XFEG
Magnification	30,000 – 52,000	75,000
C_s	2.0mm	2.7mm
Objective aperture	100µm	100µm
Spot size	2 - 3	5
Recording mode	Low dose	Low dose
Software	SerialEM	EPU
Dose rate	11 e/A^2s	17.3 e/A^2s
Expose time	5 s	4 s
Defocus range	2µm – 3.4µm	1.2µm – 2.8µm

3.2.5 Data collection and processing

For the 120kV microscope, micrographs were collected using the SerialEM software in low dose mode and analysed with ImageJ (Schindelin et al., 2012) and Relion (Scheres, 2017). Data from the 300kV microscope were recorded using the EPU software (ThermoFischer) and movies were motion corrected using MotionCor2 (Zheng et al., 2017). The defocus and astigmatism were determined within Relion using ctffind4 (Rohou and Grigorieff, 2015). Particles were picked from the dose weighted sums of each exposure either manually in Relion or automatically using the general neuronal network implemented in CrYOLO (Wagner et al., 2019). Picked particles were extracted at a box size of 200 x 200 pixels (equivalent to ≈1.5 times of the longest expected diagonal length, where the estimated average particle diameter of the Ccr4-Not complex was ≈18- 20nm). All micrographs were then processed in Relion or CisTEM (Grant et al., 2018) software packages to generate the 2D class averages and the initial models of the complex particles.

4 Results

Part I

4.1 Performance of the Falcon 3EC direct electron detector in practical use.

Single particle reconstructions using the data collected by the Falcon 3EC detector benefited from the significant increase in detection sensitivity and low readout-noise, i.e. DQE, when used in the electron counting mode especially (Kuijper et al, 2015). However, the moderate frame rate of the Falcon 3EC detector limited itself to a fairly slow throughput compared to using the integrating mode (Song et al., 2019). With respect to the different molecular sizes of the proteins, this puts forward the option for a balance between harnessing the highest quality data by collecting smaller dataset in counting mode or to maximise the potential resolution from the increased amount of data in the integrating mode, based on a typical collection period of 1-2 days for a high-end microscope set-up such as the Titan Krios (ThermoFischer). A case study for the practical capability of the Falcon 3EC detector was thus done by comparing the single particle reconstructions between the data collected in the integrating and counting modes of data acquisition. Three test protein samples of different molecular sizes and structural symmetry were used to evaluate the data quality for the Cryo-EM structural analysis, viz. the Tobacco Mosaic Virus (TMV, ~40MDa), the Hepatitis B virus capsid like particles (F97L-CLP, ~4.8MDa) and the ß-galactosidase (~465kDa) (Imaging and processing parameters in Appendix 8.1, Table 1-3). The EM maps generated from the different data sets were compared with their resolutions based on the Fourier Shell Correlation (FSC) at 0.143. This shall in general help as a recommendation for the experimenters' planning with Cryo-EM data collection strategy on similar systems. Pertaining to the second part of this thesis, the Ccr4-Not complex, which was reported to have a nominal molecular weight of 1-2MDa in *S. cerevisiae* (Chen et al., 2001 2011) and ~600kDa in *S. pombe* (Stowell et al., 2016, Ukleja et al., 2016a), falls within the size range of these test objects. Hence, making use of the information in the case study could help to make sensible decisions when collecting data for this complex.

4.1.1 Tobacco mosaic virus (TMV)

The TMV particles are very large overall and are distributed homogeneously across the vitrified ice layer as shown in the selected summed movie frames (Figure 19A). The reconstruction from the Integrating mode dataset for TMV was at 2.5Å and increased by 0.2Å after additional beam-tilt correction and per-particle ctf-refinement in Relion 3 (Zivanov et al., 2018) (Figure 19B). Applying Ewald sphere correction did not show noticeable improvement in resolution. It also suggested that the reconstructed asymmetric subunit from the integrated dataset already suffices for the automated model building, accounting for 151 out of 158 residues within an asymmetric subunit. Even the lower contrast loop region could be successfully accounted for (Figure 19C and D). Counting mode was not tested because at this size the particles already have sufficiently good contrast and ease for image alignment to reach a high resolution.

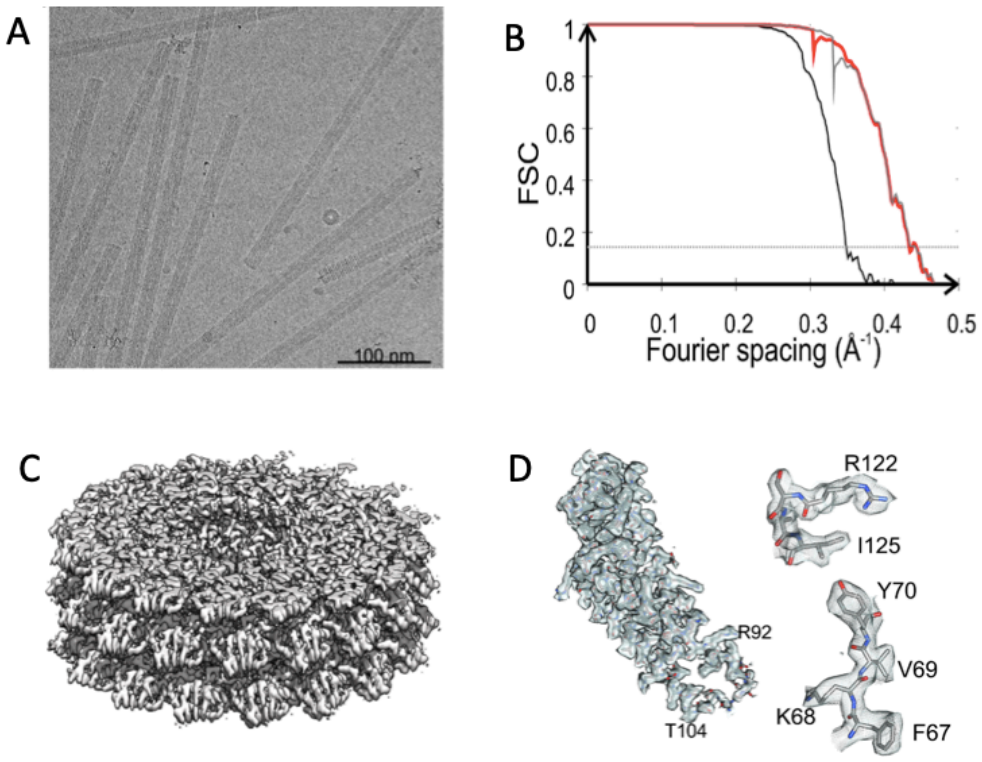

Figure 19 Cryo-EM micrograph of TMV and reconstruction from integrating mode data set. A) A motion corrected and dose-weighting averaged movie sum micrograph of TMV (Defocus: 1.2µm, total exposure: 84 e/Å^2).B) Fourier Schell correlation (FSC) plot of the masked maps after gold standard refinement; Before per-particle ctf-refinement (black line), after beam-tilt and per-particle refinement (red line) and additional Ewald sphere correction (grey line). Horizontal grey line indicates the FSC 0.143 cut-off for resolution determination (Rosenthal and Henderson, 2003). C) A segment of the non-overlapping section in the reconstruction in surface representation that was used for the automatic model building test. D) Right: EM map of the reconstruction before pre-particle ctf-refinement and beam-tilt correction from an asymmetric unit in the automatic model building, R92-T104 is a looped segment in the polypeptide chain. Left: Overlay of the automatically build model and the EM density at representative residue locations. Figure adapted from Song et al., 2019.

4.1.2 Hepatitis B virus capsid like particles (F97L-CLP)

Next, reconstructions from the smaller F97L-CLP (4.8MDa) were compared between both modes of acquisition for sample prepared on the same EM grid, in order to exclude variations from the sample preparation (Figure 20A and B). Here, the hexagonal ice surrounding the particles served as an internal resolution standard which indicates that both modes could yield motion corrected movie averages to at least 2.25 Å resolution based on the ice ring in the fast Fourier transform (FFT) of the image. However, single particle reconstructions from the integrated and counted data sets yield marginally different resolutions at 2.7 and 2.6 Å respectively (Figure 20C). Resolution of the EM map was then improved to 2.5 Å for both counted and integrated data with per particle ctf-refinement and beam-tilt correction in Relion3.0 (Zivanov et al., 2018). The final correction took into account the influence from the curvature of the Ewald sphere (Wolf et al., 2006) and gave a final resolution limit of 2.4 Å for both maps. This was further examined by using a Res Log plot overlooking at a wider range of resolutions and number of particles used for the reconstructions. The Res Log plot provided an empirical metric of the quality of the Cryo-EM reconstructions (Stagg et al., 2014) which in this case showed minimal differences, so it was consistent with the previous finding (Figure 20D and E). The results here suggested that for particles of this size, counted data has no measurable advantage from its better DQE over the integrated mode.

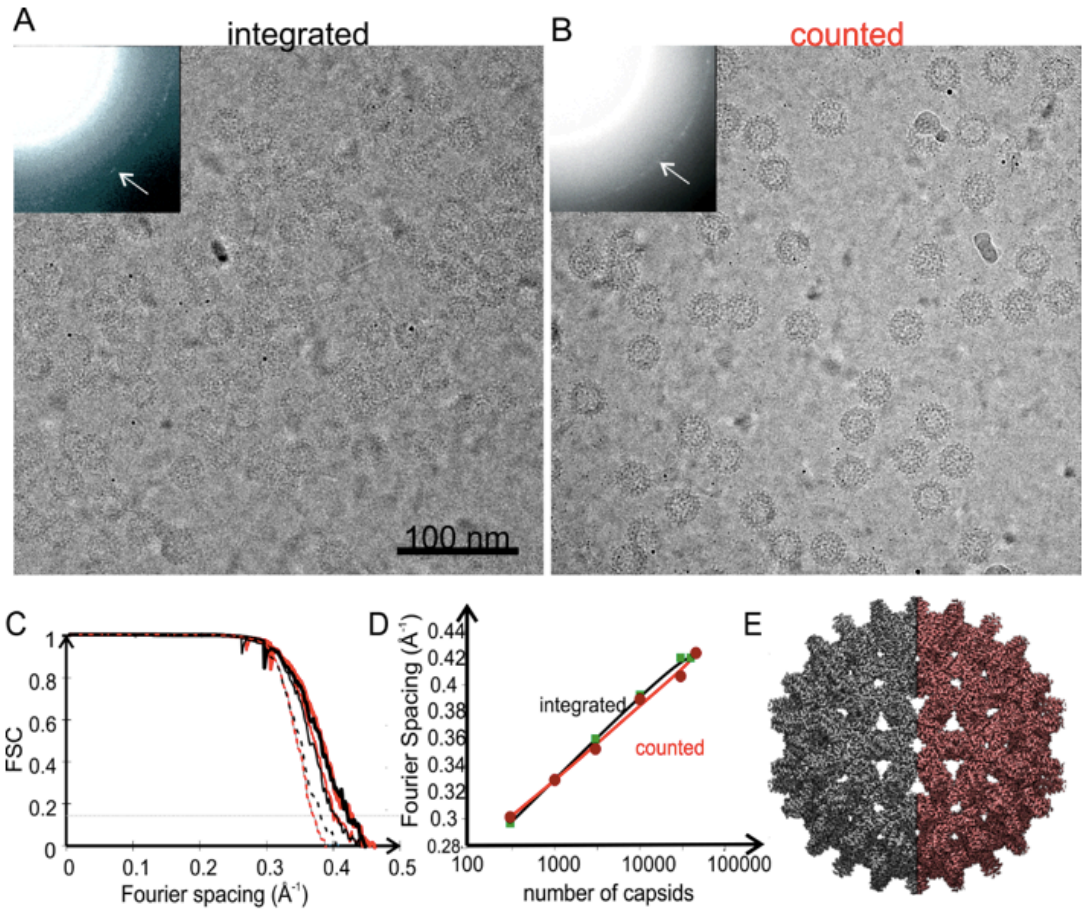

Figure 20 Single particle reconstruction of the Hepatitis B virus F97L CLP. A and B) Dose-weighted and motion-corrected movie sums of the particles from integrated and counted modes (Defocus: ~1.4µm). The use of gold grid unexpectedly resulted in the particles embedded in hexagonal ice, as seen by the ice ring (white arrow) on the FFT inset which indicates a spatial resolution of 2.25Å. C) Fourier schell correlation plots of the maps from both types of acquisition mode, black: integrated, red: counted. Thin dashed lines represent maps before per-particle ctf-refinement and beam tilt correction. Thin solid lines represent maps after these refinement and corrections. Thick solid lines represent maps with per-particle ctf-refinement, beam-tilt and Ewald sphere corrections. Grey line indicates the cut-off threshold at FSC 0.143 for map resolution.D) Res-log plots of the per particle ctf-refined and Ewald sphere corrected reconstructions of the CLP, based on randomly selected subsets of data. The spatial resolutions of each reconstruction are ploted against the number of particels in the respective maps. E) Surface representation of the EM map reconstructed from integrated data(grey) next to counted data(maroon). Figure adapted from Song et al., 2019.

4.1.3 β-galactosidase

The last test object was the much smaller β-galactosidase. Data sets were also collected from the same grid in both modes to avoid sample variations. Dose-weighted and motion corrected movie sums showed similar contrast of the protein particles in ice (Figure 21A and B) but the Thon rings in the counting mode remained conspicuous to even beyond the simulated 1/5 $Å^{-1}$ mark in spatial frequency as compared to in the other mode (Figure 21C and D) indicative of better image quality.

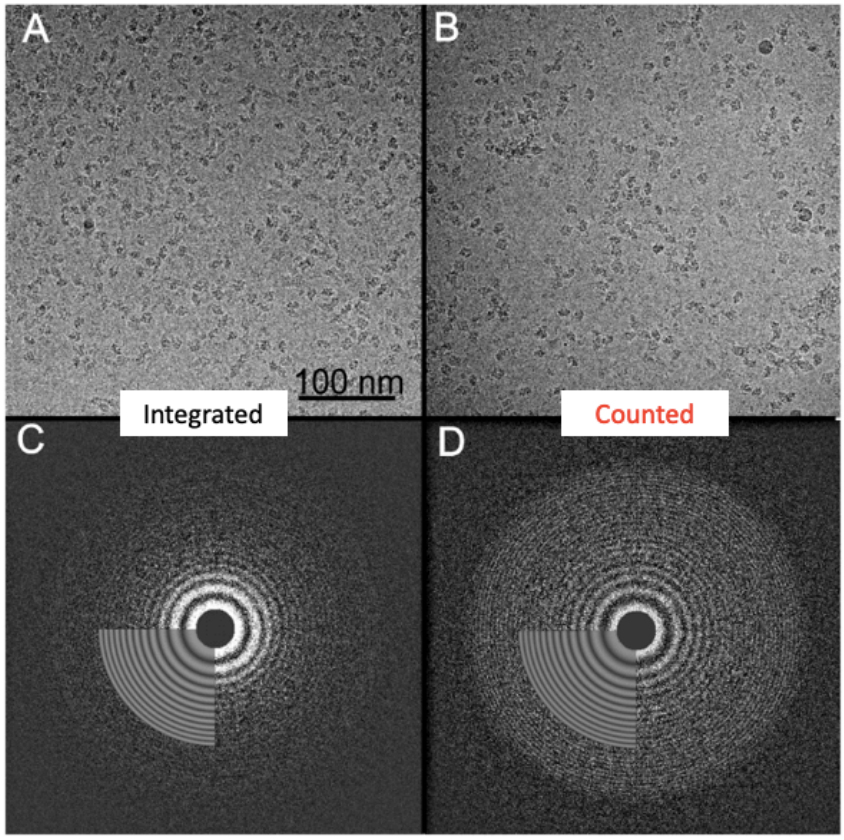

Figure 21 Motion corrected and exposure weighted movie sums and the accompanying Thon ring patterns of the beta-galactosidase. A and B shows the sample recorded at ≈1.55µm under-focus, with a total exposure of 75- 80 $e^-/Å^2$, in integrated and counted mode respectively. Movie in A consists of 25 frames/exposure and in B consists of 40 frames/exposure. C and D are background subtracted Thon ring patterns of the respective movie sums and include a simulated CTF between 5 and 30Å spatial frequencies superposed in the lower left quadrant of the Thon ring using ctffind4 (Rohou and Grigorieff, 2015). Diagram adapted from Song et al., 2019.

Subsequently, reconstructions using the two data sets of similar sizes were carried out in both the cisTEM (Grant et al., 2018) and Relion 2 (Kimanius et al., 2016) software packages. Resolutions for each reconstruction with a comparable number of particles are summarised and contrasted in Table 16. The advantage of counting mode in terms of the final map resolution is therefore quite distinct and this is amplified with the use of post-processing corrections.

Table 16 Resolutions (Å) for beta-galactosidase reconstructions from both modes using different software packages. N.B. Relion 3.0 has both per particle ctf-refinement and beam-tilt correction in post-processing. cisTEM has only per particle ctf-refinement. Relion 2.1 has none.

	Relion 2.1	**Relion 3.0**	**cisTEM**	**cisTEM (1/3 data set)**
Integrating	2.9	2.4	2.6	-
Counting	2.6	2.2	2.3	2.4

Since the rate of acquisition is about three times slower in the counting mode with our chosen parameters, it was further examined whether the higher quality data could supplement the slower acquisition rate in a reconstruction. A series of 470 movies taken en bloc from the counted data set (roughly equivalent to 1/3 of the data volume obtained by integrating mode in the same time span) was processed in cisTEM. This reconstruction showed a 2.4 Å resolution comparable to 2.6 Å from the integrated data (Table 16 and Figure 22). However, the corresponding integrated data set suffered a slight limitation from the uncorrected beam-tilt, which was remedied in Relion 3.0 (Zivanov et al., 2018) in silico and the final reconstruction also reached 2.4 Å. At this point, it is apparent that both the integrated and counted modes offer good image qualities but differed essentially at the data acquisition rate, especially when advanced per particle ctf-refinement and beam-tilt correction algorithms could be applied (Table 16 and Figure 22A and B). This observation is elaborated using the Res-log plot in which the spatial frequency of the final resolutions is plotted against the decadal logarithm of particle numbers within a random subset of the data. The trendlines for both the counted and integrated data rose in parallel at each spatial interval, and that the offset in between suggested that approximately 2.5times more particles from integrated data could be required for reaching the equivalent resolution given by the counted particles (Figure 22C). This would provide some flexibility in anticipating the EM session duration required according to the size of the protein of interest, the desired resolution and also the speed for data collection.

Nevertheless, for protein particles close to 0.5MDa or smaller, counting mode would eventually make a distinction from its higher image quality in high-resolution reconstructions beyond half of the Nyquist frequency. This is demonstrated in the DQE plot of the Falcon 3EC detector in our set-up for the Titan Krios microscope (Figure 22D). A pair of sample free images with and without a beam stop were taken at a known exposure per pixel in each mode of acquisition. The images were used in calculating the DQE by FindDQE (Ruskin et al., 2013). The exposure value was approximated using the Falcon reference manager after calibration by a service engineer for both integrating and counting mode images and does not represent the most accurate absolute values which can only be measured precisely using a Faraday's cup. Both DQE plots have a very small systematic error arising from this estimation as can be seen in the slight fluctuations near DQE (0) but the overall trend and proportion of the plot up to DQE (Nyquist) are still informative in illustrating the better performance of the detector in the counting mode. This is also consistent with similar observation made by the others (Faruqi and McMullan, 2018).

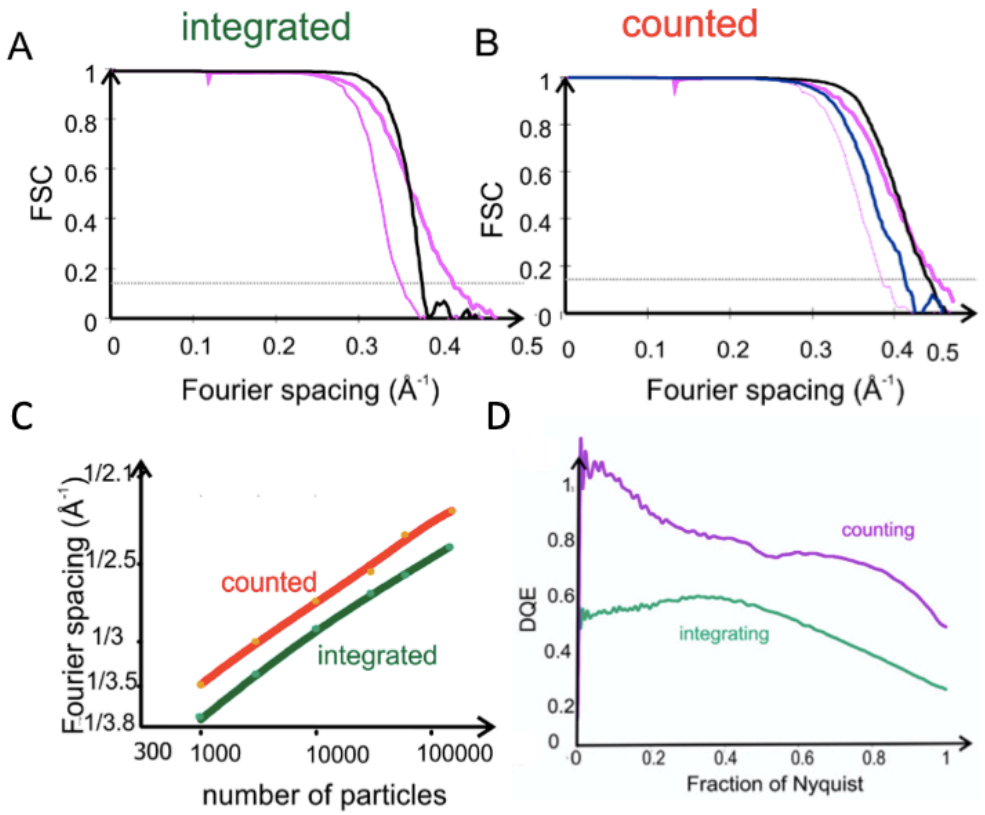

Figure 22 Comparison of the integrating and counting mode of acquisition. A) Fourier Schell correlation (FSC) plots from reconstructions using integrated data in; Relion 2.1 without per particle ctf-refinement and beam-tilt correction (thin purple), Relion 3.0 with per particle ctf-refinement and beam-tilt correction (Thick purple), cisTEM with per particle ctf-refinement. B) FSC plots of reconstructions using counted data, line convention follows as in integrated data plot in A. Blue thick line represents reconstruction with cisTEM out of a 1/3 subset of counted data. C) Res-log plots of the beta-galactosidase reconstructions for different randomly chosen subsets of data collected in each mode using Relion 3.0. D) DQE curves of the Falcon 3EC detector in both modes. Adapted from Song et al., 2019.

Part II

4.2 Purification of the Ccr4-Not complex from S. cerevisiae

To study the Ccr4-Not complex using electron microscopy methods, the yeast form of this complex is isolated from its endogenous source by affinity tag purification. Several commonly used affinity tags were considered, e.g. Tandem affinity tag (TAP), poly-histidine tag (6xHist) and FLAG tag. The affinity tag is inserted by homologous recombination at the C-terminal end of the coding sequence of a selected subunit of the complex, e.g. Not1, Not3, Not4 and Not5. The tagged subunit as well as its associated proteins, i.e. the remaining Ccr4-Not subunits, can then be isolated and enriched for EM sample preparation.

4.2.1 Affinity tag insertion by Homologous Recombination

The principle of C-terminal affinity tagging was based on such method published by Knop et. al. (1999). The plasmid containing the 3xFLAG epitope DNA sequence and an antibiotic selection marker, as well as the S288c yeast strain was a kind gift from AG Schlosser at the Rudolf-Virchow-Zentrum (RVZ). Two subunits of the *S. cerevisiae* core complex, namely, Not4 and Not5, were chosen because of their median molecular size among the other subunits and the homologous region sequence had no predicted secondary structures in their tagging primers. The exact homologous sequence has to be carefully chosen and empirically determined by PCR, since the overlapping region is very long, typically between 50 to 150bp. Correct primer design can help avoid unwanted repeats, secondary structures and non-specific annealing sites on the host genome, which can contribute to cloning artefacts and unsuccessful PCR reactions (Figure 23A). These two subunits were also reported to be stably attached to the Not1 scaffold protein in budding yeast (Bhaskar et al. 2013,2015). Not4-3xFLAG strain (N4F) and Not5-3xFLAG strain (N5F) were generated as described in the Methods and correctly transformed N4F and N5F cells were verified by colony PCRs (Figure 23).

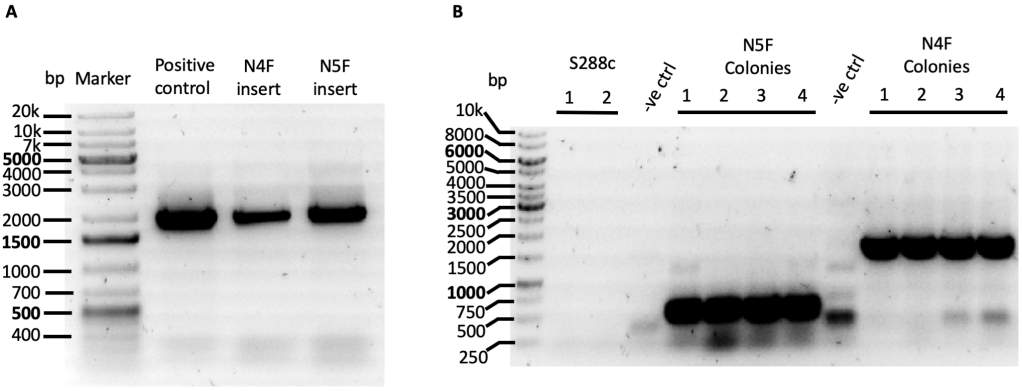

Figure 23 Agarose gel electrophoresis of PCR insertion fragments and colony PRC fragments. A) PCR products of amplified the insertion cassette, Not4-FLAG (1954 bp), Not5-FLAG (1964 bp), Control (1930 bp). DNA Marker: GeneRuler 1kb Plus. B) Colony PCR product of the selected colonies grown on the selective plates. N4F amplified 1500bp with p006 primers (Fwd&Rev), N5F amplified 556bp with p008(Fwd) & Kan-Hist-Nat(Rev) primers. Negative control was done without gDNA template using the respective primers. Colony PCR was repeated with the S288c gDNA from wild-type cells with no non-speific amplification.

Additionally, proper expression of the tagged protein and accessibility of the epitope to its antibody was checked by Western blots. Each colony was grown in 3mL reduced antibiotic potency YPD media under the standard condition and the total lysate was blotted using anti-FLAG antibody (Sigma) following a modified protocol from (Kushnirov, 2000). Not4-3xFLAG was identified at the expected molecular size of ~70kDa on the western blot (Figure 24A). Not5-3xFLAG showed one band at the expected size of around 70kDa but also had another band slightly above 37kDa which could be a degraded fragment (Figure 24B). Although Not5 tagging was carried out with the same method, the competent yeast cells seemed to resist the homologous recombination of this DNA fragment. A 5 to 10-fold higher concentration of DNA fragments had to be used to transform the cells before colonies started to appear on the antibiotic selective plates. The Not5-3xFLAG (N5F) cells also formed smaller colonies than the S288c and N4F cells on solid medium under the same growing condition.

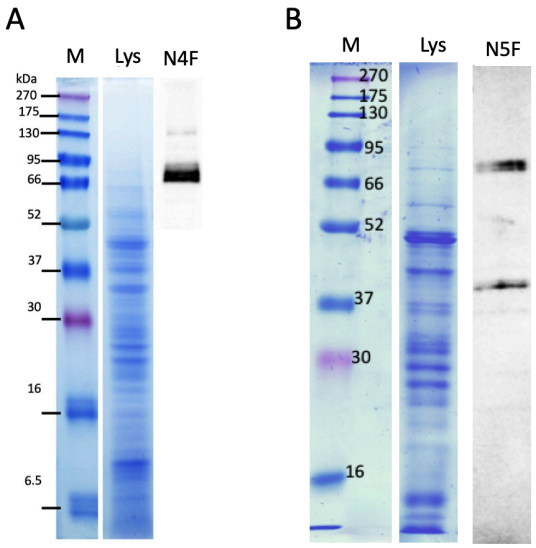

Figure 24 SDS-PAGE and western blots of FLAG tagged subunits. A) Tagging and expression checking for Not4-3xFLAG strain. M: protein marker, Lys: lysate, N4F: total protein in lysate blotted against FLAG epitope. B) Western blot for Not5-3xFLAG strain against FLAG epitope. Approximately 40-45µg of total protein was loaded per lane of sample. 12% Tris-Glycine gel was used and either Coomassie stained or transferred onto western blot membrane. For western blot: 1:5000 dilution Rabbit α-FLAG antibody in blocking buffer, 1:12,000 HRP conjugated goat α-Rabbit antibody in blocking buffer (TBST/5% w/v skimmed milk).

The insertion of a C-terminal 6xHis tag on the Not5 subunit was also attempted with the same strain. The Poly-histidine tag is commonly used for protein purifications, which has a high affinity and can be easily scaled-up to recover a large amount of the recombinant protein from the lysate. Colony PCR indicates that the insertion was successful, however, this strain did not express any stable full-length Hist-tagged target protein that was detectable on the western blot (Figure 25), while the pulled down proteins were most likely contaminants or degraded target protein.

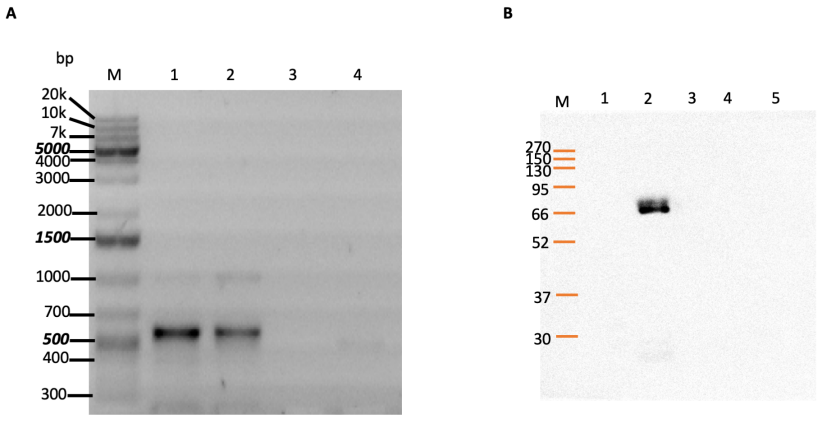

Figure 25 Colony PCR and Western blot for Not5-xHist transformation. A) Colony PCR from two unique colonies on selective plate (Lane1 and 2). Most colonies were too fluid and merged with neighbouring patches. Positive transformant would produce a PCR product of 514bp using p008 and p012 primers. Negative control from S288c cells (Lane 3 and 4). M: DNA marker. B) Western blot of aliquots for the Not5-6xHist mini-purification. M: Protein ladder. Lane1: purified Not4-3xFLAG as negative control. Lane2: 6xHist recombinant Gephyrin (~70kDa), as positive control. Lane3: SEC peak fraction. Lane4: Eluate from Ni-NTA column. Lane5: cleared lysate. 1:1000 mouse α-6xHist antibody, 1:10,000 HRP conjugated rat α-Mouse antibody.

4.2.2 Protein complex purification and strategies

After inserting the FLAG affinity tag to the Not4 and Not5 subunits, the protein stability and proper expression were examined through test purifications. The TAP tagged *S. cerevisiae* strains used (Not1-TAP, Not3-TAP and Not4-TAP) each carries a C-terminal TAP tag and were obtained from EUROSCARF. These were originally from the W303 yeast strain and are easily available, thus can save time on the cloning and tagging.

4.2.2.1 TAP tag purification

Test purifications using an adapted protocol from (Puig et al., 2001) on the TAP tagged Not4 and Not3 strains were carried out first. It was found that the procedure was lengthy and inefficient. Very little proteins were recovered after the protocol despite a large amount of starting material used. In addition, it was difficult to differentiate the core complex subunits from the contaminants and other co-eluting proteins on the SDS-PAGE gels after the purification. The apparent molecular size of the tagged protein was slightly smaller than expected too. This was based on the assumption that the TAP tag adds between 16 – 22kDa of molecular weight onto the nominal molecular weight of the tagged subunit (Gloeckner et al, 2007). In Not4-TAP trial, TEV cleavage was incomplete even after overnight incubation. In Not3-TAP purification, in particular, the tagged protein had already been suffering from significant degradation in the lysate, and only a trace of TAP tagged protein can be detected on the affinity beads incubated with the lysate (Figure 26). TAP purification was therefore rejected from being used as the main purification method.

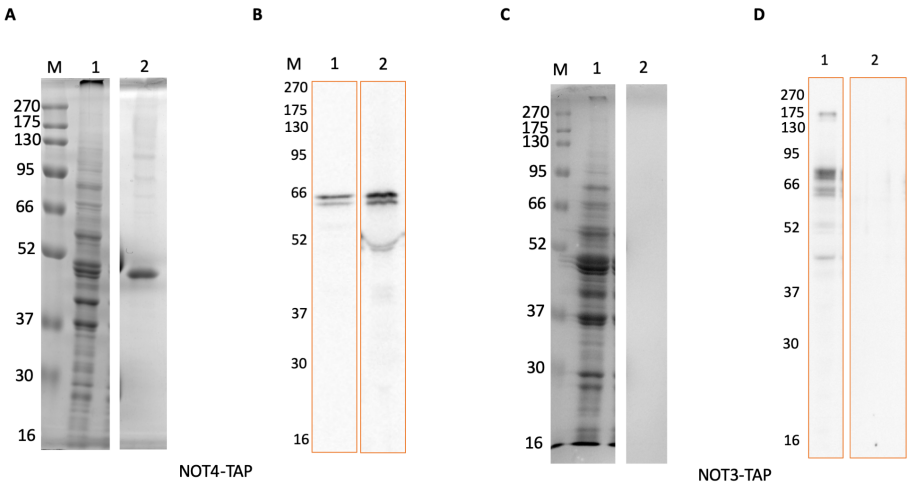

Figure 26 TAP purification using Not4-TAP and Not3-TAP. A) Coomassie gel for Not4-TAP (Expected size ~87 kDa) lane1: Cleared lysate, lane2: Co-purifying proteins boiled off the affinity beads post-TEV digestion. B) Western blot of the samples from A respectively. C) Coomassie gel for Not3-TAP (Expected size ~116 kDa), lane1: Cleared lysate, lane2: Co-purifying proteins boiled off the affinity beads post-TEV digestion. D) Western blot of sample from C respectively. Western blot parameters; 1: 1000 rabbit α-TAP antibody, 1:15,000 HRP conjugated goat α-rabbit antibody.

4.2.2.2 FLAG tag purification

Compared to the TAP method, FLAG tag purification can be milder and faster because no time-consuming and inefficient protease cleavage was necessary for the elution step. Moreover, the tandem FLAG (3xDYKDDDDK) epitope tag is nearly ten times smaller in molecular weight (an additional 4.6kDa) and more hydrophilic than the other tags. The N4F strain expressed the full length tagged protein stably during the initial trial (Figure 24). Subsequently, all of the expected nine core subunits were also identified in the co-immunoprecipitation as indicated by mass spectrometry (Figure 37). Thus, it was used for all subsequent purifications of the Ccr4-Not complex. Smaller 125ml cultures were used initially to test the tagged protein for compatibility with the previously established purification protocols (modified from Nasertorabi et. al. 2011 and existing Lab protocols) before a standard amount of 100g cell powder (≈10L of yeast culture) were used. Most subunits had a band at their expected positions on the silver stained SDS-PAGE gel and Not4-3xFLAG can be tracked by western blot at each step (Figure 27). However, the elution was yet complete as quite some signal can still be observed in the acidic glycine eluted fraction (at pH 2.8) which was used to regenerate the used beads (Figure 27 B, Lane 7). Degradation was also prominent as shown by the multiple bands of low molecular weight on the western blot. Some of the Not4 also precipitated during the incubation step with the affinity beads while this was not observed before the binding step (Figure 27 B, Lane 5 and 6 respectively).

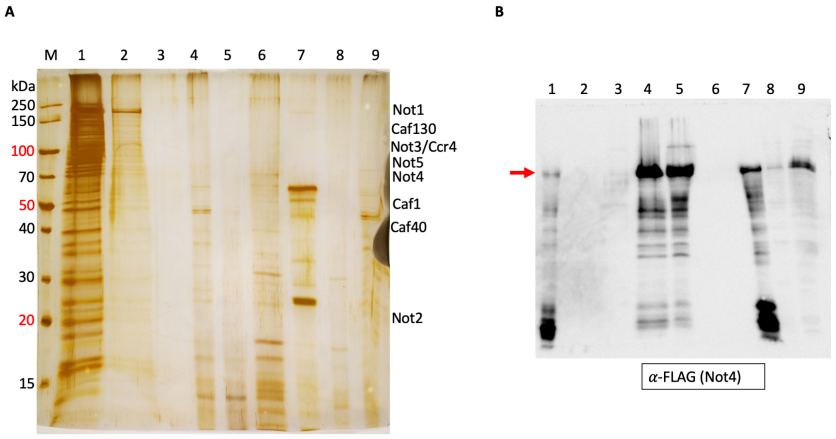

Figure 27 Example of a standard FLAG purification. A) Silver stain SDS-PAGE gel of aliquots taken from the selected steps of the purification. Lane1: Concentrated eluate, lane2: Eluted protein from affinity column without concentrating, lane3: Mock elution using HA peptide, lane4: Washing step flowthough, lane5: Flowthrough from the binding step. Lane6: precipitated protein during the binding step, lane7: Acidic wash flowthrough from eluted beads, lane8: precipitated protein before incubation with the affinity beads, lane9: cleared lysate. Expected position of subunits were indicated on the right. B) Western blot of the aliquot samples. Lane1: Eluate from the affinity column, lane2: Mock elution, lane3: Washing flowthrough, lane4: Flowthrough from binding, lane5: precipitated protein during binding, lane6: precipitated protein before incubation with beads, lane7: Acidic wash flowthrough from eluted beads, lane8: cleared lysate, lane9: FLAG positive control (~68.8kDa). 1:5000 dilution Rabbit α-FLAG antibody, 1:12,000 HRP conjugated goat α-Rabbit antibody.

One batch of the purification following this procedure could usually produce enough purified proteins for checking the composition by silver staining SDS-PAGE and western blot only. In order to increase the amount of proteins purified, 48L of YPD media (The maximum amount possible when using all 6 shakers simultaneously) was set up to provide ~600g of cell powder. Following the purification, ~300µL of eluted protein mixture at ~1.2mg/mL (~360µg of total protein) were obtained after concentrating the eluate with a 30k MWCO concentrator (Sartorius). This amount of purified protein was still insufficient for more thorough sample checking and characterisation, e.g. Running SDS-PAGEs, Thermal denaturation assays, Size exclusion chromatography-Multiangle light scattering (SEC-MALS) and preparing the EM grids etc. Yet, the characteristic protein bands for the expected subunits were already more conspicuous (Figure 28 A). The total purified proteins also contained some other protein species besides the expected nine subunits in various abundance and some could only be visualised on the more sensitive silver staining gel as extra bands. The purified protein complex was also passed through a size-exclusion chromatography column to remove any aggregates, subcomplex and contaminants before concentrating again for the EM sample preparation. The UV absorbance spectrum showed that the elution contained various UV absorbing compounds, and the prominent absorbance peaks did not correspond to the expected retention volume of a 1MDa core complex according to the calibration profile of the column used. It seemed that the expected complex had suffered from either protein degradation or disintegration since the peak fraction with the highest absorbance corresponds to less than 300kDa in molecular mass (Figure 28 B).

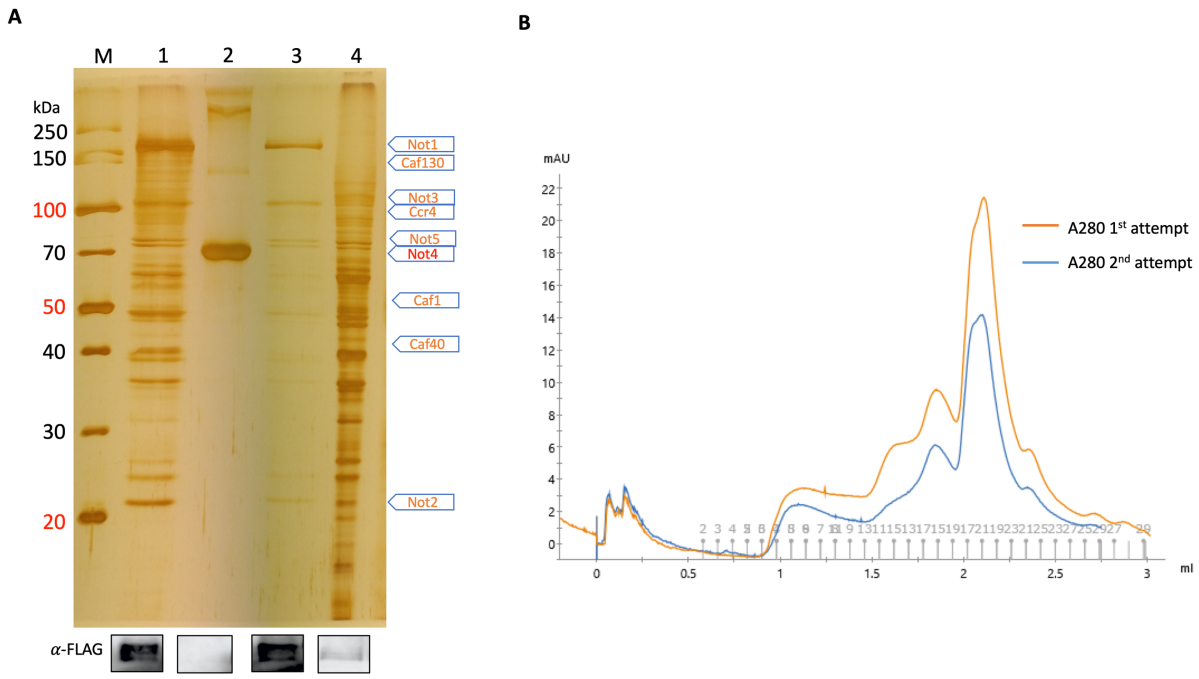

Figure 28 Large-scale FLAG purification. A) Silver stain SDS-PAGE gel of purification results. M: marker, Lane1: concentrated eluate, lane2: Flowthrough from spin concentrator, lane3: eluted protein before concentrating. Lane4: cleared lysate. Expected positions of the core complex subunits are labelled on the right. Bottom: western blot signal against the FLAG epitope for the respective lanes above. 1:5000 dilution Rabbit α-FLAG antibody, 1:12,000 dilution HRP conjugated goat α-Rabbit antibody. B) Size-exclusion chromatography UV absorbance spectrum (280nm) and elution profile. Purified proteins from two individual repeats were examined using a Superose 6 3.2/300 column. Calibrated void Vol.=0.79mL. Expected elution vol. for the intact complex is ~1 to 1.4mL. Total column Vol. = ~2.41mL.

Alternatively, a sucrose density gradient was used instead to separate the intact Ccr4-Not complex from the eluted protein mixture. This method would subject the protein complex to less physical damages than as it goes through the HPLC system. The eluted proteins separated into clusters and showed distinct bands indicative of the larger target complex that had migrated into the denser fractions of the gradient as seen on the silver stain gel below. Not4-3xFLAG was also located by western blot throughout the fractions (Figure 29). Fractions containing the FLAG signal were accompanied by a prominent band at ~240kDa which should be the co-purifying Not1 scaffold protein. Other subunits of the core complex were also present with a protein band at their expected positions. The Not4 band was not very obvious on the silver gel despite being the bait protein for the affinity step but had a strong western blot signal at those fractions with the most protein bands. Supposedly, the purified subunits might not be stochiometric here and some could be stained differently than the others either due to their amino acid compositions or length.

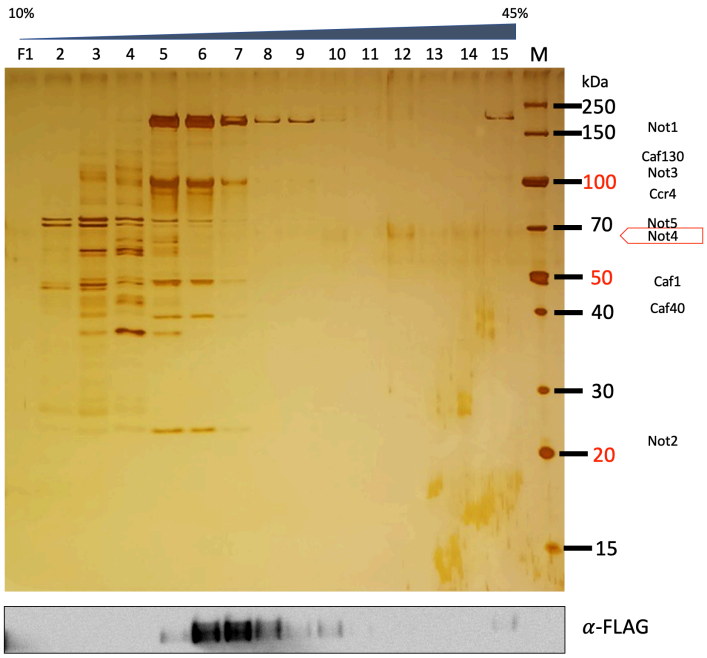

Figure 29 Sucrose density gradient separation of FLAG purified proteins. 10-45% w/v density gradient was loaded with ~300µL of concnetrated eluate at ≈0.5mg/mL. The gradient was centrifuged for 12 hours, 4°C, 35,000 rpm. Fractions of 300µL were taken from the top and 50µL aliquots from each fraction was used for SDS-PAGE and Western blot. Expected positions of subunits are indicated on the right. Fraction 5 to 10 and Fraction 15 showed presence of Not4-FLAG. 1:5000 dilution Rabbit α-FLAG antibody, 1:12,000 HRP conjugated goat α-Rabbit antibody.

Negative stain images of the total eluate loaded onto the gradient and from fraction 6 of the density gradient (Figure 30) revealed that some of the smaller fragments and aggregates were removed after the density gradient separation, and a more homogeneous population of the particles were present in this fraction where the strongest signal for FLAG epitope was detected by western blot. This representative batch of purification was the most homogenous sample from all attempts using the first FLAG protocol, but Cryo-EM grids prepared from this sample did not result in processable micrographs. This will be further elaborated below (§4.6.2)

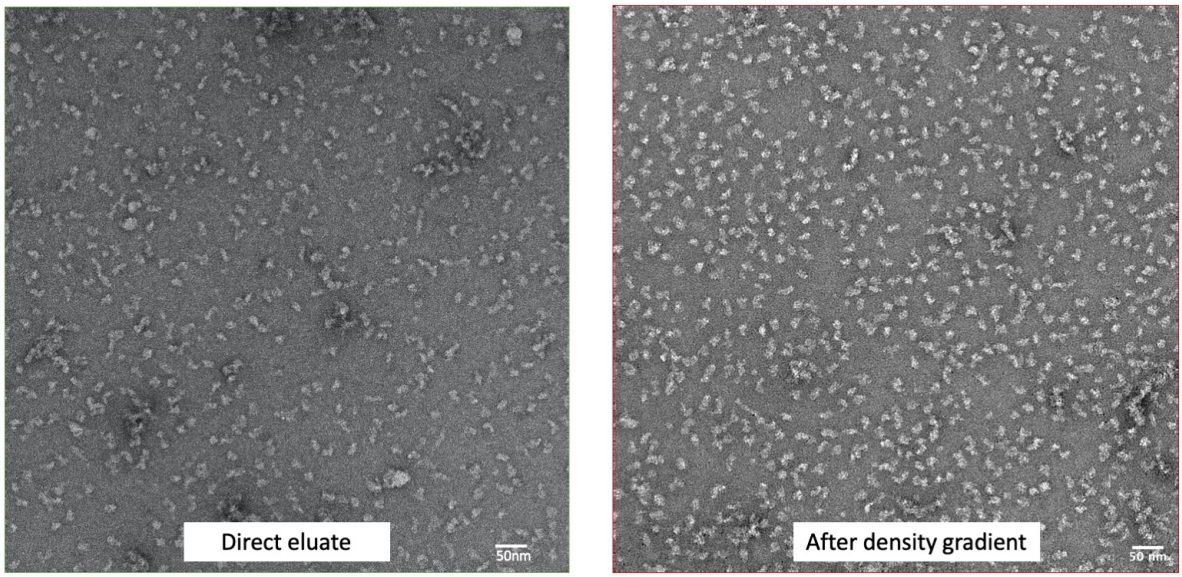

Figure 30 Negative stain micrographs showing the effect of sucrose density gradient during purification. Left:3µl of concentrated eluate (≈0.12mg/ml after 1:5 dilution) was examined with negative stain TEM. Protein particles of different sizes can be seen across the image and several aggregates were also present. Right: 3µl of sample (≈0.08mg/ml after 1:5 dilution) from Fraction 6 of the gradient was prepared and checked similarly. Distinct and nearly homogeneous particles were shown across the image. Less aggregate was visible. Both samples were imaged in low dose mode using SerialEM at 120kV and 52,000x magnification.

4.2.2.3 Modified FLAG purification

To further address the problem with low protein yield despite the increased starting material and the instability of the complex during purification, a new strategy was developed. The total protein in the cleared lysate, including the tagged Not4 and its interacting partners, were first enriched by concentrating the cleared lysate. This has two main considerations; firstly, it reduced the purification volume for easier handling such as by using less cell pellet, affinity beads and reagents. Secondly, this potentially increased the concentration of the bait protein thus enhanced its binding in the incubation step. Ammonium sulfate precipitation was chosen because it is a commonly used and well-established protein "salting-out" method. It is also recognised as a stabiliser for proteins during purification that maintains the ionic strength (Wingfield, 2001). In the initial trials, this additional step had shown on western blots to preserve most of the FLAG tagged Not4 after processing and the co-purifying proteins showed distinct strong bands at the expected locations on the gel (Figure 31). One assumption made here, however, was that most of the predicted co-purifying proteins would precipitate alongside Not4 and re-solubilise together afterwards.

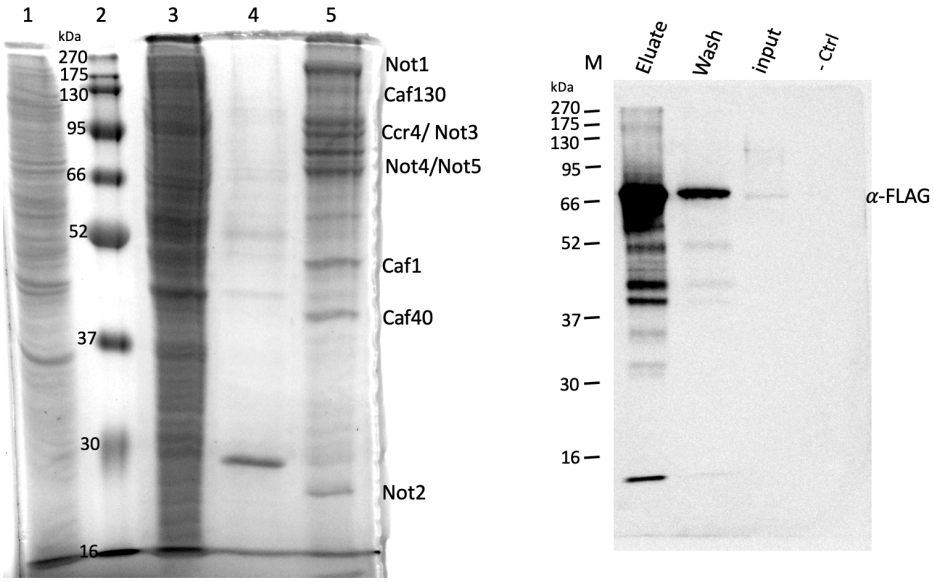

Figure 31 Initial Not4-FLAG purification with additional ammonium sulfate precipitation step. Left: Coomassie stained SDS-PAGE gel of purification aliquots. 1. Lysate, 2. Protein marker, 3. Re-solubilised pellet after dialysis, 4. Wash flowthrough, 5. Eluate. Expected sizes of subunits are annotated for the observed protein bands. Right: Western blot showing Not4-FLAG at each step of purification. ~2µg of total protein was loaded per well from each sample and a negative control using the lysate from untagged S288c cells. Not4-FLAG is highly enriched in the final sample hence resulted in saturation of the signal compared to input lysate and in wash flowthrough.

This concentrated protein solution was incubated with the FLAG affinity beads for the same period of time like before. In addition, small scale pre-trials verified that the presence of high salt concentration would not alter the properties of the target proteins or the anti-FLAG affinity beads in the solution. Cleared lysate buffered to pH between 5 and 9 with the lysis buffer, and salt concentrations between 50mM and 1M were tested. High ammonium sulfate concentration (>60% of saturation) tends to be slightly acidic, hence an adequately buffered lysate can avoid denaturing of the target proteins or losing their fragile complex integrity. It was found that, based on the gels from the cleared lysate and western blots of Not4-3xFLAG, the bait was stable at around pH 8 and in no more than 500mM of NaCl. Most of the FLAG-tagged Not4 remained in the precipitate at between 30% and 60% of ammonium sulfate saturation (Figure 32). Precipitated proteins were resolubilised thoroughly in 20-25ml of lysis buffer at pH 8 and the excess salt can be removed by dialysis.

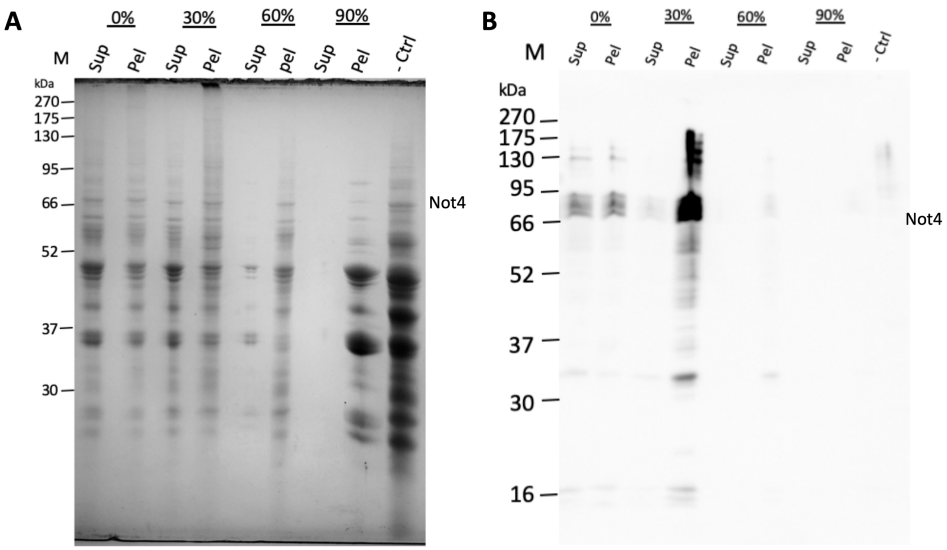

Figure 32 Tracking tagged protein in ammonium sulfate precipitation. A) Coomassie stained gel showing the total protein in the supernatant and the resolubilised pellet at different ammonium sulfate saturation steps. ~20-30µg of total protein was loaded per well. Negative control used 30µg of total protein from the untagged S288c cells. B) Western blot of the same sample as in A with double the amount of protein loaded per well. Membrane was detected with rabbit anti-FLAG antibody (1:1000 in blocking buffer) and goat anti-rabbit HRP secondary antibody (1:15,000 in blocking buffer).

Binding of the tagged protein and the elution were then processed like in the previous FLAG purifications. About 1 to 1.5mg of purified endogenous proteins can be obtained from a standard purification using ~100g of cell powder. This was about 2-5 times more than the amount from before. The eluted proteins showed clear bands for each expected subunits of the core complex on Coomassie stained gels without further concentrating(Figure 33). Less contaminants were present in the direct eluate than in the previous purification methods too. Western blot also showed that the purification was very efficient at recovering most of the bait protein, and Not4-3xFLAG was also less degraded.

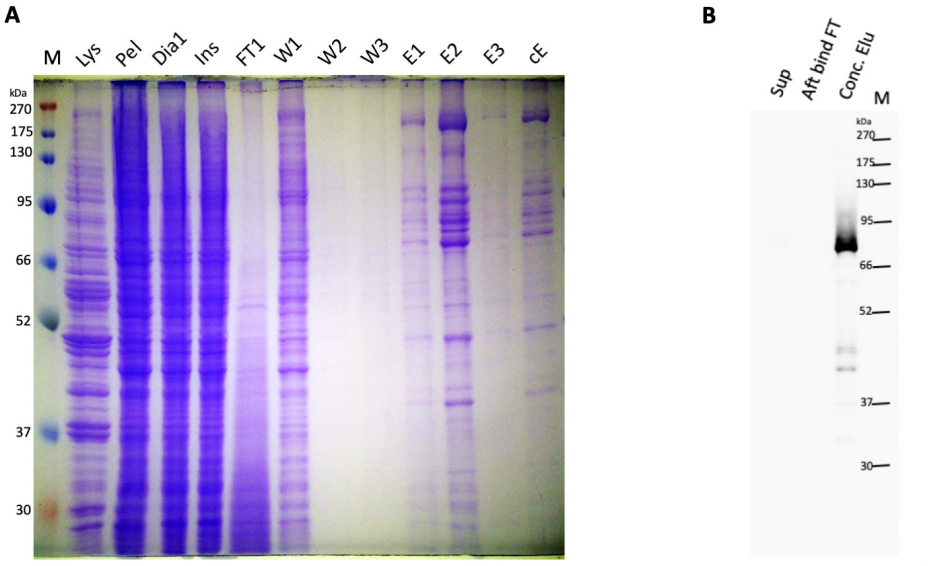

Figure 33 Modified FLAG purification for Ccr4-Not complex using 3xFLAG tagged Not4 subunit. A) Coomassie stained gel showing aliquots take during the purification. M: marker, Lys: Cleared lysate, Pel: resolubilised pellet after ammonium sulfate precipitation. Dia1: Protein solution after dialysis. Ins: Insoluble fraction from the re-solubilisation step. FT1: Unbound proteins after FLAG affinity binding step. W1-3: Washing step flowthrough (acetone precipitated), E1-3: Elution fractions. cE: Concentrated total eluate (~0.23mg/ml). B) Western blot of the selected aliquots. Sup: cleared lysate, Aft bind FT: unbound proteins in the flow-through after the binding step, Conc. Elu: Concentrated eluate. The western blot band for Not4 in the cleared supernatant was too faint to be visible together with the purified protein without oversaturating the blot. No signal was detected in the middle lane.

Size exclusion chromatography (SEC) using a Superose 6 10/300 GL column was recommendable for separating a concentrated protein solution (1-10mg/ml) in ~1-2% column volume (~250-500µl) of sample (GE Healthcare). The diluting effect of the gel filtration limited its effective resolution when filtering purified samples from the initial method because of the lower amount of eluted proteins. The modified method produced enough amount and concentration of the sample that allowed the use of gel filtration to further polish the purified proteins. Compared to density gradient, SEC significantly reduced the processing time to avoid unnecessary degradation and the elution peak can be traced and fractionated more precisely. Different from the previous SEC results, the sample here eluted in a single symmetrical peak

at around 11ml (equivalent to a ~900kDa globular protein complex) and showed nine prominent bands with the expected protein sizes on the Coomassie stained gel. Western blot also confirmed the presence of Not4-FLAG in the peak fractions (Figure 34A and B). The retention volume of the purified complex from three independent purifications were similar to each other too (Figure 34C). It would be reasonable to ascertain that this purified complex from the modified Not4-FLAG affinity purification had very high yield and purity in comparison to the previous methods and attempts (§4.2.2.2).

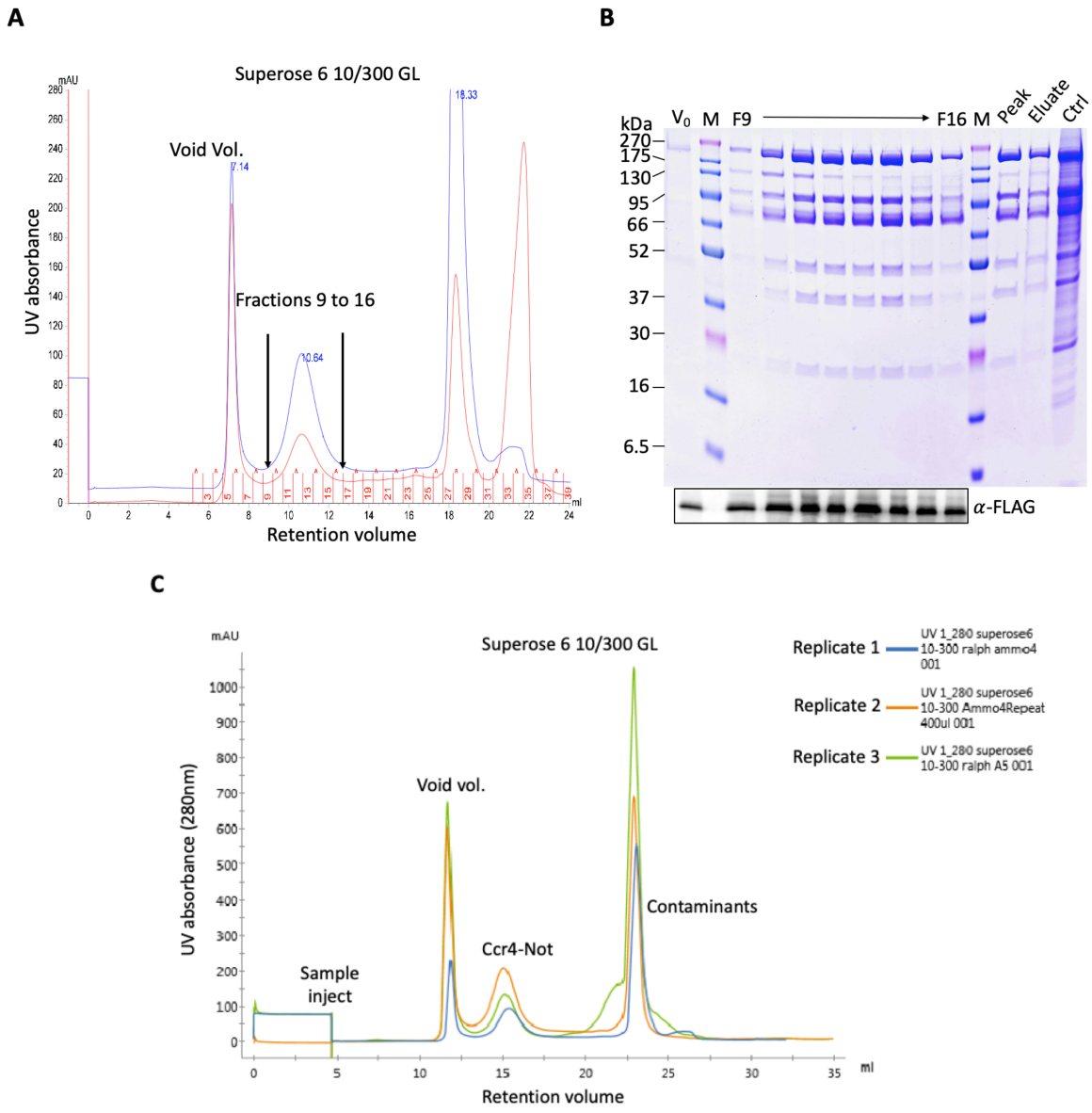

Figure 34 Size exclusion chromatography for polishing the purified Ccr4-Not complex. A) Gel filtration profile of the sample purified by the modified FLAG purification method. One single peak was present between the void volume peak and the peak for the small sized contaminants. Fraction 9 to 16 of the elution was analysed by SDS-PAGE. Blue trace: 280nm, Pink trace: 260nm. B) Coomassie stained gel of proteins present in the void volume peak, fraction 9 to 16, pooled peaks fractions and eluate before gel filtration. The control here was the concentrated eluate as in Figure 33. Western blot detected FLAG tagged Not4 in all fractions of the peak, including the void but in a smaller amount. C) Chromatography profiles from three independent repeats of the modified purification method. Absorbance lines for 280nm was overlaid for comparison. Positions of the elution peak for Ccr4-Not complex remained the same.

However, SDS-PAGE gel also showed one outlier in the peak fractions. A protein of ~130 kDa in size diminished across the main elution peak, suggesting that the leading fraction might contain a slightly larger complex that included more of this 130kDa protein (Figure 34B). This might suggest that it was only loosely associated with the core complex thus had a low occupancy (as elaborated below). Mass spectrometry identified the presence of Caf130 in the corresponding SDS-PAGE gel band cut out at this region between 130 and 175kDa. It is worth noting that Caf130 is unique to *S. cerevisiae* and also has no confirmed functional homologues in the higher eukaryotic organisms (Mauxion et al., 2013) (Review by (Collart, 2016, Xu et al., 2014))

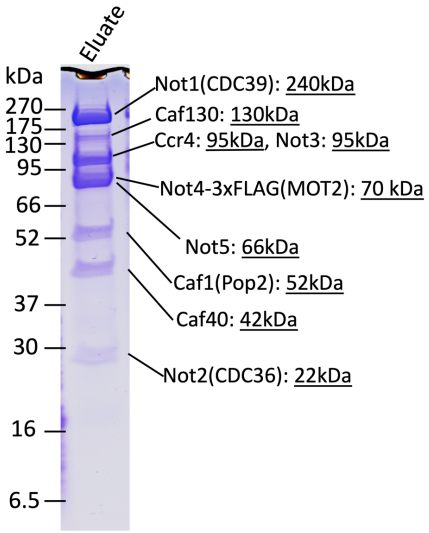

Figure 35 Identification of proteins purified by the modified FLAG method. Eluate from the modified FLAG purification method was separated on SDS-PAGE and the whole lane was analysed by Mass spectrometry. Each prominent protein band was cut out and analysed after in-gel tryptic digestion. The peptide with the highest peptide intensity detected was assigned as the main protein present in that band. Subunits of the Ccr4-Not core complex were all identified and marked accordingly with the theoretical molecular masses underlined.

The other protein bands from the modified FLAG purification were also analysed by mass spectrometry to identify the proteins on the SDS-PAGE gel (Figure 35). Protein intensities (summed intensities of the corresponding peptides) were compared in each cut-out segments of the gel lane and the highest protein intensity would be representative of the visible Coomassie stained protein band. All nine subunits were identified in the purified complex in a significant abundance. Similar protein bands were observed for the purified proteins of all subsequent purifications. The above data ensured that Not4-3xFLAG was suitable for purifying the Ccr4-Not complex via immunoaffinity pull-down, and that the modified FLAG method maintained the core complex integrity better throughout the purification.

4.2.2.4 *Stabilising the complex in bulk solution*

The Grafix method (Kastener et al, 2008) was mainly adopted at this stage to simultaneously stabilise and separate the larger complexes further from the contaminants and sub-complexes. The sample migrates under a centrifugal force through a sucrose density gradient containing a low concentration of glutaraldehyde that crosslinks at all solvent accessible lysine's primary amine side chains. When first applied to the eluted Ccr4-Not complex as a purification step, the sample from the complex containing fraction contained more distinct and compact particles than the sample treated similarly but without the cross-linker. The more heterogenous sample without glutaraldehyde implied that the complexes could be constantly undergoing dissociation and making contacts with the neighbouring particles at the disordered regions in solution after the centrifugation step (Figure 36). Due to the inherent heterogeneity and weak integrity of the native assembly, samples from the individual purifications varied in terms of the subunit composition and particle shape before the more stable modified FLAG purification protocol was employed. Afterwards, Grafix was only used to enhance the stability of the particle for Cryo-EM sample preparation and no longer for the purification step.

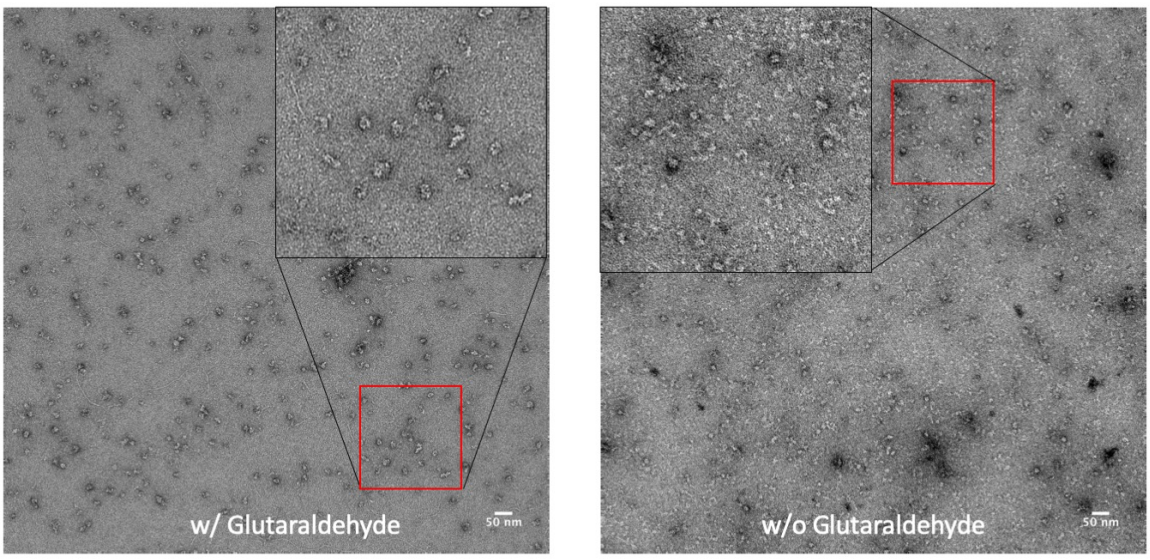

Figure 36 Effect of Grafix technique on purified Ccr4-Not complex. Left: Less aggregates were visible in the sample and more intact particles can be seen. Boxed section shows an enlarged region containing the fixed complex particles. Right: sample from the corresponding fraction of a density gradient processed in parallel without Glutaraldehyde. Protein particles shows less contrast and fuzzier outline and more small fragments.

4.3 Label-free quantitative Mass Spectrometry (MS)

Immunoprecipitation from Not4 and Not5 FLAG tagged strain were analysed by mass spectrometry to identify the co-purifying proteins that associate with Ccr4-Not. A control for each sample was also included in parallel with the affinity beads incubated in equivalent amount of cleared lysate from the untagged S288c cells. The label-free quantitative method distinguishes the co-purifying proteins from the non-specifically bound protein background by determining the protein ratios for all identified proteins based on their iBAQ (intensity-based absolute quantification) values. This value is calculated from the summed peptide intensities of a protein then normalised on the number of observable tryptic peptides. Thus the iBAQ is suitable for comparing protein intensities from proteins of different molecular sizes and used to infer the protein subunits' stoichiometry (Schwanhäusser et al., 2011). The non-specifically bound proteins are expected to have a ratio of 1 whereas specific interaction partners would have significantly higher ratio (Indicated by a right-shift on the x-axis of the dot plot).

Both tagged Not4 and Not5 subunits pulled down all components of the core complex but with a slightly different stoichiometry among the components. With Not4-FLAG, all subunits of Ccr4-Not were similarly abundant in the pull-down, except for Caf130. Not3 is located further right on the x-axis which suggested that it's more abundant in the sample than in the control. In the Not5 pulldown, core complex subunits grouped more distinctly away from the background compared to the Not4 pull-down, but Not3 was very scarce in this case. While Not5 was the most abundant protein in the sample based on the iBAQ value, this could suggest that Not3, relative to the rest of the complex, had less stable association when Not5 was used as the bait (Figure 38).

Caf130 was not abundant in either pull-downs as compared to the rest of the core subunits. SDS-PAGE of the gel filtration peaks showed that a 130kDa protein was eluting together with probably a larger complex at the beginning of the main peak, which in the pooled sample was confirmed to be the Caf130 subunit (Figure 35). Thus, Mass spectrometry data indicated again that Caf130 might not be associated with the main complex very stably. Meanwhile, an uncharacterised protein, YJR011C, was found to associate closely with Caf130 in both pull-down experiments. This 30kDa protein has unknown function but was linked to DNA damage response (Lee et. al, 2007) and has been reported to interact with Ccr4 and Caf130 in genome-wide proteomic studies (Krogan et al., 2006, Miller et al., 2018, Yu et al., 2008). This uncharacterised protein might also be involved in the metabolite stress response pathways linked to Ccr4 but is likely only conserved amongst the yeasts as no homologues are

known in the higher eukaryotes (Uniprot Database and SGD). No distinct protein band for this protein was visible on the SDS-PAGE gel other than its detection by MS (Below). Interestingly, BTT1 from the Nascent Associated Complex (NAC) was also identified in the pull-down. This complex has been reported to interact with the Ccr4-Not complex *in vivo* (Panasenko et al., 2006). No other protein complex or major interacting proteins from the known interactions were found in the immunoprecipitations despite the numerous downstream interaction partners (Introduction 1.2). In addition, it is good to bear in mind that the Co-IP LC-MS/MS results were based on samples from a standard yeast growth condition and the complex dynamic in the cell could vary under specific cell conditions/ cell cycle stages, as this complex is directly involved in regulating translation and cell cycles. This could have limited interpretations of the potentially wider implications of these interactions observed here, although the final sample submitted for MS analysis showed no visible differences on the SDS-PAGE protein bands for the purified proteins among individual replicates of the Co-IP.

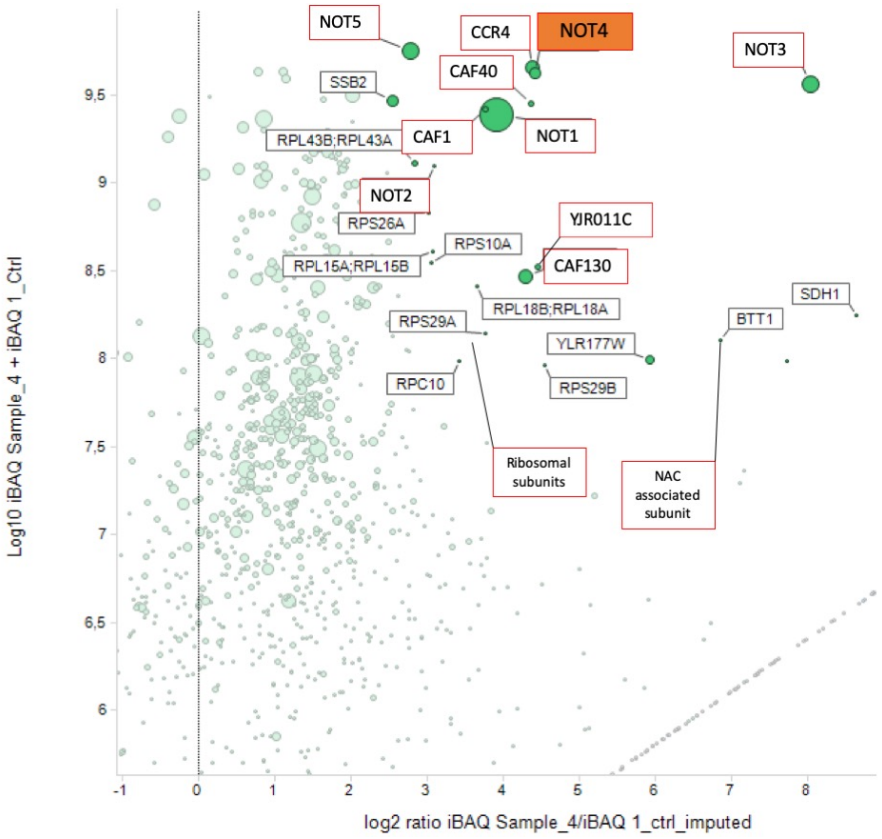

Figure 37 Mass spectrometry analysis of Not4-FLAG co-immunoprecipitation. Label free mass spectrometry quantifies the co-immunoprecipitated proteins together with the FLAG tagged bait protein, Not4. A control sample was analysed in parallel and used to subtract the background proteins. The y-axis represents the abundance of each protein co-immunoprecipitated. The x-axis represents the ratio of protein abundance between the sample and the control. Dot size is based on the number of detected peptides. Proteins pulled down non-specifically populate near the x-origin. Positions of the 9 core complex subunits and some co-immunoprecipitated proteins were marked in red box and bait protein in red block.

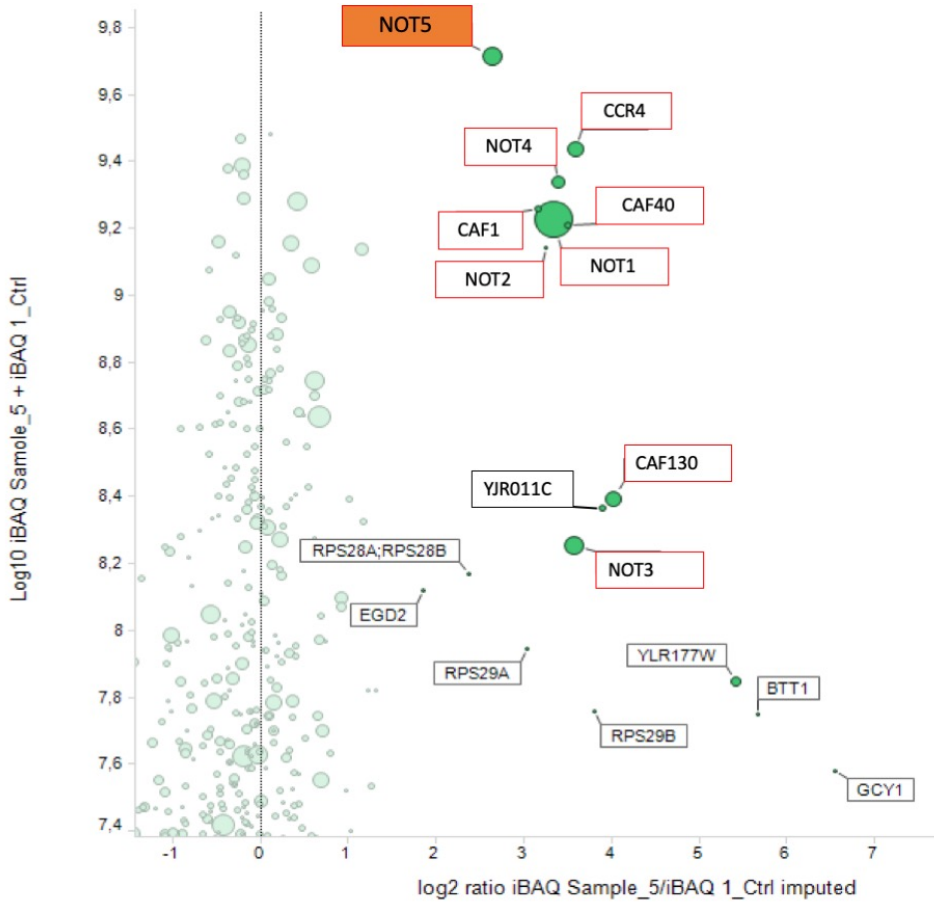

Figure 38 Mass spectrometry analysis of Not5-FLAG immunoprecipitation. Similar proteins were co-immunoprecipitated as in Not4-FLAG. The bait protein, Not5, had the highest abundance and Not3 was the least, together with Caf130.

4.4 Deadenylase activity assay

Here, the purified complex showed robust activity in trimming the poly-adenosine tail of a model mRNA substrate. The highly conserved Ccr4-Not complex is a major player in the deadenylation of cytoplasmic mRNAs prior to the onset of its decay via the generic mRNA decay pathways (Introduction 1.2.2.1). When the 5'-FAM labelled substrate mRNA (A25, 45bp) was incubated in the presence of the purified complex at 30 °C, rapid shortening of the substrate (3' → 5') can be observed. Based on the previous experiments from recombinant yeast Ccr4-Not complex, this assay was expected to show that the 25-mer Poly(A) tail would be consumed until the first non-A base like previously reported (Stowell et al., 2016) and results in a single product band at A0 (20bp). However, two products were quickly formed one at zero-length of Adenosine (A0) and another at roughly 4-5 bases after the first non-A nucleotide (A-4) towards the 5' end (Figure 39). No other product or intermediate was observed.

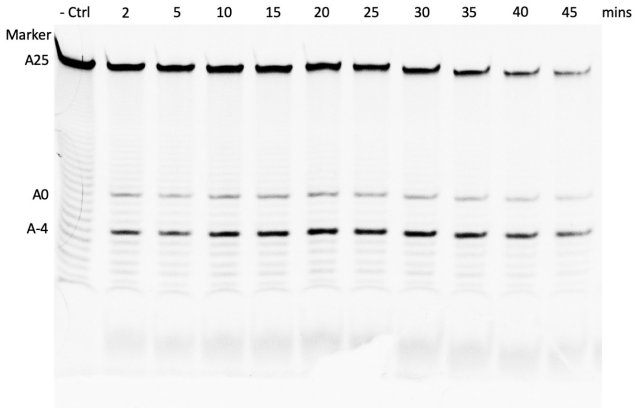

Figure 39 Time-course deadenylation reaction of the modified FLAG affinity purified Ccr4-Not complex. 200nM each of the labelled RNA substrate (6FAM-5'-cacauccaacuucucuaaau$(A)_{25}$ -3') and purified complex were incubated at 30° and aliquots were taken and analysed on denaturing polyacrylamide gels. Negative control was included without protein complex added and incubated alongside. Some spontaneous hydrolysis of the mRNA substrate can be seen as the RNA ladder pattern on the gel with single nucleotide resolution. Products of deadenylation (A0 and A-4) were already formed after 2min of incubation. Full length substrate level diminished during the time-course, but the product concentration peaked after around 20min and appeared to decrease slightly with further incubation. No products were observed in the control lane.

Fast appearance of the A0 product on the gel suggested that either the putative PRE (Pumilio Response Element) sequence (5'- UCUAAAUAA-3') located upstream of the Poly(A) tail might have interacted with a Pumilio domain in the complex (Webster et al., 2018), or the substrate could have interacted with the complex at another location that had similar effects on deadenylation. Substrate without stabilisation had been shown to lead to non-processive deadenylase activity (Ukleja et al., 2016a, Webster et al., 2018, Raisch et al., 2018). The second product (A-4) was 4-5 bases shorter than A0, which suggested that the pseudo-canonical UCU

sequence could have been the last RNA motif attached to the complex before the remainder can be completely degraded after detaching from a putative protein/RNA binding interface on the complex. The deadenylation reaction in this case, was also likely to be processive since the products appeared before the full substrate diminished.

Next, the reaction was setup with a lower molar concentration of the substrate and protein complex because by following the adopted protocol (Webster et al., 2019), at 200nM of each components, the reaction was too fast to be resolved by the time-course. Half of the amount used in the previous setup was then tested (100nM RNA: 100nM Complex) which showed a clearer change in the RNA band intensities. The products appeared after less than one minute of incubation and the full-length substrate depleted after 16min, together with the product A0. Then, product A-4 also depleted in the following time point. The RNA substrate at A0 was further digested by 4-5 nucleotides into A-4 and eventually degraded completely. RNA molecules that were degraded had also started accumulating at the beginning of the reaction at the bottom of the gel (Figure 40). Apparently, the purified complex here had a distinctive level of activity compared to the reconstituted recombinant Ccr4-Not complexes in the previous studies as these assays were conducted under similar conditions. Three independent repeats were carried out and obtained similar results.

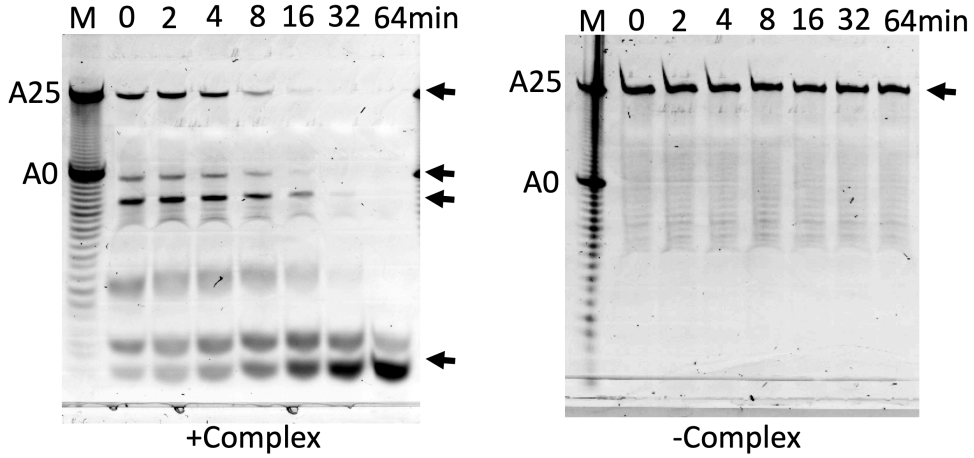

Figure 40 Deadenylation reaction with reduced substrate and complex concentration. M: RNA substrate with Poly(A) tail (A25) and without Poly(A) tail (A0) were used as size markers. Black arrows mark the position of the RNA molecules on the gel. The bottom arrow indicates the completely degraded RNA, including the fluorescein molecules. Full length substrate and reaction products decreased while the degraded RNA level increased. No change in the substrate level for the control without the complex.

Interestingly, both the Grafix treated and native complexes were able to degrade the substrate rapidly without much differences (Figure 41). These results had suggested that the purified core complex could degrade a mRNA substrate efficiently, even without additional non-enzymatic factors such as Mmi1 or Puf3 for S. Pombe Ccr4-Not complex (Webster et. al, 2019). Additionally, the deadenylase activity was also suggested to be independent of its conformational flexibility.

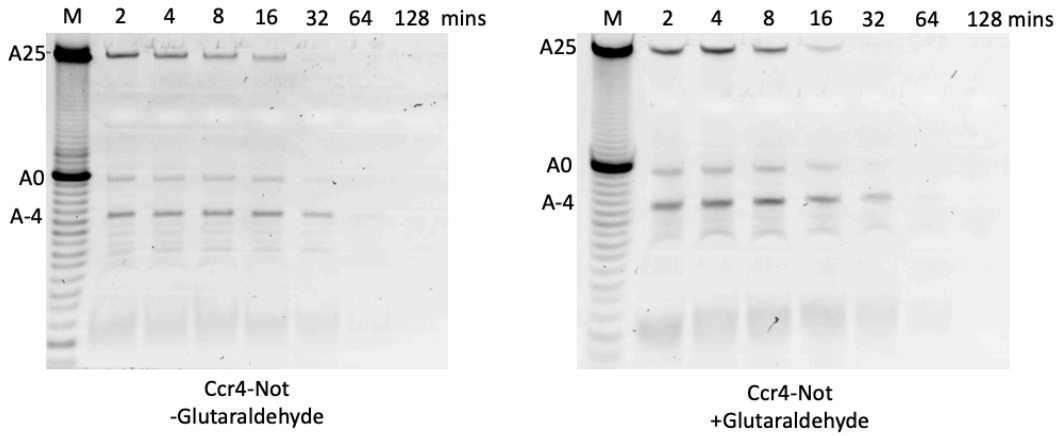

Figure 41 Deadenylation assay comparing native and fixed Ccr4-Not complex. Left: 100nM of protein complex and RNA substrate each were mixed with reaction buffer and incubated at 30°C. Right: Assay with the same set up using Grafixed complex. M: RNA substrate size marker. A25: Full length RNA substrate. A0: substrate without Poly(A) tail. A-4: RNA product about 4-5 nucleotides shorter than A0.

4.5 Ubiquitination activity assay

The purified complex was also active for the ubiquitination reaction when complemented with the E1 and E2 proteins plus ATP. Not4 is a RING E3 ubiquitin ligase and a part of the core Ccr4-Not complex in yeasts. In this study, a recombinant human E1, Uba1, was used because it's highly similar to the yeast homologue. The yeast E2 (Ubc4) was cloned from S288c genomic DNA and recombinantly purified via a N-terminal poly-histidine tag from bacteria. It is known to interact with the Not4 (Baskar et. al., 2015). High molecular weight components were observed on the Coomassie stained gel above 250kDa after incubating the reaction at 30°C (Figure 42 left). This smeared region contains ubiquitinated proteins that had an original molecular weight above 70kDa as shown in Figure 42,right (anti-ubiquitin blot). The smear was initially thought to be ubiquitinated Not4-FLAG because autoubiquitination of Not4 was also observed in another study (Mulder et al., 2007b). However, when blotting against the FLAG epitope, the blot did not show significant change in the location of the FLAG

tagged Not4 (Figure 42 middle) and was less informative due to the non-specific signals in the negative control. The 25kDa signal on the anti-ubiquitin blot should be the poly-ubiquitin chain instead of ubiquitinated Not2 because there was no clear change in its protein band as seen from the Coomassie stained gel. The diminishing band at 70kDa on the Coomassie stained gel happened to be shared by the Not4 and Not5, based on the migration position of these subunits on the SDS-PAGE confirmed by Mass spectrometry (Figure 42). Therefore, it is plausible that either Not5 or another protein in this set-up had been ubiquitinated unexpectedly. Since the pattern and location of protein ubiquitination would lead to different cellular functions, it would be interesting to carry out additional analysis to identify them from these reactions.

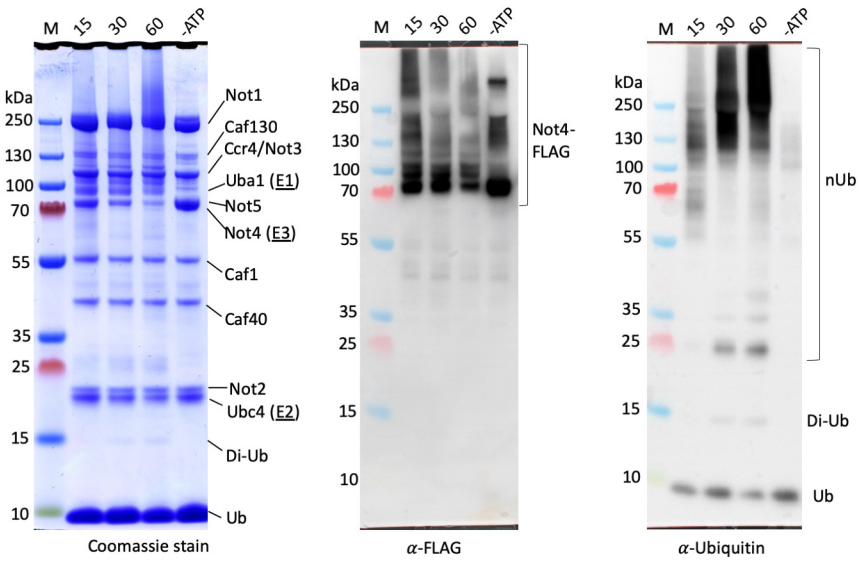

Figure 42 Ubiquitination activity assay of the purified Ccr4-Not complex. Left: SDS-PAGE showing the proteins present in the reaction and aliquots taken at 15, 30, 60min of the incubation. The negative control was done similarly without ATP added. Middle: Western blot of the same sample using rabbit anti-FLAG antibodies (1:1000 in blocking buffer) and Goat anti-rabbit HRP secondary antibodies (1:10,000 in blocking buffer). Right: Western blot using mouse anti-Ubiquitin(P4D1) antibodies (1:1000 in blocking buffer) and goat anti-mouse HRP secondary antibodies (1:10,000 in blocking buffer). Positions of the mono-ubiquitin, di-ubiquitin and poly-ubiquitin were shown. Signal at the top of the blot suggests ubiquitination of a large protein during the reaction.

4.6 Structural evaluation of the purified Ccr4-Not complex

4.6.1 Negative staining electron microscopy

The purified protein complex was intended for structure determination using single-particle reconstruction (SPR) electron cryo-microscopy. To judge its suitability for further structure determination, the purified sample's homogeneity and morphology was first examined using the negative staining method. For the initial attempts, protein samples contained large amount of aggregates and heterogenous complex particles after only one freeze-thaw cycle (The purification and sample preparation cannot be completed on the same day). Co-purifying contaminants were also visible together with the putative complex particles based on the morphology of previously published structures (Nasertorabi et al 2011, Ukleja et al. 2016).

After applying the Grafix method, distinct protein particles and less aggregates were observed. Using the more homogenous sample from one of the purifications, a small data set of 200 micrographs was collected with a 120kV T12 microscope (FEI) and 2D class averages were generated from ~18,000 picked particles using Relion. Several prominent classes showed projections of the distinctive L-shaped particle, as well as projections in a few different orientations (Figure 43). The diagonal length of this representative particle was around 18nm. Attempts were made to generate an initial 3D model from there but did not result in any convincing reconstructions or with the expected morphology of a *S. cerevisiae* complex.

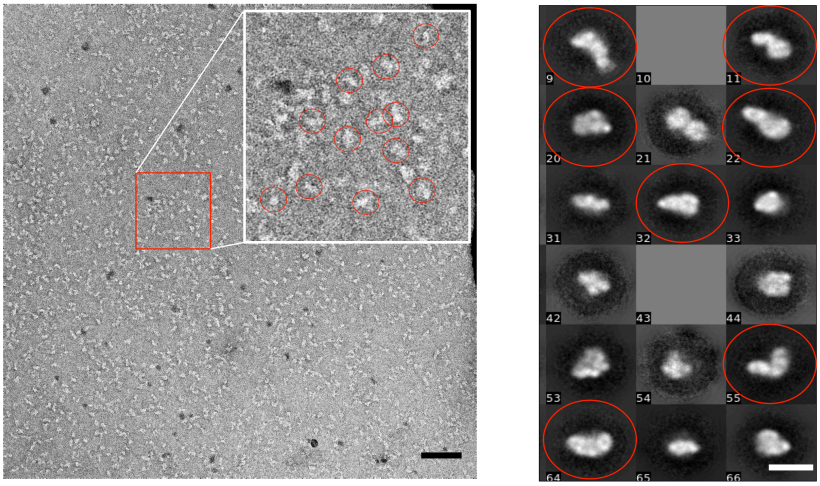

Figure 43 Negative staining TEM micrograph and 2D class averages. Left: Grafix method crosslinked complex on negative stain micrograph. Individual particles representative of the L-shaped complex was marked by red boxes. Scale bar= 50nm. Right: 2D class averages of the extracted particles after autopicking, projection in different orientations were highlighted by red box. Scale bar=15nm.

The crosslinked particles appeared slightly smaller and were more compact compared to the native complex (Figure 44). Distinct particles can still be observed without much aggregation as shown below in a representative micrograph of the non-crosslinked samples which had a less homogeneous composition of the particles in negative stain. Both types of particles were then vitrified according to the standard sample preparation procedures and further examined with Cryo-EM.

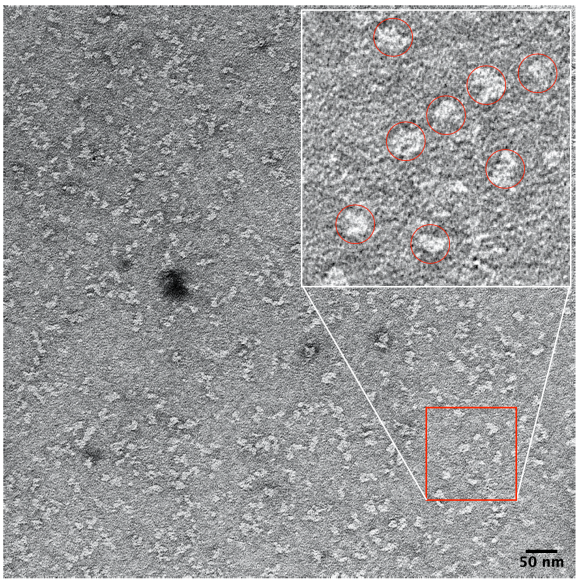

Figure 44 Micrograph of negatively stained, purified Ccr4-Not using modified FLAG purification. Complex particles were separated by gel filtration on Superose 6 10/300 column and no crosslinking. Inset shows a close-up of a section containing representative particles of the complex (highlighted in red circles).

4.6.2 Electron cryo-microscopy

Both the crosslinked and native complexes from the modified FLAG purification were examined by cryo-EM in low dose mode to preserve the beam sensitive sample. The purified proteins were vitrified at selected protein concentrations and screened first according to the overall usable area having a suitable ice thickness and visible particles. Without crosslinking, the complex was assumed to have disassembled during or just before sample preparation as the grid holes were apparently void of distinguishable particles, even in average ice thickness (≈50-100nm). Otherwise, either aggregates or smaller protein debris were observed (Figure 45, Top). Grafix treated protein sample was slightly more visible in the vitrified ice layer (Figure 45, Bottom), however, particles were also quite aggregated and not homogenously distributed like in the negative stained samples. Grids with an extra layer of 2nm carbon support or Graphene oxide film were then tested. They help to improve the protein adhesion to a support surface instead of adhering and denaturing at the air/water interfaces, where such a macromolecular complex is susceptible to (D'Imprima et al., 2019). This could also help to locally concentrate and stabilise fragile complex during sample preparation (D'Imprima et al., 2019). Unfortunately, the extra support did not make any significant changes in the behaviour of the complex particles on the grids. Consistent with the observations above, non-crosslinked particles aggregated badly and showed no discernible particles either, but the crosslinked sample had some visible particles in a less aggregated fashion (Figure 46). The additional layer of thin carbon seemed to help with the particle distribution to some extent but the extra background from the thicker material also added more background noise thus reduced the image contrast of the particles comparing to in the micrographs without extra carbon (Figure 47 and Figure 48 A). Therefore, subsequent grids were prepared without extra carbon support using crosslinked sample and then screened with a 120kV T12 microscope (FEI) for an optimal sample preparation condition (Figure 47).

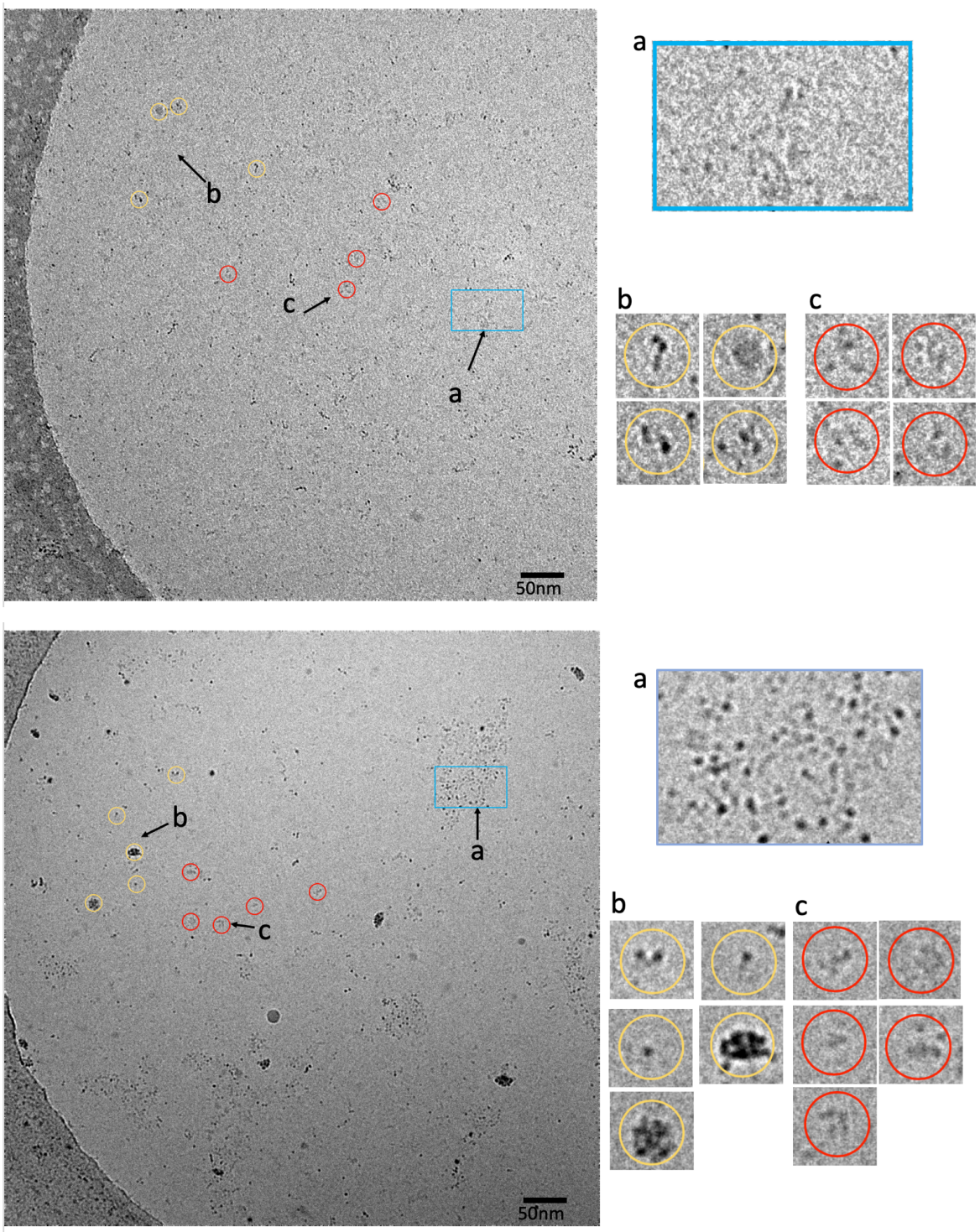

Figure 45 Cryo-EM micrograph of purified Ccr4-Not complex. Upper panel: Sample after crosslinking. Lower panel: Sample without crosslinking. Label a, protein aggregates, b, protein particles or subcomplex. c, contamination or artefacts. Gallery of selected features Zoom-in for the respective micrographs on the right.

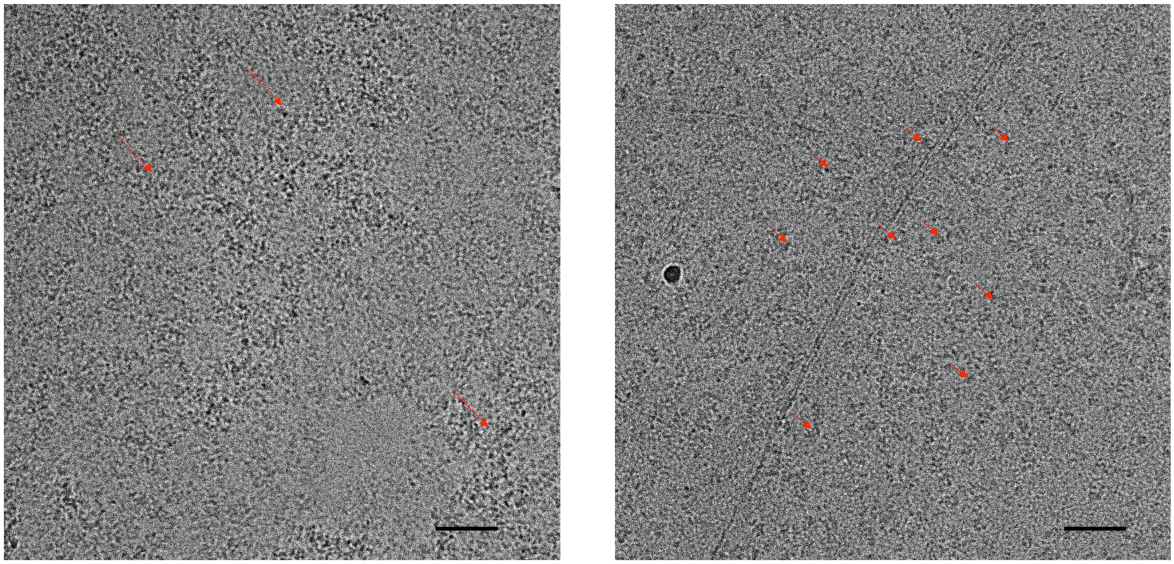

Figure 46 Cryo-EM micrographs of crosslinked/non-crosslinked sample with extra carbon support. Left: Grid hole with extra layer of Graphene oxide and un-fixed protein complex. Areas of massive aggregate after vitrification were marked with red arrow. Right: Grid with graphene oxide layer and Grafixed sample prepared in the same way as left one. Distinguishable complex particles were marked by red arrows. The extent of aggregate is much less severe than in the left micrograph. Scale bar= 50nm.

The current method of vitrifying the sample using the Vitrobot device was found to be somewhat less reliable in reproducing the desired ice thickness across the grid during sample preparation. Several grids needed to be prepared subsequently and screened before a few candidate conditions can be selected empirically for the actual data collection. This was a major issue during screening and data collection as the number of usable grid squares for each grid varied largely, therefore limiting the amount of the usable data.

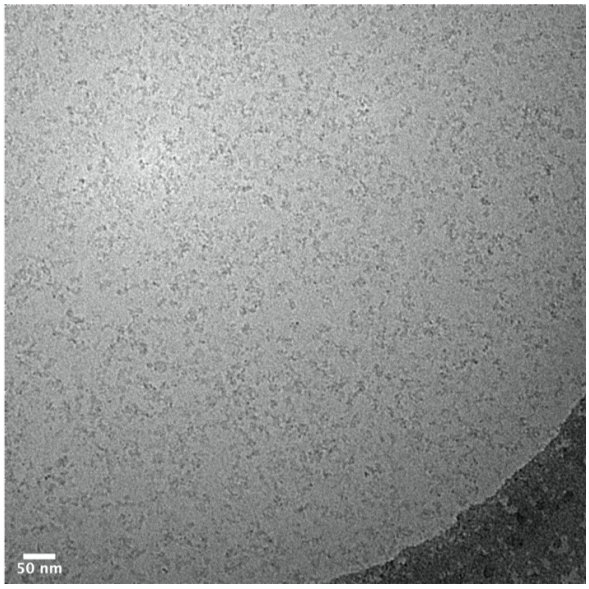

Figure 47 Cryo-EM micrograph of a representative good sample prepared in ice with Grafixed protein complex. Micrograph taken with a 120kV microscope in low-dose mode. No extra carbon layer was used, and particles were subtended in vitrified buffer only.

For the grid that appeared to contain uniformly distributed protein particles and had sufficient collectable area i.e. average ice thickness in most grid squares, it was set up for data collection using the 300kV Titan Krios microscope and Falcon 3EC detector in integrating mode (ThermoFischer) (Figure 48). The motion corrected and dose weighted averages of movie frames were automatically picked for particles on-the-fly using the CrYOLO neuronal network particle picker (Wagner et al., 2019) and subsequently processed in Relion 3 (Zivanov et al., 2018). However, the 2D class averages displayed an unexpected smaller particle with a ring-shape. There was no L-shaped classes or similar classes to the previous negative stain data (Figure 43). An initial 3D model was generated from these classes and revealed that the strange ring shape in the 2D classes could have been part of a few very flexible segments linked together (Figure 48 C and D). The overall size of this reconstructed volume resembled the structure of the core complex from *S.pombe* (Ukleja et al., 2016a). Despite having good biochemical activities and purification profile, this complex still require further improvement in sample preparations in order to be useful for high resolution Cryo-EM structural determination. These will be elaborated more in the Discussion section (§5.7 & 5.8).

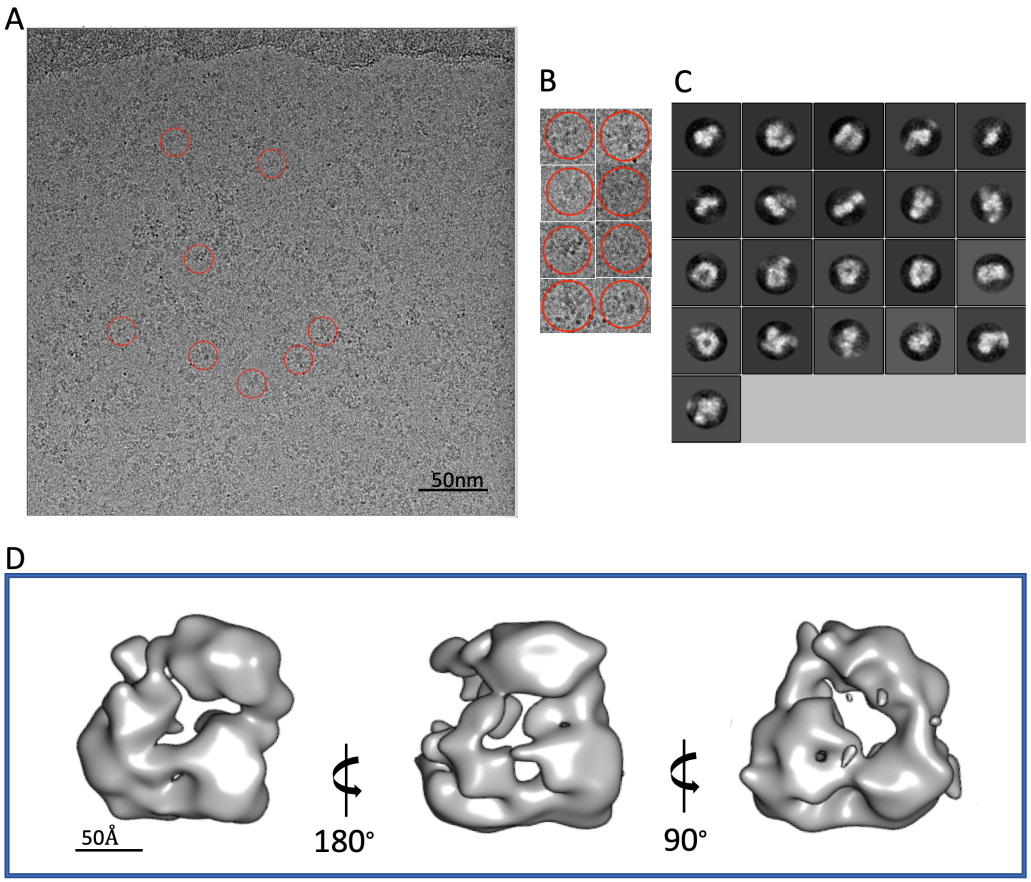

Figure 48 Cryo-EM data of crosslinked Ccr4-Not complex from one of the above preparations that showed distinguishable particles. A) Motion corrected and dose-weighted movie average of a representative micrograph from the sample in vitrified buffer taken with a 300kV microscope. B) Representative particles as seen in A. C) 2D class averages from the dataset collected on this sample. D) Initial model calculated from the above class averages.

5 Discussion

Part I

5.1 Direct electron detectors used in single particle Cryo-EM

Single-particle Cryo-EM has become a powerful and convenient method for protein structure determination (Kühlbrandt, 2014). However, there has been certain limitations that are holding back its capabilities. In particular, one important factor for obtaining high-resolution 3D reconstruction is the performance of the electron detector based on its detective quantum efficiency (DQE). DQE is an aggregate of the detector's modulation transfer function and noise power spectrum with respect to the spatial frequencies (Ruskin et al., 2013). Its value reflects how much noise is added to the output signal forming the final image at each spatial frequency i.e. Signal-to-noise ratio (SNR) (Equation below). Meanwhile, the finest details of a protein sample are conferred by the high spatial frequency signals whereas the low spatial frequency signal contributes largely to the image contrast useful for particle picking and alignment. The spatial frequency is usually represented as a fraction of the Nyquist frequency, which is the reciprocal of two times the pixel spacing in a pixelated detector. For Cryo-EM applications, it is desirable to use a recording medium that offers as high a DQE as possible across all spatial frequencies because imaging of the radiation sensitive biological specimen also restrained the maximum electron dose that should be used (Henderson, 1995). Key requirements, such as a higher efficiency of electron detection, narrower point spread function (thus better MTF towards the Nyquist frequency) and minimal noise added from the detector, are thus important benchmarks for the device. The DQE during practical use of the detector is hence represented as:

$$\boldsymbol{DQE(\omega)} = \frac{\boldsymbol{n * MTF^2(\omega)}}{\boldsymbol{NPS(\omega)}} \qquad (2)$$

ω: spatial frequency

n: electron dose

MTF: Modulation transfer function

NPS: Noise power spectrum

The lack of an electron detector that satisfies all these requirements was a major bottleneck for high-resolution reconstructions in Cryo-EM, even though the other microscope hardware development had been nearly impeccable (McMullan et al., 2009a). Conventional medium such as the film has a reasonable DQE and large field of view which was preferred for recording single particles such as viruses, but its handling was troublesome. It was complemented by the scintillator-based CCD/CMOS detectors for their instantaneous feedback with the digitised images and also better dynamic range, but they are still limited by their poorer than film DQE beyond half of the Nyquist frequency and the high intrinsic readout noise to be truly useful in high-resolution Cryo-EM (Li et al., 2013). These were attributed to the photon scattering and signal broadening at the scintillator/optic fibre coupling step (Meyer and Kirkland, 1998) and charge-sharing between the adjacent pixels. Since biological samples are sensitive to radiation damage, compensating with electron dose will simply sacrifice the high-resolution information.

The commercialised monolithic active pixels (MAPS) direct electron detectors (DED) for Cryo-EM are fundamentally better in DQE compared to all previous detectors (McMullan et al., 2014). They are radiation harden and capable of registering single electron events directly (electron counting), bypassing the scintillator conversion step or the need for the troublesome digitisation. Essentially, MAPS detectors are analogue (integrating) detectors that register electron events as a signal that is proportional to the energy deposited by the incident electron at the P/N junction in the epilayer, which follows a Landau distribution i.e. a proportion of electrons always deposit higher than the mean energy causing a large variance in signals (McMullan et al., 2009). On the other hand, primary electrons that have traversed through the detector can be backscattered and these electrons passing through the epilayer and substrate again deposit more energy as they slow down (McMullan et al, 2009). This will cause the signal from one electron event to further scatter in the pixel plane making precise localisation of the point of incidence more ambiguous. Hence, it reduces the DQE values towards the higher frequency and consequently limits the resolution. To address the later issue, newer Falcon detectors (FEI) are back thinned extensively leaving a sufficient interacting epilayer for high sensitivity but reduced the support substrate layer underneath it to a minimum (Falcon II, 50µm and Falcon 3EC, 30µm) to cut noise caused by the backscattering events (Kuijper et al., 2015). This has made significant improvement in the Falcon II and 3EC detectors' DEQ in the higher frequency range (Faruqi et al., 2015) and this is almost as good as the theoretical limit for an integrated signal at DQE(Nyquist) (McMullan et al., 2009a). To counter the first issue, MAPS detectors counts individual electron events by normalising the area spread of charge over a cluster of pixels in the area to a delta function (or similar mathematical transforms) to infer the

precise impact location (McMullan et al., 2009b, Battaglia et al., 2009b). To do this effectively, the incident electron dose rate has to be sufficiently low to a level that minimises coincidence loss i.e. double or miscounting of individual electrons and allows the distinguishing of spatially well-separated incident electrons. Thus, the detectors have to operate at a fast read-out rate to compensate for the extended exposure time at a practical level e.g., the K2 summit detector (Gatan) has an intrinsic frame rate of 400 fps and its successor the K3 is at 1500fps. Meanwhile, the Falcon II and 3EC are offering 18fps and 40fps respectively. Technically, at a moderate speed of 40fps, only Falcon 3EC has a practical exposure time, and in terms of its firmware was enabled for its use in the counting mode. These frame rates continued to enable recording in movie mode which helps minimising the beam-induced motion by using dose-fractionation and various motion correction methods (Faruqi et al., 2015). The counting algorithm improved the MTF and essentially the DQE of the counting detectors and by back-thinning the large pitch width Falcon detectors gives extra advantage in the spatial resolution and DQE of the detectors over a large stretch of the Nyquist frequency (Faruqi et al., 2015, McMullan et al., 2014). Previously, the majority of high resolution structures (<4Å) deposited on EM Databank(EMDB) were solved using the data recorded by the K2 summit detector and Falcon II lagged behind not only in numbers but the solved structures seem to skew towards larger assemblies (> 1MDa) compared to the smaller complexes that the K2 camera was able to resolve quite well. However, the counting capability in K2 makes the comparison unfair. Since Falcon 3EC is the first counting enabled detector in its series, it would be worthwhile to further examine the practical use of its counting mode on top of the said improvements in the integrating mode.

5.2 Practical evaluation of the Falcon 3EC detector for high-resolution cryo-EM

The electron counting mode implemented in the new Falcon 3EC detector has significantly improved the DQE at all spatial frequencies over the already quite good integrating mode DQE (Figure 22) (Faruqi et al., 2015). Although this comes with a longer exposure time used to ensure accurate counting, the low electron flux otherwise helped to reduce the beam-induced movement and preserved the molecular integrity during the longer exposure (Chen et al., 2008). The performance of this new detector together with the new Titan Krios microscope here in Würzburg were benchmarked by comparing the counting and integrating mode using subjects of different sizes between 500kDa and 40MDa (Song et al., 2019). The EM maps obtained could resolve at resolutions that were approaching the theoretical resolution limit imposed by the Nyquist frequency in the set-up, e.g. β-galactosidase in counting mode at 97% of Nyquist frequency and 89% in integrating mode. This indicates that the detector has very high sensitivity and in this chosen microscope set-up, resolutions approaching the Nyquist frequency can be practically achievable. The user can then optimise the magnification i.e. the number of single particles per micrograph, to accommodate to the desired resolution and output. Consequently, an efficient data collection strategy that applies to similar sized protein of interest in this range, e.g. the Ccr4-Not complex, could be catered so that it maximises the time and output from a typical user session.

The advantage in counting mode is more prominent for smaller proteins than the large ones in this case-study. The best resolved object is the β-galactosidase at 2.24Å, with a sampling size of 1.063Å/px. Counting mode data resulted in better reconstruction than the integrated data when similar amount of particle images are compared. However, the larger integrating mode dataset produced within the same time span appears better in overall information content than the smaller but higher quality counting mode dataset. Since the Fourier Schell correlation of a full-sized counting mode data extends nearly to the Nyquist frequency, the limitation on resolution is then probably due to the pixel size used for imaging and the high frequency noise causing aliasing near to the sampling limit. This difference between the integrating and counting mode detector performance is further demonstrated in the Res-Log plot (Figure 22C) where about 2.5 times more particle images are needed for reconstructions to yield similar resolutions as compared to the counting mode data. This observation can be correlated to about 1.8 – 2.1x of difference in ratio between the DQE of each mode (Figure 22D). Therefore, this ratio of extra particle images from the integrating mode are needed for supplementing the lower spatial SNR. Besides, the high initial gain in

DQE at the starting low spatial frequency in counting mode led to an enhanced accuracy in particle image orientation determination due to this boost in the spatial SNR. Meanwhile, a lower magnification can be used to increase the number of particles with a larger field of view since the detector can retain structural information much closer to the Nyquist frequency in both modes.

For the 4.8MDa F97L-CLPs that was tested, the difference in the FSC of the reconstructions from both modes of acquisition is very marginal. This can be seen from the almost identical Res-Log plot (Figure 20) where very little differences can be seen across a wide range of resolutions and particle numbers. Comparing the higher resolutions, about 20% less particles are required for giving the same resolution as in the counting mode. This might suggest that an intrinsic limit to the resolution was a result of particle disorder. These capsid particles have a diameter up to 36nm which means that the small depth of field in their particle images could also limit the resolution without correcting for the Ewald sphere effect (Wolf et al., 2006). This can be compared to previous studies of the same object using counting mode data collected from the K2 detector (Gatan) and the resolution is very similar when neither was corrected for the Ewald curvature (Böttcher and Nassal, 2018). After correcting for the curvature and doing per particle ctf refinement, resolution increased by about 0.3Å for reconstructions using either integrating or counting mode data (Song et al., 2019). Thus, there should be no difference in resolution from collecting data in counting mode with either the K2 or the Falcon detectors for large particles at this size without further corrections in post-processing. Alternatively, the geometry of the particles would defer with the previous conclusion to an extent, as shown by the TMV at a molecular size of around 40MDa but the tubular architecture of the particle with 18nm in diameter is not limited by the Ewald curvature. The integrating mode data collected on TMV using Falcon 3EC was resolved to 2.3Å in this case-study which is already much better than the resolutions reported from X-ray fibre diffraction (Namba et al., 1989) and previous reconstructions using data from the Falcon II and K2 summit detectors (Fromm et al., 2015). Although it is also essential to note that the reconstructions from Fromm et al. consisted of ¾ less averaged asymmetric units as used in this case study so that the differences in resolution should not be attributed entirely to the detector performance.

Similarly, imaging conditions would also have an effect on the resolutions. Recently, the resolution record for TMV single particle reconstruction has improved to 1.9 Å using data collected from the K2 detector in Super-resolution mode but 2-5 times less asymmetric units than in the Falcon 3EC case-study were used (Schmidli et al., 2019, Weis et al., 2019). These

two studies have both used a higher magnification and in one of them a much smaller defocus and dose rate/total dose (Weis et al., 2019) than in the Falcon 3EC case-study. Consequently, this would also imply that the different detectors were able to retain the structural information at about 92% of the Nyquist frequency for the Falcon 3EC detector compared to ≈85% (Schmidli et al., 2019) and ≈67%(Weis et al., 2019) for the K2 summit detector while using similar microscopes. Therefore, as noted above, the difference in the detectors' performance should be compared more fairly like in the previous study (Fromm et al., 2015) and not solely based on the final resolutions.

The expected dimensions and weight of the Ccr4-Not complex is closer to a typical medium sized protein complex at about 0.9 – 1MDa, and its diagonal length is around 200-250Å (Ukleja et al., 2016a, Nasertorabi et al., 2011, Chen et al., 2001). Those observations and conclusions from the β-galactosidase test would hence be quite informative for deciding on the data collection strategies. Assuming that sample variability is minimised as much as possible in the sample preparation, integrated data should be collected for the initial reconstruction and sorting of the conformational heterogeneities. This would save time and take advantage of the higher spatial SNR in the lower frequency range as discussed above. Counting data could then be collected when the higher-resolution signals are desired to refine a better resolved reconstruction. Whereas for larger proteins, counting mode data could not improve the resolution further than the limitations imposed by other corrections needed in image processing. Afterall, the duration of data acquisition and intended resolution can be balanced when using similar equipment to effectively reduce the time and cost for an experiment based on the size of the protein of interest and a similar microscope facility.

Part II

5.3 Efficient epitope tagging using yeast homologous recombination

Not4 and Not5 proteins were selected as the bait for the endogenous immuno-affinity purification via a C-terminal 3xFLAG epitope inserted using the PCR-based homologous recombination tagging method (Knop et al. 1999, Puig et al, 1998, Wach et al., 1997). This method is advantageous for its versatility and convenience in introducing an affinity tag as a modular construct and a selection marker is also included in the genomic DNA that gives reliable antibiotic resistance on the selective plates. Although, in this case, the efficiency and stability of the transformation were somewhat inferior to that described in the original paper, even when carried out under very similar conditions i.e. lower transform efficiency in terms of colonies per μg of PCR product used for transformation, and the length of incubation before stable colonies appeared. Such deviation might have been specific to the gene of interest or was related to the homologous sequence length and the transform competence of the yeast strain used (Knop et al., 1999). Ideally, C-terminal tagging reduces the chance of the insert interfering with normal gene expression in contrast to an N-terminal insert, other than indicating for the translation of the full-length protein of interest. However, there is a probability of the inserted selection marker sequence interrupting any downstream regulatory sequence or even causes a change in the target gene's mRNA abundance or protein stability since the endogenous regulatory elements are further downstream (Lind and Norbeck, 2009, Khmelinskii et al., 2011).

In the case of Not4, the tag was successfully added after extending the length of homologous sequence to 50bp (At least 45bp was recommended in Knop et al., 1999) so that the PCR fragment can target the Not4 C-terminal locus more efficiently and protein expression was also not disrupted (Figure 24). Lengthy primer, however, is prone to form secondary structures and cause non-specific annealing during PCR amplification of the insert. This might lead to failed PCR amplification or erroneous PCR fragments being produced. In addition, an excessive homologous sequence may increase the chance of non-specific annealing and recombination at other loci. Thus, leading to the PCR fragment not being inserted correctly or at all. Either way, no-growth or retarded growth of cells on the selective plate could happen.

A similar procedure was also used for the Not5-FLAG tagging. The transformants formed smaller colonies as compared to the original S288c strain and the Not4-3xFLAG transformants, and a higher than suggested dose of PCR fragments (Knop et al., 1999) had to

be used before the stably transformed colonies appear on the selective plate. In the case of Not5-6xHist transformation, its colony PCR result showed a positive insertion, but no tagged protein could be detected by western blot in the lysate(Figure 25). Both cases of C-terminal Not5 tagging have shown an occurrence of many false positive transformants under the G418 antibiotic selection. Studies have suggested that Not5 is related to the translation mechanism via a physical interaction with the ribosome (Panasenko and Collart, 2012, Buschauer et al., 2020) and is needed for many other functions that involves recruiting the Ccr4-Not complex (Review by (Collart et al., 2013)). A recent study has elucidated the link between the N-terminal domain of the Not5 protein that bridges stalled ribosomes to the Ccr4-Not complex to initiate transcript decay when non-optimal codons are encountered (Buschauer et al., 2020). For this particular transformation, the C-terminal positively charged poly-histidine tag may have caused changes to the expression of the Not5 protein unintentionally (Aslantas and Surmeli, 2019) and undermined its ability to associate with the Ccr4-Not complex or maintain its functions in the cell.

The overall benefit of this method is that a small library of the tagged protein constructs can be generated relatively quickly and easily by PCR and then inserted into different genes of interest in the host genome. The transformed cells will also express the tagged protein permanently in contrast to a plasmid expression. The protein of interest is also regulated by its native promoter and translation factors hence is suitable for purifying endogenous protein complexes. Nonetheless, checking for gene dependent factors that might affect the tagging and careful optimisation of the transformation steps should be taken into consideration to avoid any disruptions and delay in the protein expression (Maeder et al., 2007).

5.4 Purification of the endogenous Ccr4-Not complex

5.4.1 Protein complex abundance

The endogenous Ccr4-Not complex was purified via the FLAG-tagged Not4 subunit using the Anti-FLAG antibody conjugated M2 agarose beads (Sigma), along with any other co-purifying factors. The use of this tag has reduced the probability of interfering with the target protein's expression and the short hydrophilic polypeptide would potentially enhance the solubility of the bait protein. It has displayed a high specificity in the lysate environment and allows competitive elution under mild conditions using a synthetic 3xFLAG peptide (Waugh, 2005, Einhauer and Jungbauer, 2001b). However, in this study, the total eluted proteins from one purification experiment by the conventional procedure (Gerace and Moazed, 2015a) was usually between 50µg/100g starting cell mass and up to around 200µg/500g cell mass when more material could be used. This was approximately equivalent to around 58-233pmol of the core complex (at 809kDa theoretical molecular size), the equivalent of 50µL of 1.2-4.7µM Ccr4-Not complex in buffer. Therefore, imposing a restriction to the number of SDS-PAGE runs, the size and resolution of the gel-filtration column used due to the sample dilution factor, and also the number of EM grids that can be prepared. More importantly, the eluted sample was still quite heterogenous, as seen on the SDS-PAGE gels (Figure 27) and in the negative stain EM protein particles (Figure 36, right). Most EM images showed a mixture of smaller sub-complex and not a distinct population of the expected L-shaped particles. In fact, the anti-FLAG beads have a reported binding capacity of just ≈0.6mg/ml of beads slurry (Sigma) though it seemed to have worked efficiently on many other proteins or eukaryotic expression systems with very high specificity and has a K_d value in the nanomolar range (Gerace and Moazed, 2015b, Baughman et al., 2011, DeCaprio and Kohl, 2019, Kimple et al., 2013, Einhauer and Jungbauer, 2001a). The problem here could have been due to the higher volume of the lysate used (≈200 to 500ml) where the endogenous concentration of the bait protein was not high enough for an efficient binding while the non-specific cytoplasmic proteins also competed for binding with the bait and its associated proteins at the same time. Longer than the recommended 2-4 hours of incubation time not only needed replenishing of the protease inhibitor periodically (e.g. PSMF half-life in aqueous solution, pH 8 is ≈ 30-55min) (James, 1978) but the target complex was also exposed to unnecessarily long period of potential proteolysis in the lysate environment. Not4 is reported to have an average cellular abundance of 4767 molecules/cell (mpc) according to the *saccharomyces* genome database (SGD) which

is close to the median value of 2622 mpc for the yeast proteome abundance level (Total range: 3 to $7.5x10^5$ mpc) (Ho et al., 2018). The rest of the core complex subunits also have a similar average abundance except for Caf130 which is about two to five times less abundant than the rest of the subunits (SGD). 67% of the proteome in yeast cells has an abundance level between 1000 and 10000 mpc, which should include all the core Ccr4-Not subunits (Ho et al., 2018). This puts the bait amongst many similarly abundant proteins in the lysate. Moreover, the mild native condition used could also have unexpectedly slow subunit association, especially for a potentially dynamic complex like the Ccr4-Not (discussed below). Although larger preparative scale purifications helped to obtain slightly more purified proteins, this purification approach was unlikely to have exceptionally high output and efficiency in bigger preparations compared to the other affinity tag systems (LaCava et al., 2016, Terpe, 2003) except that the specificity is applaudable. To avoid any potential disruption to the physiological functions and altering the native state of the complex *in vivo*, overexpression of the bait protein to increase its abundance was not considered.

The modified purification strategy later has ameliorated the problem with low recovery of the native complex from the cell lysate and provided sufficient purified complex for EM and functional assay. Ammonium sulfate protein precipitation fractionates the total soluble proteins in the lysate by the "salting-out" effect in high concentration of ammonium sulfate solution (Duong-Ly and Gabelli, 2014). This increases the concentration and stability of the precipitating complex through preferential solvation around the protein and its surrounding (Wingfield, 1998). In the presence of very high salt concentration, as well as the hydrophobic interactions between the protein hydration shell and the salt ions resulted in the proteins adopting a more compact, thermodynamically favourable conformation to minimise the surface to volume ratio and contact area with the hydrophobic surrounding. This would have the effect of strengthening the complex assembly and re-organising of unstructured regions on the complex-solvent interface (Giege et al., 1982). The ammonium sulfate fractions that contained the FLAG tagged bait protein according to western blot (Figure 32) was assumed at first to include the rest of the core complex subunits and this was confirmed by both SDS-PAGE and MS later (Figure 35). This indicates that the subunits associated with Not4 are forming a more stable complex under the 'salting-out' condition. The additional step in the purification drastically increased the amount of proteins eluted from tens of µg to almost one mg per purification from the same amount of starting material as before with endogenous source. This suggested that more bait proteins are binding with the antibodies on the affinity beads than previously due to a concentration dependent shift in the binding constant. Judging from the

absence of western blot signals in higher ammonium sulphate saturation fractions, it is estimated that the precipitated proteins, or at least for FLAG tagged Not4, could be about twelve times more concentrated than before (Initial lysate volume of 200-300ml and the precipitate was reconstituted in a volume of 25-50ml). Therefore, the anti-FLAG affinity beads should be better saturated after shorter period of incubation and less non-specific proteins would be competing with the bait protein in the resuspended solution.

The eluted proteins thus had better stability and homogeneity, and showed distinct bands corresponding to their expected molecular sizes (Figure 33, lane E2). Subsequently, a much quicker polishing step using the gel filtration method instead of a sucrose density gradient also became feasible because the sample volume and concentration were not marginally low for the available SEC columns. Therefore, the complex avoided from either aggregating extensively or falling apart due to the diluting effect in the gel filtration step. The reconstituted complex was probably already being stabilised during the 'salting-out' step and suffered less degradation compared to being in the bulk lysate for too long previously. The increased complex concentration in the resuspension could also have contributed to better stability by the molecular crowding effect (Wang et al., 2012). Since most of the RNA processing complexes, including the Ccr4-Not, are aggregating at the cytoplasmic loci such as the p-body (Reijns et al., 2008) where they are naturally very crowded.

5.4.2 Complex stability during processing

The varied abundance of the detected subunits and their relative association in the core complex was inferred from the MS data where the subunits were not present in stoichiometry with respect to the scaffold protein in the immuno-pulldown via the bait (§4.3 above). For such experiment, the stable Ccr4-Not core complex (Chen et al., 2001, Nasertorabi et al., 2011) would have its subunits appear in a tighter grouping on the scatter plot and in a distinctly higher ratio over the background of the non-specific proteins, away from the x-axis origin (Uthe et al., 2017). The iBAQ (intensity-based absolute quantification) value along the y-axis was used to estimate the interaction stoichiometry in the complex (Hein et al., 2015, Smits et al., 2013, Uthe et al., 2017). For Caf130, the much lower abundance in pulldowns from both baits suggested that its interaction with the core complex is much weaker and apparently sub-stochiometric in the purified complex after processing. This *S. cerevisiae* specific protein was also found to be under-represented in another study which purified the endogenous Ccr4-Not from the same species using the TAP-tagged Caf40 (Stowell et al., 2016) but its apparent functions in the yeast remain unclear (Collart, 2016). Whereas the rest of the core subunits (Not1, Not2, Not4, Caf1, Ccr4, Caf40) interact more tightly with each other, showing similar abundance in the pulldown sample. However, the paralogous Not5 and Not3 subunits might be mutually exclusive in binding to the core complex.

As described (Introduction 1.2.3), the NOT module includes the Not1 C-terminal scaffold domain, Not2, Not3 and Not5 subunits. Not4 is also binding to the Not1 in proximity but is functionally distinct and does not contain the NOT box domain (Review by: (Collart, 2016, Ukleja et al., 2016b)). Although it is believed that the Not3 and Not5 proteins are paralogues that resulted from gene duplication in yeast, only the Not5 is orthologous to the human CNOT3 protein (Collart et al., 2013). The N-terminal sequence of these two proteins is very similar between Not3 and Not5 with 44% sequence identity (Oberholzer and Collart, 1998). Recently, the very N-terminal domain of the Not5 protein has been shown to interact with ribosomes stalled by a sub-optimal codon on the transcript by utilising several conserved key residues within this domain but the co-purifying Not3 which shares a majority of the sequence at this region is however not involved in this mechanism (Buschauer et al., 2020). Following another shared domain called the NOT box, the two proteins mainly differ at the very C-terminal end (Appendix 8.3). Crystal structures of the NOT modules (Boland et al., 2013b, Bhaskar et al., 2013b) showed that Not5/CNOT3 interaction with the scaffold is dependent on their conserved Not1-interaction domain at the N-terminal extended region of

the NOT box and also on the key residues within the NOT box dimerisation interface. The NOT box region on Not5 contributes to a dimerisation interface with the complementary Not box region of the Not2 protein that promotes their recruitment and binding to the complex in addition to the Not1 interacting region common to both the Not5 and Not3 (Bhaskar et al., 2013a). The Not5 protein is found to be physiologically and functionally more relevant and essential than the Not3 in yeast, and such distinction is linked to the variable C-terminal region which is neither conserved nor involved in binding with the Ccr4-Not complex (Oberholzer and Collart, 1998). Meanwhile, the Not3 protein was suggested to be less favourable at forming the NOT module because only the Not2 and Not5 could interact synergistically to bind Not1 (Bhaskar et al., 2013b). In addition, the region that wraps onto the Not1 scaffold favours the heterodimerisation of the NOT box containing proteins while the reconstituted free NOT box proteins alone tend to aggregate and precipitate (Boland et al., 2013a). This may imply that Not5 could potentially compete with Not3 for binding to the Not1 scaffold and seeks stabilisation in solution. This may also affect recruitment of the Ccr4-Not complex to the ribosome because they have very similar Not1 interacting region and the putative ribosome interacting domain, at least in the yeast.

To an extent, this was hinted by the lower Not3 abundance in the pulldown via Not5 compared to using the Not4 as the bait (Figure 38). Using Not5 as the bait may have preferentially enriched the more stable Not5-associated sub-population of the complex from the lysate since Not3 does not interact with Not2 interdependently. The local concentration of Not5 that increases during the co-immunoprecipitation may have led to a shift in the binding equilibrium and thus showed higher occupancy of Not5 in the purified complex. Assuming that the molar abundance of the core complex in Not5 pulldown can be represented based on the mean iBAQ value of the majority of the subunits (Not1, Not2, Not4, Caf1, Caf40, Ccr4), ($\bar{X} = \log_{10} 9.3\,, n = 6$). Then, Not3 (iBAQ≈8.2) present in this sample can only occupy at most 8% of the core complex while Not5 (iBAQ≈9.7) is 2.5 times in molar excess. Therefore, even though both subunits are identified as high confidence interactors i.e. similar X-values, their absolute molar abundance differed by about 32 times in the pulldown.

Meanwhile, the co-immunoprecipitated complex via Not4 showed a stochiometric abundance for Not3 and Not5 in the pulldown together with the rest of the core subunits. (similar Y-values), meaning that both subunits could participate in the binding to Not1 at an equivalent molarity. The presence of both Not3 and Not5 in the purified complex via e.g. Not4 had also been observed in other studies and whether they occupy the exact same binding region

on Not1 is uncertain in spite of their sequence similarity (Stowell et al., 2016, Buschauer et al., 2020). However, Not3 in this case appears to have less non-specific binding to the beads as its iBAQ ratio (sample/control) on the X-axis is much higher than the rest of the complex. The exact reason and significance for this observation would need further investigation because it could also be a random anomaly from the co-immunoprecipitation procedure or due to degradations in the control sample. The later seems more plausible since typically Not3 is also poorly represented on the SDS-PAGE for the isolated complex (This thesis and (Stowell et al., 2016)) while the complex bound Not3 would be more stable. Essentially, such behaviours of the Not3 and Not5 could implicate in the complex stability and the functions of the NOT module in the Ccr4-Not complex, perhaps also linked to mRNA degradation (Bhaskar et al., 2013b, Wahle and Winkler, 2013, Buschauer et al., 2020). These observations may suggest an alternative complex assembly mechanism in yeast or even in human and *Drosophila*, since CNOT4 (Not4 in yeast) is also not a stable subunit of the core complex and CNOT3 is deemed the only orthologue from yeast Not5 (Raisch et al., 2018, Temme et al., 2010, Lau et al., 2009, Collart et al., 2013). Compositionally heterogenous sub-complexes might exist and function *in vivo* as an ad-hoc complex recruited transiently via specific interaction partners and released soon after the signal is alleviated.

5.5 Deadenylation by the endogenous yeast Ccr4-Not complex

The purified endogenous *S. cerevisiae* Ccr4-Not complex in this work is active and digested the Poly(A) tail of a model mRNA rapidly (Figure 39). The deadenylase module (Caf1:Ccr4) of this complex is responsible for the generic deadenylation reported in yeast (Wiederhold and Passmore, 2010, Collart and Panasenko, 2012). Consistently, the highly conserved nucleases are also mediating deadenylation in human (Yi et al., 2018). Here, the model substrate was selected because it resembles the 3'-UTR of a typical mRNA and that it has no predicted secondary structures. It also included a 20 nucleotide 5' extended element harbouring a putative Pumilio Response Element (PRE) (Raisch et al., 2019). Similar substrates had also been used in other deadenylation studies of the Ccr4-Not deadenylases (Stowell et al., 2016, Webster et al., 2017, Webster et al., 2019, Wang et al., 2010, Morita et al., 2007). The PRE consists of a short 5'-UGUAAAUA-3' motif located within the 3' UTR that could interact with proteins containing the Pumilio domain (PUM) and accelerates deadenylation (Webster et al., 2019). Previously, enhanced activity in the recombinant *S. pombe* complex (Webster et al., 2017, Webster et al., 2019) were either attributed to the co-

purifying RNA-interacting protein (Mmi1) or to the addition of PUM containing protein (Puf3) that bridges the RNA substrate and the nucleases on the complex (Figure 49A). However, Raisch et al. (2019) showed that their reconstituted full-length human complex alone exhibits enhanced deadenylation *in vitro* too (Figure 49B). It was argued that the substrate selectivity and accelerated deadenylation was due to the 5' extended sequence length beyond the last consecutive adenine bases and not only by an external factor's sequence recognition i.e. Ccr4-Not has both extrinsic and intrinsic means of substrate recognition.

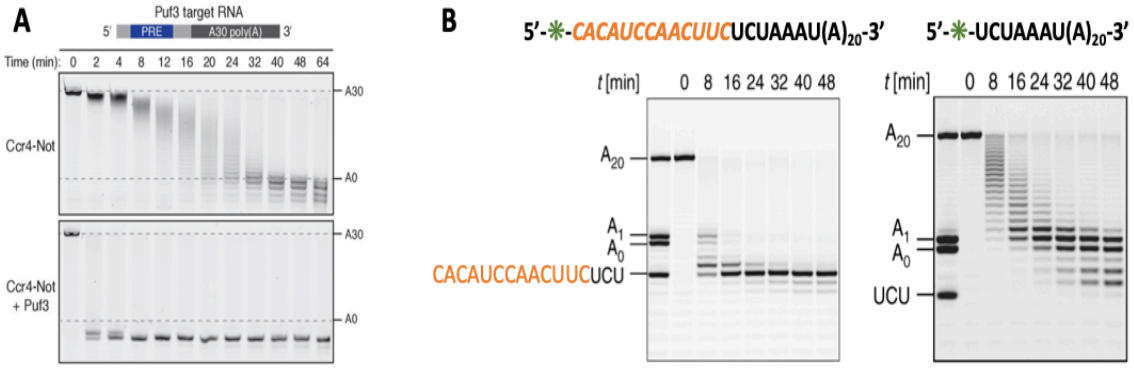

Figure 49 Accelerated deadenylation by reconstituted S.pombe and human Ccr4-Not complex in vitro. A) Recombinantly purified S. Pombe Ccr4-Not complex degrade the Poly(A) substrate gradually up to end of the tail (A0) and proceeded further by several bases after a short pause as seen by the accumulated A0 RNA between 32 and 40min on the time-course. RNA is labelled with 5' 6-FAM (Fluorescein). Below is the same assay with mRNA substrate pre-incubated with Puf3 protein before purified complex is added and started the reaction. Reaction product is already visible in the first time point and intact substrate had diminished. An accumulation of product is indicated by the increasing intensity of the band. Nucleolytic reaction proceeded through to the product beyond A0 without delay as compared to above. B) Left: Deadenylation of the mRNA substrate having a 5' extended sequence (orange) is rapid and intact substrate had been exhausted in the first 8min. Tail-less A0 product accumulated shortly and degradation continued for another four bases before stopping. Assay using recombinant human Ccr4-Not complex to demonstrate the effect of 5' extended element in accelerating deadenylation. Right: Same assay set-up with substrate lacking the 5' extended sequence. Deadenylation is more gradual as indicated by the ladder of substrate with decreasing length but no product was visible at 8min. Reaction slowed down as the A1 and A0 product accumulated and these were further digested until the UCU product. Reproduced with permission and modified according to CC license from (Webster et al., 2019) and (Raisch et al., 2019) respectively.

In these studies, it was pointed out (Raisch et al., 2019) that the reconstituted nuclease module (Caf1:Ccr4) alone could not degrade an equimolar of Poly(A) construct very efficiently due to the lack of an RNA substrate stabilising site. Thus, showing the single based ladder of gradually decreasing mRNA length along the time-coursed assay similar to in Figure 49, which indicates that a non-processive nuclease activity is likely due to this non-stabilisation. Whereas in the case of a whole Ccr4-Not complex that putatively anchors its mRNA substrate, either via extrinsic RNA binding factors e.g. Puf proteins (Webster et al., 2019, Bhandari et al., 2014b) or at the intrinsic RNA interacting interfaces e.g. Caf40, Not5 and any unstructured or charged regions on Not1 (Chen et al., 2014a, Bhaskar et al., 2013a, Raisch et al., 2019), the appearance of the deadenylation product (Figure 39 and Figure 49) is much sooner and conspicuous.

Among the non-catalytic subunits of the purified Ccr4-Not complex here, only Caf40 and Not5 are most likely to interact with the model RNA (Garces et al., 2007, Bhaskar et al., 2013b). Not5 is not directly linked to the nucleases but shows an RNA binding motif in its crystal structure. Alternatively, the Not4 E3 ligase also has a predicted RNA recognition motif (RRM) but any contribution towards the deadenylation remains poorly characterised (Chen et al., 2018). In comparison, Caf40 is in a proximity to the nucleases on the Not1 scaffold and can even pulldown Caf1 directly (Van Etten et al., 2012). Its Armadillo repeats domain (ARM) can form a positively charged cleft surface that is curved towards the solvent front away from its Not1 binding site (Garces et al., 2007, Mathys et al., 2014b)(Also see Figure 6) and is structurally quite similar to the RNA binding PUM domain (Miller et al., 2008, Mathys et al., 2014b). The PUM specifically recognises a conserved UGU triplet bases on the 3' UTR of its target (Wang et al., 2002) which, however, is replaced with a non-canonical UCU motif here. Therefore, an interaction between the complex and the substrate was less likely to be facilitated by any unexpected co-purifying Puf proteins. Furthermore, Caf40 was shown to interact with RNA *in vitro* by Raisch et al. (2019). This insinuates that the 5' extended sequence on the substrate in this work was likely to be also stabilised on the yeast complex via Caf40 and that would agree with the observations made by Raisch et al. (2019) who tested an RNA substrate with the same sequence using their full-length recombinant human complex. Interestingly, the *S. pombe* complex (Webster et al., 2019) also included the Caf40 ortholog Rcd1 but did not demonstrate the enhanced activity alone yet needed a Puf3 protein additionally (Figure 49).

Another common observation in the human complex was that the degradation carried on roughly four bases (AAAU) beyond the last consecutive Poly(A) bases, from A0 (CACAUCCAACUUCUCUAAAU) to A-4 (CACAUCCAACUUCUCU), showing two catalytic products on the gel (Figure 39 , Figure 40 and Figure 49B). While both nucleases have a strong preference for Poly(A) sequence in a 3' to 5' exonucleolytic reaction, Caf1 has a broader specificity at digesting non-A bases, especially in the yeast than in the human (Niinuma et al., 2016, Bianchin et al., 2005, Thore et al., 2003). This implies that a putative intrinsic cooperation is in place between the two nucleases where Ccr4-Not mediated deadenylation is both Poly(A) specific and could also tolerate short Non-A bases to some extent given that an upstream Poly(A) segment is present (Niinuma et al., 2016). Taken together, this rationalises the observation in the yeast assay here where both A0 and A-4 products also began to diminish within several minutes after the full-length substrate depleted (Figure 40). Therefore, the remaining substrate was assumed to be eventually degraded by the less sequence specific yeast complex. The human complex, which is perhaps more fine-tuned, terminated right after the last

consecutive adenosines (Raisch et al., 2019). Such observation would agree with the proposed conformational recognition of Poly(A) tail junction by Caf1 based on the unique helical structure of a single stranded Poly(A) sequence that marked the limit to deadenylation (Tang et al., 2019). Meanwhile, the accumulation of intermediate A0 product also suggests that the nucleases were retarded briefly before continuing from where the optimal Poly(A) nucleotides ended. Surprisingly, the nuclease module, when in molar excess, also produced the UCU product in the reconstituted human nuclease subcomplex (Raisch et al., 2019), which implied that the formation of the A-4 product could have marked a final degradation limit, independent of the rest of the complex and the Poly(A) tail. The *S.pombe* complex plus Puf3 adaptor also showed this continuation after the end of Poly(A) tail sequence digestion but without any delay i.e. no A0 accumulation (Figure 49A). Therefore, complicating the anchoring hypothesis mentioned above by showing a possible differential activity between the putative extrinsic and intrinsic anchoring mode during deadenylation. Those discrepancies from *in vitro* deadenylation assays could be further investigated, preferably also with *in vivo* observations, or with longer, more natural substrates using the endogenous full-length Ccr4-Not complex.

Overall, the accelerated deadenylation was most prominent between the full-length complex and substrates containing a putative recognition element or a 5' extended motif to the Poly(A) tail, while the nuclease module alone showed a deficient nucleolytic activity in comparable conditions (Raisch et. al., 2019). The use of the non-stabilised, i.e. high dissociation rate substrates typically showed delayed appearance of the reaction products and a non-processivity in equimolar reactions (Raisch et. al., 2019 and Webster et. al., 2019) which means that the RNA substrate is perhaps most efficiently processed if localised in proximity to the nuclease subunits. The Ccr4-Not complex is well-known to be involved with extrinsic RNA binding adaptors for its roles in the mRNA turnover in cells (Sgromo et al., 2017, Sgromo et al., 2018, Semotok et al., 2005, Goldstrohm et al., 2006, Goldstrohm et al., 2007, Bhandari et al., 2014b, Raisch et al., 2016, Suzuki et al., 2010, Van Etten et al., 2012). Therefore, it would be logical for such an enzymatic catalysis reaction (Fromm and Hargrove, 2012) to be influenced by the substrate binding affinity, availability (Agrawal et al., 2008), temperature, salt and divalent metal ion co-factors concentration etc.(Viswanathan et al., 2004). Conformational flexibility also did not seem to influence the nuclease activity in this set-up since the reaction products appeared in nearly the same time span when the crosslinked Ccr4-Not was tested in parallel with the native complex. (Figure 41). This may be due to the relatively close proximity of the subunits (Basquin et al., 2012) and a sufficient length for the substrate to thread through the active site/s, but the effect of a 5' extended element (or in

general 3' UTR) length was yet to be examined in this case. For example, Not4 also has a predicted N-terminally located RRM between its E3 and Not1-binding domain (Bhaskar et al., 2015) which could potentially interact with a longer 3' UTR sequence. The endogenous *S. cerevisiae* core complex *in vitro* was capable of rapidly deadenylating the RNA substrate without additional proteins, in a similar fashion to the recombinant human counterpart. Such behaviour of this complex is worth more attention on a potentially less known intrinsic means of regulating the rate of reaction and the substrate selectivity during the mRNA deadenylation, either in generic turnover or during a response to specific cellular signals.

It was also noticed that this *S. cerevisiae* complex does not produce any intermediates between the intact substrate and the digested products on the gel (would be seen as ensuing bands of decreasing nucleotide length, this is different from the occasional faint non-specific hydrolytic degradation bands seen in the negative control lanes). This elicited an interesting question and hypothesis that the complex might function both as an endonuclease and an exonuclease, given the assumption that other nuclease contamination could be ruled out as much as possible by using 0.2micron syringe filtered, double autoclaved reaction buffer/water and the sample complex had also been freshly isolated through gel filtration or density gradient separation. Judging from the high activity, the amount of random nucleases co-purified or contaminating in the sample must have shown up as a unique protein band/s on the SDS-PAGE gel but this was not observed and mass spectrometry result also did not identify any visible bands as a known nuclease in the yeast genome. As illustrated below, the proposed models of Ccr4-Not deadenylation (Figure 50) are based on the observations from the recombinant *S.pombe complex* (Webster et al., 2019), recombinant Human complex (Raisch et al., 2019) and endogenous *S. cerevisiae complex* (In this work). In the exonuclease only model, both the human and the yeast complex stalled at A0 and A-4(UCU in Raisch et al., 2019), but human complex terminated thereafter and very likely that the remainder substrate was not released or had extremely slow dissociation because no further degradation product was seen, at least at the end of the time-course (Figure 49B). In contrary, the stalled nuclease/s could continue degrading the substrate once the precursor/product was depleted (Figure 40) and apparently slowed down since degradation bands can be seen underneath and in a non-processive manner. In the endonuclease/exonuclease model, the first excision could have been made at the end of the Poly(A) sequence that produced the band at A0 (20bp in length) from the initial A25 (45bp in length) band directly. Then, either a progressive 3' to 5' degradation or a second cut was made at the boundary of the putative binding sequence (UCU in green) that resulted in the A-4 product (~16bp in length). The bound motif was then likely to be released and continued

degradation but at a slower speed, probably because of the Poly(A) sequence preference in the nucleases and a lack of stabilisation site.

These interesting and unexpected observations would certainly invoke further investigations in respect to these inferred models. For example, what determines the release of the deadenylated substrate in both cases and if any, the non-release of the substrate from the human complex? Alternatively, whether the tentative endonuclease excisions require sequence specificity or conformational specificity (Tang et al., 2019) and the subunit or sequence motif that is involved could also be given some attention. Future works following these directions may help to better understand the differences in the deadenylation rate and the mechanisms among the Ccr4-Not complexes for these three different species of eukaryotic organisms.

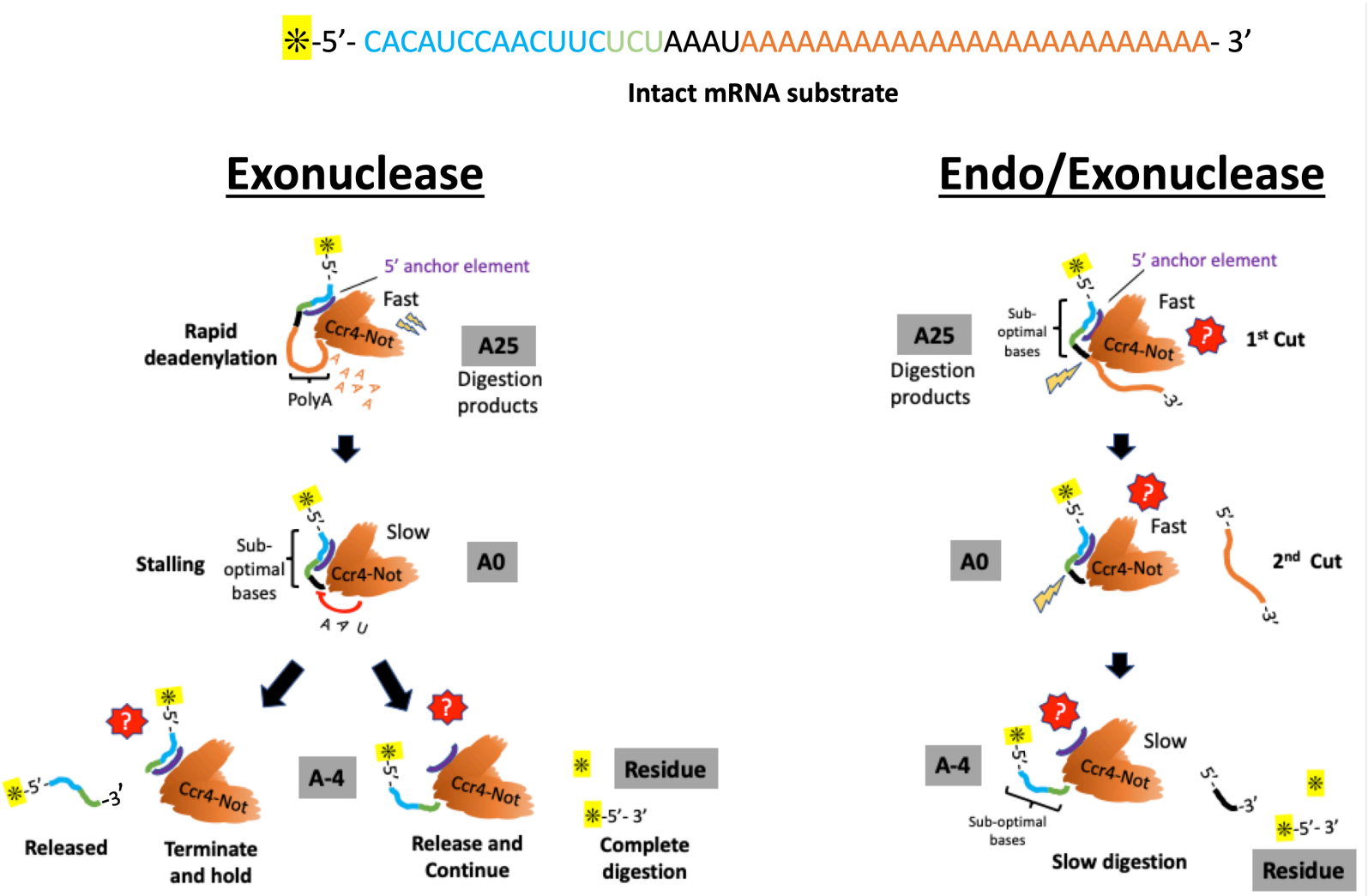

Figure 50 Proposed models for mRNA degradation by the Ccr4-Not complex. Left: Exonuclease only mode, where both nucleases follow the consensus 3'-5' exonuclease activity with a preference to Poly(A) (Collart, 2016). Right: Endo/Exonuclease mode, where no intermediate substrate is observed, and mRNA is cut twice to give rise to the observed product length before the remainder is fully digested in a 3' -5' manner. Yellow asterisk represents 5'-FAM fluorescein and only RNA with the 5' label intact is visible on the gel.

5.6 Ubiquitination activity of the purified complex

The Not4-mediated ubiquitination targets several proteins involved in the transcription, translational quality control and in the proteasomal degradation (Dimitrova et al., 2009, Panasenko and Collart, 2011, Panasenko and Collart, 2012, Panasenko et al., 2006, Fu et al., 2018, Jiang et al., 2019). Despite being considered a core complex subunit in the yeast (Reviewed in (Collart and Panasenko, 2012)), its homologues in the higher eukaryotes are not stably associated with the Ccr4-Not complex and the protein functions more or less independently (Jeske et al., 2006, Lau et al., 2009). Protein sequence alignment among the yeast, human and mouse Not4 suggested that the higher eukaryotes lacked the Not-interacting-domain (NID) at the C-terminal end but the N-terminal RING and RRM domains remain conserved (Appendix §8.3 c). The Not4 E3 ligase in the purified yeast complex here is active and showed auto-ubiquitination *in vitro* in the presence of a recombinant human E1 (Uba1-C terminal), yeast E2 (Ubc4) and the purified Ccr4-Not complex (Figure 42, right) which is consistent with a previous observation (Mulder et al., 2007b). However, the recombinant Not4 in another *in vitro* assay would not auto-ubiquitinate in the presence of its downstream target, Rpt5 (Fu et. al., 2018). In the budding yeast, Not4 mono-ubiquitination of the ribosomal subunit eS7 is a prerequisite for the Not5-dependent codon optimality monitoring and transcript decay by the linked Ccr4-Not complex (Buschauer et al., 2020). Therefore, the presence of a cognate downstream target should be essential for the functions of Not4 (Buschauer et al., 2020), and the Not4 might also be self-regulating in this context as this is also a common feature found in many E3 ubiquitin ligases (Deshaies and Joazeiro, 2009, Metzger et al., 2014, Bourgeois-Daigneault and Thibodeau, 2012).

However, the attempt to validate the Not4 auto-ubiquitination by western blot using the anti-FLAG antibody was not so informative as non-specific western blot signals in both the sample and negative control lanes were present (Figure 42, Middle). Thus, using antibodies specifically against the individual subunits of the complex or a mass spectrometry analysis would have been better to determine the exact protein/s being ubiquitinated. Mass spectrometry can also identify the location and pattern of the ubiquitination as such information can give more insights to the function of Not4 here. Meanwhile, conformational flexibility of the complex did not appear to have obvious effects on the ubiquitination reaction either, since the crosslinked complex showed similar patterns of ubiquitination on the western blot too (Appendix §8.4). Therefore, the ubiquitination of another protein besides Not4 in this assay

would have involved intermolecular ubiquitination between the complexes because previous structural data implied that the ligase is not likely to act on the NOT module subunits in *cis* (Xu et al., 2014). Nevertheless, it will be interesting to identify the ubiquitination sites and the chain patterns on the ubiquitinated proteins in this reaction, since Caf1(CNOT6L) ubiquitination dependent deadenylation had been reported in the human but involves another E3 ligase (Cano et al., 2015). This may help to reveal the underlying roles that Not4 plays in concert with the Ccr4-Not complex too.

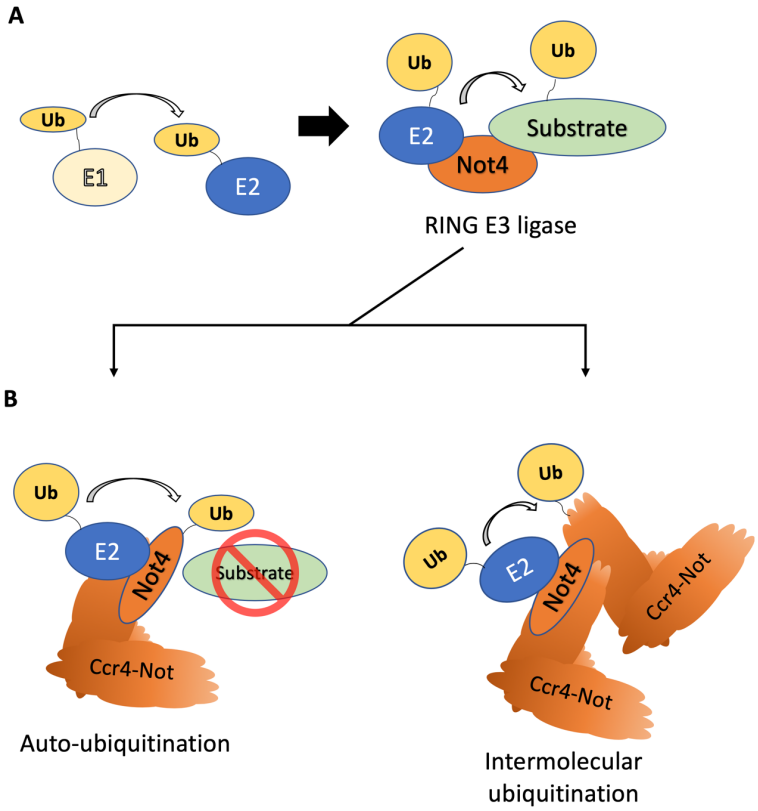

Figure 51 Illustration of ubiquitination by Not4 in vitro. A) Cartoon showing the transfer of ubiquitin substrate from the cognate E1, E2 and E3 in the RING ligase pathway. B) Left: Not4 might undergo self-ubiquitination in the absence of a substrate *in vitro. Right: Crosslinked Ccr4-Not complex might ubiquitinate another protein in the nearby molecule.*

5.7 The Ccr4-Not complex in negative stain TEM

Negative staining TEM for particulate biological specimen with Uranyl acetate (UA) solution (van Bruggen et al., 1960) is used here to contrast the protein particles adsorbed to a continuous carbon support layer on the EM grid. This method generates a reverse silhouette of the protein particles that reveals their morphological shapes, average sizes and arrangements. Although it is a widely used heavy metal salt stain in TEM and has an intrinsic fixative effect that can help to stabilise biological samples (Zhao and Craig, 2003, Silva et al., 1968), the preparation procedure subjects the protein sample to changes in ion concentration, pH, and to dehydration and flattening that could potentially produce structural artefacts (Reviewed in (De Carlo and Harris, 2011)). UA in this case, was used mainly for rapid determination of the sample quality between batches of purification (Figure 30 and Figure 43). For micrographs with a homogeneous particle distribution and even staining, 2D classification can be performed on the extracted particle images (Figure 43). The 2D classes showed a roughly L-shaped particle with a diagonal length of approximately 18nm and the particles appeared to have shorter arms on each end of the scaffold protein and are overall smaller compared to the other *S. cerevisiae* structure (Both are endogenously purified and Grafixed). This is somehow but consistent with the dimensions of another EM structure from *S. pombe* (≈540kDa) but not with the *S. cerevisiae* (≈700kDa) Ccr4-Not complex (Ukleja et al., 2016a, Nasertorabi et al., 2011). In another paper from Raisch et al., (2019) where the recombinant human complex (≈659kDa) was only shown in negative stain micrograph after Grafix, the complex particles looked very similar to this smaller *S. cerevisiae* complex (below).

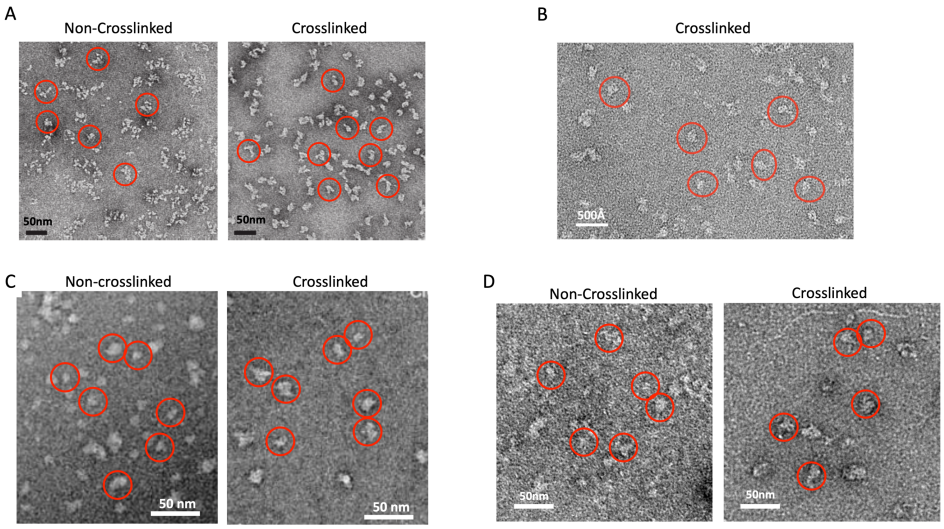

Figure 52 Comparison of negative stain EM for Ccr4-Not complex. A) Recombinant human complex, adapted from Raisch et al., 2019. B) Endogenous S. pombe complex. Adapted from Ukleja et al., 2016. Non-crosslinked sample micrograph was not available. C) Endogenous S. cerevisiae complex, adapted from Nasertorabi et al., 2011. D) Endogenous S. cerevisiae complex from this work.

A comparison of these complexes from different species and studies can also be seen in Figure 52, for the effect of crosslinking the complex after purification. Non-crosslinked particles all have high heterogeneity in their particle sizes and shapes. They are less distinctive in the micrograph compared to their fixed counterparts, and many adopted an "extended" conformation with flexible long arms or protrusions around the central density of the complex in the micrographs. This implies that the complex could have a very dynamic composition and might adopt to interchangeable conformational states constantly *in vitro*. This would however not be visible on a SDS-PAGE. Whereas the crosslinked samples were mostly very distinct particles with a more discrete morphology. This type of variations made 2D classification from the negative stain images more difficult to interpret. It was mentioned by Raisch et al. (2019) that they could not arrive at a convincing 2D class average from their samples. But such comparisons on the complex based on few micrographs can be easily over-interpreted because they are still quite preliminary and can even be simply artefacts from sample preparation e.g., due to the pH changes during staining or drying. In this work, no sensible 3D initial model could be derived from the 2D class averages too and probably due to the high conformational flexibility (Raisch et al., 2019) or interference from the large contrast variation and heterogenous grainy background across the different micrographs in the small negative stain dataset collected. Therefore the sample was less than optimal for single particle Cryo-EM, because ideally it requires the protein particles to be largely homogeneous, able to be mono-dispersed across a thin layer of ice and be in random orientations as much as possible (Cheng et al., 2015, Passmore and Russo, 2016).

The negative stain method should essentially serve to reveal the integrity and homogeneity of the purified protein complex before Cryo-grids are prepared from the same sample (Lyumkis, 2019). During the screening, samples from each purification was checked for the presence of the expected L-shaped particles of the core Ccr4-Not complex, as well as for any excessive aggregates or contaminants. Excessive aggregation would probably predict protein denaturation during the preparative steps and that buffer conditions should be further optimised. Occasionally, a very small portion of the co-purifying proteins may also include weak interaction partners, e.g. ribosomal or proteasomal subunits, due to the mild purification condition used and a plethora of functions that this complex is linked to in the cells (Stowell et al., 2016). These inclusions could further complicate interpretations of the negative stain images. Nevertheless, all previous studies (Nasertorabi et al., 2011, Raisch et al., 2016, Ukleja et al., 2016a) that showed either 3D reconstructions or simply a micrograph of the purified complexes converged on the idea that the use of Grafix method helped to stabilise the subunits

of this complex for the EM application. This reiterated the fact that the Ccr4-Not complex is inherently dynamic and may require some intervention to reduce this instability for doing Cryo-EM structural studies, especially if the native complex is examined.

Nonetheless, the negative stain method still helped visualizing the Ccr4-Not complexes in different orientations and rapidly checked for homogeneity of the purified sample therefore giving some valuable feedbacks to improve on the protein purification protocol and minimising the sample heterogeneity.

5.8 Cryo-EM of the Ccr4-Not complex and sample preparation

The method of vitrifying a purified protein in liquid ethane was developed by Dubochet et al. (Dubochet et al., 1988). It satisfies the need for preserving and supporting the protein particles within a thin film of ice/buffer in a hydrated, near-native environment when inserted into the high vacuum of the microscope (Cheng et al., 2015). In contrast to negative staining, the protein solution is subtended within numerous uniformly sized holes on a carbon layer by forming a thin film of liquid after blotting with a filter paper (Passmore and Russo, 2016). The thickness of this thin film of buffer as well as its coverage across the holey carbon layer in each grid square is crucial for the integrity and distribution of the particles during sample preparation, and consequently, the resolution too (Dobro et al., 2010). After establishing a successful purification protocol that can routinely purify the Baker's yeast Ccr4-Not complex in ample amount (Figure 34), both the native and crosslinked protein samples were screened extensively by Cryo-EM.

Holding the previous assumption that the mild purification condition used could have given rise to a spectrum of compositionally heterogenous subcomplex of the Ccr4-Not complex, additional stabilisation and separation step such as the Grafix method (Kastner et al., 2008a) was applied. Ideally, the larger 9-subunit complete core complex (Chen et al., 2001) could be isolated as well-separated and stable assemblies suitable for the single particle analysis in Cryo-EM. Grafix isolated complex particles in the negative staining micrographs showed better homogeneity than the native complex but the estimated average particle diameter was slightly shorter compared to the previous EM structure of the same complex (Nasertorabi et al., 2011). Its morphology somehow resembles better to another EM structure of the Ccr4-Not complex obtained from *Schizosaccharomyces pombe* (Ukleja et al., 2016a) in terms of shape and sizes. The *S. pombe* complex is smaller (540kDa) than the *S. cerevisiae* complex (700kDa in Nasertorabi et al., 2011, though estimated in this work was at ≈900kDa (Figure 34), and it has

less Glutamine/Asparagine (NQ) rich regions on most of the subunits (Stowell et al., 2016). Such region can cause the complex to be less stable during the purification as they are often represented as disordered, aggregation-prone sequence regions in other proteins (Michelitsch and Weissman, 2000). However, this could not explain the more compact particles after Grafix since cross-linking was also used in Nasertorabi et al. (2011). The non-crosslinked native particles in Cryo-EM showed that the particles tend to disintegrate into many smaller fragments that have little visible contrast. However, the cross-linked particles also had high propensity to aggregation when vitrified and could not form a mono-dispersed particle layer in the ice. This type of aggregation could have been partially due to the polymeric nature of the glutaraldehyde crosslinker interacting with the disordered regions on these subunits and causing intermolecular crosslinking unintentionally.

On the other hand, both the crosslinked and the native complexes could be observed as intact particles only by negative staining but not after vitrification. This observation seemed similar to the previously mentioned case of protein denaturation when the protein complex come into contact with the air/water interfaces during sample preparation (Glaeser and Han, 2017, Carragher et al., 2019). Macromolecular protein complex has a tendency to adsorb to the air/liquid interfaces, especially as the excess liquid is blotted away before vitrifying (Noble et al., 2018). The drastically reduced volume to surface area ratio of the liquid phase could lead to as much as 90% of the proteins to be adsorbed to this interface and risk denaturing when portions of the particle is constantly or repeatedly exposed to this hydrophobic interface (D'Imprima et al., 2019). Based on the diffusion rate of protein particles in solution, such particle movements can recur within a period of milliseconds, well within the time frame of the few seconds spent between sample blotting and freezing (Israelachvili, 2015). The adsorbed proteins would start to unfold due to the altered surface charge or high hydrophobic interactions and form an extended layer of aggregates spanning the interface. Some of the remaining protein particles would be excluded from contacting the interface further thus remain in solution (Glaeser and Han, 2017). The purified Ccr4-Not complex in this case might eventually have experienced such unfavourable condition during sample preparation. On top of that, the Ccr4-Not complex is structurally very dynamic as seen in the negative staining EM. Its subunits also contain long segments of unstructured regions on the surfaces (Villanyi and Collart, 2016, Ukleja et al., 2016a) supposedly because of their involvement in the nucleic acid processing (Parker and Sheth, 2007) and these are probably necessary for the complex integrity too (Raisch et al., 2019). Therefore, it explains the observed native particles here and in other studies, appearing with a fuzzy, undefined outline in the micrographs which required chemical

crosslinking to stabilise during Cryo-EM sample preparation (Ukleja et al., 2016a, Raisch et al., 2019, Nasertorabi et al., 2011). The complex *in vitro* therefore could have made many contacts with its surrounding and between themselves through these unstructured regions, and only after crosslinking the particles appeared more compact and had enough contrast in the CryoEM images. Such property could have hindered the purification of this complex especially from endogenous sources via affinity tags which also resulted in its instability as a discrete complex particle in the CryoEM.

Remedies to the protein denaturing air/water interface problem had been proposed and utilised by many (Bai et al., 2013, Dandey et al., 2018, Scapin et al., 2018, Wei et al., 2018) and with varying results. However, the technical niche involved in some of the methods practically precluded their application in this work. Hence simpler methods for modifying the thin film formation and particle spreading were tried here, such as using EM grid with an extra layer of thin amorphous carbon or graphene oxide (D'Imprima et al., 2019). Amorphous continuous carbon layer has, despite being only several nanometres thick, increased the background of the micrographs significantly and in this case did not help with the particle distribution or instability problem on the examined grids. Furthermore, it could also contribute to more beam-induced motion which further degrades any high-resolution signals (Russo and Passmore, 2014). Graphene oxide layer on the standard 400 mesh R1.2/1.3 Quantifoil grids did not rescue the native complex from denaturing too. But it improved the particle distribution for the more stable, crosslinked sample (Figure 45 vs Figure 46), at the cost of extra background. This would hinder the particle picking accuracy and subsequent processing to a certain extent. It is also necessary to point out that the controlled application of the monolayer graphene oxide is essential for such method (D'Imprima et al., 2019) but in this case it was difficult and inefficient. Many grid squares had multilayers of graphene oxide and the coverage across the holey carbon was often partially complete. It would require that a reproducible graphene oxide layering protocol to be empirically determined first and then the prepared grids can be screened for their quality by observing the distinct diffraction patterns from the monolayer graphene oxide in TEM (D'Imprima et al., 2019) before actual sample is applied.

Alternatively, it seemed sensible to also vary the ice thickness and blotting parameters, such as the blot force, blot time and ambient temperatures (Passmore and Russo, 2016), since the crosslinked sample was more or less stable even without extra carbon support. Indeed, thicker ice layer could accommodate the crosslinked complex particles better as shown in a representative carbon hole from the screening in Figure 47. Optimisations carried out using those blotting parameters to vary the ice thickness and using different grid treatments (Figure

46) were hopeful at minimising the effect of protein denaturation at the air/water interface (D'Imprima et al., 2019) but it seemed that conventional sample preparation method could not ameliorate the denaturation problem for this particular complex. Meanwhile, Cryo-EM data collected from the replicate grids in those conditions have produced a low resolution 3D initial model which showed a related conformation but incomplete density volume compared to previous EM structures (Figure 53).

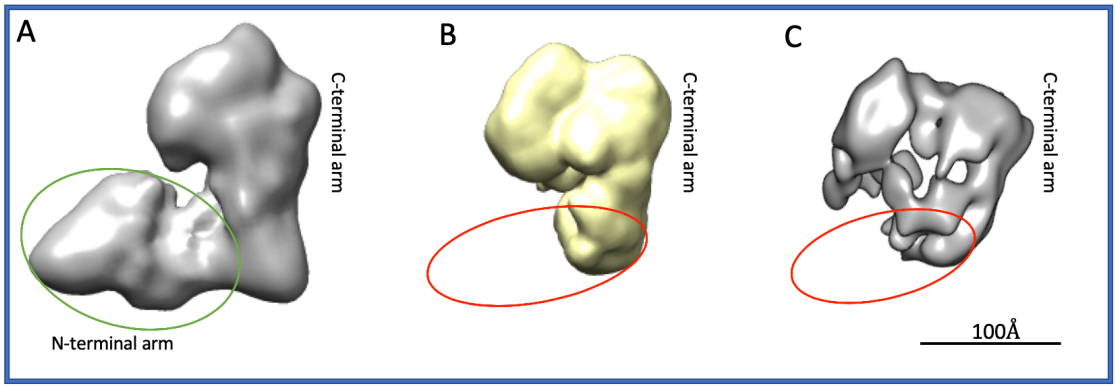

Figure 53 Comparison of Ccr4-Not EM structures. A) Negative stain EM map from S. cerevisiae crosslinked complex (Nasertorabi et al., 2011). B) Cryo-EM map from S. pombe crosslinked complex (Ukleja et al., 2016a). C) Cryo-EM map from S. cerevisiae crosslinked complex as in Figure 48.Red circles mark the putative arrangement of the two arms of the Not1 scaffold based on the morphology. Red arrow points to the indistinguishable interlinking region where the two arms could be connected. Illustrations were reproduced in Chimera software and labelling of subunits were based on the respective published papers.

Altogether, the 9-subunit *S. cerevisiae* core complex is about 809kDa theoretically, according to the online *S. cerevisiae* database (SGD) and was reported to be between 700kDa to 1MDa by different studies experimentally (Chen et al., 2001, Nasertorabi et al., 2011). In this work, the stable complex is estimated at around 900kDa according to the gel filtration retention volume (Figure 34). The *S. pombe* complex, meanwhile, has 8 subunits and is about 544kDa in theoretical mass (Ukleja et al., 2016a). The structure from Nasertorabi et al. (2011) had the N-terminal longer arms of the L-shaped Not1 scaffold for the *S. cerevisiae* complex which likely accommodated the Caf130 subunit, and the majority of the other subunits associated around the C-terminal end based on the larger EM map density (Figure 53A). In comparison, both of the other models (B and C) probably showed just the shorter C-terminal arm of the putative Not1 scaffold region and the density surrounding this scaffold is especially more tightly arranged for *S. pombe*. The overall EM densities also resembled the larger *S. cerevisiae* structure without its N-terminal region as marked by the red circles in Figure 53 B and C. The Not1 scaffold proteins in both species of yeasts have similar molecular weight and Caf130 is unique to the budding yeast. The EM density of the initial model from this work,

however, is the smallest among the three thus prompting the assumption that the N-terminal region and very likely that Not3 was missing in this density, based on the observations discussed above (§5.4.2) . Unexpectedly, the overall dimension that this model represent was apparently smaller than its estimated molecular mass on the Size exclusion chromatography which may indicate that the particle might have sustained partial damage either before or during the sample preparation (above).

Previously, it was shown that biochemically stable macromolecular complex could suffer from damage at the negatively charged and highly hydrophobic air/water interface (Glaeser, 2018) and this is not easily distinguishable from the particle spread in a top-down view in the micrographs (D'Imprima et al., 2019). The exposed regions of the complex suffering from partial damages could have resulted in a skewed or distorted structure in the reconstruction and increased the difficulties to properly interpret those density at low resolution. Meanwhile, the dynamic nature of this complex (Ukleja et al., 2016a, Raisch et al., 2019) could have also led to the representation of this one particular conformation or sub-complex, unintentionally, among many others that co-exist in the preparation *in vitro.* Indirectly, this also justifies the 2D class averages and the limited resolution for the structure in this work, as well as claimed by the others (Ukleja et al., 2016a, Raisch et al., 2019). Perhaps for this difficult complex, further optimisation on the sample preparation could help to avoid the protein adsorption at the hazardous air/water interface, including the use of detergents that can form an exclusion layer (Carragher et al., 2019). Alternatively, the sample quality could also be improved by using the recent advanced technologies in microscale sample applications (Schmidli et al., 2019) that circumvent the pit holes laid out during the thin film formation. Such as those that were also discussed by many experts in Cryo-EM (Drulyte et al., 2018, Glaeser and Han, 2017, Passmore and Russo, 2016, Russo and Passmore, 2014, Glaeser et al., 2016). Despite the unexpected hindrance in studying this native yeast complex using Cryo-EM, which behaved quite differently in both conventional purification and sample preparation procedures compared to other protein assemblies used previously (§4.1), the current results have laid out directions that future works can follow and make more stable particles that could results in much higher resolution Cryo-EM structure of this complex.

6 Conclusions and Outlook

In this study, the *S. cerevisiae* Ccr4-Not complex has been successfully purified from the endogenous source under a mild condition via immunoaffinity precipitation. The stable complex is also verified by Mass spectrometry to contain all nine subunits of the core complex. Both the deadenylation and the RING E3 ubiquitin ligase functions were also active *in vitro.* Electron microscopy has been used for the evaluation of the purification results and sample qualities, such as complex morphology, heterogeneity and integrity before the sample is prepared for high-resolution single particle Cryo-EM. One key factor in high-resolution Cryo-EM is the performance of the imaging detector and the Falcon 3EC direct electron detector used in parts of this study was also systematically evaluated for its practical use which offered helpful information for studying macromolecular complex using EM in this study.

The Ccr4-Not complex produced here displayed an enhanced activity in deadenylation of a model mRNA substrate. To further understand this underlying mechanism, it would be necessary to carry out more elaborate studies, perhaps by using different types of substrates or non-hydrolysable analogues and even by introducing mutations to key residues. The other enzymatic function via the Not4 RING E3 ligase could also be examined in further details by providing a downstream target protein and by identifying the autoubiquitination sites/patterns by Mass spectrometry. The use of electron microscopy methods also provided a good overview of the purified complex particle in both negative stain EM and Cryo-EM, where the complex is shown to be inherently dynamic in conformation and partially disordered. Such heterogeneity and structural arrangement have led to the use of methods for stabilising the complex in order to derive at a stable structural analysis from the EM data. Despite the attempts to remedy the suspected protein denaturation problem, Cryo-EM data generated from these sample have not been able to determine a high-resolution structure but only a minimal model that closely resembles the density of the same complex from other studies. Thus, future efforts could focus on sample optimisation and rescuing the complex during sample preparation, and probably to reduce the sample's numerous conformational states, so that it can be better resolved by the single particle analysis. It is apparent that the limiting factor here for getting to the high-resolution structure of this complex is the sample itself and its unexpected behaviour during Cryo-EM sample preparation. Therefore, when those issues interfering with the complex stability and distribution on the Cryo-EM grids are remedied or avoided successfully, better CryoEM data can be collected for solving a high-resolution structure of the Ccr4-Not complex.

7 Bibliography

ACHARYA, K. R. & LLOYD, M. D. 2005. The advantages and limitations of protein crystal structures. *Trends in Pharmacological Sciences,* 26**,** 10-14.

AGRAWAL, M., SANTRA, S., ANAND, R. & SWAMINATHAN, R. 2008. Effect of macromolecular crowding on the rate of diffusion-limited enzymatic reaction. *Pramana,* 71**,** 359-368.

ALBERT, T. K., HANZAWA, H., LEGTENBERG, Y. I. A., DE RUWE, M. J., VAN DEN HEUVEL, F. A. J., COLLART, M. A., BOELENS, R. & TIMMERS, H. T. M. 2002. Identification of a ubiquitin-protein ligase subunit within the CCR4-NOT transcription repressor complex. *Embo Journal,* 21**,** 355-364.

ALBERT, T. K., LEMAIRE, M., VAN BERKUM, N. L., GENTZ, R., COLLART, M. A. & TIMMERS, H. T. M. 2000. Isolation and characterization of human orthologs of yeast CCR4-NOT complex subunits. *Nucleic Acids Research,* 28**,** 809-817.

ANDERSEN, K. R., JONSTRUP, A. T., VAN, L. B. & BRODERSEN, D. E. 2009. The activity and selectivity of fission yeast Pop2p are affected by a high affinity for Zn2+ and Mn2+ in the active site. *Rna,* 15**,** 850-61.

ANDERSON, J. S. J. & PARKER, R. 1998. The 3′ to 5′ degradation of yeast mRNAs is a general mechanism for mRNA turnover that requires the SKI2 DEVH box protein and 3′ to 5′ exonucleases of the exosome complex. *The EMBO Journal,* 17**,** 1497-1506.

ASLANTAS, Y. & SURMELI, N. B. 2019. Effects of N-Terminal and C-Terminal Polyhistidine Tag on the Stability and Function of the Thermophilic P450 CYP119. *Bioinorganic Chemistry and Applications,* 2019.

BAI, X. C., FERNANDEZ, I. S., MCMULLAN, G. & SCHERES, S. H. 2013. Ribosome structures to near-atomic resolution from thirty thousand cryo-EM particles. *Elife,* 2**,** e00461.

BAI, Y. L., SALVADORE, C., CHIANG, Y. C., COLLART, M. A., LIU, H. Y. & DENIS, C. L. 1999. The CCR4 and CAF1 proteins of the CCR4-NOT complex are physically and functionally separated from NOT2, NOT4, and NOT5. *Molecular and Cellular Biology,* 19**,** 6642-6651.

BAKER, T. & HENDERSON, R. 2006. Electron cryomicroscopy of biological macromolecules. *International tables for crystallography***,** 593-614.

BARTESAGHI, A. 2015. 2.2 A resolution cryo-EM structure of [beta]-galactosidase in complex with a cell-permeant inhibitor. *Science,* 348**,** 1147-1151.

BARTESAGHI, A., AGUERREBERE, C., FALCONIERI, V., BANERJEE, S., EARL, L. A., ZHU, X., GRIGORIEFF, N., MILNE, J. L. S., SAPIRO, G., WU, X. & SUBRAMANIAM, S. 2018. Atomic Resolution Cryo-EM Structure of beta-Galactosidase. *Structure,* 26**,** 848-856.e3.

BASQUIN, J., ROUDKO, V. V., RODE, M., BASQUIN, C., SERAPHIN, B. & CONTI, E. 2012. Architecture of the Nuclease Module of the Yeast Ccr4-Not Complex: the Not1-Caf1-Ccr4 Interaction. *Molecular Cell,* 48**,** 207-218.

BATTAGLIA, M., CONTARATO, D., DENES, P., DOERING, D., GIUBILATO, P., KIM, T. S., MATTIAZZO, S., RADMILOVIC, V. & ZALUSKY, S. 2009a. A rad-hard CMOS active pixel sensor for electron microscopy. *Nuclear Instruments and Methods in Physics Research Section A: Accelerators, Spectrometers, Detectors and Associated Equipment,* 598**,** 642-649.

BATTAGLIA, M., CONTARATO, D., DENES, P. & GIUBILATO, P. 2009b. Cluster imaging with a direct detection CMOS pixel sensor in Transmission Electron Microscopy. *Nuclear Instruments and Methods in Physics Research Section A: Accelerators, Spectrometers, Detectors and Associated Equipment,* 608**,** 363-365.

BAUGHMAN, J. M., PEROCCHI, F., GIRGIS, H. S., PLOVANICH, M., BELCHER-TIMME, C. A., SANCAK, Y., BAO, X. R., STRITTMATTER, L., GOLDBERGER, O., BOGORAD, R. L., KOTELIANSKY, V. & MOOTHA, V. K. 2011. Integrative genomics identifies MCU as an essential component of the mitochondrial calcium uniporter. *Nature,* 476**,** 341-5.

BAWANKAR, P., LOH, B., WOHLBOLD, L., SCHMIDT, S. & IZAURRALDE, E. 2013. NOT10 and C2orf29/NOT11 form a conserved module of the CCR4-NOT complex that docks onto the NOT1 N-terminal domain. *Rna Biology,* 10**,** 228-244.

BHANDARI, D., RAISCH, T., WEICHENRIEDER, O., JONAS, S. & IZAURRALDE, E. 2014a. Structural basis for the Nanos-mediated recruitment of the CCR4-NOT complex and translational repression. *Genes Dev,* 28**,** 888-901.

BHANDARI, D., RAISCH, T., WEICHENRIEDER, O., JONAS, S. & IZAURRALDE, E. 2014b. Structural basis for the Nanos-mediated recruitment of the CCR4-NOT complex and translational repression. *Genes & development,* 28**,** 888-901.

BHASKAR, V., BASQUIN, J. & CONTI, E. 2015. Architecture of the Ubiquitylation Module of the Yeast Ccr4-Not Complex. *Structure,* 23**,** 921-928.

BHASKAR, V., ROUDKO, V., BASQUIN, J., SHARMA, K., URLAUB, H., SERAPHIN, B. & CONTI, E. 2013a. Structure and RNA-binding properties of the Not1-Not2-Not5 module of the yeast Ccr4-Not complex. *Nat Struct Mol Biol,* 20**,** 1281-8.

BHASKAR, V., ROUDKO, V., BASQUIN, J., SHARMA, K., URLAUB, H., SERAPHIN, B. & CONTI, E. 2013b. Structure and RNA-binding properties of the Not1-Not2Not5 module of the yeast Ccr4-Not complex. *Nature Structural & Molecular Biology,* 20**,** 1281-U207.

BIANCHIN, C., MAUXION, F., SENTIS, S., SÉRAPHIN, B. & CORBO, L. 2005. Conservation of the deadenylase activity of proteins of the Caf1 family in human. *RNA (New York, N.Y.),* 11**,** 487-494.

BOECK, R., TARUN, S., JR., RIEGER, M., DEARDORFF, J. A., MULLER-AUER, S. & SACHS, A. B. 1996. The yeast Pan2 protein is required for poly(A)-binding protein-stimulated poly(A)-nuclease activity. *J Biol Chem,* 271**,** 432-8.

BOGAERTS, J., DIERICKX, B., MEYNANTS, G. & UWAERTS, D. 2003. Total dose and displacement damage effects in a radiation-hardened CMOS APS. *IEEE Transactions on electron devices,* 50**,** 84-90.

BOLAND, A., CHEN, Y., RAISCH, T., JONAS, S., KUZUOGLU-OZTURK, D., WOHLBOLD, L., WEICHENRIEDER, O. & IZAURRALDE, E. 2013a. Structure and assembly of the NOT module of the human CCR4-NOT complex. *Nature Structural & Molecular Biology,* 20**,** 1289-U218.

BOLAND, A., CHEN, Y., RAISCH, T., JONAS, S., KUZUOĞLU-ÖZTÜRK, D., WOHLBOLD, L., WEICHENRIEDER, O. & IZAURRALDE, E. 2013b. Structure and assembly of the NOT module of the human CCR4–NOT complex. *Nat Struct Mol Biol,* 20**,** 1289-1297.

BOLOGNANI, F. & PERRONE-BIZZOZERO, N. I. 2008. RNA–protein interactions and control of mRNA stability in neurons. *Journal of Neuroscience Research,* 86**,** 481-489.

BONNEAU, F., BASQUIN, J., EBERT, J., LORENTZEN, E. & CONTI, E. 2009. The yeast exosome functions as a macromolecular cage to channel RNA substrates for degradation. *Cell,* 139**,** 547-59.

BÖTTCHER, B. & NASSAL, M. 2018. Structure of Mutant Hepatitis B Core Protein Capsids with Premature Secretion Phenotype. *Journal of molecular biology,* 430**,** 4941-4954.

BOURGEOIS-DAIGNEAULT, M.-C. & THIBODEAU, J. 2012. Autoregulation of MARCH1 expression by dimerization and autoubiquitination. *The Journal of Immunology,* 188**,** 4959-4970.

BRAUN, J. E., HUNTZINGER, E., FAUSER, M. & IZAURRALDE, E. 2011. GW182 proteins directly recruit cytoplasmic deadenylase complexes to miRNA targets. *Mol Cell,* 44**,** 120-33.

BRAUN, J. E., HUNTZINGER, E. & IZAURRALDE, E. 2013. The role of GW182 proteins in miRNA-mediated gene silencing. *Adv Exp Med Biol,* 768**,** 147-63.

BRAUN, J. E., TRUFFAULT, V., BOLAND, A., HUNTZINGER, E., CHANG, C. T., HAAS, G., WEICHENRIEDER, O., COLES, M. & IZAURRALDE, E. 2012. A direct interaction between DCP1 and XRN1 couples mRNA decapping to 5' exonucleolytic degradation. *Nat Struct Mol Biol,* 19**,** 1324-31.

BRENNER, S. & HORNE, R. W. 1959. A negative staining method for high resolution electron microscopy of viruses. *Biochim Biophys Acta,* 34**,** 103-10.

BROOKS, S. A. & BLACKSHEAR, P. J. 2013. Tristetraprolin (TTP): interactions with mRNA and proteins, and current thoughts on mechanisms of action. *Biochim Biophys Acta,* 1829**,** 666-79.

BRÜGGELLER, P. & MAYER, E. 1980. Complete vitrification in pure liquid water and dilute aqueous solutions. *Nature,* 288**,** 569-571.

BUSCHAUER, R., MATSUO, Y., SUGIYAMA, T., CHEN, Y. H., ALHUSAINI, N., SWEET, T., IKEUCHI, K., CHENG, J., MATSUKI, Y., NOBUTA, R., GILMOZZI, A., BERNINGHAUSEN, O., TESINA, P., BECKER, T., COLLER, J., INADA, T. & BECKMANN, R. 2020. The Ccr4-Not complex monitors the translating ribosome for codon optimality. *Science,* 368.

CADE, R. M. & ERREDE, B. 1994. MOT2 encodes a negative regulator of gene expression that affects basal expression of pheromone-responsive genes in Saccharomyces cerevisiae. *Mol Cell Biol,* 14**,** 3139-49.

CAMPBELL, M. G., CHENG, A., BRILOT, A. F., MOELLER, A., LYUMKIS, D., VEESLER, D., PAN, J., HARRISON, S. C., POTTER, C. S. & CARRAGHER, B. 2012. Movies of ice-embedded particles enhance resolution in electron cryo-microscopy. *Structure,* 20**,** 1823-1828.

CANO, F., RAPITEANU, R., SEBASTIAAN WINKLER, G. & LEHNER, P. J. 2015. A non-proteolytic role for ubiquitin in deadenylation of MHC-I mRNA by the RNA-binding E3-ligase MEX-3C. *Nature Communications,* 6**,** 8670.

CARRAGHER, B., CHENG, Y., FROST, A., GLAESER, R. M., LANDER, G. C., NOGALES, E. & WANG, H.-W. 2019. Current outcomes when optimizing 'standard' sample preparation for single-particle cryo-EM. *Journal of Microscopy,* 276**,** 39-45.

CHEKULAEVA, M., MATHYS, H., ZIPPRICH, J. T., ATTIG, J., COLIC, M., PARKER, R. & FILIPOWICZ, W. 2011. miRNA repression involves GW182-mediated recruitment of CCR4-NOT through conserved W-containing motifs. *Nat Struct Mol Biol,* 18**,** 1218-26.

CHEN, C. Y. & SHYU, A. B. 1995. AU-rich elements: characterization and importance in mRNA degradation. *Trends Biochem Sci,* 20**,** 465-70.

CHEN, H., SIRUPANGI, T., WU, Z.-H., JOHNSON, D. L. & LARIBEE, R. N. 2018. The conserved RNA recognition motif and C3H1 domain of the Not4 ubiquitin ligase regulate in vivo ligase function. *Scientific Reports,* 8**,** 8163.

CHEN, J. J., RAPPSILBER, J., CHIANG, Y. C., RUSSELL, P., MANN, M. & DENIS, C. L. 2001. Purification and characterization of the 1.0 MDa CCR4-NOT complex identifies two novel components of the complex. *Journal of Molecular Biology,* 314**,** 683-694.

CHEN, J. Z., SACHSE, C., XU, C., MIELKE, T., SPAHN, C. M. T. & GRIGORIEFF, N. 2008. A dose-rate effect in single-particle electron microscopy. *Journal of structural biology,* 161**,** 92-100.

CHEN, Y., BOLAND, A., KUZUOĞLU-ÖZTÜRK, D., BAWANKAR, P., LOH, B., CHANG, C.-T., WEICHENRIEDER, O. & IZAURRALDE, E. 2014a. A DDX6-CNOT1 complex and W-binding pockets in CNOT9 reveal direct links between miRNA target recognition and silencing. *Molecular cell,* 54**,** 737-750.

CHEN, Y., BOLAND, A., KUZUOGLU-OZTURK, D., BAWANKAR, P., LOH, B., CHANG, C. T., WEICHENRIEDER, O. & IZAURRALDE, E. 2014b. A DDX6-CNOT1 complex and W-binding pockets in CNOT9 reveal direct links between miRNA target recognition and silencing. *Mol Cell,* 54**,** 737-50.

CHENG, Y., GRIGORIEFF, N., PENCZEK, P. A. & WALZ, T. 2015. A primer to single-particle cryo-electron microscopy. *Cell,* 161**,** 438-449.

CHIU, W. & GLAESER, R. M. 1977. Factors affecting high resolution fixed-beam transmission electron microscopy. *Ultramicroscopy,* 2**,** 207-17.

CLARK, L. B., VISWANATHAN, P., QUIGLEY, G., CHIANG, Y. C., MCMAHON, J. S., YAO, G., CHEN, J., NELSBACH, A. & DENIS, C. L. 2004. Systematic mutagenesis of the leucine-rich repeat (LRR) domain of CCR4 reveals specific sites for binding to CAF1 and a separate critical role for the LRR in CCR4 deadenylase activity. *J Biol Chem,* 279**,** 13616-23.

COLLART, M. A. 2003. Global control of gene expression in yeast by the Ccr4-Not complex. *Gene,* 313**,** 1-16.

COLLART, M. A. 2013. The Not4 RING E3 Ligase: A Relevant Player in Cotranslational Quality Control. *ISRN Mol Biol,* 2013**,** 548359.
COLLART, M. A. 2016. The Ccr4-Not complex is a key regulator of eukaryotic gene expression. *Wiley Interdisciplinary Reviews-Rna,* 7**,** 438-454.
COLLART, M. A. & PANASENKO, O. O. 2012. The Ccr4-Not complex. *Gene,* 492**,** 42-53.
COLLART, M. A., PANASENKO, O. O. & NIKOLAEV, S. I. 2013. The Not3/5 subunit of the Ccr4-Not complex: A central regulator of gene expression that integrates signals between the cytoplasm and the nucleus in eukaryotic cells. *Cellular Signalling,* 25**,** 743-751.
COLLART, M. A. & STRUHL, K. 1994. NOT1(CDC39), NOT2(CDC36), NOT3, and NOT4 encode a global-negative regulator of transcription that differentially affects TATA-element utilization. *Genes Dev,* 8**,** 525-37.
D'IMPRIMA, E., FLORIS, D., JOPPE, M., SÁNCHEZ, R., GRININGER, M. & KÜHLBRANDT, W. 2019. Protein denaturation at the air-water interface and how to prevent it. *eLife,* 8**,** e42747.
DANDEY, V. P., WEI, H., ZHANG, Z., TAN, Y. Z., ACHARYA, P., ENG, E. T., RICE, W. J., KAHN, P. A., POTTER, C. S. & CARRAGHER, B. 2018. Spotiton: New features and applications. *J Struct Biol,* 202**,** 161-169.
DAUGERON, M.-C., MAUXION, F. & SÉRAPHIN, B. 2001. The yeast POP2 gene encodes a nuclease involved in mRNA deadenylation. *Nucleic Acids Research,* 29**,** 2448-2455.
DE CARLO, S. & HARRIS, J. R. 2011. Negative staining and cryo-negative staining of macromolecules and viruses for TEM. *Micron (Oxford, England : 1993),* 42**,** 117-131.
DE ROSIER, D. & KLUG, A. 1968. Reconstruction of three dimensional structures from electron micrographs. *Nature,* 217**,** 130-134.
DECAPRIO, J. & KOHL, T. O. 2019. Tandem Immunoaffinity Purification Using Anti-FLAG and Anti-HA Antibodies. *Cold Spring Harb Protoc,* 2019.
DENIS, C. L. 1984. Identification of new genes involved in the regulation of yeast alcohol dehydrogenase II. *Genetics,* 108**,** 833-44.
DENIS, C. L. & MALVAR, T. 1990. The CCR4 gene from Saccharomyces cerevisiae is required for both nonfermentative and spt-mediated gene expression. *Genetics,* 124**,** 283-91.
DESHAIES, R. J. & JOAZEIRO, C. A. P. 2009. RING Domain E3 Ubiquitin Ligases. *Annual Review of Biochemistry,* 78**,** 399-434.
DIMITROVA, L. N., KUROHA, K., TATEMATSU, T. & INADA, T. 2009. Nascent Peptide-dependent Translation Arrest Leads to Not4p-mediated Protein Degradation by the Proteasome. *Journal of Biological Chemistry,* 284**,** 10343-10352.
DLAKIĆ, M. 2000. Functionally unrelated signalling proteins contain a fold similar to Mg2+-dependent endonucleases. *Trends in biochemical sciences,* 25**,** 272-273.
DOBRO, M. J., MELANSON, L. A., JENSEN, G. J. & MCDOWALL, A. W. 2010. Plunge freezing for electron cryomicroscopy. *Methods Enzymol,* 481**,** 63-82.
DOIDGE, R., MITTAL, S., ASLAM, A. & WINKLER, G. S. 2012. Deadenylation of cytoplasmic mRNA by the mammalian Ccr4-Not complex. *Biochem Soc Trans,* 40**,** 896-901.
DOMA, M. K. & PARKER, R. 2007. RNA quality control in eukaryotes. *Cell,* 131**,** 660-8.
DRAPER, M. P., LIU, H. Y., NELSBACH, A. H., MOSLEY, S. P. & DENIS, C. L. 1994. CCR4 is a glucose-regulated transcription factor whose leucine-rich repeat binds several proteins important for placing CCR4 in its proper promoter context. *Molecular and Cellular Biology,* 14**,** 4522.
DRULYTE, I., JOHNSON, R. M., HESKETH, E. L., HURDISS, D. L., SCARFF, C. A., PORAV, S. A., RANSON, N. A., MUENCH, S. P. & THOMPSON, R. F. 2018. Approaches to altering particle distributions in cryo-electron microscopy sample preparation. *Acta Crystallogr D Struct Biol,* 74**,** 560-571.
DUBOCHET, J., ADRIAN, M., CHANG, J. J., HOMO, J. C., LEPAULT, J., MCDOWALL, A. W. & SCHULTZ, P. 1988. Cryo-electron microscopy of vitrified specimens. *Q Rev Biophys,* 21**,** 129-228.
DUBOCHET, J. & MCDOWALL, A. W. 1981. VITRIFICATION OF PURE WATER FOR ELECTRON MICROSCOPY. *Journal of Microscopy,* 124**,** 3-4.

DUONG-LY, K. C. & GABELLI, S. B. 2014. Salting out of proteins using ammonium sulfate precipitation. *Methods in enzymology.* Elsevier.
EINHAUER, A. & JUNGBAUER, A. 2001a. Affinity of the monoclonal antibody M1 directed against the FLAG peptide. *J Chromatogr A,* 921**,** 25-30.
EINHAUER, A. & JUNGBAUER, A. 2001b. The FLAG™ peptide, a versatile fusion tag for the purification of recombinant proteins. *Journal of Biochemical and Biophysical Methods,* 49**,** 455-465.
ELMLUND, D. & ELMLUND, H. 2012. SIMPLE: Software for ab initio reconstruction of heterogeneous single-particles. *Journal of structural biology,* 180**,** 420-427.
ERICKSON, H. & KLUG, A. 1971. Measurement and compensation of defocusing and aberrations by Fourier processing of electron micrographs. *Philosophical Transactions of the Royal Society of London. B, Biological Sciences,* 261**,** 105-118.
ERICKSON, H. P., KLUG, A., HUXLEY, H. E. & KLUG, A. 1971. Measurement and compensation of defocusing and aberrations by Fourier processing of electron micrographs. *Philosophical Transactions of the Royal Society of London. B, Biological Sciences,* 261**,** 105-118.
FABIAN, M. R., CIEPLAK, M. K., FRANK, F., MORITA, M., GREEN, J., SRIKUMAR, T., NAGAR, B., YAMAMOTO, T., RAUGHT, B., DUCHAINE, T. F. & SONENBERG, N. 2011. miRNA-mediated deadenylation is orchestrated by GW182 through two conserved motifs that interact with CCR4-NOT. *Nat Struct Mol Biol,* 18**,** 1211-7.
FABIAN, M. R., FRANK, F., ROUYA, C., SIDDIQUI, N., LAI, W. S., KARETNIKOV, A., BLACKSHEAR, P. J., NAGAR, B. & SONENBERG, N. 2013a. Structural basis for the recruitment of the human CCR4-NOT deadenylase complex by tristetraprolin. *Nat Struct Mol Biol,* 20**,** 735-9.
FABIAN, M. R., FRANK, F., ROUYA, C., SIDDIQUI, N., LAI, W. S., KARETNIKOV, A., BLACKSHEAR, P. J., NAGAR, B. & SONENBERG, N. 2013b. Structural basis for the recruitment of the human CCR4-NOT deadenylase complex by tristetraprolin. *Nature Structural & Molecular Biology,* 20**,** 735-+.
FABIAN, M. R., MATHONNET, G., SUNDERMEIER, T., MATHYS, H., ZIPPRICH, J. T., SVITKIN, Y. V., RIVAS, F., JINEK, M., WOHLSCHLEGEL, J., DOUDNA, J. A., CHEN, C. Y., SHYU, A. B., YATES, J. R., 3RD, HANNON, G. J., FILIPOWICZ, W., DUCHAINE, T. F. & SONENBERG, N. 2009. Mammalian miRNA RISC recruits CAF1 and PABP to affect PABP-dependent deadenylation. *Mol Cell,* 35**,** 868-80.
FABIAN, M. R. & SONENBERG, N. 2012. The mechanics of miRNA-mediated gene silencing: a look under the hood of miRISC. *Nature Structural & Molecular Biology,* 19**,** 586-593.
FÄRBER, V., ERBEN, E., SHARMA, S., STOECKLIN, G. & CLAYTON, C. 2012. Trypanosome CNOT10 is essential for the integrity of the NOT deadenylase complex and for degradation of many mRNAs. *Nucleic Acids Research,* 41**,** 1211-1222.
FARUQI, A. R. & HENDERSON, R. 2007. Electronic detectors for electron microscopy. *Curr Opin Struct Biol,* 17**,** 549-55.
FARUQI, A. R., HENDERSON, R. & MCMULLAN, G. 2015. Chapter Two - Progress and Development of Direct Detectors for Electron Cryomicroscopy. *In:* HAWKES, P. W. (ed.) *Advances in Imaging and Electron Physics.* Elsevier.
FARUQI, A. R. & MCMULLAN, G. 2018. Direct imaging detectors for electron microscopy. *Nuclear Instruments and Methods in Physics Research Section A: Accelerators, Spectrometers, Detectors and Associated Equipment,* 878**,** 180-190.
FICA, S. M. & NAGAI, K. 2017. Cryo-electron microscopy snapshots of the spliceosome: structural insights into a dynamic ribonucleoprotein machine. *Nature Structural & Molecular Biology,* 24**,** 791-799.
FILIPOWICZ, W. & SONENBERG, N. 2015. The long unfinished march towards understanding microRNA-mediated repression. *Rna,* 21**,** 519-24.
FRANK, J. 1975. Averaging of low exposure electron micrographs of non-periodic objects. *Ultramicroscopy,* 1**,** 159-162.
FROMM, H. J. & HARGROVE, M. 2012. Essentials of biochemistry. Berlin ; New York: Springer.

FROMM, S. A., BHARAT, T. A. M., JAKOBI, A. J., HAGEN, W. J. H. & SACHSE, C. 2015. Seeing tobacco mosaic virus through direct electron detectors. *Journal of structural biology,* 189**,** 87-97.

FROMM, S. A., TRUFFAULT, V., KAMENZ, J., BRAUN, J. E., HOFFMANN, N. A., IZAURRALDE, E. & SPRANGERS, R. 2012. The structural basis of Edc3- and Scd6-mediated activation of the Dcp1:Dcp2 mRNA decapping complex. *The EMBO Journal,* 31**,** 279-290.

FU, X., SOKOLOVA, V., WEBB, K. J., OLD, W. & PARK, S. 2018. Ubiquitin-dependent switch during assembly of the proteasomal ATPases mediated by Not4 ubiquitin ligase. *Proceedings of the National Academy of Sciences,* 115**,** 13246.

FUNAKOSHI, Y., DOI, Y., HOSODA, N., UCHIDA, N., OSAWA, M., SHIMADA, I., TSUJIMOTO, M., SUZUKI, T., KATADA, T. & HOSHINO, S.-I. 2007. Mechanism of mRNA deadenylation: evidence for a molecular interplay between translation termination factor eRF3 and mRNA deadenylases. *Genes & development,* 21**,** 3135-3148.

GARCES, R. G., GILLON, W. & PAI, E. F. 2007. Atomic model of human Rcd-1 reveals an armadillo-like-repeat protein with in vitro nucleic acid binding properties. *Protein Science,* 16**,** 176-188.

GERACE, E. & MOAZED, D. 2015a. Affinity Pull-Down of Proteins Using Anti-FLAG M2 Agarose Beads. *Methods in enzymology,* 559**,** 99-110.

GERACE, E. & MOAZED, D. 2015b. Affinity Purification of Protein Complexes Using TAP Tags. *Methods in enzymology,* 559**,** 37-52.

GIEGE, R., LORBER, B., EBEL, J. P., MORAS, D., THIERRY, J. C., JACROT, B. & ZACCAI, G. 1982. Formation of a catalytically active complex between tRNAAsp and aspartyl-tRNA synthetase from yeast in high concentrations of ammonium sulphate. *Biochimie,* 64**,** 357-62.

GLAESER, R. M. 2018. PROTEINS, INTERFACES, AND CRYO-EM GRIDS. *Curr Opin Colloid Interface Sci,* 34**,** 1-8.

GLAESER, ROBERT M., HAN, B.-G., CSENCSITS, R., KILLILEA, A., PULK, A. & CATE, JAMIE H. D. 2016. Factors that Influence the Formation and Stability of Thin, Cryo-EM Specimens. *Biophysical Journal,* 110**,** 749-755.

GLAESER, R. M. & HAN, B. G. 2017. Opinion: hazards faced by macromolecules when confined to thin aqueous films. *Biophys Rep,* 3**,** 1-7.

GOLDSTROHM, A. C., HOOK, B. A., SEAY, D. J. & WICKENS, M. 2006. PUF proteins bind Pop2p to regulate messenger RNAs. *Nature Structural & Molecular Biology,* 13**,** 533-539.

GOLDSTROHM, A. C., SEAY, D. J., HOOK, B. A. & WICKENS, M. 2007. PUF protein-mediated deadenylation is catalyzed by Ccr4p. *J Biol Chem,* 282**,** 109-14.

GRANT, T., ROHOU, A. & GRIGORIEFF, N. 2018. cisTEM, user-friendly software for single-particle image processing. *eLife,* 7**,** e35383.

GRIMM, C., HILLEN, H. S., BEDENK, K., BARTULI, J., NEYER, S., ZHANG, Q., HÜTTENHOFER, A., ERLACHER, M., DIENEMANN, C., SCHLOSSER, A., URLAUB, H., BÖTTCHER, B., SZALAY, A. A., CRAMER, P. & FISCHER, U. 2019. Structural Basis of Poxvirus Transcription: Vaccinia RNA Polymerase Complexes. *Cell,* 179**,** 1537-1550.e19.

HALBACH, F., REICHELT, P., RODE, M. & CONTI, E. 2013. The yeast ski complex: crystal structure and RNA channeling to the exosome complex. *Cell,* 154**,** 814-26.

HALTER, D., COLLART, M. A. & PANASENKO, O. O. 2014. The Not4 E3 Ligase and CCR4 Deadenylase Play Distinct Roles in Protein Quality Control. *PLOS ONE,* 9**,** e86218.

HANZAWA, H., DE RUWE, M. J., ALBERT, T. K., VAN DER VLIET, P. C., TIMMERS, H. T. & BOELENS, R. 2001. The structure of the C4C4 ring finger of human NOT4 reveals features distinct from those of C3HC4 RING fingers. *J Biol Chem,* 276**,** 10185-90.

HEIN, M. Y., HUBNER, N. C., POSER, I., COX, J., NAGARAJ, N., TOYODA, Y., GAK, I. A., WEISSWANGE, I., MANSFELD, J., BUCHHOLZ, F., HYMAN, A. A. & MANN, M. 2015. A human interactome in three quantitative dimensions organized by stoichiometries and abundances. *Cell,* 163**,** 712-23.

HENDERSON, R. 1995. The potential and limitations of neutrons, electrons and X-rays for atomic resolution microscopy of unstained biological molecules. *Q Rev Biophys,* 28**,** 171-93.

HERZIK, M. A., WU, M. & LANDER, G. C. 2019. High-resolution structure determination of sub-100 kDa complexes using conventional cryo-EM. *Nature Communications,* 10**,** 1032.
HIROI, N., ITO, T., YAMAMOTO, H., OCHIYA, T., JINNO, S. & OKAYAMA, H. 2002. Mammalian Rcd1 is a novel transcriptional cofactor that mediates retinoic acid-induced cell differentiation. *The EMBO Journal,* 21**,** 5235-5244.
HO, B., BARYSHNIKOVA, A. & BROWN, G. W. 2018. Unification of Protein Abundance Datasets Yields a Quantitative Saccharomyces cerevisiae Proteome. *Cell Syst,* 6**,** 192-205.e3.
HOUSELEY, J. & TOLLERVEY, D. 2009. The many pathways of RNA degradation. *Cell,* 136**,** 763-76.
HU, W., SWEET, T. J., CHAMNONGPOL, S., BAKER, K. E. & COLLER, J. 2009. Co-translational mRNA decay in Saccharomyces cerevisiae. *Nature,* 461**,** 225-229.
HUNTZINGER, E., BRAUN, J. E., HEIMSTÄDT, S., ZEKRI, L. & IZAURRALDE, E. 2010. Two PABPC1-binding sites in GW182 proteins promote miRNA-mediated gene silencing. *The EMBO journal,* 29**,** 4146-4160.
HUNTZINGER, E. & IZAURRALDE, E. 2011. Gene silencing by microRNAs: contributions of translational repression and mRNA decay. *Nature Reviews Genetics,* 12**,** 99-110.
INADA, T. & AIBA, H. 2005. Translation of aberrant mRNAs lacking a termination codon or with a shortened 3'-UTR is repressed after initiation in yeast. *Embo j,* 24**,** 1584-95.
INADA, T. & MAKINO, S. 2014. Novel roles of the multi-functional CCR4-NOT complex in post-transcriptional regulation. *Frontiers in genetics,* 5**,** 135-135.
ISRAELACHVILI, J. N. 2015. *Intermolecular and surface forces*, Academic press.
JAENISCH, R. & BIRD, A. 2003. Epigenetic regulation of gene expression: how the genome integrates intrinsic and environmental signals. *Nature Genetics,* 33**,** 245-254.
JAMES, G. T. 1978. Inactivation of the protease inhibitor phenylmethylsulfonyl fluoride in buffers. *Analytical Biochemistry,* 86**,** 574-579.
JANUSZYK, K. & LIMA, C. D. 2014. The eukaryotic RNA exosome. *Curr Opin Struct Biol,* 24**,** 132-40.
JESKE, M., MEYER, S., TEMME, C., FREUDENREICH, D. & WAHLE, E. 2006. Rapid ATP-dependent deadenylation of nanos mRNA in a cell-free system from Drosophila embryos. *Journal of Biological Chemistry,* 281**,** 25124-25133.
JIANG, H., WOLGAST, M., BEEBE, L. M. & REESE, J. C. 2019. Ccr4–Not maintains genomic integrity by controlling the ubiquitylation and degradation of arrested RNAPII. *Genes & development,* 33**,** 705-717.
JONSTRUP, A. T., ANDERSEN, K. R., VAN, L. B. & BRODERSEN, D. E. 2007. The 1.4-A crystal structure of the S. pombe Pop2p deadenylase subunit unveils the configuration of an active enzyme. *Nucleic acids research,* 35**,** 3153-3164.
KADYROVA, L. Y., HABARA, Y., LEE, T. H. & WHARTON, R. P. 2007a. Translational control of maternal Cyclin B mRNA by Nanos in the Drosophila germline. *Development,* 134**,** 1519.
KADYROVA, L. Y., HABARA, Y., LEE, T. H. & WHARTON, R. P. 2007b. Translational control of maternal Cyclin B mRNA by Nanos in the Drosophila germline. *Development,* 134**,** 1519-1527.
KAMATH, R. S. & AHRINGER, J. 2003. Genome-wide RNAi screening in Caenorhabditis elegans. *Methods,* 30**,** 313-321.
KASTNER, B., FISCHER, N., GOLAS, M. M., SANDER, B., DUBE, P., BOEHRINGER, D., HARTMUTH, K., DECKERT, J., HAUER, F. & WOLF, E. 2008a. GraFix: sample preparation for single-particle electron cryomicroscopy. *Nature methods,* 5**,** 53-55.
KASTNER, B., FISCHER, N., GOLAS, M. M., SANDER, B., DUBE, P., BOEHRINGER, D., HARTMUTH, K., DECKERT, J., HAUER, F., WOLF, E., UCHTENHAGEN, H., URLAUB, H., HERZOG, F., PETERS, J. M., POERSCHKE, D., LUHRMANN, R. & STARK, H. 2008b. GraFix: sample preparation for single-particle electron cryomicroscopy. *Nat Methods,* 5**,** 53-5.
KERVESTIN, S. & JACOBSON, A. 2012. NMD: a multifaceted response to premature translational termination. *Nat Rev Mol Cell Biol,* 13**,** 700-12.

KESKENY, C., RAISCH, T., SGROMO, A., IGREJA, C., BHANDARI, D., WEICHENRIEDER, O. & IZAURRALDE, E. 2019. A conserved CAF40-binding motif in metazoan NOT4 mediates association with the CCR4-NOT complex. *Genes & development,* 33**,** 236-252.

KHMELINSKII, A., MEURER, M., DUISHOEV, N., DELHOMME, N. & KNOP, M. 2011. Seamless gene tagging by endonuclease-driven homologous recombination. *PloS one,* 6**,** e23794-e23794.

KIMANIUS, D., FORSBERG, B. O., SCHERES, S. H. W. & LINDAHL, E. 2016. Accelerated cryo-EM structure determination with parallelisation using GPUs in RELION-2. *eLife,* 5**,** e18722.

KIMPLE, M. E., BRILL, A. L. & PASKER, R. L. 2013. Overview of affinity tags for protein purification. *Current protocols in protein science,* 73**,** 9.9.1-9.9.23.

KNOP, M., SIEGERS, K., PEREIRA, G., ZACHARIAE, W., WINSOR, B., NASMYTH, K. & SCHIEBEL, E. 1999. Epitope tagging of yeast genes using a PCR-based strategy: more tags and improved practical routines. *Yeast,* 15**,** 963-72.

KOHL, H. & REIMER, L. 2008. *Transmission electron microscopy: physics of image formation*, Springer.

KROGAN, N. J., CAGNEY, G., YU, H., ZHONG, G., GUO, X., IGNATCHENKO, A., LI, J., PU, S., DATTA, N., TIKUISIS, A. P., PUNNA, T., PEREGRÍN-ALVAREZ, J. M., SHALES, M., ZHANG, X., DAVEY, M., ROBINSON, M. D., PACCANARO, A., BRAY, J. E., SHEUNG, A., BEATTIE, B., RICHARDS, D. P., CANADIEN, V., LALEV, A., MENA, F., WONG, P., STAROSTINE, A., CANETE, M. M., VLASBLOM, J., WU, S., ORSI, C., COLLINS, S. R., CHANDRAN, S., HAW, R., RILSTONE, J. J., GANDI, K., THOMPSON, N. J., MUSSO, G., ST ONGE, P., GHANNY, S., LAM, M. H., BUTLAND, G., ALTAF-UL, A. M., KANAYA, S., SHILATIFARD, A., O'SHEA, E., WEISSMAN, J. S., INGLES, C. J., HUGHES, T. R., PARKINSON, J., GERSTEIN, M., WODAK, S. J., EMILI, A. & GREENBLATT, J. F. 2006. Global landscape of protein complexes in the yeast Saccharomyces cerevisiae. *Nature,* 440**,** 637-43.

KÜHLBRANDT, W. 2014. The Resolution Revolution. *Science,* 343**,** 1443.

KUIJPER, M., VAN HOFTEN, G., JANSSEN, B., GEURINK, R., DE CARLO, S., VOS, M., VAN DUINEN, G., VAN HAERINGEN, B. & STORMS, M. 2015. FEI's direct electron detector developments: Embarking on a revolution in cryo-TEM. *J Struct Biol,* 192**,** 179-87.

KUSHNIROV, V. V. 2000. Rapid and reliable protein extraction from yeast. *Yeast,* 16**,** 857-60.

LACAVA, J., FERNANDEZ-MARTINEZ, J., HAKHVERDYAN, Z. & ROUT, M. P. 2016. Protein Complex Purification by Affinity Capture. *Cold Spring Harb Protoc,* 2016.

LAPOINTE, C. P., WILINSKI, D., SAUNDERS, H. A. J. & WICKENS, M. 2015. Protein-RNA networks revealed through covalent RNA marks. *Nature methods,* 12**,** 1163-1170.

LARIBEE, R. N., SHIBATA, Y., MERSMAN, D. P., COLLINS, S. R., KEMMEREN, P., ROGUEV, A., WEISSMAN, J. S., BRIGGS, S. D., KROGAN, N. J. & STRAHL, B. D. 2007. CCR4/NOT complex associates with the proteasome and regulates histone methylation. *Proceedings of the National Academy of Sciences,* 104**,** 5836-5841.

LAU, N. C., KOLKMAN, A., VAN SCHAIK, F. M. A., MULDER, K. W., PIJNAPPEL, W. W. M. P., HECK, A. J. R. & TIMMERS, H. T. M. 2009. Human Ccr4-Not complexes contain variable deadenylase subunits. *Biochemical Journal,* 422**,** 443-453.

LEBERER, E., DIGNARD, D., HARCUS, D., WHITEWAY, M. & THOMAS, D. Y. 1994. Molecular characterization of SIG1, a Saccharomyces cerevisiae gene involved in negative regulation of G-protein-mediated signal transduction. *The EMBO Journal,* 13**,** 3050-3064.

LI, X., ZHENG, S. Q., EGAMI, K., AGARD, D. A. & CHENG, Y. 2013. Influence of electron dose rate on electron counting images recorded with the K2 camera. *Journal of Structural Biology,* 184**,** 251-260.

LIND, K. & NORBECK, J. 2009. A QPCR-based reporter system to study post-transcriptional regulation via the 3' untranslated region of mRNA in Saccharomyces cerevisiae. *Yeast,* 26**,** 407-13.

LIU, H., RODGERS, N. D., JIAO, X. & KILEDJIAN, M. 2002. The scavenger mRNA decapping enzyme DcpS is a member of the HIT family of pyrophosphatases. *The EMBO Journal,* 21**,** 4699-4708.

LIU, H. Y., BADARINARAYANA, V., AUDINO, D. C., RAPPSILBER, J., MANN, M. & DENIS, C. L. 1998. The NOT proteins are part of the CCR4 transcriptional complex and affect gene expression both positively and negatively. *The EMBO journal,* 17**,** 1096-1106.

LODISH, H. F. & DARNELL, J. E. 2000. Molecular cell biology. 4th ed. New York: W.H. Freeman.

LOH, B., JONAS, S. & IZAURRALDE, E. 2013. The SMG5-SMG7 heterodimer directly recruits the CCR4-NOT deadenylase complex to mRNAs containing nonsense codons via interaction with POP2. *Genes Dev,* 27**,** 2125-38.

LYUMKIS, D. 2019. Challenges and opportunities in cryo-EM single-particle analysis. *J Biol Chem,* 294**,** 5181-5197.

MAEDER, C. I., MAIER, P. & KNOP, M. 2007. 4 A Guided Tour to PCR-based Genomic Manipulations of S.cerevisiae (PCR-targeting). *In:* STANSFIELD, I. & STARK, M. J. R. (eds.) *Methods in Microbiology.* Academic Press.

MAILLET, L. & COLLART, M. A. 2002. Interaction between Not1p, a component of the Ccr4-Not complex, a global regulator of transcription, and Dhh1p, a putative RNA helicase. *Journal of Biological Chemistry,* 277**,** 2835-2842.

MAILLET, L., TU, C., HONG, Y. K., SHUSTER, E. O. & COLLART, M. A. 2000. The essential function of not1 lies within the Ccr4-Not complex. *Journal of Molecular Biology,* 303**,** 131-143.

MARYATI, M., AIRHIHEN, B. & WINKLER, G. S. 2015. The enzyme activities of Caf1 and Ccr4 are both required for deadenylation by the human Ccr4-Not nuclease module. *Biochemical Journal,* 469**,** 169-176.

MATHYS, H., BASQUIN, J., OZGUR, S., CZARNOCKI-CIECIURA, M., BONNEAU, F., AARTSE, A., DZIEMBOWSKI, A., NOWOTNY, M., CONTI, E. & FILIPOWICZ, W. 2014a. Structural and Biochemical Insights to the Role of the CCR4-NOT Complex and DDX6 ATPase in MicroRNA Repression. *Molecular Cell,* 54**,** 751-765.

MATHYS, H., BASQUIN, J., OZGUR, S., CZARNOCKI-CIECIURA, M., BONNEAU, F., AARTSE, A., DZIEMBOWSKI, A., NOWOTNY, M., CONTI, E. & FILIPOWICZ, W. 2014b. Structural and biochemical insights to the role of the CCR4-NOT complex and DDX6 ATPase in microRNA repression. *Mol Cell,* 54**,** 751-65.

MATSUDA, R., IKEUCHI, K., NOMURA, S. & INADA, T. 2014. Protein quality control systems associated with no-go and nonstop mRNA surveillance in yeast. *Genes to Cells,* 19**,** 1-12.

MAUXION, F., PREVE, B. & SERAPHIN, B. 2013. C2ORF29/CNOT11 and CNOT10 form a new module of the CCR4-NOT complex. *Rna Biology,* 10**,** 267-276.

MCINTYRE, M. E. 1997. Lucidity and science I: Writing skills and the pattern perception hypothesis. *Interdisciplinary science reviews,* 22**,** 199-216.

MCMULLAN, G., CHEN, S., HENDERSON, R. & FARUQI, A. R. 2009a. Detective quantum efficiency of electron area detectors in electron microscopy. *Ultramicroscopy,* 109**,** 1126-1143.

MCMULLAN, G., CLARK, A. T., TURCHETTA, R. & FARUQI, A. R. 2009b. Enhanced imaging in low dose electron microscopy using electron counting. *Ultramicroscopy,* 109**,** 1411-6.

MCMULLAN, G., FARUQI, A. R., CLARE, D. & HENDERSON, R. 2014. Comparison of optimal performance at 300keV of three direct electron detectors for use in low dose electron microscopy. *Ultramicroscopy,* 147**,** 156-163.

MENON, K. P., SANYAL, S., HABARA, Y., SANCHEZ, R., WHARTON, R. P., RAMASWAMI, M. & ZINN, K. 2004. The translational repressor Pumilio regulates presynaptic morphology and controls postsynaptic accumulation of translation factor eIF-4E. *Neuron,* 44**,** 663-76.

METZGER, M. B., PRUNEDA, J. N., KLEVIT, R. E. & WEISSMAN, A. M. 2014. RING-type E3 ligases: Master manipulators of E2 ubiquitin-conjugating enzymes and ubiquitination. *Biochimica et Biophysica Acta (BBA) - Molecular Cell Research,* 1843**,** 47-60.

MICHELITSCH, M. D. & WEISSMAN, J. S. 2000. A census of glutamine/asparagine-rich regions: implications for their conserved function and the prediction of novel prions. *Proc Natl Acad Sci U S A,* 97**,** 11910-5.

MILLER, J. E. & REESE, J. C. 2012. Ccr4-Not complex: the control freak of eukaryotic cells. *Critical Reviews in Biochemistry and Molecular Biology,* 47**,** 315-333.
MILLER, J. E., ZHANG, L., JIANG, H., LI, Y., PUGH, B. F. & REESE, J. C. 2018. Genome-Wide Mapping of Decay Factor-mRNA Interactions in Yeast Identifies Nutrient-Responsive Transcripts as Targets of the Deadenylase Ccr4. *G3 (Bethesda),* 8**,** 315-330.
MILLER, M. T., HIGGIN, J. J. & HALL, T. M. 2008. Basis of altered RNA-binding specificity by PUF proteins revealed by crystal structures of yeast Puf4p. *Nat Struct Mol Biol,* 15**,** 397-402.
MORITA, M., SUZUKI, T., NAKAMURA, T., YOKOYAMA, K., MIYASAKA, T. & YAMAMOTO, T. 2007. Depletion of Mammalian CCR4b Deadenylase Triggers Elevation of the p27^{Kip1} mRNA Level and Impairs Cell Growth. *Molecular and Cellular Biology,* 27**,** 4980-4990.
MULDER, K. W., BRENKMAN, A. B., INAGAKI, A., VAN DEN BROEK, N. J. F. & TIMMERS, H. T. M. 2007a. Regulation of histone H3K4 tri-methylation and PAF complex recruitment by the Ccr4-Not complex. *Nucleic Acids Research,* 35**,** 2428-2439.
MULDER, K. W., INAGAKI, A., CAMERONI, E., MOUSSON, F., WINKLER, G. S., DE VIRGILIO, C., COLLART, M. A. & TIMMERS, H. T. M. 2007b. Modulation of Ubc4p/Ubc5p-Mediated Stress Responses by the RING-Finger-Dependent Ubiquitin-Protein Ligase Not4p in <em>Saccharomyces cerevisiae</em&gt. *Genetics,* 176**,** 181.
NAMBA, K., PATTANAYEK, R. & STUBBS, G. 1989. Visualization of protein-nucleic acid interactions in a virus. Refined structure of intact tobacco mosaic virus at 2.9 A resolution by X-ray fiber diffraction. *J Mol Biol,* 208**,** 307-25.
NASERTORABI, F., BATISSE, C., DIEPHOLZ, M., SUCK, D. & BOTTCHER, B. 2011. Insights into the structure of the CCR4-NOT complex by electron microscopy. *Febs Letters,* 585**,** 2182-2186.
NEIMAN, A. M., CHANG, F., KOMACHI, K. & HERSKOWITZ, I. 1990. CDC36 and CDC39 are negative elements in the signal transduction pathway of yeast. *Cell Regul,* 1**,** 391-401.
NIINUMA, S., FUKAYA, T. & TOMARI, Y. 2016. CCR4 and CAF1 deadenylases have an intrinsic activity to remove the post-poly(A) sequence. *RNA (New York, N.Y.),* 22**,** 1550-1559.
NOBLE, A. J., DANDEY, V. P., WEI, H., BRASCH, J., CHASE, J., ACHARYA, P., TAN, Y. Z., ZHANG, Z., KIM, L. Y., SCAPIN, G., RAPP, M., ENG, E. T., RICE, W. J., CHENG, A., NEGRO, C. J., SHAPIRO, L., KWONG, P. D., JERUZALMI, D., DES GEORGES, A., POTTER, C. S. & CARRAGHER, B. 2018. Routine single particle CryoEM sample and grid characterization by tomography. *Elife,* 7.
NOGALES, E. & SCHERES, SJORS H. W. 2015. Cryo-EM: A Unique Tool for the Visualization of Macromolecular Complexity. *Molecular Cell,* 58**,** 677-689.
NOMOTO, S., NAKAYAMA, N., ARAI, K. & MATSUMOTO, K. 1990. Regulation of the yeast pheromone response pathway by G protein subunits. *The EMBO journal,* 9**,** 691-696.
OBERHOLZER, U. & COLLART, M. A. 1998. Characterization of NOT5 that encodes a new component of the Not protein complex. *Gene,* 207**,** 61-69.
OKAZAKI, N., OKAZAKI, K., WATANABE, Y., KATO-HAYASHI, M., YAMAMOTO, M. & OKAYAMA, H. 1998. Novel Factor Highly Conserved among Eukaryotes Controls Sexual Development in Fission Yeast. *Molecular and Cellular Biology,* 18**,** 887.
OLIVAS, W. & PARKER, R. 2000. The Puf3 protein is a transcript-specific regulator of mRNA degradation in yeast. *The EMBO journal,* 19**,** 6602-6611.
ORLOVA, E. V. & SAIBIL, H. R. 2011. Structural analysis of macromolecular assemblies by electron microscopy. *Chemical reviews,* 111**,** 7710-7748.
OTSUKA, H., FUKAO, A., FUNAKAMI, Y., DUNCAN, K. E. & FUJIWARA, T. 2019. Emerging Evidence of Translational Control by AU-Rich Element-Binding Proteins. *Frontiers in genetics,* 10**,** 332-332.
PANASENKO, O., LANDRIEUX, E., FEUERMANN, M., FINKA, A., PAQUET, N. & COLLART, M. A. 2006. The yeast Ccr4-not complex controls ubiquitination of the nascent-associated polypeptide (NAC-EGD) complex. *Journal of Biological Chemistry,* 281**,** 31389-31398.

PANASENKO, O. O. & COLLART, M. A. 2011. Not4 E3 Ligase Contributes to Proteasome Assembly and Functional Integrity in Part through Ecm29. *Molecular and Cellular Biology,* 31**,** 1610.
PANASENKO, O. O. & COLLART, M. A. 2012. Presence of Not5 and ubiquitinated Rps7A in polysome fractions depends upon the Not4 E3 ligase. *Molecular Microbiology,* 83**,** 640-653.
PANASENKO, O. O., DAVID, F. P. & COLLART, M. A. 2009. Ribosome association and stability of the nascent polypeptide-associated complex is dependent upon its own ubiquitination. *Genetics,* 181**,** 447-60.
PARKER, R. 2012. RNA degradation in Saccharomyces cerevisae. *Genetics,* 191**,** 671-702.
PARKER, R. & SHETH, U. 2007. P bodies and the control of mRNA translation and degradation. *Mol Cell,* 25**,** 635-46.
PASSMORE, L. A. & RUSSO, C. J. 2016. Specimen Preparation for High-Resolution Cryo-EM. *Methods Enzymol,* 579**,** 51-86.
PENCZEK, P. A. 2010. Image restoration in cryo-electron microscopy. *Methods in enzymology,* 482**,** 35-72.
PENCZEK, P. A., GRASSUCCI, R. A. & FRANK, J. 1994. The ribosome at improved resolution: new techniques for merging and orientation refinement in 3D cryo-electron microscopy of biological particles. *Ultramicroscopy,* 53**,** 251-70.
PETTERSEN, E. F., GODDARD, T. D., HUANG, C. C., COUCH, G. S., GREENBLATT, D. M., MENG, E. C. & FERRIN, T. E. 2004. UCSF Chimera--a visualization system for exploratory research and analysis. *J Comput Chem,* 25**,** 1605-12.
PIAO, X. H., ZHANG, X., WU, L. G. & BELASCO, J. G. 2010. CCR4-NOT Deadenylates mRNA Associated with RNA-Induced Silencing Complexes in Human Cells. *Molecular and Cellular Biology,* 30**,** 1486-1494.
PUIG, O., CASPARY, F., RIGAUT, G., RUTZ, B., BOUVERET, E., BRAGADO-NILSSON, E., WILM, M. & SÉRAPHIN, B. 2001. The Tandem Affinity Purification (TAP) Method: A General Procedure of Protein Complex Purification. *Methods,* 24**,** 218-229.
PUNJANI, A., RUBINSTEIN, J. L., FLEET, D. J. & BRUBAKER, M. A. 2017. cryoSPARC: algorithms for rapid unsupervised cryo-EM structure determination. *Nature Methods,* 14**,** 290-296.
RAISCH, T., BHANDARI, D., SABATH, K., HELMS, S., VALKOV, E., WEICHENRIEDER, O. & IZAURRALDE, E. 2016. Distinct modes of recruitment of the CCR4-NOT complex by Drosophila and vertebrate Nanos. *Embo Journal,* 35**,** 974-990.
RAISCH, T., CHANG, C.-T., LEVDANSKY, Y., MUTHUKUMAR, S., RAUNSER, S. & VALKOV, E. 2019. Reconstitution of recombinant human CCR4-NOT reveals molecular insights into regulated deadenylation. *Nature Communications,* 10**,** 3173.
RAISCH, T., SANDMEIR, F., WEICHENRIEDER, O., VALKOV, E. & IZAURRALDE, E. 2018. Structural and biochemical analysis of a NOT1 MIF4G-like domain of the CCR4-NOT complex. *J Struct Biol,* 204**,** 388-395.
RASMUSSEN, T., FLEGLER, V. J., RASMUSSEN, A. & BOTTCHER, B. 2019. Structure of the Mechanosensitive Channel MscS Embedded in the Membrane Bilayer. *J Mol Biol,* 431**,** 3081-3090.
REED, S. I. 1980. The Selection of S. CEREVISIAE Mutants Defective in the Start Event of Cell Division. *Genetics,* 95**,** 561-577.
REIJNS, M. A. M., ALEXANDER, R. D., SPILLER, M. P. & BEGGS, J. D. 2008. A role for Q/N-rich aggregation-prone regions in P-body localization. *Journal of Cell Science,* 121**,** 2463-2472.
REIMER, L. 1989. Specimen Damage by Electron Irradiation. *Transmission Electron Microscopy.* Berlin, Heidelberg: Springer.
RODRÍGUEZ-GIL, A., RITTER, O., SAUL, V. V., WILHELM, J., YANG, C.-Y., GROSSCHEDL, R., IMAI, Y., KUBA, K., KRACHT, M. & SCHMITZ, M. L. 2017. The CCR4-NOT complex contributes to repression of Major Histocompatibility Complex class II transcription. *Scientific Reports,* 7**,** 3547.

ROHOU, A. & GRIGORIEFF, N. 2015. CTFFIND4: Fast and accurate defocus estimation from electron micrographs. *Journal of Structural Biology,* 192**,** 216-221.
ROSENTHAL, P. B. & HENDERSON, R. 2003. Optimal determination of particle orientation, absolute hand, and contrast loss in single-particle electron cryomicroscopy. *J Mol Biol,* 333**,** 721-45.
ROSS, J. 1995. mRNA stability in mammalian cells. *Microbiol Rev,* 59**,** 423-50.
RUBINSON, E. H. & EICHMAN, B. F. 2012. Nucleic acid recognition by tandem helical repeats. *Current opinion in structural biology,* 22**,** 101-109.
RUSKIN, R. S., YU, Z. & GRIGORIEFF, N. 2013. Quantitative characterization of electron detectors for transmission electron microscopy. *Journal of Structural Biology,* 184**,** 385-393.
RUSSO, C. J. & PASSMORE, L. A. 2014. Controlling protein adsorption on graphene for cryo-EM using low-energy hydrogen plasmas. *Nat Methods,* 11**,** 649-52.
SAKAI, A., CHIBAZAKURA, T., SHIMIZU, Y. & HISHINUMA, F. 1992. Molecular analysis of POP2 gene, a gene required for glucose-derepression of gene expression in Saccharomyces cerevisiae. *Nucleic Acids Res,* 20**,** 6227-33.
SANDLER, H., KRETH, J., TIMMERS, H. T. & STOECKLIN, G. 2011. Not1 mediates recruitment of the deadenylase Caf1 to mRNAs targeted for degradation by tristetraprolin. *Nucleic Acids Res,* 39**,** 4373-86.
SANDUJA, S., BLANCO, F. F., YOUNG, L. E., KAZA, V. & DIXON, D. A. 2012. The role of tristetraprolin in cancer and inflammation. *Frontiers in bioscience (Landmark edition),* 17**,** 174-188.
SCAPIN, G., DANDEY, V. P., ZHANG, Z., PROSISE, W., HRUZA, A., KELLY, T., MAYHOOD, T., STRICKLAND, C., POTTER, C. S. & CARRAGHER, B. 2018. Structure of the insulin receptor-insulin complex by single-particle cryo-EM analysis. *Nature,* 556**,** 122-125.
SCHERES, S. H. 2014. Beam-induced motion correction for sub-megadalton cryo-EM particles. *elife,* 3**,** e03665.
SCHILBACH, S., HANTSCHE, M., TEGUNOV, D., DIENEMANN, C., WIGGE, C., URLAUB, H. & CRAMER, P. 2017. Structures of transcription pre-initiation complex with TFIIH and Mediator. *Nature,* 551**,** 204-209.
SCHMIDLI, C., ALBIEZ, S., RIMA, L., RIGHETTO, R., MOHAMMED, I., OLIVA, P., KOVACIK, L., STAHLBERG, H. & BRAUN, T. 2019. Microfluidic protein isolation and sample preparation for high-resolution cryo-EM. *Proceedings of the National Academy of Sciences,* 116**,** 15007-15012.
SCHWANHÄUSSER, B., BUSSE, D., LI, N., DITTMAR, G., SCHUCHHARDT, J., WOLF, J., CHEN, W. & SELBACH, M. 2011. Global quantification of mammalian gene expression control. *Nature,* 473**,** 337.
SEMOTOK, J. L., COOPERSTOCK, R. L., PINDER, B. D., VARI, H. K., LIPSHITZ, H. D. & SMIBERT, C. A. 2005. Smaug recruits the CCR4/POP2/NOT deadenylase complex to trigger maternal transcript localization in the early Drosophila embryo. *Current Biology,* 15**,** 284-294.
SGROMO, A., RAISCH, T., BACKHAUS, C., KESKENY, C., ALVA, V., WEICHENRIEDER, O. & IZAURRALDE, E. 2018. Drosophila Bag-of-marbles directly interacts with the CAF40 subunit of the CCR4–NOT complex to elicit repression of mRNA targets. *RNA,* 24**,** 381-395.
SGROMO, A., RAISCH, T., BAWANKAR, P., BHANDARI, D., CHEN, Y., KUZUOGLU-OZTURK, D., WEICHENRIEDER, O. & IZAURRALDE, E. 2017. A CAF40-binding motif facilitates recruitment of the CCR4-NOT complex to mRNAs targeted by Drosophila Roquin. *Nature Communications,* 8.
SHARIF, H. & CONTI, E. 2013. Architecture of the Lsm1-7-Pat1 Complex: A Conserved Assembly in Eukaryotic mRNA Turnover. *Cell Reports,* 5**,** 283-291.
SHE, M., DECKER, C. J., SVERGUN, D. I., ROUND, A., CHEN, N., MUHLRAD, D., PARKER, R. & SONG, H. 2008. Structural basis of dcp2 recognition and activation by dcp1. *Mol Cell,* 29**,** 337-49.
SHIRAI, Y.-T., SUZUKI, T., MORITA, M., TAKAHASHI, A. & YAMAMOTO, T. 2014. Multifunctional roles of the mammalian CCR4-NOT complex in physiological phenomena. *Frontiers in genetics,* 5**,** 286-286.

SIGWORTH, F. J. 2016. Principles of cryo-EM single-particle image processing. *Microscopy (Oxf),* 65**,** 57-67.
SILVA, M. T., CARVALHO GUERRA, F. & MAGALHÃES, M. M. 1968. The fixative action of uranyl acetate in electron microscopy. *Experientia,* 24**,** 1074-1074.
SMITS, A. H., JANSEN, P. W., POSER, I., HYMAN, A. A. & VERMEULEN, M. 2013. Stoichiometry of chromatin-associated protein complexes revealed by label-free quantitative mass spectrometry-based proteomics. *Nucleic Acids Res,* 41**,** e28.
SONG, B., LENHART, J., FLEGLER, V. J., MAKBUL, C., RASMUSSEN, T. & BÖTTCHER, B. 2019. Capabilities of the Falcon III detector for single-particle structure determination. *Ultramicroscopy,* 203**,** 145-154.
SPASSOV, D. S. & JURECIC, R. 2003. The PUF family of RNA-binding proteins: does evolutionarily conserved structure equal conserved function? *IUBMB Life,* 55**,** 359-66.
STAGG, S. M., NOBLE, A. J., SPILMAN, M. & CHAPMAN, M. S. 2014. ResLog plots as an empirical metric of the quality of cryo-EM reconstructions. *J Struct Biol,* 185**,** 418-26.
STOWELL, J. A. W., WEBSTER, M. W., KOGEL, A., WOLF, J., SHELLEY, K. L. & PASSMORE, L. A. 2016. Reconstitution of Targeted Deadenylation by the Ccr4-Not Complex and the YTH Domain Protein Mmi1. *Cell Reports,* 17**,** 1978-1989.
SUZUKI, A., IGARASHI, K., AISAKI, K., KANNO, J. & SAGA, Y. 2010. NANOS2 interacts with the CCR4-NOT deadenylation complex and leads to suppression of specific RNAs. *Proc Natl Acad Sci U S A,* 107**,** 3594-9.
SUZUKI, A., SABA, R., MIYOSHI, K., MORITA, Y. & SAGA, Y. 2012. Interaction between NANOS2 and the CCR4-NOT deadenylation complex is essential for male germ cell development in mouse. *PLoS One,* 7**,** e33558.
TANG, T. T. L., STOWELL, J. A. W., HILL, C. H. & PASSMORE, L. A. 2019. The intrinsic structure of poly(A) RNA determines the specificity of Pan2 and Caf1 deadenylases. *Nature Structural & Molecular Biology,* 26**,** 433-442.
TEMME, C., ZAESSINGER, S., MEYER, S., SIMONELIG, M. & WAHLE, E. 2004. A complex containing the CCR4 and CAF1 proteins is involved in mRNA deadenylation in Drosophila. *The EMBO journal,* 23**,** 2862-2871.
TEMME, C., ZHANG, L. B., KREMMER, E., IHLING, C., CHARTIER, A., SINZ, A., SIMONELIG, M. & WAHLE, E. 2010. Subunits of the Drosophila CCR4-NOT complex and their roles in mRNA deadenylation. *Rna-a Publication of the Rna Society,* 16**,** 1356-1370.
TERPE, K. 2003. Overview of tag protein fusions: from molecular and biochemical fundamentals to commercial systems. *Applied Microbiology and Biotechnology,* 60**,** 523-533.
THARUN, S. & PARKER, R. 2001. Targeting an mRNA for decapping: displacement of translation factors and association of the Lsm1p-7p complex on deadenylated yeast mRNAs. *Mol Cell,* 8**,** 1075-83.
THORE, S., MAUXION, F., SÉRAPHIN, B. & SUCK, D. 2003. X-ray structure and activity of the yeast Pop2 protein: a nuclease subunit of the mRNA deadenylase complex. *EMBO reports,* 4**,** 1150-1155.
TOYOSHIMA, C. & UNWIN, N. 1988. Contrast transfer for frozen-hydrated specimens: determination from pairs of defocused images. *Ultramicroscopy,* 25**,** 279-91.
TUCKER, M., STAPLES, R. R., VALENCIA-SANCHEZ, M. A., MUHLRAD, D. & PARKER, R. 2002a. Ccr4p is the catalytic subunit of a Ccr4p/Pop2p/Notp mRNA deadenylase complex in Saccharomyces cerevisiae. *The EMBO Journal,* 21**,** 1427-1436.
TUCKER, M., STAPLES, R. R., VALENCIA-SANCHEZ, M. A., MUHLRAD, D. & PARKER, R. 2002b. Ccr4p is the catalytic subunit of a Ccr4p/Pop2p/Notp mRNA deadenylase complex in Saccharomyces cerevisiae. *EMBO J,* 21**,** 1427-36.
TUCKER, M., VALENCIA-SANCHEZ, M. A., STAPLES, R. R., CHEN, J., DENIS, C. L. & PARKER, R. 2001. The transcription factor associated Ccr4 and Caf1 proteins are components of the major cytoplasmic mRNA deadenylase in Saccharomyces cerevisiae. *Cell,* 104**,** 377-86.

UKLEJA, M., CUELLAR, J., SIWASZEK, A., KASPRZAK, J. M., CZARNOCKI-CIECIURA, M., BUJNICKI, J. M., DZIEMBOWSKI, A. & VALPUESTA, J. M. 2016a. The architecture of the Schizosaccharomyces pombe CCR4-NOT complex. *Nature Communications,* 7.

UKLEJA, M., VALPUESTA, J. M., DZIEMBOWSKI, A. & CUELLAR, J. 2016b. Beyond the known functions of the CCR4-NOT complex in gene expression regulatory mechanisms. *BioEssays***,** n/a-n/a.

UKLEJA, M., VALPUESTA, J. M., DZIEMBOWSKI, A. & CUELLAR, J. 2016c. Beyond the known functions of the CCR4-NOT complex in gene expression regulatory mechanisms New structural insights to unravel CCR4-NOT mRNA processing machinery. *Bioessays,* 38**,** 1048-1058.

UTHE, H., VANSELOW, J. T. & SCHLOSSER, A. 2017. Proteomic Analysis of the Mediator Complex Interactome in Saccharomyces cerevisiae. *Sci Rep,* 7**,** 43584.

VAN BRUGGEN, E. F. J., WIEBENGA, E. H. & GRUBER, M. 1960. Negative-staining electron microscopy of proteins at pH values below their isoelectric points. Its application to hemocyanin. *Biochimica et Biophysica Acta,* 42**,** 171-172.

VAN BRUGGEN, E. F. J., WIEBENGA, E. H. & GRUBER, M. 1962. Structure and properties of hemocyanins: I. Electron micrographs of hemocyanin and apohemocyanin from Helix pomatia at different pH values. *Journal of Molecular Biology,* 4**,** 1-IN6.

VAN ETTEN, J., SCHAGAT, T. L., HRIT, J., WEIDMANN, C. A., BRUMBAUGH, J., COON, J. J. & GOLDSTROHM, A. C. 2012. Human Pumilio proteins recruit multiple deadenylases to efficiently repress messenger RNAs. *Journal of Biological Chemistry,* 287**,** 36370-36383.

VAN HOOF, A., FRISCHMEYER, P. A., DIETZ, H. C. & PARKER, R. 2002. Exosome-mediated recognition and degradation of mRNAs lacking a termination codon. *Science,* 295**,** 2262-4.

VENTURINI, G., ROSE, A. M., SHAH, A. Z., BHATTACHARYA, S. S. & RIVOLTA, C. 2012. CNOT3 is a modifier of PRPF31 mutations in retinitis pigmentosa with incomplete penetrance. *PLoS Genet,* 8**,** e1003040.

VILLANYI, Z. & COLLART, M. A. 2016. Building on the Ccr4-Not architecture. *BioEssays,* 38**,** 997-1002.

VINOTHKUMAR, K. R. & HENDERSON, R. 2016. Single particle electron cryomicroscopy: trends, issues and future perspective. *Q Rev Biophys,* 49**,** e13.

VISWANATHAN, P., OHN, T., CHIANG, Y. C., CHEN, J. & DENIS, C. L. 2004. Mouse CAF1 can function as a processive deadenylase/3'-5'-exonuclease in vitro but in yeast the deadenylase function of CAF1 is not required for mRNA poly(A) removal. *J Biol Chem,* 279**,** 23988-95.

WAGNER, T., MERINO, F., STABRIN, M., MORIYA, T., ANTONI, C., APELBAUM, A., HAGEL, P., SITSEL, O., RAISCH, T., PRUMBAUM, D., QUENTIN, D., RODERER, D., TACKE, S., SIEBOLDS, B., SCHUBERT, E., SHAIKH, T. R., LILL, P., GATSOGIANNIS, C. & RAUNSER, S. 2019. SPHIRE-crYOLO is a fast and accurate fully automated particle picker for cryo-EM. *Communications Biology,* 2**,** 218.

WAHLE, E. & WINKLER, G. S. 2013. RNA decay machines: Deadenylation by the Ccr4-Not and Pan2-Pan3 complexes. *Biochimica Et Biophysica Acta-Gene Regulatory Mechanisms,* 1829**,** 561-570.

WANG, H., MORITA, M., YANG, X., SUZUKI, T., YANG, W., WANG, J., ITO, K., WANG, Q., ZHAO, C., BARTLAM, M., YAMAMOTO, T. & RAO, Z. 2010. Crystal structure of the human CNOT6L nuclease domain reveals strict poly(A) substrate specificity. *The EMBO journal,* 29**,** 2566-2576.

WANG, X., MCLACHLAN, J., ZAMORE, P. D. & HALL, T. M. T. 2002. Modular Recognition of RNA by a Human Pumilio-Homology Domain. *Cell,* 110**,** 501-512.

WANG, Y., SARKAR, M., SMITH, A. E., KROIS, A. S. & PIELAK, G. J. 2012. Macromolecular Crowding and Protein Stability. *Journal of the American Chemical Society,* 134**,** 16614-16618.

WANG, Y.-C., PETERSON, S. E. & LORING, J. F. 2014. Protein post-translational modifications and regulation of pluripotency in human stem cells. *Cell Research,* 24**,** 143-160.

WANG, Z. & KILEDJIAN, M. 2001. Functional link between the mammalian exosome and mRNA decapping. *Cell,* 107**,** 751-62.

WASMUTH, E. V., JANUSZYK, K. & LIMA, C. D. 2014. Structure of an Rrp6–RNA exosome complex bound to poly(A) RNA. *Nature,* 511**,** 435-439.
WAUGH, D. S. 2005. Making the most of affinity tags. *Trends in Biotechnology,* 23**,** 316-320.
WEBSTER, M. W., CHEN, Y. H., STOWELL, J. A. W., ALHUSAINI, N., SWEET, T., GRAVELEY, B. R., COLLER, J. & PASSMORE, L. A. 2018. mRNA Deadenylation Is Coupled to Translation Rates by the Differential Activities of Ccr4-Not Nucleases. *Mol Cell,* 70**,** 1089-1100.e8.
WEBSTER, M. W., STOWELL, J. A. & PASSMORE, L. A. 2019. RNA-binding proteins distinguish between similar sequence motifs to promote targeted deadenylation by Ccr4-Not. *Elife,* 8.
WEBSTER, M. W., STOWELL, J. A. W., TANG, T. T. L. & PASSMORE, L. A. 2017. Analysis of mRNA deadenylation by multi-protein complexes. *Methods,* 126**,** 95-104.
WEI, H., DANDEY, V. P., ZHANG, Z., RACZKOWSKI, A., RICE, W. J., CARRAGHER, B. & POTTER, C. S. 2018. Optimizing "self-wicking" nanowire grids. *J Struct Biol,* 202**,** 170-174.
WEIS, F., BECKERS, M., VON DER HOCHT, I. & SACHSE, C. 2019. Elucidation of the viral disassembly switch of tobacco mosaic virus. *EMBO reports,* 20**,** e48451.
WICKENS, M., BERNSTEIN, D. S., KIMBLE, J. & PARKER, R. 2002. A PUF family portrait: 3'UTR regulation as a way of life. *Trends Genet,* 18**,** 150-7.
WIEDERHOLD, K. & PASSMORE, L. A. 2010. Cytoplasmic deadenylation: regulation of mRNA fate. *Biochemical Society transactions,* 38**,** 1531-1536.
WINGFIELD, P. 1998. Protein Precipitation Using Ammonium Sulfate. *Current Protocols in Protein Science,* 13**,** A.3F.1-A.3F.8.
WINGFIELD, P. 2001. Protein precipitation using ammonium sulfate. *Current protocols in protein science,* Appendix 3**,** Appendix-3F.
WOLF, M., DEROSIER, D. J. & GRIGORIEFF, N. 2006. Ewald sphere correction for single-particle electron microscopy. *Ultramicroscopy,* 106**,** 376-382.
WREDEN, C., VERROTTI, A. C., SCHISA, J. A., LIEBERFARB, M. E. & STRICKLAND, S. 1997. Nanos and pumilio establish embryonic polarity in Drosophila by promoting posterior deadenylation of hunchback mRNA. *Development,* 124**,** 3015.
XU, K., BAI, Y. W., ZHANG, A. L., ZHANG, Q. L. & BARTLAM, M. G. 2014. Insights into the structure and architecture of the CCR4-NOT complex. *Frontiers in Genetics,* 5.
YAMASHITA, A., CHANG, T. C., YAMASHITA, Y., ZHU, W., ZHONG, Z., CHEN, C. Y. & SHYU, A. B. 2005. Concerted action of poly(A) nucleases and decapping enzyme in mammalian mRNA turnover. *Nat Struct Mol Biol,* 12**,** 1054-63.
YI, H., PARK, J., HA, M., LIM, J., CHANG, H. & KIM, V. N. 2018. PABP Cooperates with the CCR4-NOT Complex to Promote mRNA Deadenylation and Block Precocious Decay. *Mol Cell,* 70**,** 1081-1088.e5.
YU, H., BRAUN, P., YILDIRIM, M. A., LEMMENS, I., VENKATESAN, K., SAHALIE, J., HIROZANE-KISHIKAWA, T., GEBREAB, F., LI, N., SIMONIS, N., HAO, T., RUAL, J. F., DRICOT, A., VAZQUEZ, A., MURRAY, R. R., SIMON, C., TARDIVO, L., TAM, S., SVRZIKAPA, N., FAN, C., DE SMET, A. S., MOTYL, A., HUDSON, M. E., PARK, J., XIN, X., CUSICK, M. E., MOORE, T., BOONE, C., SNYDER, M., ROTH, F. P., BARABÁSI, A. L., TAVERNIER, J., HILL, D. E. & VIDAL, M. 2008. High-quality binary protein interaction map of the yeast interactome network. *Science,* 322**,** 104-10.
ZEKRI, L., HUNTZINGER, E., HEIMSTADT, S. & IZAURRALDE, E. 2009. The silencing domain of GW182 interacts with PABPC1 to promote translational repression and degradation of microRNA targets and is required for target release. *Mol Cell Biol,* 29**,** 6220-31.
ZHANG, K., LI, S., KAPPEL, K., PINTILIE, G., SU, Z., MOU, T.-C., SCHMID, M. F., DAS, R. & CHIU, W. 2019. Cryo-EM structure of a 40 kDa SAM-IV riboswitch RNA at 3.7 Å resolution. *Nature Communications,* 10**,** 5511.
ZHANG, X., VIRTANEN, A. & KLEIMAN, F. E. 2010. To polyadenylate or to deadenylate: that is the question. *Cell Cycle,* 9**,** 4437-49.
ZHAO, F.-Q. & CRAIG, R. 2003. Capturing time-resolved changes in molecular structure by negative staining. *Journal of structural biology,* 141**,** 43-52.

ZHENG, S. Q., PALOVCAK, E., ARMACHE, J.-P., VERBA, K. A., CHENG, Y. & AGARD, D. A. 2017. MotionCor2: anisotropic correction of beam-induced motion for improved cryo-electron microscopy. *Nature methods,* 14**,** 331-332.

ZIVANOV, J., NAKANE, T., FORSBERG, B. O., KIMANIUS, D., HAGEN, W. J. H., LINDAHL, E. & SCHERES, S. H. W. 2018. New tools for automated high-resolution cryo-EM structure determination in RELION-3. *eLife,* 7**,** e42166.

ZWARTJES, C. G., JAYNE, S., VAN DEN BERG, D. L. & TIMMERS, H. T. 2004. Repression of promoter activity by CNOT2, a subunit of the transcription regulatory Ccr4-not complex. *J Biol Chem,* 279**,** 10848-54.

8 Appendix

8.1 Data collection information for the evaluation of Falcon 3EC direct detector.

(Reproduced with permission according to CC license from Song et al., 2019)

Table 1 Data acquisition and image analysis of TMV

Magnification	75000		
Acquisition-mode	integrating		
Total Exposure (e^-/Å²)	58		
Exposure rate (e^-/Å²s)	12		
Exposure Time (s)	5,0		
Number of Frames	25		
Beam diameter (nm)	1000		
Number of Movies	1000		
Frame alignment	Motioncor2		
Defocus range (nm)	620-1870		
Processing Software	Relion		
Number of selected segments	393692		
Segments in best class	91927		
averaged units in best class	2941664		
Resolution (Å)*	2.53	2.30	2.30
WARP-ARP refinement # of built amino acids of helical patch of 34 ncs copies	5283	n.d.	n.d.
Warp/Arp Rfree	0.40	n.d.	n.d.

*) Resolution: The 1st number refers to the resolution at the end of image processing with relion 2.1- The 2nd number refers to the resolution with additional per particle ctf-refinement and per data set beam tilt correction (relion 3.0). The 3rd number refers to the resolution after additional correction for the curvature of the Ewald-sphere (relion 3.0).

Table 2 Data acquisition and image analysis of F97L -CLPs

Magnification	75000			75000		
Acquisition-mode	integrating			counting		
Total Exposure (e^-/Å²)	50			40		
Exposure rate (e^-/Å²s)	17			0.5		
Exposure Time (s)	3.0			75		
Number of Frames	40			31		
Beam diameter (nm)	1000			1000		
Number of Movies	2928			1616		
Frame alignment	Motioncor2			Motioncor2		
Defocus range (nm)	350-1200			350-1280		
Processing Software	Relion			Relion		
Number of selected particles	110487			88711		
Particles after 2D-classification	74080			65758		
Particles in best class	39382			45444		
averaged units in best class	2362920			2726640		
Resolution (Å)*	2.64	2.50	2.38	2.70	2.51	2.36

*) Resolution: The 1st number refers to the resolution at the end of image processing with relion 2.1. The 2nd number refers to the resolution with additional per particle ctf-refinement and per data set beam tilt correction (relion 3.0). The 3rd number refers to the resolution after additional correction for the curvature of the Ewald-sphere (relion 3.0).

Table 3 Data acquisition and image analysis of β-Galactosidase.

Magnification	75000			75000			
Acquisition-mode	integrating			counting			
Total Exposure ($e^-/Å^2$)	52			52			
Exposure rate ($e^-/Å^2s$)	12			0.8			
Exposure Time (s)	4.3			65			
Number of Frames	25			40			
Beam diameter (nm)	1000			1000			
Number of Movies	1389		1389	1748		1748	470
Frame alignment	Motioncor2		Motioncor2	Unblur		Unblur	Unblur
Defocus range (nm)	1150-2750		1150-2750	420-3260		460-3280	460-3280
Processing Software	Relion		cisTEM	Relion		cisTEM	cisTEM
Number of selected particles	307321		306289	374916		346781	96252
Particles after 2D-classification	245520		234222	n.d.		201858	66622
Particles in best class	146475		198059	152791		151117	60029
averaged units in best class	585900		792236	611164		604468	240116
Resolution (Å)*	2.85	2.41	2.63	2.62	2.24	2.28	2.42
WARP-ARP refinement # of built amino acids	4063	n.d.	4080	4071	n.d.	4083	4059
Warp/Arp R_{free}	0.33	n.d	0.38	0.33	n.d.	0.37	0.38

*) For the relion reconstructions: The 1st number refers to the resolution at the end of image processing with relion 2.1. The 2nd number refers to the resolution at the end of image processing with relion 3.0 (per particle ctf-refinement, per data set beam tilt correction).

8.2 Genomic DNA sequence used for epitope tagging and cloning.

a) *S. cerevisiae* Ubc4 genomic DNA. Reproduced from SGD website.

>UBC4 YBR082C SGDID:S000000286, chrII:406628..407169+/- 1kb

```
   1 GAACCGAGTA GGCCACACAT GTTTTGAATA TTGTAAGTGT GTACAATAAG CTGCAGTACT
  61 CTTTTGATTC TGTAGGAAAC CAGCGAAGAA CGTACTCTTG CCTGAAGAGA AGTTTTTTTT
 121 ATTTATTTAT ATTTTGTTCT GGAAGCTCTT TACAGAATGG AGTAGGAAAA TATATAGAGA
 181 GGAAAAGCGA AATCGTTACG AGAATAAATA ATCAAGAAAA GAAACTTGAA CTTGGCTTTT
 241 CCAAAACAAC AGAAGTAGCG TTAATTTACT TTCACCGTAA AATTCAACTC TTTAAATATA
 301 GTCCACTTAG TAAATTCTTG CCAATTTGCA TGATAAATTC GAACCCATTC CTCAAAATAA
 361 AGGGTCCTCA TACATTCCAT GGAAAGAAAG TTTTCTTGAA CATTAAGAAT AAAAAGGCAA
 421 AAAAGAAAAA AAAAAGCACA GCTACTGTTT TAGTCAACAT TCCTTTCTCA CTGGAATGCA
 481 CAAGGTGTCA TTCCTGAACA AGGGTAACTG CACTATTCAT ATGTCCACCT TATGACTTCA
 541 TAAAAAGTTT GACAATAAGT AGTCTTACGT GATAAGAAAT GATGTAACAT AAGGCTAATG
 601 TCCTTATTCC AAAGTATCTC ATTTATACAA TAAACAAAAC TGATCTTACC GCCTATCCTC
 661 CTCTCCGCAC TAATCAATTG TTATAGTTTT TCTCGAAGCG AGGATCAAAT GGCCGAGCAA
 721 CAGGAAAAGG AGTACCGGCG GTCACATGGT CTGCGAGATT TTTCCCGCTG CGGAAAAACC
 781 TGGCAACAGC TCACCTTGAA AGGCCTTGGC CTGTATTTTT CTTTTTTCTT CATCCTTCTT
 841 TCTTTTTCTT TATTCTTATT TTTCATCTTA ATAAATAATC CAGAGAATAA ATCTATCCTG
 901 AAAAAAAATA AAGTAAAGAA GCCAGGAAAA TCACTATCGC CACAAGTAAA TAAATTTCAC
 961 TGACTATAGA GTACATACAT AAACAAGCAT CCAAAAAAAC ATGTCTTCTT CTAAACGTAT
1021 TGCTAAAGAA CTAAGTGATC TAGAAAGGTA TGTCTAAAGT TATGGCCACG TTTCAAATGC
1081 GTGCTTTTTT TTTAAAACTT ATGCTCTTAT TTACTAACAA AATCAACATG CTATTGAACT
1141 AGAGATCCAC CTACTTCATG TTCAGCCGGT CCAGTCGGCG ATGATCTATA TCACTGGCAA
1201 GCATCCATCA TGGGACCTGC CGATTCCCCA TATGCCGGCG GTGTTTTCTT CTTGTCTATC
1261 CATTTCCCAA CCGACTACCC ATTCAAGCCA CCAAAGATCT CCTTCACAAC CAAGATATAT
1321 CATCCAAATA TCAATGCCAA TGGTAACATC TGTCTGGACA TCCTAAAGGA TCAATGGTCT
1381 CCAGCTCTAA CTCTATCGAA GGTCCTATTA TCCATCTGTT CTTTGTTAAC AGACGCTAAT
1441 CCTGACGATC CTTTAGTACC AGAAATCGCT CATATCTACA AGACTGACAG ACCCAAGTAC
1501 GAAGCTACAG CCAGAGAATG GACAAAGAAA TACGCTGTAT AAACAGAAGT CCTTACTCAG
1561 CTGAAAAAGA GAAGCAAGAT TTATATGGGA TTGGACGATG AAAAGAATAT TAGATACAAT
1621 GTATTTAAGA AAGAATACAA TAAAATATAT GTATATTCTA TCTCTAATAA CATAGATTTA
1681 CTGATATAAG ATATAAGACT ATTGTTGGCA ACAGTACAGG GGAACCTTTT TTTTTTTTTC
1741 CAAACAACTC GAATCGTAAA CCTTAATTTA ATTTATTCAG GGGAGATTCA TGAACATTTT
1801 TTTCCTCGAA CAGTATGGAG AATTTTTGCT TAGTTACATG CACGCAAGCG CGGGTATATC
1861 CCGCATATAT TTCAGTTGTG GTTCATATTT GACCTAACTT GTCGAGGGAG CGTCAACGTT
1921 AACCGTACCT TTTTCATTTC TAGTCTATCT GTAGGTTAAT TACTATTGTC ATTAACATCA
1981 TTTCTGGGGT GAAGCCTATT TAAATTTTTG AAGTTCAACG CATAGCTAGT ATATGTAATC
2041 AACGATCAAT GACTGGTTCT CTGTTTGGCA AAAATTCTGA GGAGCATTAC ACTGTACTAA
2101 GGAGGCAGAA GAATAACTGC AGGAGTAGCC AAAAAAATCT CCGCGACGGG GAATTGAACC
2161 CCGATCTGGC ACGCGACAAG CGCCCATTCT GACCATTAAA CTATCACGGA AGAAACAAAG
2221 CACTCACGAT GGGGGTCGAA CCCATAATCT TCTGATTAGA AGTCAGACGC GTTGCCATTA
2281 CGCCACGCGA GCTACTATTT GTTGAAGGTT TTATGAAATA ACGAAAACAT GTTTCCTCTA
2341 AAGATGGATG TGCTTCCAGT ATTATTCTTG TATGACAATT CATTTGTTTT TGGTGTCGGC
2401 TTGTATTAAA GACTTATATC TGTAATATAT CTGTATAAAT ACCAATGCAA GGATATATTA
2461 AATGAAAGTT AGCATATTTC AATTGGCTTT TTAGAATAAA GACGAAATTT TTTTAAAGGT
2521 AAAATACCCC ACTGAAACCT TA
```

Coding sequence
Introns

b) Ubc4 Expression and purification from bacteria

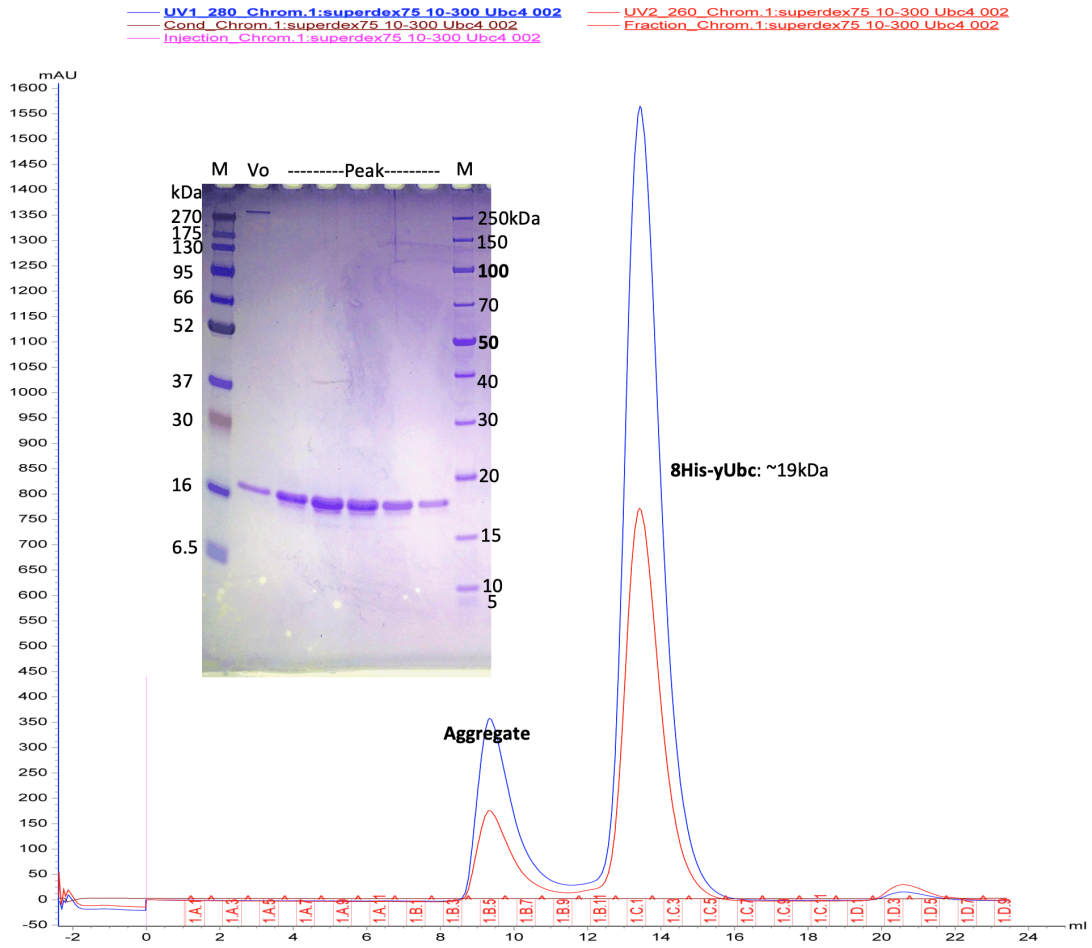

Appendix IV Figure 1 Size exclusion chromatogram from purifying yeast Ubc4. Inset: Coomassie stained SGS-PAGE showing migration of purified Ubc4 elution peak and void peak.

c) *S. cerevisiae* Not4/MOY2 genomic DNA. Reproduced from SGD website.

> MOT2 YER068W SGDID:S000000870, chr5.1:3214..4977

```
   1 TTCGTCTCCA CTTTAAATGA CAAAGAAGGA TAAGAAGGAA GTAAAAGTTC AAACGGTTAC
  61 CACGGAGGAT GGTGAAACCG TGAAAGTTTT TGAAGACCTG CAGGGTTTTG AAACTTTCAT
 121 TGCCAATGAA ACTGAAGATG ATGATTTCGA TCATTTGCAC TGTAAATTAA ATTACTACCC
 181 ACCATTTGTG CTACACGAGT CGCACGAGGA CCCTGAAAAA ATTAGTGATG CTGCAAATTC
 241 TCATTCTAAG AAGTTCGTGC GTCACCTGCA CCAGCATATT GAAAAGCATC TTTTGAAAGA
 301 TATTAAGCAA GCCGTTAGGA AACCTGAGCT TAAATTTCAC GAAAAATCGA AGGAAGAGAC
 361 ATTTGATAAA ATCACCTGGC ATTACGGTGA GGAAACTGAA TACCATGGTA GACCTTTCAA
 421 GATAGACGTT CAAGTAGTTT GCACACATGA AGATGCTATG GTATTTGTCG ATTACAAAAC
 481 ACATCCTGTA GGCGCAAATT AAAGGTTGTG TCATAGAGAA TGTGTTAGTA CTGAATCCTA
 541 ACCTCCCAAA TTCATAAGTA GTTTTATGTA CCTTTAATGA TTTACGATTA GCAACTTTTT
 601 GAATTTTTTT TATTGAAATG TTGAGCCCGA AGACGTGAAA CGCTATAAAG TAGTATCACT
 661 GTTACGCCGC GAAACCTGAT AATGTATTGT TAAACTACTA CCTGGTCGAT GATTATATCG
 721 ACGCTTCTAA AATGAATGCT ATTACCCGAA CTTCCACTTG ATTGCCGTCT CTTCCCGGGT
 781 AACATTGTAA GTGTGAATAT GATTTTTTTT TTTGCTTTCT CTTTTCAAAA TTTCCGAAAA
 841 GCATATCAAG ACGTGTACTA CATACAGTAA AAGCCCTCCT AGGGTTTTCA GTAGTGGTTC
 901 GAATAGTATA GATTACTGCT TTTGTTACTC TGCAACAATC CCAAAACTTA ATAAAAAGTA
 961 CAAAAGACCA AATAAAAGTA TCGTATATAA TCCAGTCATA ATGATGAATC CACACGTTCA
1021 AGAAAATTTG CAAGCAATCC ACAACGCCTT AAGCAATTTT GATACGTCAT TTTTATCGGA
1081 GGATGAAGAA GATTATTGCC CTCTTTGTAT TGAACCAATG GATATTACTG ATAAAAATTT
1141 TTTTCCTTGT CCCTGTGGTT ATCAAATTTG TCAATTTTGC TACAATAATA TCAGACAAAA
1201 TCCAGAATTA AATGGCCGTT GCCCAGCATG TCGTCGTAAA TATGATGACG AGAACGTCAG
1261 ATACGTCACA TTATCTCCGG AGGAGTTAAA AATGGAGAGA GCCAAGCTCG CTAGGAAGGA
1321 GAAAGAAAGA AAGCATAGAG AAAAAGAACG TAAAGAGAAT GAATATACGA ATAGGAAACA
1381 TTTATCTGGT ACCAGAGTTA TCCAAAAGAA TTTAGTGTAC GTTGTTGGCA TCAATCCTCC
1441 TGTTCCATAC GAGGAAGTTG CGCCCACTCT GAAATCTGAA AAATATTTTG GCCAATATGG
1501 TAAGATAAAT AAGATTGTGG TTAATAGAAA AACACCCCAT TCTAACAACA CAACCAGCGA
1561 GCATTATCAC CATCATTCAC CAGGATATGG CGTTTACATA ACCTTCGGAT CCAAGGACGA
1621 TGCTGCAAGA TGTATAGCTC AGGTAGACGG GACGTATATG GATGGCCGCC TGATCAAAGC
1681 TGCCTACGGT ACTACTAAAT ACTGTTCTTC TTATTTAAGA GGATTGCCAT GCCCAAATCC
1741 CAACTGTATG TTTTTGCATG AACCTGGTGA AGAAGCTGAT TCTTTTAATA AAAGAGAACT
1801 CCACAATAAA CAACAAGCGC AACAGCAAAG TGGCGGAACT GCATTCACTA GATCTGGAAT
1861 ACACAACAAT ATATCTACCA GTACCGCTGG TTCAAATACC AATTTACTAA GTGAAAATTT
1921 CACAGGCACA CCTTCACCGG CGGCGATGAG GGCTCAGTTA CATCATGACA GCCATACAAA
1981 CGCTGGAACA CCGGTATTAA CACCTGCTCC GGTCCCTGCA GGGTCAAATC CTTGGGGAGT
2041 TACTCAATCA GCAACACCTG TAACCTCTAT CAATCTCTCT AAAAACAGCA GCTCCATAAA
2101 CTTGCCAACA TTAAATGATT CTCTGGGCCA TCATACTACC CCCACAACAG AGAATACCAT
2161 CACAAGTACG ACAACTACTA CCAATACCAA TGCTACAAGT CACTCCCATG GTAGCAAGAA
2221 GAAGCAATCT CTTGCTGCAG AGGAATACAA AGATCCTTAT GACGCACTAG GGAATGCTGT
2281 TGACTTTTTG GATGCAAGAC TACATTCTCT ATCAAATTAT CAGAAGCGCC CTATATCTAT
2341 CAAATCCAAT ATTATTGACG AAGAAACTTA TAAAAAGTAT CCGTCTTTGT TTTCTTGGGA
2401 CAAGATTGAG GCCTCAAAGA AAAGTGACAA TACATTAGCC AACAAACTTG TGGAGATCCT
2461 GGCTATAAAG CCAATAGACT ACACTGCTTC TGTCGTTCAA TTCTTGCAGA GTGTCAATGT
2521 TGGTGTAAAT GACAATATTA CAATCACAGA TAATACGAAA ACTCCCACCC AACCAATAAG
2581 ACTGCAAACC GTCTCACAGC AAATCCAACC ACCATTAAAC GTCAGTACCC CTCCACCGGG
2641 TATCTTTGGT CCACAACATA AGGTTCCTAT TCAGCAGCAA CAAATGGGTG ATACAAGCTC
2701 AAGAAATTCC TCTGATTTAC TAAATCAACT AATCAACGGA AGGAAAATTA TCGCCGGTAA
2761 TTAATCCGAC TCTAAATATT TTTCTTGTTT GCATTAACCA TAATTTTATC TATTTTTATT
2821 TCTCATGAAT ATATAATCTC TCCGTTTATA ACGAAATGCA AGAAAAAAAA ATCTCACCCA
2881 TTTTTTTAAA CCTTTGACGT GGAAAGGTAT CTGGGAAAGG TATCTGGCTA ATGAATAATG
2941 CCATAGCATA TACCAGTATA GTCTATTTAC TCGTTACAAC GTATGAAAGC GTCAGCGCTG
3001 CAAGAATGAC TAATTCATAG AAAATAATCA TCATGATATA TATCATAATG CACGGAACCT
3061 GCTTCGCTAA TTTTTTCACT TAAATCACAT TTTTTCAACG AAATCTCTTG CGCAGTTGGT
3121 TGGAATTCTT ATCCGAATGA CTCAGTCTAC ATCAAAAAAC TGTGGCCGAA TGGTGGTAAT
3181 TGATGACTCT TCTATTTTTT TTTTTCATAT AAAGAGCTTG CGCGCGTGTT GTTGTTCGCT
3241 ATCCATTTCC ATTAGGAACA TTTTTGGATA TTATTTTTCA GACCCGTAAT ATACTTAACA
3301 CATATACCAC TAAAGGCAAA AGAAAGAGAG ATCTGAAGTG AGAAATAAGT CTGCATCATT
3361 ATGCCATCTG CTAGCTTACT CGTCTCGACA AAGAGACTTA ACGCTTCCAA ATTCCAAAAA
3421 TTTGTGTCTT CATTAAACAA ATCCACCATA GCAGGATTTG CATCTGTACC CTTGAGAGCT
3481 CCACCATCCG TTGCATTTAC GAGAAAGAAA GTCGGATACT CAAAGAGGTA TGTTTCATCT
3541 ACTAACGGCT TTTCAGCTAC TAGATCCACT GTGATCCAAC TGTTGAACAA TATCAGCACA
3601 AAAAGAGAGG TTGAACAATA TTTGAAATAT TTCACTTCCG TCTCACAACA ACAATTTGCT
3661 GTGATCAAGG TGGGTGGTGC CATTATCAGC GACAATCTAC ACGAACTCGC TTCCTGCTTG
3721 GCATTTTTGT ATCATGTTGG TCTATATCCA ATAGTTTTAC ATGG
```

Coding sequence

d) *S. cerevisiae* Not5 genomic DNA. Reproduced from SGD website.

```
   1 GATAGAGGTT ATAATTTTAG ACAGGCAAAA TATTCTAGCA CTTCTCGAGG GCATAGGCAT
  61 CCCTAAAAGG GAATCAATAA TTTTACATAA TGATATTACC ATATCTTTTA TACTTTCTTG
 121 AGATCTGGAG AATTTTGTAA AATTGTTGGG ATTCCATAGT CGATAATATT ATATATACAG
 181 AATATGCTAG AAGTTCCAAT CATTACACTT TAACTTCAAT AAAAAATTTG GCGACTACTT
 241 CCCAATCTTT ATGTCATCTT CTTGCATCGT ATATGACAAT ATGTAACAGT AATATGAATA
 301 ATAGTCAAAA AATAATATAT AATATTCATT CCAACACTCT TAGTGTCCCT AGCTAGAATT
 361 ACTTCTGCTA GTGAAACACT CATCATCAAT ATAAGGAAAT TAATTTTAGT CAGATGTTTT
 421 TAATACCTTC CGTTTTCTAA CACTACCAGA TTATTTTGGG CACTATGGCC GAGTGGTTAA
 481 GGCGACAGAC TTGAAATCTG TTGGGCTCTG CCCGCGCTGG TTCAAATCCT GCTGGTGTCG
 541 TATTATTTTT TGAAATTATT TTTCAATAAC CACCATGTCA GCACCAGGTT CTTTTACAAT
 601 TATACAAACA CACATATCTC AAAATCACTC AAGAGGTCAT GGACCAATAT GGCAACTTGC
 661 TACGAAAGTC ATACGGTAAC ATATCAGCTT GTCTAAACAT ACCATACTTT ACCCATTTTT
 721 TTGTGCTTGT TATATGGCGC CATAAATTGC TCGAACATGG TCATGTGATG CAAAACATTG
 781 TATTACCCTT CTTTATTGAT TTTTCGACAA TCCACCAATT CTAACTACGA AACTTTTTAT
 841 AGCATAAAAG TACTTCCACA TTTTTGGTGC AATGAACTAA TTTAGATAAT AACAAGATCA
 901 AACAGCGTCC CTTCCGCGTC AATAAATAAT TAGGAACTGT AATTGAACCT CTATTAGTAT
 961 ATTTTTTTAT TGATTGCATG AAACATCCGC TCATTCTGTC ATGTCTCAAA GAAAGCTACA
1021 ACAGGATATC GATAAGCTTT TGAAGAAGGT GAAGGAAGGT ATTGAAGACT TCGATGACAT
1081 ATACGAAAAA TTTCAGTCAA CAGACCCCTC CAATTCTTCG CATAGAGAAA AACTGGAATC
1141 TGACTTAAAA AGAGAAATCA AGAAGCTGCA AAAACATAGG GATCAAATAA AAACATGGCT
1201 CAGCAAAGAA GATGTAAAGG ATAAGCAAAG TGTTCTGATG ACTAATAGGA GGTTGATTGA
1261 AAATGGCATG GAAAGATTTA AGTCCGTGGA GAAGCTAATG AAGACAAAAC AGTTTTCAAA
1321 GGAGGCTTTA ACAAATCCAG ATATAATCAA AGACCCTAAA GAACTCAAAA AAAGAGATCA
1381 GGTCTTATTT ATTCACGATT GTTTAGATGA GCTACAAAAG CAATTGGAAC AGTATGAGGC
1441 TCAAGAAAAT GAAGAACAAA CAGAAAGACA CGAATTTCAC ATCGCCAACC TAGAGAATAT
1501 CTTGAAAAAA CTTCAGAATA ATGAAATGGA CCCAGAGCCC GTAGAAGAAT TCCAAGACGA
1561 TATAAAGTAC TATGTAGAAA ATAACGATGA TCCCGATTTC ATTGAATACG ATACAATTTA
1621 TGAGGACATG GGTTGCGAAA TACAACCTTC ATCAAGTAAT AATGAGGCTC CAAAAGAAGG
1681 AAACAATCAA ACTTCTTTAT CTAGCATTCG CTCATCAAAA AAACAAGAAC GTTCTCCAAA
1741 GAAAAAAGCT CCGCAGAGGG ATGTTTCTAT ATCAGACAGG GCGACGACTC CAATCGCGCC
1801 AGGTGTAGAA TCAGCCTCGC AATCTATATC TTCTACGCCA ACACCTGTGT CAACTGATAC
1861 GCCATTGCAT ACAGTGAAAG ATGATTCAAT AAAATTCGAT AATTCTACCC TTGGTACACC
1921 AACTACACAT GTGTCTATGA AAAAGAAGGA ATCGGAAAAC GACTCGGAGC AACAACTAAA
1981 TTTCCCACCG GATAGAACTG ATGAAATTCG AAAAACCATC CAGCACGATG TAGAGACGAA
2041 TGCAGCTTTT CAAAATCCCT TATTCAACGA CGAATTAAAA TACTGGTTAG ACTCGAAAAG
2101 GTACTTAATG CAACCTCTTC AAGAAATGTC ACCAAAGATG GTATCGCAAT TAGAATCTTC
2161 GCTATTGAAT TGTCCAGATT CTCTAGATGC CGATTCGCCA TGTCTATACA CCAAACCATT
2221 ATCTTTGCCT CACCCAACGT CAATCTTTTT TCCCAATGAA CCAATTCGAT TTGTTTATCC
2281 GTACGATGTA CCTTTAAATT TAACGAATAA TGAAAATGAT ACTGACAATA AGTTCGGTAA
2341 AGATAGTAAA GCAAAATCTA AGAAAGATGA TGATATCTAT TCCAGAACCT CACTAGCCAG
2401 AATATTTATG AAATTTGATC TTGATACTTT ATTTTTCATA TTCTATCATT ACCAAGGATC
2461 ATATGAACAG TTTTTAGCTG CTAGAGAACT TTTTAAAAAT AGAAACTGGC TATTCAACAA
2521 GGTAGATCGC TGCTGGTATT ATAAAGAAAT CGAAAAGTTA CCACCAGGAA TGGGCAAATC
2581 TGAGGAGGAA TCATGGAGAT ACTTTGATTA TAAAAAAAGT TGGTTAGCGA GACGTTGCGG
2641 TAACGACTTC GTATATAATG AAGAAGATTT CGAAAAACTG TAAACAGTTT CCTTTTACTT
2701 ATATAATTCT CATCGTGATT TACTAGGTAA ATGTAGTATT CAAAATCTCC AATTTGTACT
2761 CTTTAACTTC ACCTTCACAT ATTATCTTTT TACTCGATGT AGACCGCACC ATCATTACTT
2821 GCTAGCTTAT AACTCTTTTT TTAAAAACTG TTTGGAGAAA TAGGTGATTT GTTTGAAGTT
2881 GTACTCGAAA TCTTGTATGT CACCATACCA AGGATCTTCA ATAATGGTCT GCACAGTGCC
2941 ATCATTAGTA TTCCAATCAC CAAAAAGGCA AACTTTAGCT TTAGAACCTT CAGGTTGTAT
3001 TTTTTTTAGG TTATTAATGT TGGATTCATC CATACCGATT ATATAGTCAT ATTCATCGAA
3061 GTGTTTGGTC TTTATTTGTT TCCCTTTATG ATTAATCTTG ACGCCATGTT GCTTACAAAT
3121 GGACACTGTA CGATGATCAG GGCTTTCCCC CACATGATAA TTAGAAGTGC CAAATGAATC
3181 AATCTTGTTG AATCGATTTT CTAGATTAGC CTTTTCGACT TCATGTTTGA AAATGGCTTC
3241 CGCCATTGGT GATCTACAGA AGTTACCCAA ACAAATGAAT GCGACCGATA TTTTTGGTTT
3301 TTCAATTGTC ATTTTCGTGT TAACTTTCCC TTCTCAGTTT TCTATCGCTT ATCAAAAATC
3361 ACAGGGTTTC AATTAGCCTT TTAGGAGTTA TATTCTTTAT TGGCTTTATA CTTGAATGGT
3421 GTGATTCTCT CGAAGGGTTT AACATTCAAG CTCGGCCATG TGCTGGTACA AGGAAAAAGA
3481 AAGAAAAAGT AATCATTGAA ATTTTTCTAT AATACGTACA CCTATAATAT AAGAAGGAAA
3541 AGGACTGAGT GTTTGGAATA TTGTTAAAAG TTTGAAACTA TTTTTTTGCT TAATCGTTTA
3601 TAAAAAAAGT TGTATTTAAG TTGTATAAAG TTTTATTTCA TTTTTTCACA AATAATATCA
3661 TATCAAATCT GATGATCTAC GAT
```

Coding sequence

8.3 Sequence alignment from Uniprot database.

a) *S. cerevisiae* Not3/Not5 sequence alignment.

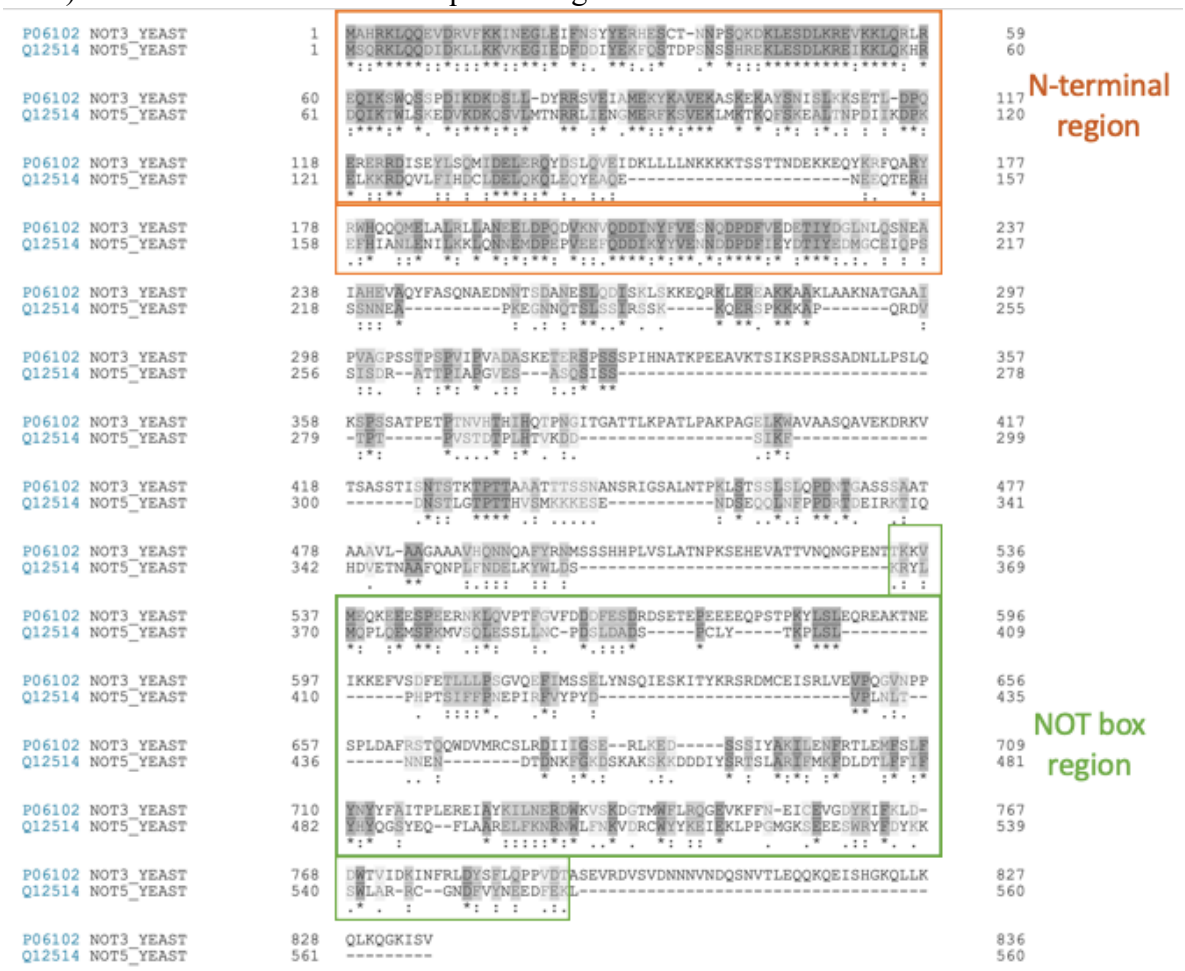

b) *S. cerevisiae* Not5/Not2 sequence alignment.

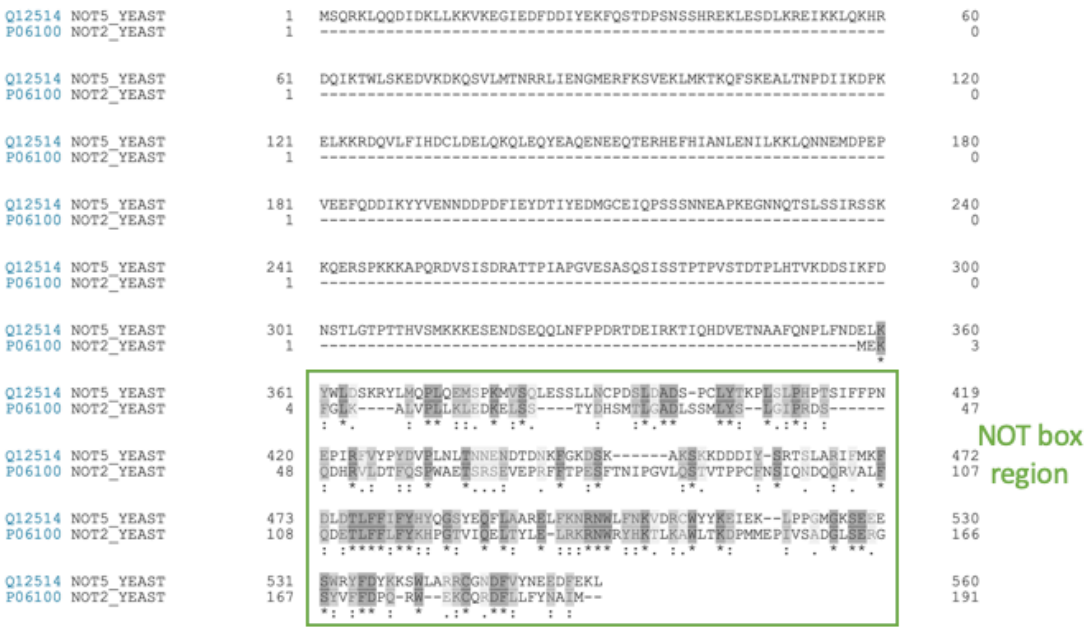

c) *S. cerevisiae, Human and Mouse* Not4 sequence alignment.

8.4 Ubiquitination assay with crosslinked Ccr4-Not

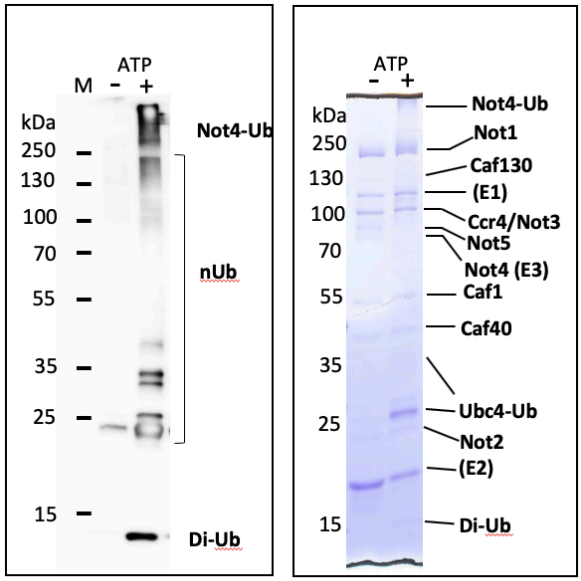

Appendix Figure 2. Ubiquitination assay using Grafix crosslinked Ccr4-Not complex. Reaction was set-up according to ubiquitination protocol described in Methods. Left) Western blot against Ubiquitin. High molecular weight component is visible above 250kDa for sample with ATP. Right) Proteins resolved on 12% polyacrylamide SDS-PAGE, smearing of high molecular weight components above 250kDa and similar to in the western blot can be seen.

Abbreviations

2D	2-dimension
3D	3-dimension
Abs	absorbance
ADC	analogue-to-digital convertor
AMP	adenosine monophosphate
APS	ammonium persulfate
ARM	armadillo repeat motif
ATP	adenosine triphosphate
AWI	air-water-interface
BSA	bovine serum albumin
CCD	charge-coupled device
Ccr4-Not	carbon catabolite repression—negative on tata-less
CMOS	complementary metal oxide semiconductor
CP	catalytic particle
CryoEM	transmission electron cryo-microscopy
CTF	contrast transfer function
DED	direct electron detector
DQE	detective quantum efficiency
DNA	deoxyribonucleic acids
DMSO	dimethyl sulfoxide
dNTP	deoxynucleotide triphosphate
DTT	dithiothreitol
EC	electron counting
EDTA	ethylenediaminetetraacetic acid
EM	electron microscopy
FAM	fluorescein amidites
FEG	field emission gun
FT	Fourier transform
GA	glutaraldehyde
GF	gel filtration
Grafix	gradient density fixation
HEAT	huntingtin, elongation factor 3, subunit of protein phosphatase2a and the TOR lipid kinase
HEPES	4-(2-hydroxyethyl)-1-piperazineethanesulfonic acid
HPLC	high performance liquid chromatography
HRP	horse reddish peroxidase
IPTG	isopropyl β- d-1-thiogalactopyranoside
LB	luria–bertani medium
LFQ-MS	label-free quantitative mass spectrometry
MAPS	monolithic active pixel sensors
mRNA	messenger ribonucleic acid
MWCO	molecular weight cut-off
NAC	nascent polypeptide associated complex
NAD	nicotinamide adenine dinucleotide
NGD	no-go decay
NMD	nonsense mediated decay

NSD	non-stop decay
OD_{600}	optical density at 600nm
PABP	PolyA binding protein
PAGE	polyacrylamide gel electrophoresis
PCR	polymerase chain reaction
PEG	polyethylene glycol
PMSF	phenylmethane sulfonyl fluoride
Poly(A)	poly-adenosine
PRE	Puf response element
PUF	pumilio homology domain factor
PVDF	polyvinylidene difluoride
RBP	rna binding protein
RING	really interesting gene
RNA	ribonucleic acid
RP	regulatory particle
RRM	rna recognition motif
SDS	sodium dodecyl sulfate
SEC	size exclusion chromatography
SNR	signal-noise-ratio
SORB	sorbitol
SPA	single particle analysis
ß-ME	beta-mercaptoethanol
TAE	tris acetate-edta
TAP	tandem affinity purification
TBE	tris borate-edta
TBS	tris-buffered saline
TBST	tris-buffered saline/tween20
TCEP	tris(2-carboxyethyl) phosphine
TEM	transmission electron microscope
TEMED	n,n,n',n'-tetramethylethane-1,2-diamine
TGX	tris-glycine
Tris	tris(hydroxymethyl)aminomethane
UA	uranyl acetate
UTR	untranslated region
UV	ultraviolet

List of Figures

List of Tables

This page intentionally left blank.

This page intentionally left blank.

This page intentionally left blank.